

# **Application and Optimisation of the Spatial Phase Shifting Technique in Digital Speckle Interferometry**

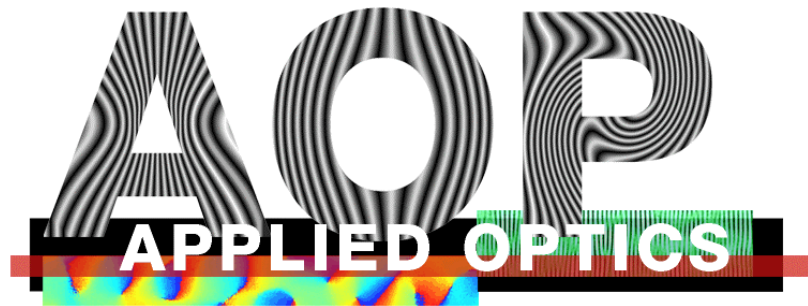
Vom Fachbereich Physik der  
Carl von Ossietzky Universität Oldenburg  
zur Erlangung des Grades eines  
Doktors der Naturwissenschaften (Dr. rer. nat.)

angenommene Dissertation von

**Jan Burke**

geboren am 13. Juli 1967

in Kiel

The logo for Applied Optics (AOP) features the letters 'AOP' in a large, bold font. Each letter is filled with a different optical interference pattern: the 'A' has a triangular pattern, the 'O' has a circular pattern, and the 'P' has a wavy pattern. Below the letters, the words 'APPLIED OPTICS' are written in a smaller, white, sans-serif font on a black rectangular background. The background of the logo is a colorful, multi-colored pattern.

Erstreferent: Prof. Dr. Klaus Hinsch

Korreferent: Prof. Dr. Volker Mellert

Tag der Disputation: 25. Oktober 2000

---

<b>1 INTRODUCTION</b>	<b>3</b>
<b>2 STATISTICAL PROPERTIES OF SPECKLE PATTERNS</b>	<b>7</b>
<b>2.1 Experimental set-up</b>	<b>7</b>
<b>2.2 First-order speckle statistics</b>	<b>10</b>
2.2.1 Basic probability-density function	10
2.2.2 Intensity and phase	11
2.2.3 Gradients in one dimension	12
2.2.4 Gradients in two dimensions	21
2.2.5 Zero-intensity minima	26
<b>2.3 Second-order speckle statistics</b>	<b>33</b>
2.3.1 Intensity autocorrelation	33
2.3.2 Phase autocorrelation	35
2.3.3 Second-order probability densities	37
<b>3 ELECTRONIC OR DIGITAL SPECKLE PATTERN INTERFEROMETRY</b>	<b>47</b>
<b>3.1 Subtraction-mode ESPI</b>	<b>49</b>
<b>3.2 Phase-shifting ESPI</b>	<b>51</b>
3.2.1 Calculation of phase changes in ESPI	54
3.2.2 Spectral transfer properties of few-sample phase shifting formulae	61
<b>3.3 Temporal phase shifting</b>	<b>75</b>
3.3.1 Speckle "size" in interferograms	76
<b>3.4 Spatial phase shifting</b>	<b>79</b>
3.4.1 Geometrical description of spatial phase shift	81
3.4.2 Evaluation of SPS interferograms	83
3.4.3 Relation of speckle size and magnification	85
3.4.4 Spatial phase shifting on speckle fields	86
3.4.5 Spectral side-effects of spatial phase calculation	88
3.4.6 Distorted phase distributions due to miscalibrated phase shift	94
<b>4 QUANTIFICATION OF DISPLACEMENT-MEASUREMENT ERRORS</b>	<b>99</b>
<b>4.1 Previous methods</b>	<b>99</b>
4.1.1 Processing of correlation fringes	99
4.1.2 Processing of sawtooth fringes	101
<b>4.2 Noise quantification in this work</b>	<b>106</b>

<b>5 COMPARISON OF NOISE IN PHASE MAPS FROM TPS AND SPS</b>	<b>111</b>
5.1 The experimental set-up	112
5.2 Preliminary investigations	114
5.2.1 Choice of phase shift	114
5.2.2 Reproducibility of the $\sigma_d$ values	115
5.3 Zero-displacement-gradient measurements	116
5.4 Out-of-plane displacements	118
5.5 In-plane displacements	120
5.5.1 Mixed-sensitivity interferometer	121
5.5.2 Purely in-plane sensitive interferometer for TPS	123
5.5.3 Purely in-plane sensitive interferometer for SPS	124
5.5.4 Direct comparison of the in-plane geometries	128
5.6 Impact of light efficiency	129
<b>6 IMPROVEMENTS ON SPS</b>	<b>133</b>
6.1 Optimisation of experimental parameters	133
6.1.1 Beam ratio	133
6.1.2 Phase shift	135
6.1.3 Speckle aspect ratio	137
6.2 Modified phase reconstruction formulae	140
6.2.1 Consideration of speckle intensity gradients	140
6.2.2 Consideration of speckle phase gradients	142
6.2.3 Combined intensity and phase gradient compensation	144
6.3 Modified phase shifting geometry	146
6.4 Reduction of speckle size	152
6.5 Fourier transform method of phase determination	153
6.6 Use of depolarisation to eliminate invalid pixels	159
6.7 Extensions of SPS by temporal unwrapping	164
6.7.1 Temporal unwrapping of speckle phases	166
6.7.2 Long-term observation of biological object	168
6.7.3 Relative displacements of discontinuous object	171
<b>7 SUMMARY</b>	<b>175</b>
<b>8 REFERENCES</b>	<b>179</b>

## 1 Introduction

The present era of high technology, with its enormous production capacities and ever-increasing rate of invention, has generated a great need for tools to make new solutions reliable and safe. It is indispensable to test prototypes experimentally to find design flaws, improve concepts and increase outputs. In serial production of delicate and expensive items, it is desirable to distinguish faulty pieces quickly from good ones without subjecting them to excessive stress and possibly destroying them; consequently, these methods are referred to as non-destructive.

While non-destructive testing (NDT) supports industrial development, it is also suitable to deal with some consequences of industrialisation, which has given rise to environmental pollution, changing into destruction in the past few decades. Due to air pollution, the decay of historical buildings and monuments has accelerated in a disquieting way since about the middle of the 20<sup>th</sup> century. In exact opposite to serial production, the role of NDT in this context is to assist in valuation of measures to preserve unique works of art. The Applied Optics workgroup at the Carl von Ossietzky University of Oldenburg has been working in this field for more than two decades.

Interferometry is an elegant way to accomplish these contradictory tasks, with the additional benefit of being non-contacting, in contrast to, e.g., strain gauges. The sensitivity of interferometric methods depends largely on the wavelength of the used radiation; for the optical wavelength range, the sub- $\mu\text{m}$  scale is therefore easily accessible, and with some care, even the nm scale can be reached. Since the invention of strong sources of coherent light [Mai60], interferometric methods can be conveniently utilised for a multitude of measuring problems.

However, with the advent of masers and lasers, the so-called speckle effect, known since the 19<sup>th</sup> century, became very important. As opposed to classical interferometry with polished parts like lenses and mirrors, optically smooth surfaces are generally rare; they seldom occur in industrial processes, and almost never in studies of historical objects. The wavefront coming back from a scattering object has a random intensity and phase structure, the speckle pattern; therefore, a general approach to interferometry requires comparing such a wavefront with itself.

This was initially done by holographic interferometry, where a hologram of the object provides the reference. By viewing the object through the hologram, a real-time interference of the reference and the slightly different momentary wavefront is observed. Depending on whether the wavefronts are locally in phase or out of phase, the object appears covered by a pattern of bright and dark fringes that can easily be interpreted as iso-lines of equal object deformation. Thanks to the high spatial resolution of holographic silver halide emulsions, these fringes are very clear for the most part and very small speckles are allowable.

A significant disadvantage of holographic interferometry is the necessity of relatively long exposure times, typically about a second; therefore great stability, most probably in a laboratory, is required, or

pulse lasers must be used. Also, the wet processing of the holographic plate takes some time. Therefore, it is difficult to carry out in-situ measurements, or quick serial testing, with holographic interferometry.

Moreover, it has been realised quite early [But71, Enn97] that holographic resolution is superfluous in many applications and that useful displacement information can also be obtained from a much coarser speckle pattern. This enables the use of two-dimensional solid-state light detector arrays with a relatively poor resolution, but high sensitivity and short exposure times in the ms range, and electronic image processing. This was the invention of TV holography or electronic speckle pattern interferometry (ESPI) that has evolved into a very powerful diagnostic method in the 1970s. The disadvantage of high speckle noise in the fringe patterns is more than outweighed by the mobility and real-time capability. Moreover, ESPI is more environmentally friendly since no chemical waste is produced.

When computer technology gathered speed in the 1980s, ESPI was soon extended by digital image processing methods and called digital speckle pattern interferometry (DSPI) but today the term ESPI includes both analogue and digital methods, enabling e.g. analysis of microstructure changes and static as well as periodical or transient dynamic displacements.

Since the brightness of the (two-beam) interference has a cosinusoidal profile, it does not reveal information about the sign of the displacement gradient, e.g., an elevation on the object gives the same fringe pattern as a depression of the same magnitude. To get rid of this ambiguity, a technique called synchronous detection was adopted from communication theory, initially for interferometry of smooth surfaces. It relies on retrieving several samples of the interference intensity while the optical phase difference between object and reference wavefront is being varied stepwise or linearly. With the intensity being proportional to the cosine of the phase difference, one can establish an equation system into which the actual intensity readings are inserted to solve for the phase difference unambiguously. This approach is today known as temporal phase shifting (TPS). It enhances accuracy and opens up a way to largely automatic data evaluation. In practice however, the shifts of the reference phase never coincide perfectly with theory, since time- and space-dependent disturbances, as vibrations of the interferometer, fluctuations of the medium's optical properties, or even occasional rapid movement of the object itself, are hard to suppress. Hence, measurement errors are introduced or the data are even useless.

The time-dependent part of the disturbances can be efficiently minimised when the phase-shifted data are recorded simultaneously. There are several ways to do so; all of them can be summarised under the term spatial phase shifting (SPS). For this approach, the necessary phase-shifted images are generated statically on several image sensors, or on separate or interlocked parts of one sensor; hence the phase shifts are constant in time. Provided the exposure time is sufficiently short, it thus becomes possible to "freeze" all motion and obtain clear phase maps even under adverse conditions. Space-dependent errors, as generated by, say, inhomogeneities of the medium, cannot be suppressed by SPS either.

As no dynamic phase shifting is involved, SPS systems do not require moving parts and controlling subsystems, which is advantageous in mobile use. Moreover, the built-in capability of real-time phase

retrieval can help to increase the temporal resolution of measurements. The implementation of SPS is by far easiest with the so-called "spatial-carrier" approach; in a different terminology, this method would be called off-axis image-plane (TV) holography (cf. [Lei62]). By suitable adjustment of the reference wavefront, the speckle interferogram acquires a "carrier" fringe pattern, so that the phase difference between object and reference wave varies linearly in one spatial direction. The phase signal is encoded in slight variations of this carrier fringe pattern and the phase-shifted data are available from a one-dimensional spatial sequence of sensor pixels.

With this simple method however, there are some disadvantages to SPS in speckle interferometry. The abovementioned equation system for phase reconstruction contains three unknowns: the background intensity, the interferometric modulation depth, and the phase difference between the interfering wavefronts. These quantities are assumed constant in solving for the phase difference, but the phase-shifted intensity data come from – at least three – adjacent sensor elements, this is, different portions of the object's speckle field. Therefore the random spatial variations of intensity and phase that are characteristic of (and ultimately make up) a speckle pattern will impair the phase calculation because the constancy assumptions are always more or less violated. Hence, the speckle size must be large enough to obtain the phase-shifted data (statistically) from an area with sufficient spatial coherence, i.e. with tolerable fluctuations of the interferometric parameters. This entails a loss in spatial resolution of the measurement, as well as a less economic utilisation of the object light, because the imaging aperture must be stopped down to obtain larger speckles.

Due to these "built-in" drawbacks, deformation measurements with SPS can be expected to yield a somewhat inferior fringe quality than those with TPS, as long as the latter can operate in a sufficiently stable environment. Indeed, SPS appears to be considered as an alternative in speckle interferometry only under very unstable conditions, and much effort has been spent on using TPS even in such applications. Consequently, TPS has been investigated much more thoroughly than SPS.

Spatial-carrier SPS set-ups are so easy to construct and use that one can expect them to be rather useful in practice. However there seemed to be a need for a deeper understanding of why, how, and how well spatial phase sampling works in speckle interferometry.

The first aim of the present study is to provide a theoretical background for what one is doing when extracting phases from a speckle field. While it has been observed before that phase measurements are easily made with the SPS technique, the speckle aspect of the measurement has received only marginal attention; in fact, little material is hitherto available that goes beyond the basic observations already stated above.

A second main objective is to settle the question whether the common preference of TPS is justified, and to see in what situations one could possibly do without TPS and still obtain "good" measurements with SPS. In this context, it is also worthwhile to utilise the theoretical insights for improving the phase reconstruction by SPS, and also to explore the versatility of SPS in practical tasks.

Chapter 2 starts with a detailed survey of first- and second-order speckle statistics; but besides compiling and grouping today's knowledge of this field, we will keep an eye on the intended application to SPS, where the phase shift takes place in one spatial direction, and put some emphasis on the one-dimensional intensity and phase gradients. To illustrate the theoretical findings, experimental results from a large-speckle interferometer are provided.

In Chapter 3, we will review and discuss the groundwork for ESPI and phase shifting, spending some theoretical and experimental effort on finding the best way to calculate speckle phase differences. Then, since SPS must rely on simple phase-sampling formulae with 3 or 4 samples, we examine the spectral characteristics of such formulae by Fourier analysis and become acquainted with a useful generalisation of their spectral behaviour. In the subsection on TPS, an easy way to determine small speckle sizes is presented. The remainder of the chapter is concerned with a thorough investigation of the peculiarities of SPS in ESPI.

Since it is our aim to quantify measurement accuracies, we need to obtain reference data with which we can compare the experimental results. Chapter 4 is dedicated to this subject and starts with an overview of methods that can be used to approximate ideal data, pointing out their strengths and weaknesses. This discussion leads to the proposal of a new method which can generate noise-free images from a certain class of fringe patterns with almost arbitrary amounts of noise, so that a standardised error quantification is at our disposal.

In Chapter 5, the performance of SPS and TPS is experimentally compared to settle the question how close the accuracy delivered by SPS measurements can get to that of the widespread and well-established TPS method. Various experimental parameters are explored, such as object/reference intensity ratio, phase shift, speckle size/shape and fringe density. The most common interferometer geometries are implemented for both TPS and SPS to get a "three-dimensional" view of the measurement errors. The last subsection is dedicated to the issue of light efficiency that is among the most critical ones in practice.

Having learnt about the performance of SPS when implemented in a "standard" manner, we explore various ways in Chapter 6 to improve the phase determination by means of SPS. Some computational methods to diminish the influence of speckle intensity and/or phase fluctuations are discussed; but also a change in the direction of the phase shift is shown to be helpful. With the assistance of these improvements, we make the speckles as small as possible without sacrificing accuracy. Leaving the terrain of phase sampling, we also consider the Fourier transform method as a candidate for *a posteriori* data processing.

The last possibility of error reduction that we study is the merging of informations from orthogonally polarised speckle fields produced by a de-polarising object, which reduces the influence of noisy pixels.

Finally, the single-frame measurement capability of SPS is combined with the temporal phase unwrapping method to solve two practical tasks in ESPI: automatic control of data storage in long-term observations and displacement measurement of discontinuous objects.



## 2 Statistical Properties of Speckle Patterns

When a rough object is illuminated coherently, e.g. by a laser, the light field scattered back from it acquires a random, grainy structure. The object can be considered "rough" as soon as the surface height variations are on the scale of the light's wavelength. The irregular light field extends into space, and at each spatial point we find a coherent superposition of many scattered elementary waves that all have random intensities and phases. This produces a speckle pattern whose spatial intensity and phase structure is random as well. Speckle noise is what makes holographic interferometry and ESPI measurements inherently more noisy than those of classical interferometry. But the speckle effect is not restricted to electromagnetic radiation; it has also received some attention in ultrasound research [Bur78, Wag83, Hon97].

To get an idea of the phenomenon, we will consider the properties of speckle patterns in this chapter. These are of course treated with the tools of statistics, and a wealth of knowledge has been collected since the first pioneering studies [All63, Gol65, Low70, McKe74]. We begin with the first-order statistics of intensity and phase and their gradients, putting some emphasis on the 1-D gradients that play an important role for SPS. The gradient statistics provide useful facts for changes of the speckle field over distances well below the coherence length, or speckle size; to get a description of the field for two points that are arbitrarily far apart, we need the explicit second-order statistics. These are particularly important for SPS.

The discussion is restricted to the so-called fully developed speckle patterns, since these are generated by the great majority of objects that are not optically smooth; in fact, the scatterers to produce partially developed speckle patterns have to be specially prepared [Cha79, Tak75, Kad85, Mol90a]; a good general survey on this topic is [Tak86]. Moreover, we assume the light to be perfectly monochromatic and polarised. The treatment will be valid for free-space propagation (objective speckles) as well as image fields (subjective speckles), provided the object's microstructure is not resolved (see 2.2.1).

### 2.1 Experimental set-up

Where appropriate, we illustrate the findings by experimental results from a large-objective-speckle interferometer with spatial phase measurement that was built as shown in Fig. 2.1 [Kun97]. Large subjective speckles would be rather dark due to the small aperture needed; and also, since most apertures are polygons, one would obtain anisotropic speckles. Of course, it is possible to design subjective-speckle interferometers, and experimental findings for image-plane speckles produced by weak scatterers have been reported in [Kad85].

The basic set-up is of Mach-Zehnder type. In contrast to [Kol99], our geometry should compensate for the spherical part of the scattered field, so that we measure its speckled part only. This is indispensable if we are to find out something about phase gradients. The adjustment of the interferometer therefore requires special care, since the curvatures of the wavefronts should match exactly when they are brought back

together. Another interesting possibility of measuring speckle phases is the Fizeau configuration reported in [Mol90a,b].

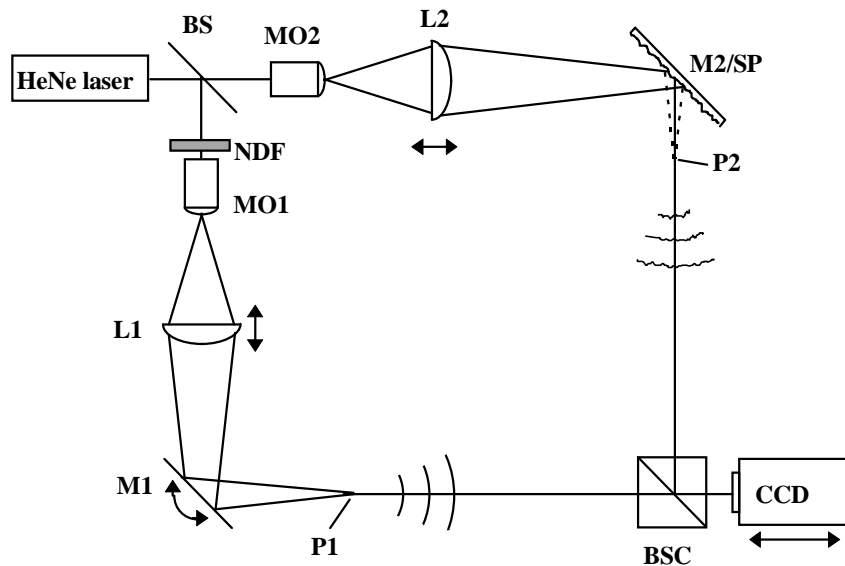


Fig. 2.1: Optical set-up for generation of large speckles and phase measurement by SPS. Abbreviations: BS(C), beam splitter (cube), NDF, neutral density filter, MO, microscope objectives, L, lenses, M, mirrors, SP, scattering plate.

The laser beam is divided, expanded by microscope objectives of the same type and made convergent again by lenses of the same type ( $f=120$  mm); we call the path with component index 1 the reference path. To adjust the speckle size, the scattering plate (matt white painted metal) is fit and L2 is slid back or forth to produce the proper spot diameter (in our case,  $\cong 3.1$  mm). The neutral density filter is chosen so as to maximise the modulation of the speckle interferogram. Here, we set  $R/\langle I \rangle \cong 7:6$ . Then SP is replaced by M2 and L1 is moved so that P1 and P2 acquire the same distance from the CCD chip; thus the curvatures of the two spherical waves are matched. By rotating M1, the spatial phase shift can be adjusted with no de-focusing: P1 is merely shifted sideways as M1 is rotated. The lateral offset between P1 and P2 determines the fringe density on the CCD, i.e., the spatial phase shift. An explanation of the underlying geometry can be found in Chapter 3.4.1. Uniting the two fields involves sending at least one of them through glass, which introduces spherical aberrations. Here, we subject both waves to almost the same alteration by using a beam splitter cube with high-planarity surfaces. The attainable flatness of the measured wavefront depends on the quality of the optical components; a residual error of about  $\lambda/4$  was found, which is tolerable for our range of speckle sizes. Also, any misalignment of the spatial phase shift will generate an additional phase ramp; but since it is linear, we can easily detect and remove it by the fitting procedure described in Chapter 4.2.

Once this calibration is done, M2 must be replaced by SP again, and their surfaces should be in exactly the same position. For this purpose, we used an auxiliary adjustment frame that was removed afterwards. The scattered light is weakly de-polarised ( $\cong 1:10$ ); but as we will see, very little impact on the statistics is found (for a detailed survey on partially polarised speckle fields, see [Bar85]). The laser beam has a

Gaussian intensity profile; after expanding, only its innermost part is being transmitted by the lenses, so that we can approximate the illuminated scattering spot by a circle of uniform brightness.

Moving the CCD camera away from BSC offers the additional possibility to scan the speckle field in the direction of propagation, which we label  $z$ . It is then not necessary to re-align the spatial phase shift: the ratio of fringe density to speckle size, being the relative resolution of the speckle phase maps, will remain constant. For a series of images with varying fringe density, the phase maps can most conveniently be obtained by the Fourier transform method (see Chapter 6.5). A non-integer number of carrier fringes will leave a residual global phase ramp after the FT evaluation. This bogus wavefront tilt must be removed if we are to measure speckle phases only; and again, the "fringe" fitting algorithm of Chapter 4.2 is capable of finding the global ramp that we have to subtract.

The CCD camera used for this experiment was a SONY XC-75 with interline transfer sensor (dust cover removed) and a resolution of  $736 \times 576$  pixels of  $\cong (8.5 \mu\text{m})^2$  each; we call  $d_p = 8.5 \mu\text{m}$  the pixel size. The video signal was digitised to 8 bits (256 grey levels) by a Data Translation DT3852B-2 frame grabber, driven by the camera's pixel clock.

The example image that we will use to check our theoretical results has an average speckle size of  $d_s \cong 26 d_p$  and a mean brightness of  $\langle I \rangle \cong 56.2$  grey levels. It is displayed in Fig. 2.2 together with its interferogram.

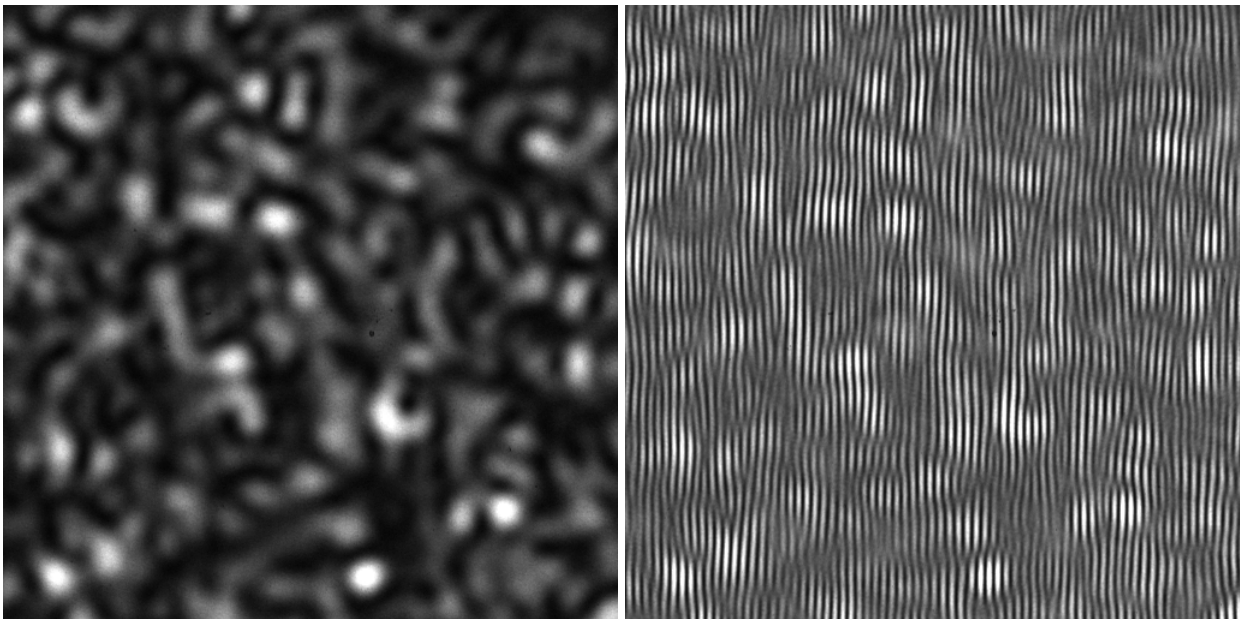


Fig. 2.2: Left: sample speckle image; right: corresponding interferogram with spatial phase shift.

The interferogram has a carrier fringe spacing of  $\cong 7 d_p$ ; on closer scrutiny, one finds many forks, both upward and downward, in the fringe pattern. These indicate the so-called phase singularities that we will discuss in detail in 2.2.5. The phase map (Fig. 2.17) was calculated by the Fourier method, which is why we consider  $512^2$  pixels here.

## 2.2 First-order speckle statistics

To simplify and generalise the treatment of first-order speckle properties, we will first derive a joint probability density function containing all the quantities of interest and then eliminate whatever we want by integrating it.

### 2.2.1 Basic probability-density function

A light-scattering rough object can be regarded as an array of individual, mutually uncorrelated microscopic scatterers, each of which sends an elementary wave into space. The coherent superposition of all these contributions at a certain spatial point determines the speckle intensity and phase at that point. The treatment is also valid for imaging geometries, provided that several point images of scatterers overlap at each point of the image plane. This condition is also referred to as unresolved microstructure.

The elementary waves are most conveniently regarded as vectors  $\mathbf{A}$  in the complex plane, with the squared modulus  $|\mathbf{A}|^2$  corresponding to their intensity  $I$  and the argument giving the phase  $\varphi$ . This representation is well known and very useful; the complex vectors  $\mathbf{A}$  are usually named phasors, or complex amplitudes. Assumed that

- (i) the waves' amplitudes  $|\mathbf{A}|$  are independent of their phases,
- (ii) the phases are uniformly distributed over  $[-\pi, \pi)$ , and
- (iii) the number  $N$  of scatterers is large enough (which begins to hold from  $N \cong 50$  on),

the summation of the contributions may be visualised as a random walk in the complex plane, putting  $N$  phasors together in the manner of vector addition. Then we may use the central limit theorem [Pap65, p. 266] to treat the speckle pattern formation as an asymptotically Gaussian process. If we denote the real and imaginary parts of the phasors by  $A_r$  and  $A_i$ , the two are called jointly Gaussian variables [Goo75]. This assumption has been experimentally confirmed in [Mol90b]. As derived in [Pap65, pp. 253 and 475], also the spatial derivatives  $A_{r,x}$ ,  $A_{i,x}$ ,  $A_{r,y}$  and  $A_{i,y}$ , where  $A_{r,x} := \partial A_r / \partial x$  etc., are jointly Gaussian with  $A_r$  and  $A_i$ . Assumed the standard deviation of  $A_r$  and  $A_i$  is  $\sigma$ , we can establish

$$p(A_r, A_i, A_{r,x}, A_{i,x}, A_{r,y}, A_{i,y}) = \frac{1}{2\sigma^2\pi} \exp\left(-\frac{A_r^2 + A_i^2}{2\sigma^2}\right) \cdot \frac{1}{4C_0^2\pi^2} \exp\left(-\frac{A_{r,x}^2 + A_{i,x}^2 + A_{r,y}^2 + A_{i,y}^2}{2C_0}\right) \quad (2.1)$$

as detailed in [Och83, Fre95c, Leh98], with  $\langle \bullet \rangle$  denoting the ensemble average;  $2\sigma^2$  is indeed the average speckle intensity  $\langle I \rangle$  as will be derived in (2.7).  $C_0$  depends on the shape and size of the scattering spot or aperture. It is essentially the curvature of the spatial amplitude autocorrelation function at its peak,  $\partial^2(\mathbf{R}_{\mathbf{AA}^*}(\Delta x, \Delta y))|_{\Delta x=0, \Delta y=0} / \partial(\Delta x)^2 = \partial^2(\mathbf{R}_{\mathbf{AA}^*}(\Delta x, \Delta y))|_{\Delta x=0, \Delta y=0} / \partial(\Delta y)^2$ , provided the source is symmetrical. For circular scattering spots, we get [Fre95c, Leh98]

$$C_0 = \frac{\langle I \rangle \pi^2}{8} \left( \frac{D}{\lambda z} \right)^2, \quad (2.2)$$

with  $D$  being the diameter of the spot,  $\lambda$  the wavelength and  $z$  the distance between scattering plane and point of observation.  $C_0$  is inversely proportional to the square of the speckle size and scales the gradients  $A_{r,x}$  etc. For our example image, we find  $C_0 \cong 0.152$  grey levels/ $d_p^2$ .

In order to come from the amplitude description to intensities and phases, we convert the variables to polar co-ordinates:

$$\begin{aligned} A_r &= \sqrt{I} \cos \varphi & A_i &= \sqrt{I} \sin \varphi \\ A_{r,x} &= \frac{I_x}{2\sqrt{I}} \cos \varphi - \varphi_x \sqrt{I} \sin \varphi & A_{i,x} &= \frac{I_x}{2\sqrt{I}} \sin \varphi + \varphi_x \sqrt{I} \cos \varphi \\ A_{r,y} &= \frac{I_y}{2\sqrt{I}} \cos \varphi - \varphi_y \sqrt{I} \sin \varphi & A_{i,y} &= \frac{I_y}{2\sqrt{I}} \sin \varphi + \varphi_y \sqrt{I} \cos \varphi \end{aligned} \quad (2.3)$$

with the Jacobian  $\|\mathbf{J}\|=1/8$ ; the procedure is described in more detail in [Och83]. We arrive at

$$\begin{aligned} p(I, \varphi, I_x, \varphi_x, I_y, \varphi_y) &= \\ \frac{1}{\langle I \rangle 2\pi} \exp\left(-\frac{I}{\langle I \rangle}\right) &\cdot \frac{1}{16C_0^2 \pi^2} \exp\left(-\frac{I_x^2 + I_y^2}{8IC_0}\right) \exp\left(-\frac{I(\varphi_x^2 + \varphi_y^2)}{2C_0}\right) \end{aligned} \quad (2.4)$$

with  $0 \leq I < \infty$ ,  $-\pi \leq \varphi < \pi$ ,  $-\infty \leq (I_x, \varphi_x, I_y, \varphi_y) \leq \infty$ . Any desired marginal or joint probability density function of the involved quantities can be found from this expression. More general cases are of course the two-dimensional gradients; the corresponding functions of  $|\nabla I|$  and/or  $|\nabla \varphi|$  are easily found from (2.4), and we will also consider them below.

### 2.2.2 Intensity and phase

Now in a first step, we integrate over all gradients to find  $p(I, \varphi)$ , and obtain

$$p(I, \varphi) = \frac{1}{\langle I \rangle 2\pi} \exp\left(-\frac{I}{\langle I \rangle}\right); \quad (2.5)$$

we note that  $\varphi$  does not turn up in this equation, which means that  $I$  and  $\varphi$  are statistically independent of each other. Therefore, one can also write  $p(I, \varphi) = p(I) \cdot p(\varphi)$ , which functions are

$$\begin{aligned} p(I) &= \frac{1}{\langle I \rangle} \exp\left(-\frac{I}{\langle I \rangle}\right) & (I \geq 0) \\ p(\varphi) &= \frac{1}{2\pi} & (-\pi \leq \varphi < \pi). \end{aligned} \quad (2.6)$$

So the speckle intensity exhibits a negative exponential distribution and the speckle phases are uniformly distributed. Furthermore we can state mean values and standard deviations for  $I$  (using (2.1) and  $\langle I^n \rangle / \langle I \rangle^n = n!$  [Goo75]) and  $\varphi$ :

$$\begin{aligned} \langle I \rangle &= 2\sigma^2 & \sigma_I &= \sqrt{\langle I^2 \rangle - \langle I \rangle^2} = \langle I \rangle \\ \langle \varphi \rangle &= 0 & \sigma_\varphi &= \frac{\pi}{\sqrt{3}} \end{aligned} \quad (2.7)$$

An intensity distribution like the one predicted here would be very inconvenient for interferometry, since the most frequent speckle intensity is zero, whence no signal can be obtained. On the other hand, this fraction is still very small in relation to the rest of the intensity scale. Moreover, any physically existing detector has a finite area, which shifts the maximum of the intensity distribution function the farther away from zero the more "speckle areas" fit into a pixel area [Goo75, p. 54]. The resulting function favours speckle interferometry; but in any case, a fraction of dark pixels remains that deliver only a weak interference signal upon superposition with a reference wave. In many ESPI measurements, these low-response pixels are the main origin of the so-called "salt-and-pepper" noise in sawtooth images.

As for the phases, it can be easily understood from the random-walk model that there is no preferred phase value in the speckle pattern; therefore the phases are uniformly distributed over their range. It has been demonstrated that the measured speckle phase distribution can be helpful in calibration of phase-sampling procedures; details on this will follow in Chapter 3.4.6.

The statement that the phase is a "free" quantity in our pdf's is of course valid for (2.4) as well; therefore we can integrate  $\varphi$  out, rewrite (2.4) as

$$p(I, I_x, \varphi_x, I_y, \varphi_y) = \frac{1}{\langle I \rangle} \exp\left(-\frac{I}{\langle I \rangle}\right) \cdot \frac{1}{16C_0^2 \pi^2} \exp\left(-\frac{I_x^2 + I_y^2}{8IC_0}\right) \exp\left(-\frac{I(\varphi_x^2 + \varphi_y^2)}{2C_0}\right) \quad (2.8)$$

and proceed to the gradients.

### 2.2.3 Gradients in one dimension

In TPS, each pixel area integrates over some portion of the speckle pattern; if there are intensity and/or phase deviations in it, the "pixel interferometer" will still function correctly, although with decreased interferometric contrast. In SPS however, the fluctuations of intensity and phase play a significant role for the measurement, since in this case we will encounter different mean intensities, modulation contrasts, and phase offsets for adjacent pixels. As the spatial phase shift takes place in one spatial direction, we start by investigating the gradients  $I_x$  and  $\varphi_x$ . Nonzero values of these quantities will result in linear deviations of bias intensity and speckle phase; the latter is equivalent to a linear phase-shift miscalibration. The 1-D treatment accounts for all directions of phase shift, as we are free to choose the co-ordinates in the most convenient way.

## 2.2.3.1 Intensity gradients

From (2.8) we get [Ebe79b; Gra94, formula 3.325]

$$p(I_x) = \frac{1}{2\sqrt{2C_0\langle I \rangle}} \exp\left(-\frac{|I_x|}{\sqrt{2C_0\langle I \rangle}}\right), \quad -\infty < I_x < \infty, \quad (2.9)$$

which function is called Laplacian density. It is a negative exponential function for either sign of  $I_x$  with a mean value and standard deviation of

$$\langle I_x \rangle = 0 \quad \sigma_{I_x} = 2\sqrt{C_0\langle I \rangle}, \quad (2.10)$$

and has been experimentally verified in [Ebe79a]. The similarity between the distributions of the intensity and its gradient has a simple and astonishing reason that has been found in [Fre96b]: speckles tend to be "congruent", i.e. to have very similar intensity profiles, irrespective of their brightness. Hence, bright spots are associated with large intensity gradients, while smaller gradients belong to dim speckles. The speckles' congruence propagates the negative exponential intensity distribution to the gradients.

This observation implies that we find an interaction of the speckle intensity and its derivative in the corresponding pdf. Indeed, the intensity and its gradient are not statistically independent since their joint density

$$p(I, I_x) = \frac{1}{\langle I \rangle} \exp\left(-\frac{I}{\langle I \rangle}\right) \cdot \frac{1}{2\sqrt{2\pi I C_0}} \exp\left(-\frac{I_x^2}{8IC_0}\right), \quad (2.11)$$

found from (2.8) by integration, is not separable. This joint density function is plotted in Fig. 2.3.

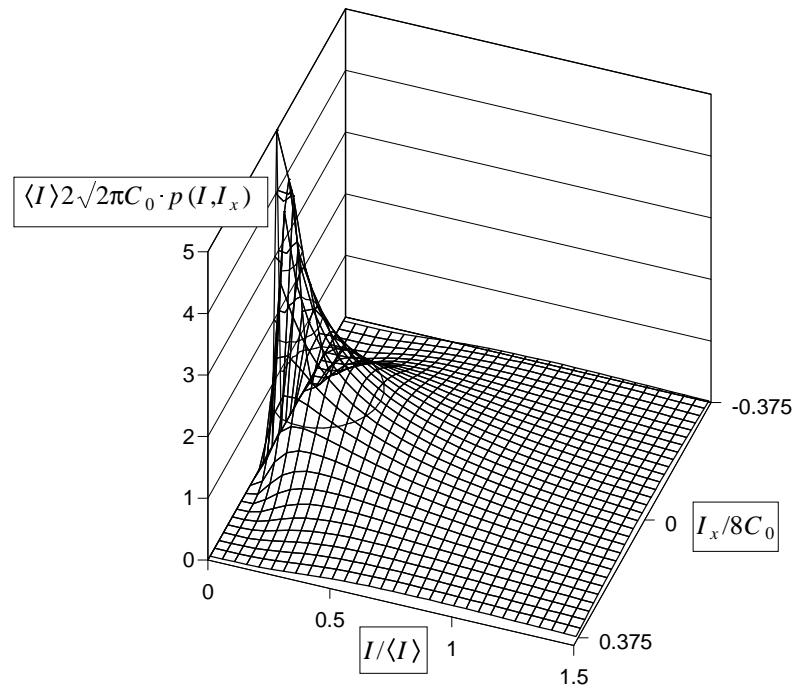


Fig. 2.3: Pseudo-3D plot of  $p(I, I_x)$ .

This graph shows that for small  $I$ ,  $I_x$  also tends to be small; indeed it approaches 0 as  $I \rightarrow 0$ : loci of zero intensity must at the same time be minima with vanishing intensity gradient (see also Fig. 2.15). A proof of this property has been given in [Kow83]. Hence, the correlation of  $I$  and  $I_x$  is nearly perfect in regions of low intensity. To learn how the gradients are distributed on the rest of the intensity scale, we consider the correlation of  $I$  and  $|I_x|$ . To obtain  $p(|I_x|)$  and  $p(I, |I_x|)$ , we multiply the right-hand sides of (2.9) and (2.11) with 2 and set  $0 < |I_x| < \infty$ . Calculating the average of  $|I_x|$ , we now obtain a non-zero value:

$$\langle |I_x| \rangle = \sqrt{2} \sqrt{C_0 \langle I \rangle} = \sigma_{|I_x|}. \quad (2.12)$$

Assuming a uniformly bright circular illumination of the scattering spot,  $\langle |I_x| \rangle \cong 1.92 \langle I \rangle / d_s$ . This demonstrates that it is almost certain to find substantial intensity variations on neighbour pixels, except when the intensity itself is very low. To formulate this quantitatively, we calculate the correlation coefficient of  $I$  and  $|I_x|$  [Pap65, p. 210] to be

$$r_{I, |I_x|} = \frac{\langle I |I_x| \rangle - \langle I \rangle \langle |I_x| \rangle}{\sigma_I \sigma_{|I_x|}} = \frac{\frac{3\sqrt{C_0} \langle I \rangle^{3/2}}{\sqrt{2}} - \langle I \rangle \sqrt{2C_0 \langle I \rangle}}{\langle I \rangle \sqrt{2C_0 \langle I \rangle}} = 0.5, \quad (2.13)$$

where  $\langle I |I_x| \rangle := \int_0^\infty \int_0^\infty I |I_x| p(I, |I_x|) dI dI_x$ . This result is disadvantageous for spatial phase shifting: it indicates a significant tendency of large intensity gradients, and hence phase errors, in those portions of the speckle pattern that deliver the best interferometric signal due to their brightness, although, as pointed out in [Ebe80], integration over the pixel area increases the probability of finding small gradients.

Having derived  $p(I, I_x)$ , we can obtain another useful quantity: given a threshold brightness level  $I_t$ , the above-level dwell distance  $d_+(I_t)$  of speckle intensity reveals the spatial extent of structures that are brighter than  $I_t$ . To clarify the meaning of  $d_+(I_t)$  and to get an impression of the intensity fluctuations, we consider the intensity profile at row 256, i.e. at the vertical centre, of our sample speckle pattern. This gives the intensity curve  $I(x, 256)$  plotted in Fig. 2.4, where  $x$  is the column number.

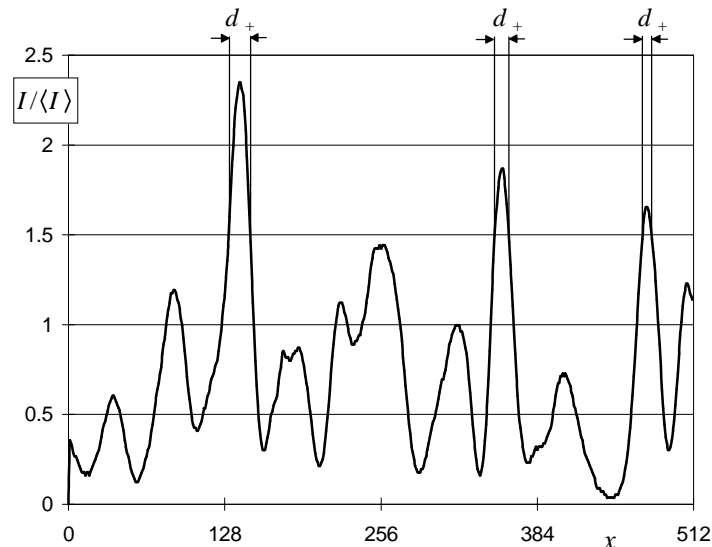


Fig. 2.4: Intensity profile of row 256 of speckle image (Fig. 2.2, left side), normalised by  $\langle I \rangle$ .



We see that  $d_+(I_t)$  is the distance over which  $I$  remains above the threshold  $I_t$ , which is set to  $1.5\langle I \rangle$  in this example. We find three above-threshold events and hence obtain three different measurements of  $d_+(1.5\langle I \rangle)$ . But instead of collecting events, it makes of course more sense to aim analytically for an average of the above-level distance,  $\langle d_+ \rangle(I_t)$ , and fortunately its theoretical derivation is available.

The number of events per length unit that the signal crosses  $I_t$ , the so-called level-crossing density, can be calculated by means of a long-known formula by Rice, as detailed in [Ebe79b, Bar80]:

$$\langle \rho(I_t) \rangle = \int_{-\infty}^{\infty} |I_x| p(I_t, I_x) dI_x = \sqrt{\frac{8C_0}{\pi}} \frac{\sqrt{I_t}}{\langle I \rangle} \exp\left(-\frac{I_t}{\langle I \rangle}\right) = \frac{1.22\sqrt{\pi}}{d_s} \sqrt{\frac{I_t}{\langle I \rangle}} \exp\left(-\frac{I_t}{\langle I \rangle}\right) \quad (2.14)$$

(see also Appendix A), where we have used (2.2) and (2.43) to relate the expression to the speckle size  $d_s$  produced by a circular scattering spot; an example for a square spot is given in [Bah80]. The average number of level crossings per speckle size  $d_s$  is depicted in Fig. 2.5, and reveals that  $\langle I \rangle/2$  is being crossed almost once per speckle size (for pixel-integrated speckle it should, and does, contract about  $\langle I \rangle$  [Bar88]).

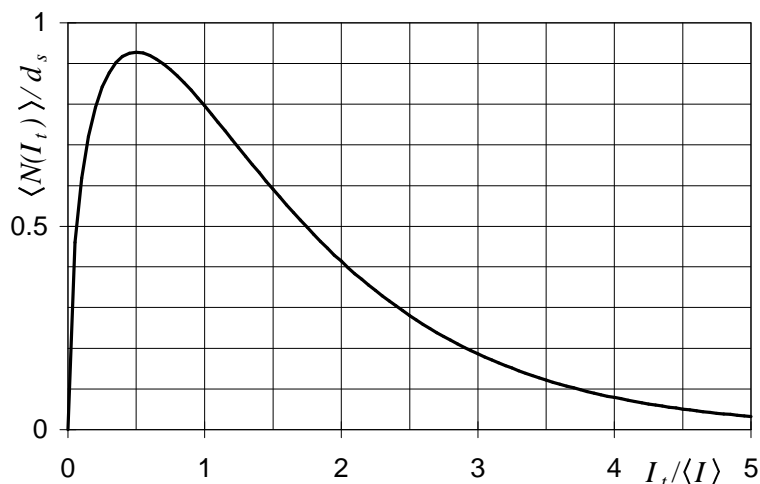


Fig. 2.5: Expected number  $\langle N(I_t) \rangle$  per speckle size  $d_s$  of crossings of intensity level  $I_t$  as a function of normalised threshold intensity  $I_t/\langle I \rangle$ . This curve follows simply from setting  $d_s=1$  in (2.14).

Being aware, however, that (2.14) accounts for both positive and negative crossings, we conclude that  $I(x)$  goes beyond or below  $\langle I \rangle/2$  every other speckle size. Now we can answer the question over what distance  $I$  remains above/below a certain  $I_t$ , by evaluating the expressions for the average above- and below-level dwell distances [Bar80\*],

$$\langle d_+ \rangle(I_t) = \frac{\int_{I_t}^{\infty} p(I) dI}{\frac{1}{2} \langle \rho(I_t) \rangle} = \frac{2d_s}{1.22\sqrt{\pi}} \sqrt{\frac{\langle I \rangle}{I_t}} \quad ; \quad \langle d_- \rangle(I_t) = \frac{1 - \int_{I_t}^{\infty} p(I) dI}{\frac{1}{2} \langle \rho(I_t) \rangle} = \frac{2d_s}{1.22\sqrt{\pi}} \sqrt{\frac{\langle I \rangle}{I_t}} \left( \exp\left(\frac{I_t}{\langle I \rangle}\right) - 1 \right), \quad (2.15)$$

which are the total fractions of distance that the intensity spends beyond/below  $I_t$ , divided by the mean density of upward/downward level crossings. Of these latter, each contributes of course one half to the

\* With a misprint in Eq. (16), where  $\sigma$  and  $\mu$  must be swapped.

total  $\langle \rho_f(I) \rangle$ . Fig. 2.6 shows the two functions in units of  $d_s$ .

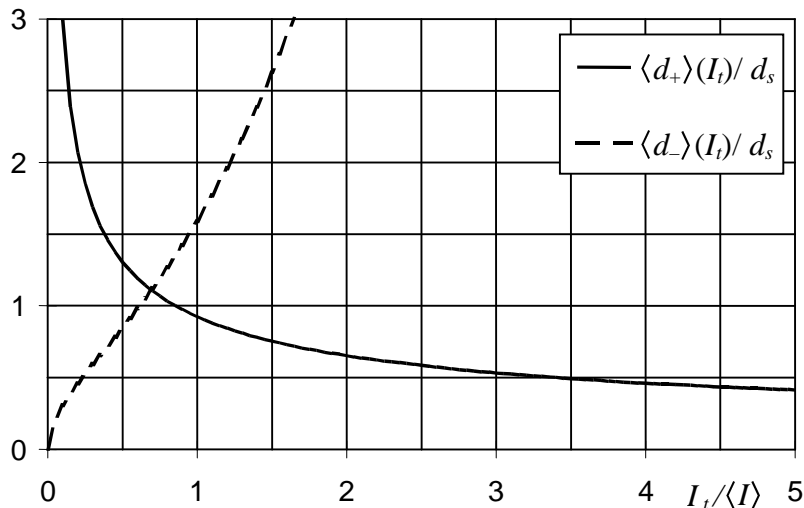


Fig. 2.6: Average above-level distance  $\langle d_+ \rangle$  (solid line) and below-level distance  $\langle d_- \rangle$  (dashed line) in units of  $d_s$  as a function of normalised threshold intensity  $I_t/\langle I \rangle$ .

The graph for  $\langle d_+ \rangle(I_t)$  affirms the visual impression of a speckle pattern: moderately bright spots ( $I_t \cong \langle I \rangle$ ) have indeed a width of about the typical speckle size. This coincides nicely with the experimental findings in [Mar91]. The very bright parts of the peaks are of course narrower. For  $I_t=0$ , we have  $\langle d_+ \rangle(0) \rightarrow \infty$ : the intensity in the speckle pattern is almost always greater than, and certainly never crosses, zero. On the other hand,  $\langle d_- \rangle(I_t)$  shows that very dark structures are really narrow; but the typical extent of structures where the intensity remains below  $\langle I \rangle$  is  $\cong 1.6 d_s$ . For large  $I_t$ , we have to go very far along  $x$  to encounter a brighter speckle (consider, e.g., the length of the below-threshold events for  $I_t=1.5\langle I \rangle$  in Fig. 2.4).

The balanced point at which  $\langle d_+ \rangle(I_t) = \langle d_- \rangle(I_t)$  occurs at  $I_t/\langle I \rangle = \ln 2$ , and the average extension of the bright and dark structures is then  $\cong 1.11 d_s$ . On binarising the sample speckle image at the appropriate intensity level and evaluating the length distributions of black and white line segments, I obtained  $\langle d_+ \rangle(I_t) \cong 1.14 d_s$  and  $\langle d_- \rangle(I_t) \cong 1.18 d_s$ , which is in reasonable agreement with the theoretical value.

The way from the mere average descriptions to the pdf's of level-crossing intervals is long, but has been shown in [You96]; interestingly, it turns out that for scattering spots with step-function edges, the pdf's oscillate, but for Gaussian scattering spots the oscillation is damped out. In short, if  $I$  has crossed  $I_t$  and fails to do so again after one speckle size, it must wait until the next speckle appears on the way along  $x$ ; in between, the transition is indeed somewhat less probable. Several double and triple peaks and valleys can be found in Fig. 2.2 to make this plausible.

Very recently, older work about the zero crossing rate of  $I_x$  [Oht82] has been verified and extended [Kes98]. An account of this thorough study about level-crossing densities of  $A_r$ ,  $A_i$ ,  $I$  and  $\varphi$ , and all their first and second derivatives, is definitely beyond the scope of this chapter; but it will be valuable for a still deeper understanding of what changes in the field quantities one probably finds on a straight line through the speckle pattern.

We conclude this subsection with another interesting and comparatively easy interpretation of speckle intensity maps, namely as smooth 2-D surfaces or landscapes. Hence, considerations about the laws of "twinkling" of a sunlit sea surface [Lon60] are indeed applicable to the spatial intensity structure of a speckle pattern. This allows one to establish for the relative numbers of speckle (zero and non-zero) intensity minima,  $N_{min}$ , maxima,  $N_{max}$ , and saddle points,  $N_{sad}$ , respectively [Lon60]:

$$N_{min} + N_{max} = N_{sad}. \quad (2.16)$$

More recently, this has been re-derived with the concept of singularities of the normalised vector field  $\nabla I/|\nabla I|$ , in which minima, maxima and saddle points appear as topological singularities [Fre95b], and the evolution rule for speckle fields has been formulated that a new extremum must always appear, or vanish, together with a saddle point. It has further been found that  $N_{min}:N_{max}=3:2$ , this is, we encounter more minima than maxima in a speckle pattern [Wei82a,b]; the typical spatial arrangement is that of chains of alternating minima and saddles in the dark valleys between the bright spots (cf. Fig. 2.2). For a circular aperture, the statistical densities of the intensity features have been determined by computer simulation as [Fre95b]

$$\begin{aligned} \rho(I_{zero}) &\cong 0.46/A_s \\ \rho(I_{min}) &\cong 0.13/A_s \\ \rho(I_{max}) &\cong 0.39/A_s \\ \rho(I_{sad}) &\cong 0.98/A_s, \end{aligned} \quad (2.17)$$

$A_s$  being the speckle area defined in (2.36), and  $\rho(I_{zero})$  denoting the density of zero-intensity minima, to be further investigated in 2.2.5. Thus, the rule (2.16) is confirmed, and in total we have almost two of these "critical points" of intensity per speckle area. The density of parameters necessary to describe all the features in (2.17) is almost 6 times the sampling density required to properly resolve the speckle field; this means that the features cannot really be statistically independent and hence must be more or less correlated [Fre95b, Fre98a].

It is now interesting to learn at what intensity levels these features occur most frequently; in this respect the values

$$\begin{aligned} \langle I_{max} \rangle &\cong 2.5 \langle I \rangle \\ \langle I_{min} \rangle &\cong 0.07 \langle I \rangle \\ \langle I_{sad} \rangle &\cong 0.5 \langle I \rangle \end{aligned} \quad (2.18)$$

are given in [Fre96b]; the separate class of zero-intensity minima is here excluded from  $\langle I_{min} \rangle$ . The most frequent peak-intensity level (at the centres of the bright speckles) is  $\cong 1.8 \langle I \rangle$ , which supports (2.13): most of the bright spots stand out strongly and are necessarily associated with large intensity slopes. This can also be seen in Fig. 2.4.

There are other structural correlations, non-obvious orders and quasi-lattices [Fre95b, Fre95c, Fre97b, Fre98a] in speckle patterns, again too numerous to describe here; but there should now be no doubt that a

significant influence of the varying speckle intensities can be expected when phase calculations are carried out with neighbouring pixels as input data.

### 2.2.3.2 Phase gradients

The probability density function of the phase gradient in  $x$ -direction is [Och83]

$$p(\varphi_x) = \frac{C_0 \sqrt{\langle I \rangle}}{(2C_0 + \langle I \rangle \varphi_x^2)^{3/2}}, \quad (2.19)$$

a bell-shaped function that approaches zero distinctly more slowly than a Gaussian function of similar peak width; this result has been verified experimentally with the help of a Shack-Hartmann sensor in [Voe91]. Evidently, it has  $\langle \varphi_x \rangle = 0$ ; unfortunately,  $\sigma_{\varphi_x}$  cannot be determined from (2.19) because a divergent integral appears in the calculation of  $\langle \varphi_x^2 \rangle$ . This is physically correct, since the phase gradient indeed diverges at the phase singularities; nonetheless, we will need a way to circumvent this problem, which is shown below.

The joint density function of the phase gradient and the intensity is given by

$$p(I, \varphi_x) = \frac{\sqrt{I}}{\sqrt{2\pi C_0 \langle I \rangle}} \exp\left(-\frac{I}{\langle I \rangle}\right) \exp\left(-\frac{\varphi_x^2}{2C_0}\right) \quad (2.20)$$

and displayed graphically in Fig. 2.7.

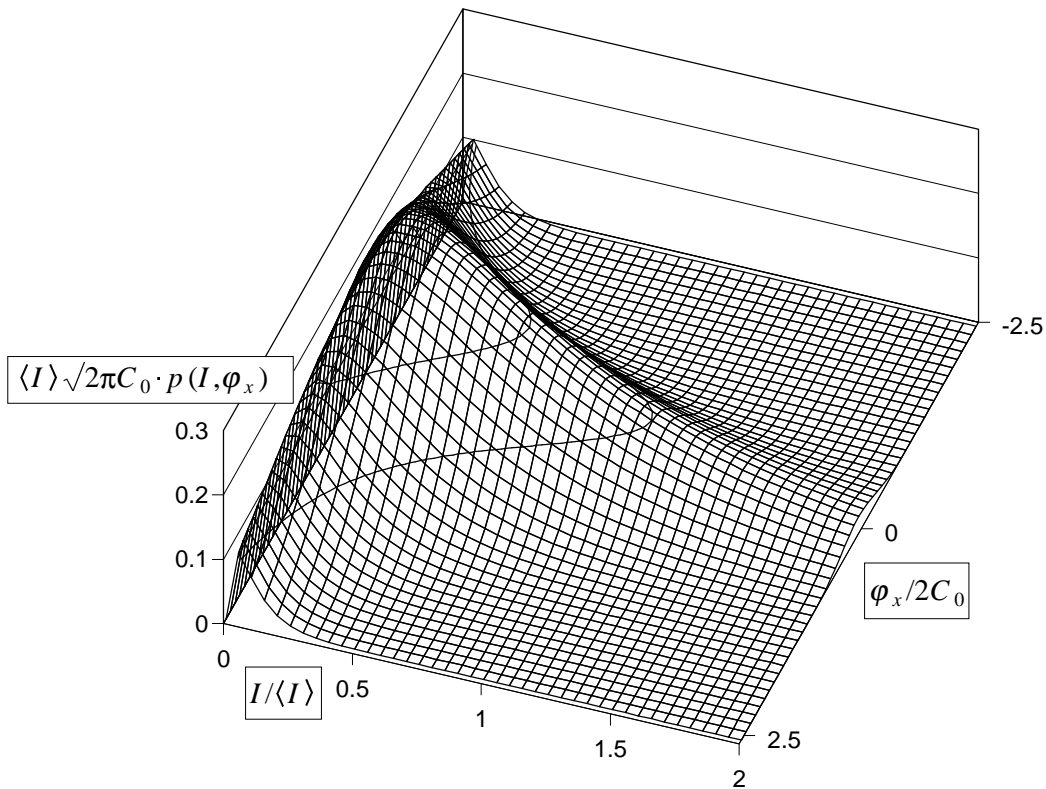


Fig. 2.7: Pseudo-3D plot of  $p(I, \varphi_x)$ .

Although  $p(I, \varphi_x)$  shows some coincidence of small  $I$  with small  $\varphi_x$ , we also find a significant contribution from large  $I$  with small  $\varphi_x$ , and vice versa. Note that there is again a special behaviour for  $I \rightarrow 0$ : the distribution of  $\varphi_x$  flattens out, which means that very high phase gradients can and do occur near zero-intensity minima. At  $I=0$  however,  $p(I, \varphi_x)|_{I=0} \equiv 0$ : where the wavefield vanishes, there is no phase either. On switching from  $\varphi_x$  to  $|\varphi_x|$ , we get

$$\langle |\varphi_x| \rangle = \sqrt{\frac{2C_0}{\langle I \rangle}}, \quad (2.21)$$

which amounts to  $\cong 110^\circ$  per speckle size for a uniformly bright, circular scattering spot. But as in the case of intensity gradients, it seems worthwhile to investigate the interrelation of  $I$  and  $\varphi_x$ . However, as stated above,  $r_{I, \varphi_x}$  cannot be calculated. Therefore, in analogy with [Fre95a,c], we will make use of a variable transformation and calculate  $r_{I, \phi_x}$ , where  $\phi_x$  is given by

$$\phi_x = \arctan\left(\frac{|\varphi_x|}{\langle |\varphi_x| \rangle}\right), \quad 0 \leq \phi_x \leq \frac{\pi}{2}. \quad (2.22)$$

This confines the integration and allows the calculation of whatever statistical moment is desired. The results will reproduce the behaviour of  $p(I, \varphi_x)$  quite well, since the mapping is quasi-linear in the region of low phase gradients, and substantial compression takes place only for that (small) fraction of the speckle field where the phase gradient is very high. Converting  $p(\varphi_x)$  to  $p(\phi_x)$  [Pap65, p. 126], one gets

$$p(\phi_x) = \cos \phi_x. \quad (2.23)$$

The statistical quantities required for  $r_{I, \phi_x}$  are

$$\langle \phi_x \rangle = \frac{\pi}{2} - 1 \quad \langle \phi_x^2 \rangle = \frac{\pi^2}{4} - 2 \quad \sigma_{\phi_x} = \sqrt{\pi - 3}; \quad (2.24)$$

for the corresponding quantities of  $I$ , we can of course refer to (2.7). With  $\|\mathbf{J}\| = \langle |\varphi_x| \rangle / \cos^2 \phi_x$ , it follows from (2.20) that

$$p(I, \phi_x) = \frac{2\sqrt{I}}{\langle I \rangle^{3/2} \sqrt{\pi} \cos^2 \phi_x} \exp\left(-\frac{I}{\langle I \rangle \cos^2 \phi_x}\right), \quad (2.25)$$

from which we get  $\langle I \cdot \varphi_x \rangle = (3\pi - 7)\langle I \rangle / 6$ , and finally,

$$r_{I, \phi_x} = \frac{\frac{3\pi - 7}{6} \langle I \rangle - \langle I \rangle \left(\frac{\pi}{2} - 1\right)}{\langle I \rangle \sqrt{\pi - 3}} = -0.443. \quad (2.26)$$

This significant anticorrelation between  $I$  and  $\phi_x$  indeed indicates that high intensities tend to go with low phase gradients  $\varphi_x$ , and vice versa, as also depicted in Fig. 2.8.

The peak shows that the coincidence of low intensity and high phase gradient  $\phi_x$  (where  $\phi_x \cong \pi/2$ ) is nearly perfect. On the other hand, we also find a significant probability of  $\phi_x = 0$  for low intensities. This however need not hold for  $\nabla\phi$ , and a good deal of the contribution at  $\phi_x = 0$  comes from the selection of the  $x$  component of  $\nabla\phi$ .

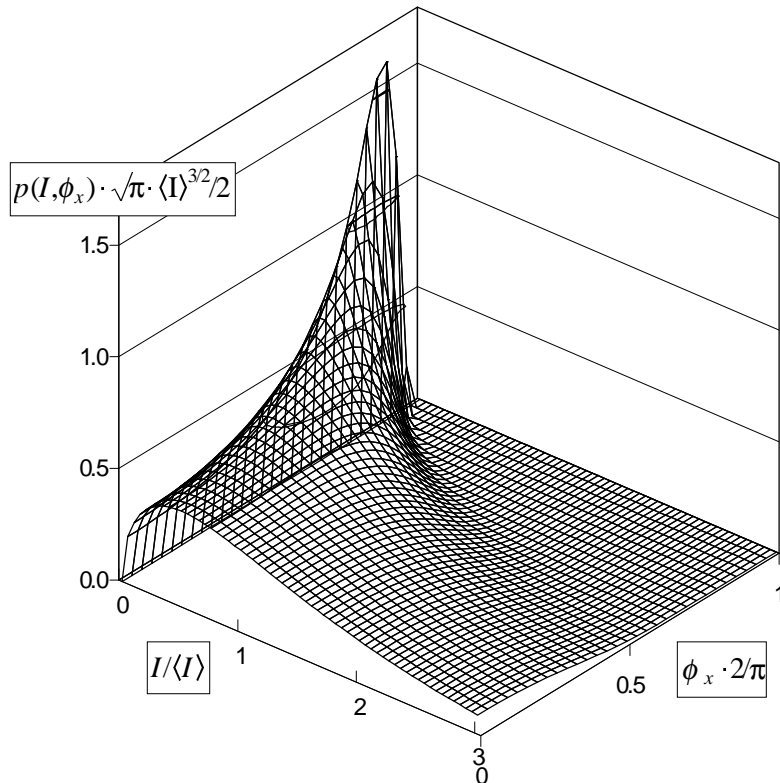


Fig. 2.8: Pseudo-3D plot of  $p(I, \phi_x)$ .

Applied to interferometry, this result alleviates the disadvantage that the high value of  $\langle |\varphi_x| \rangle$  seems to imply. The highest phase gradients tend to occur in regions of the speckle pattern that are rather dark and noise-burdened anyway, whilst in brighter regions it is fortunately more likely to encounter moderate phase slopes.

To finish, let us check our results experimentally. From (2.12), we have  $\langle |I_x| \rangle \cong 4.1$  grey levels/pixel, and from (2.21),  $\langle |\varphi_x| \rangle \cong 4.2^\circ/\text{pixel}$ . Approximating  $|I_x|$  by the absolute intensity differences and  $|\varphi_x|$  by the absolute phase differences from pixel to pixel, our test image yields  $\langle |I_x| \rangle \cong 3.9$  grey levels/pixel and  $\langle |\varphi_x| \rangle \cong 4.2^\circ/\text{pixel}$ . The spatial distribution of the gradients, appropriately converted to grey-scale images, can be seen in Fig. 2.9; the  $|I_x|$  map has been brightened up for display, and the largest  $|\varphi_x|$  detectable and shown is  $180^\circ/\text{pixel}$ .

The black spots in the brightest regions of  $|I_x|$  are due to camera saturation by very bright speckles. This partly explains why the experimental  $\langle |I_x| \rangle$  is somewhat too low:  $|I_x|$  is greatly underestimated where the detected speckle intensity is clipped. Moreover, a minor impact of the non-perfect polarisation cannot be excluded. The scale chosen for  $|\varphi_x|$  does not at all account for the divergence near the singularities; but due to the very small area fraction of these critical regions, the measured  $\langle |\varphi_x| \rangle$  remains correct. From the

positive correlation of  $I$  and  $I_x$  and the anticorrelation of  $I$  and  $\varphi_x$ , an anticorrelation of  $I_x$  and  $\varphi_x$  results that is impressively illustrated by the figure: the worm-like structures of high  $|\varphi_x|$  circumscribe the bright speckles (being regions of high  $|I_x|$ ) almost exactly. The white boxes assist in finding examples. The pinched maxima of  $|\varphi_x|$  indicate phase singularities (see Fig. 2.17).

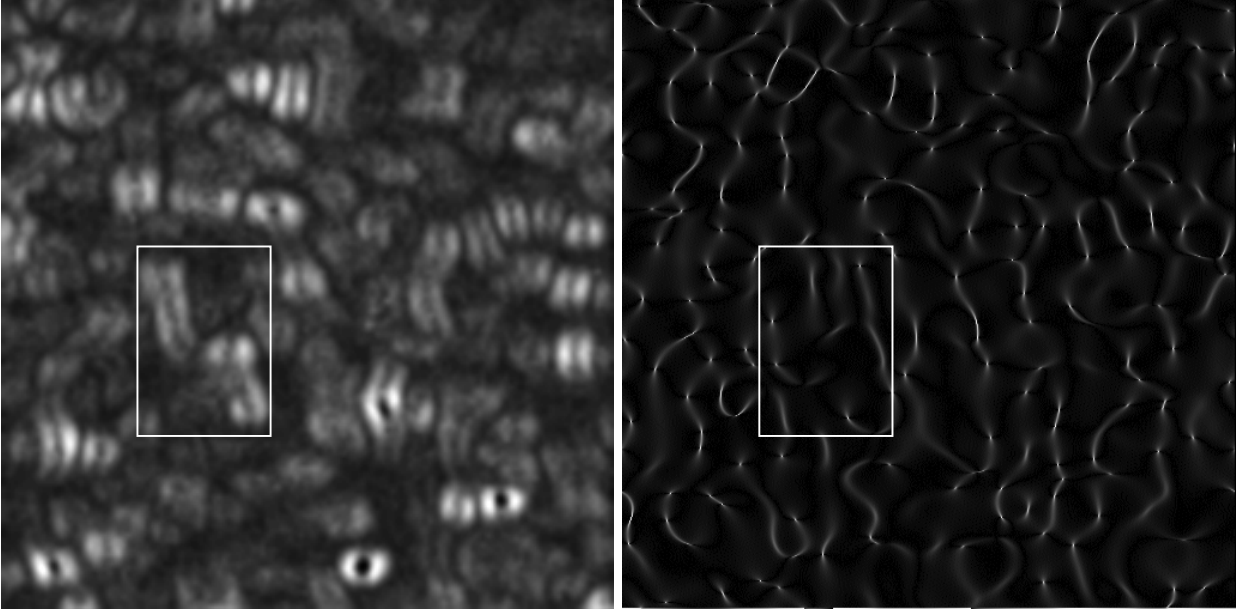


Fig. 2.9: Maps of  $|I_x|$  (left) and  $|\varphi_x|$  (right). White boxes allow comparison of details.

#### 2.2.4 Gradients in two dimensions

The previous treatment, although particularly relevant for our subject of spatial phase measurement, does not provide a complete insight into the structure of speckle intensity and phase. Therefore we consider also the two-dimensional gradients,

$$\begin{aligned} |\nabla I| &= \sqrt{I_x^2 + I_y^2} & \text{with} & \quad \theta_I = \arctan\left(\frac{I_y}{I_x}\right) \\ |\nabla \varphi| &= \sqrt{\varphi_x^2 + \varphi_y^2} & \text{with} & \quad \theta_\varphi = \arctan\left(\frac{\varphi_y}{\varphi_x}\right). \end{aligned} \quad (2.27)$$

The pdf's in terms of  $|\nabla I|$ ,  $|\nabla \varphi|$  are easily obtained from functions involving  $I_x$ ,  $I_y$ ,  $\varphi_x$ ,  $\varphi_y$  by integrating over  $\theta_I$  and/or  $\theta_\varphi$  on the circles given by  $\sqrt{I_x^2 + I_y^2}$  and/or  $\sqrt{\varphi_x^2 + \varphi_y^2}$ , which gives factors of  $2\pi|\nabla I|$  and  $2\pi|\nabla \varphi|$ , respectively. This changes (2.8) to

$$p(I, |\nabla I|, |\nabla \varphi|) = \frac{1}{\langle I \rangle} \exp\left(-\frac{I}{\langle I \rangle}\right) \frac{|\nabla I| |\nabla \varphi|}{4C_0^2} \exp\left(-\frac{|\nabla I|^2}{8IC_0}\right) \exp\left(-\frac{I |\nabla \varphi|^2}{2C_0}\right), \quad (2.28)$$

from which we can derive

$$p(I, |\nabla I|) = \frac{1}{\langle I \rangle} \exp\left(-\frac{I}{\langle I \rangle}\right) \frac{|\nabla I|}{4IC_0} \exp\left(-\frac{|\nabla I|^2}{8IC_0}\right), \quad (2.29)$$

plotted in Fig. 2.10.

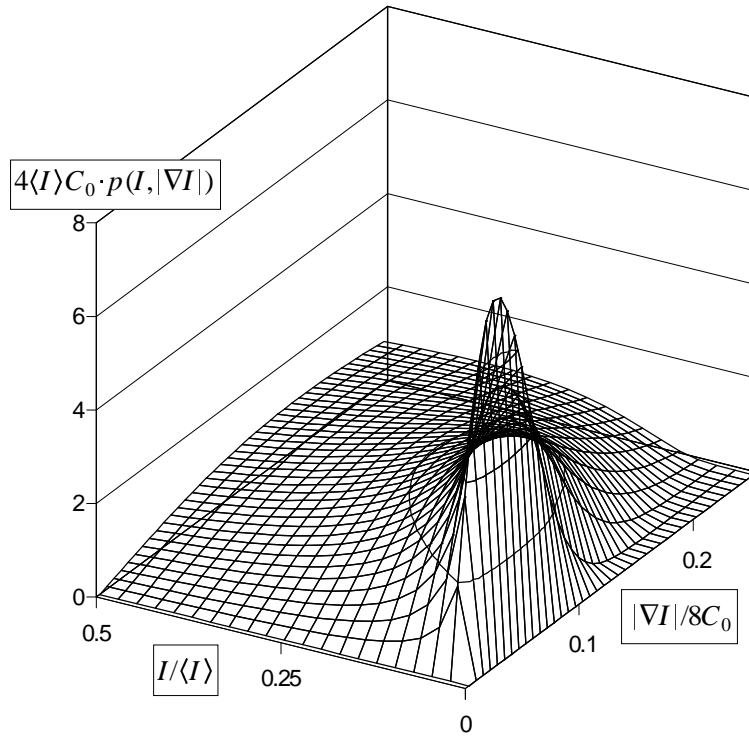


Fig. 2.10: Pseudo-3D plot of  $p(I, |\nabla I|)$ .

On comparison with Fig. 2.3, a qualitative difference between  $p(I, I_x)$  and  $p(I, |\nabla I|)$  is evident. While in both functions no intensity gradients at all occur for zero intensity, there is a significant probability of  $I_x=0$  for  $I > 0$ ; this is because (2.11) selects the  $x$  component only. In contrast, the probability for  $|\nabla I|=0$  vanishes for the whole intensity scale:  $p(I, |\nabla I|)|_{|\nabla I|=0} \equiv 0$ . This reflects the fact that the – certainly existent – intensity extrema and saddle points constitute a set of measure zero, as explained in [Kin77, p. 88]. The same observation holds when we switch from  $p(|I_x|)$  to  $p(|\nabla I|)$ ; by integration of (2.29), we then get [Gra94, formula 3.471.12]

$$p(|\nabla I|) = \frac{|\nabla I|}{2C_0 \langle I \rangle} K_0\left(\frac{|\nabla I|}{\sqrt{2C_0 \langle I \rangle}}\right) \quad \text{with} \quad \langle |\nabla I| \rangle = \frac{\pi}{\sqrt{2}} \sqrt{C_0 \langle I \rangle}, \quad (2.30)$$

which has been derived in [Kow83] and [Fre95c] before.  $K_0$  here denotes the modified Bessel function of second kind and zero order. In contrast to (2.9), and by the above argument, the probability for vanishing intensity gradient is zero:  $p(|\nabla I|)|_{|\nabla I|=0} \equiv 0$ . For a uniformly bright, circular scattering spot, we get  $\langle |\nabla I| \rangle \cong 3.01 \langle I \rangle$  per speckle size. It is the relatively sharp outlines of the bright speckles that give rise to so large a gradient; in addition, it changes its sign at least once over the distance of a speckle spot. Therefore it is very difficult to put a simple assumption about the course of the intensity into a phase



calculation formula. However, it has been shown that the integration over the pixels' finite apertures can alleviate the problem somewhat [Bar91].

Considering the two-dimensional phase gradients, we derive from (2.28)

$$p(I, |\nabla\phi|) = \frac{1}{\langle I \rangle} \exp\left(-\frac{I}{\langle I \rangle}\right) \frac{I|\nabla\phi|}{C_0} \exp\left(-\frac{I|\nabla\phi|^2}{2C_0}\right), \quad (2.31)$$

which is plotted in Fig. 2.11.

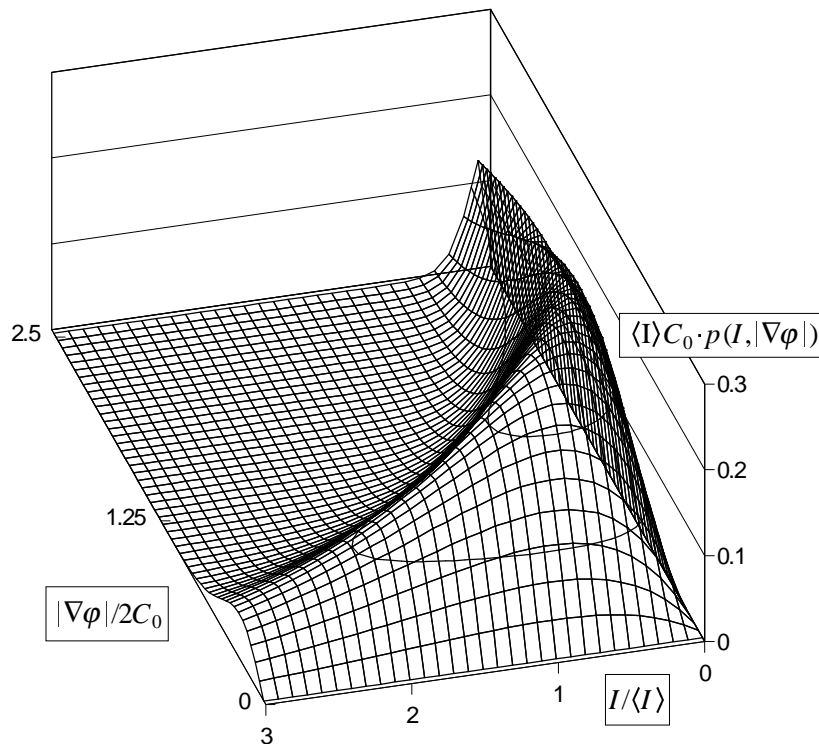


Fig. 2.11: Pseudo-3D plot of  $p(I, |\nabla\phi|)$ .

In this figure, the stationary points of the phase (extrema and saddle points, for which  $|\nabla\phi|=0$ ) lie on the  $I$  axis and the zero-intensity minima on the  $|\nabla\phi|$  axis. They are both existent but of measure zero, again in qualitative difference to the one-dimensional case. The phase gradient alone obeys

$$p(|\nabla\phi|) = 4\langle I \rangle C_0 \frac{|\nabla\phi|}{\left(2C_0 + \langle I \rangle |\nabla\phi|^2\right)^2} \quad \text{with} \quad \langle |\nabla\phi| \rangle = \frac{\pi}{\sqrt{2}} \sqrt{\frac{C_0}{\langle I \rangle}}, \quad (2.32)$$

which results in  $\langle |\nabla\phi| \rangle \cong 172^\circ$  per speckle size. But like Fig. 2.8, Fig. 2.11 clearly reveals anticorrelation between intensity and phase gradient, so that we can expect  $|\nabla\phi|$  to fall below  $\langle |\nabla\phi| \rangle$  in the brighter regions of the field. This is demonstrated in [Shva95]: bright speckles tend to lie close to, but not exactly over, the stationary points of phase; the phase is found to vary by typically  $45\text{-}90^\circ$  over the half width of a speckle, with  $\langle |\nabla\phi| \rangle_{I_{max}} \cong 49^\circ/d_s$  at the intensity maxima. Most of the stationary points of phase are saddles; phase extrema contribute only  $\cong 1/15$ . This distinct qualitative difference between phase and intensity field will be briefly interpreted in 2.2.5.

Moreover, the study [Shva95] shows that the major part of the anticorrelation is due to higher intensities and lower phase gradients. This is mainly due to the relative areas: while intensity minima coincide almost perfectly with very high phase gradients, they contribute only a very small area fraction to the speckle field.

As above, we conclude the considerations by confronting them with the experimental findings. Inserting our  $C_0$  and  $\langle I \rangle$  into (2.30) and (2.32), we now find  $\langle |\nabla I| \rangle \cong 6.5$  grey levels/pixel and  $\langle |\nabla \phi| \rangle \cong 6.6^\circ/\text{pixel}$ . From the sample image we get measurements of  $\langle |\nabla I| \rangle \cong 6.1$  grey levels/pixel and  $\langle |\nabla \phi| \rangle \cong 6.3^\circ/\text{pixel}$ , where the gradients are approximated by the square root of horizontal plus vertical squared pixel-to-pixel-differences. This time, the slight systematic underestimations mentioned above affect both results, since they are increased by the inclusion of two dimensions; but still the agreement is good. The spatial distribution of the 2-D gradients, converted in the same way as above for Fig. 2.9, is shown in Fig. 2.12; this may be compared with the results of a computer simulation presented in [Fre96b].

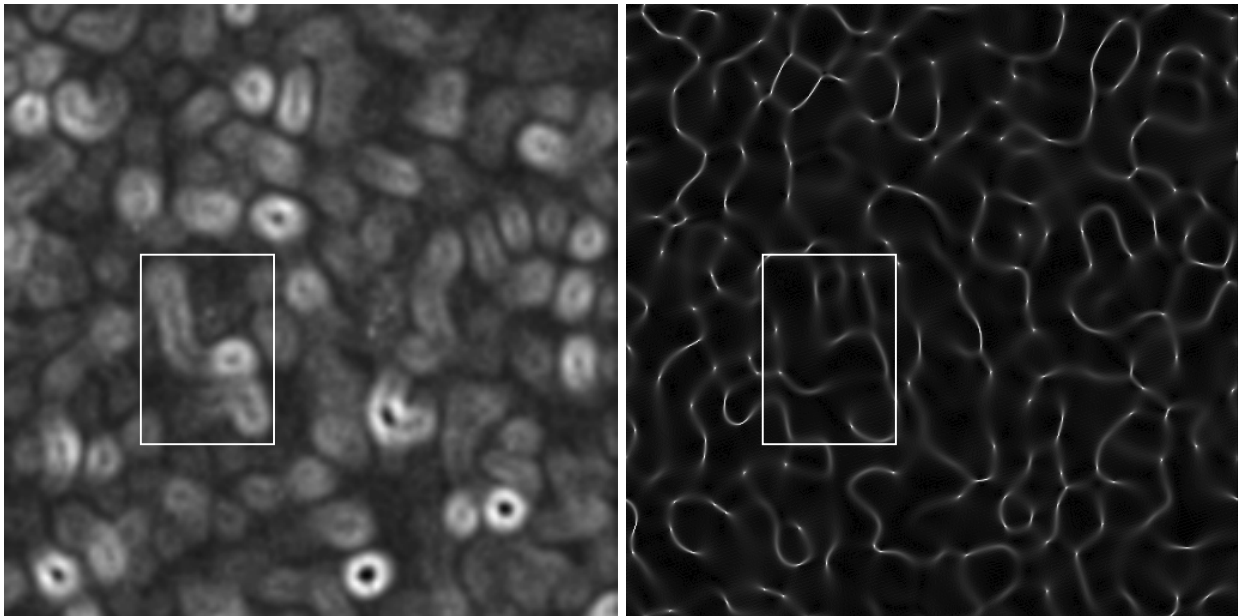


Fig. 2.12: Maps of  $|\nabla I|$  (left) and  $|\nabla \phi|$  (right). White boxes enclose same portions as in Fig. 2.9.

Not surprisingly, these maps round off the findings above and show that within the bright speckles, the phase field is co-operative for SPS thanks to moderate gradients; on crossing the dark speckle "boundaries" however, the phase may leap considerably, and mostly does; according to [Fre98b], the phase difference from one intensity maximum to the next assumes values from  $\pm\pi/2$  to  $\pm 3\pi/2$  with almost constant probability, and is almost never zero.

Eventually it may be worth noting that

$$\frac{\langle |I_x| \rangle}{\langle |\nabla I| \rangle} = \frac{\langle |\phi_x| \rangle}{\langle |\nabla \phi| \rangle} = \frac{2}{\pi} = \langle |\cos \theta| \rangle, \quad -\pi < \theta \leq \pi, \quad (2.33)$$

which is exactly what should result from a projection.

Apart from statistical considerations, a very simple explanation of the phenomenon is the phasor interpretation suggested in [Bur98a, Leh98] and shown in Fig. 2.13.

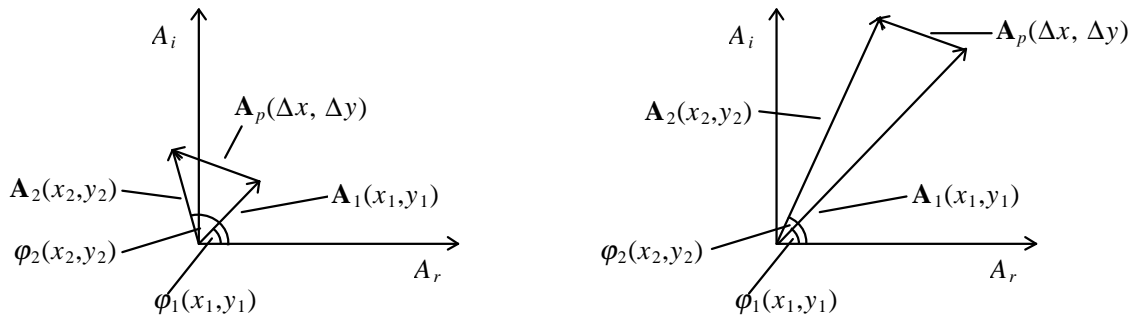


Fig. 2.13: Variation of a speckle phasor  $\mathbf{A}_1$  due to a perturbation  $\mathbf{A}_p$  for different amplitudes  $|\mathbf{A}_1(x_1, y_1)|$ .  $\varphi_1(x_1, y_1)$  and  $\mathbf{A}_p(\Delta x, \Delta y)$  are the same in both cases.

If a phasor  $\mathbf{A}_1(x_1, y_1)$  undergoes a change  $\mathbf{A}_p(\Delta x, \Delta y)$  while we move from  $(x_1, y_1)$  to  $(x_2, y_2)$  in the speckle field, then the phase change will greatly depend on the length of  $\mathbf{A}_1(x_1, y_1)$ . In the sketch to the left, the phase  $\varphi$  changes considerably on the way from  $(x_1, y_1)$  to  $(x_2, y_2)$ , since  $|\mathbf{A}_1(x_1, y_1)|$  is relatively small. The drawing to the right demonstrates the higher stability of brighter regions against changes: when  $|\mathbf{A}_1(x_2, y_2)|$  is large, the same  $\mathbf{A}_p(\Delta x, \Delta y)$  leads to a distinctly smaller phase change. This is valid for all arguments of  $\mathbf{A}_p$  except  $\pm\varphi_1$ . Unfortunately, this model is not suitable to understand the correlation of intensity and intensity gradients. To conclude with, Fig. 2.14 gives an impression of the relation between intensities and phases in the sample speckle field.

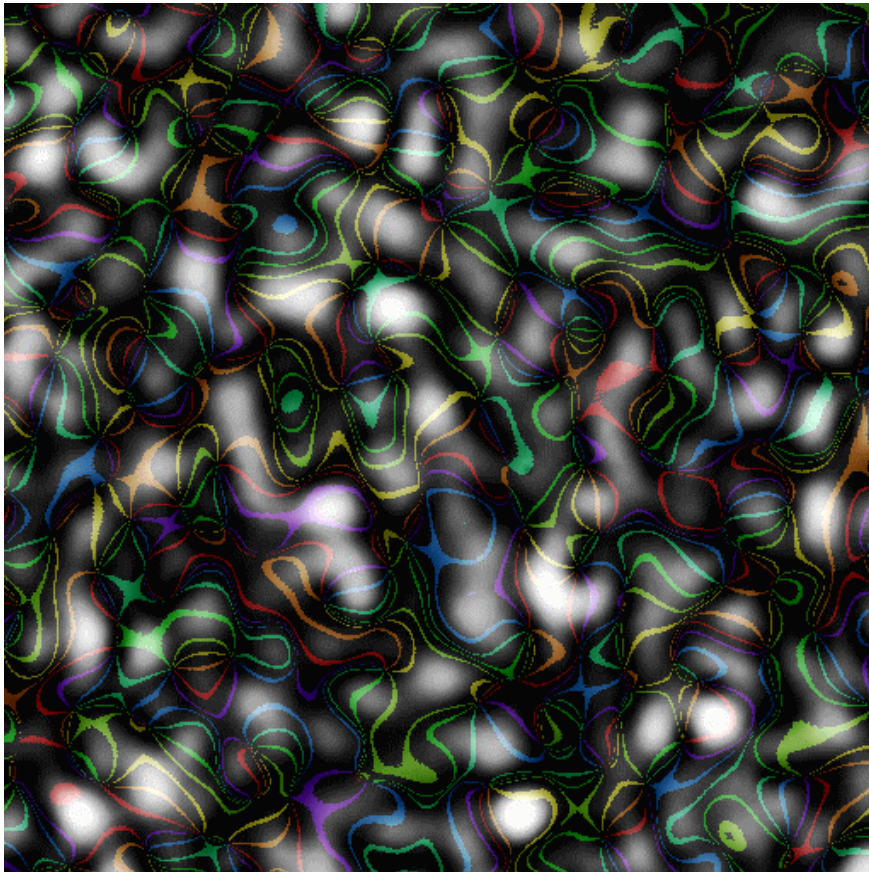


Fig. 2.14: Intensity (black/white) and phase (coloured isolines with  $45^\circ$  spacing) of a speckle field.

It can clearly be seen that the phase changes relatively slowly in the brighter regions, while in the dark valleys the isophase lines tend to get very dense. Many phase saddles are discernible by their X-shaped isophase lines, and some few closed phase contours indicate the presence of phase extrema. Moreover, the 1-D phase gradient mostly changes little as we cross bright speckles, which we will use for developing suitable phase calculation methods in Chapter 3.2.2.4. The most problematic features are the junctions of the isophase lines that are associated with rapid changes in the direction of the 2-D phase gradient. These points, forming a network connected by isophase lines, are the so-called phase singularities to which we will dedicate the following subsection.

### 2.2.5 Zero-intensity minima

In the darkest regions of a speckle pattern, we find a class of very interesting features: the zero-intensity minima, also known as phase singularities, discontinuities, screw dislocations, or vortices. They have first received attention as peculiarities in sound fields [Nye74, Ber78], and later as obstacles for phase conjugation of speckle fields [Bar81, Bar83, Fri98]; another example are the phase singularities that have been found in the phase distribution of the global tides [Nye88]. Indeed, singularities occur in almost any complex-structured two- or three-dimensional wave field. The field amplitude is exactly zero at these particular points, or lines in space, and the consequences for the phase are remarkable. Indeed, all of the terms given above refer to a property of the phase: it becomes undefined where there is no amplitude, and on crossing the minimum, the phase jumps by  $\pi$  (as also known from simpler interference experiments). This can be understood with the help of Fig. 2.15 that gives an overview of the wavefield's quantities. The drawings are generally applicable to first-order singularities (see below), since  $A_r(x,y)$  and  $A_i(x,y)$  are smooth functions and can always be approximated by tangential planes in a small region ( $dx, dy$ ) of the wave field.

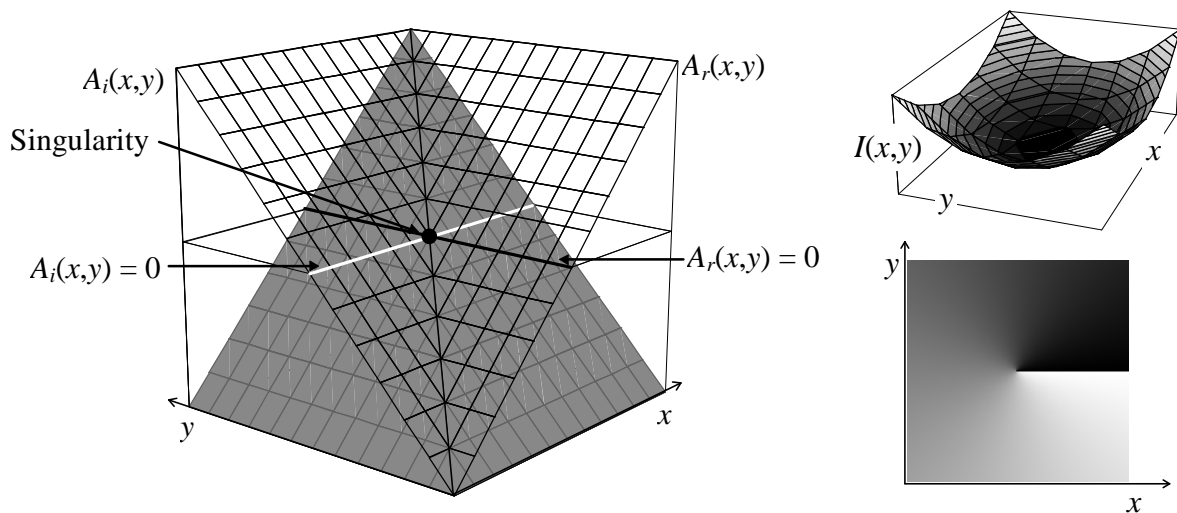


Fig. 2.15: Left: pseudo-3D plot of  $A_r(x,y)$  and  $A_i(x,y)$  in the immediate vicinity of a phase singularity. For visual clarity of the intersection, each tangential plane is plotted half as mesh grid and half as solid grey area. Right: corresponding intensity (top) and phase, coded as grey values (bottom).

As we can see from (2.1),  $A_r(x, y)$  and  $A_i(x, y)$  are statistically independent; hence they will independently fluctuate with a mean value of zero in the speckle field. The zero crossings of either function form closed contours in the  $(x, y)$ -plane; and frequently these lines intersect. In Fig. 2.15, they do so at a right angle, which is a special case. On moving along the  $A_r(x, y)=0$  line in positive  $y$ -direction, the phase of the wavefield remains constant until  $A_i(x, y)$  vanishes at the singularity and then flips sign, which results in a phase jump of  $\pi$ . The new phase value also remains constant as we move away from the minimum. Since  $A_r(x, y)$  and  $A_i(x, y)$  can be approximated by planes, the intensity has a quadratic minimum. It has been shown in [Fre96b] that these "intensity wells" are very narrow: their typical diameter is only  $1/7$  that of the speckles. The model singularity shown here is, by definition, positive and of order  $+1$ : during a counterclockwise loop around it, the phase increases by  $+1 \cdot 2\pi$ . This non-vanishing rotation of the phase has led to the term "vortices". If the zero points of  $A_r(x, y)$  and  $A_i(x, y)$  are saddle points or extrema, a dislocation of order  $N$ , i.e. with a phase progression of  $N \cdot 2\pi$  per revolution, can occur [Fre99a,b]; but these are very unstable [Fre00] and of no practical importance in speckle patterns.

The correspondence of phase dislocations and vanishing field amplitude is indicated in Fig. 2.16. Since the speckle field is not completely polarised, the dislocations do not always coincide with points of zero speckle intensity, but they certainly appear at the zeros of interferometric modulation, as the interferometric phase measurement extracts that state of polarisation from the speckle image which is co-polarised with the reference wave. For this reason, Fig. 2.16 uses the map of modulation rather than the speckle intensities as the underlying field. As to be seen by comparison with Fig. 2.2, it resembles the total speckle intensity closely but not exactly. The signs of the dislocations are not indicated here; see Fig. 2.17 for this purpose.

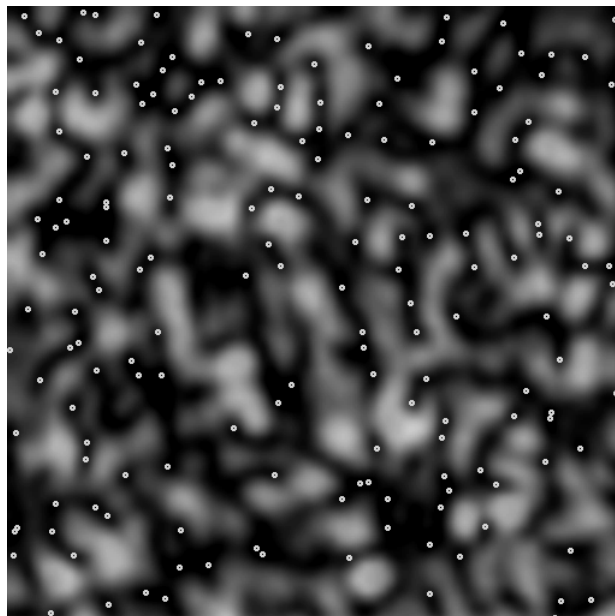


Fig. 2.16: Distribution of phase dislocations (white dots) vs. interferometric modulation of Fig. 2.2, right side.

Phase dislocations of order  $\pm 1$  are topological features in the speckle field [Nye74]; they always appear and vanish in pairs of opposite sign [Fre93]. In analogy to the intensity map, one can also define a normalised vector field  $\nabla\varphi/|\nabla\varphi|$  to find phase dislocations as well as phase minima, maxima and saddle

points, which appear as "phase topological singularities" in the vector field [Fre95d]. This leads to the rule that a new pair of phase dislocations must simultaneously create two new phase saddles. Therefore, phase saddles are at least as dense in speckle phase maps as phase singularities, leaving little space for phase extrema.

Moreover, Fig. 2.14 demonstrates that most of the isophase lines are open contours that connect the singularities; but phase extrema are of course found in closed isophase lines only. This is in qualitative difference to intensity fields, where all iso-intensity lines are closed contours and extrema are very frequent. To compare with (2.17), we list the statistical densities of critical points of the phase that have been found by computer simulation in [Fre98a]:

$$\begin{aligned}
 \rho(\varphi_{dist}) &\cong 0.460 / A_s \\
 \rho(\varphi_{min}) &\cong 0.021 / A_s \\
 \rho(\varphi_{max}) &\cong 0.015 / A_s \\
 \rho(\varphi_{sad}) &\cong 0.492 / A_s
 \end{aligned}
 \tag{2.34}$$

from which we see that the phase field shows less structure, or spatial variation, than the intensity field. The feature density is about half that of the intensity map; but still the required parameter density is some three times greater than the density of the required sampling points, which indicates that there are significant correlations also between the critical points of the phase. However there is no physical reason why phase minima should be more likely than maxima; with a larger ensemble, their densities should be equal [Fre98a].

The case depicted in Fig. 2.15, i.e. right-angle intersections of the zero-crossing lines of  $A_r(x, y)$  and  $A_i(x, y)$ , corresponds to the special case of a so-called isotropic phase dislocation. This means that the isophase lines radiate outward from such features with constant angular density, i.e. on a circular path around the dislocation, the phase slope is constant. For this case, an interesting analogy arises: the phase field generated by a distribution of isotropic singularities is similar to an electric field generated by a set of point charges, and completely free of extrema, i.e. closed field lines. This is, however, not the generic case: the zero-crossing lines of  $A_r(x, y)$  and  $A_i(x, y)$  frequently intersect at angles different from  $90^\circ$ , which concentrates isophase lines within the acute angles that they enclose, and thins them out in the obtuse angles; see [Fre93, Fre94a, Fre97a] and Fig. 2.17. In the limit, when the zero lines of  $A_r(x, y)$  and  $A_i(x, y)$  coincide (this is, the "screw" dislocation becomes an "edge" dislocation, see below), we have constant phase of the wave field on either side, and a phase jump of  $\pi$  on crossing them. To give an impression of how the structure of  $A_r(x, y)$  and  $A_i(x, y)$  generates phase singularities, Fig. 2.17 presents the phases of our sample field together with the zero lines of its real and imaginary parts (that, of course, depend on the momentary interferometric phase; but it is easy to see that the lines' intersection points will remain unaffected by whatever phase shift).

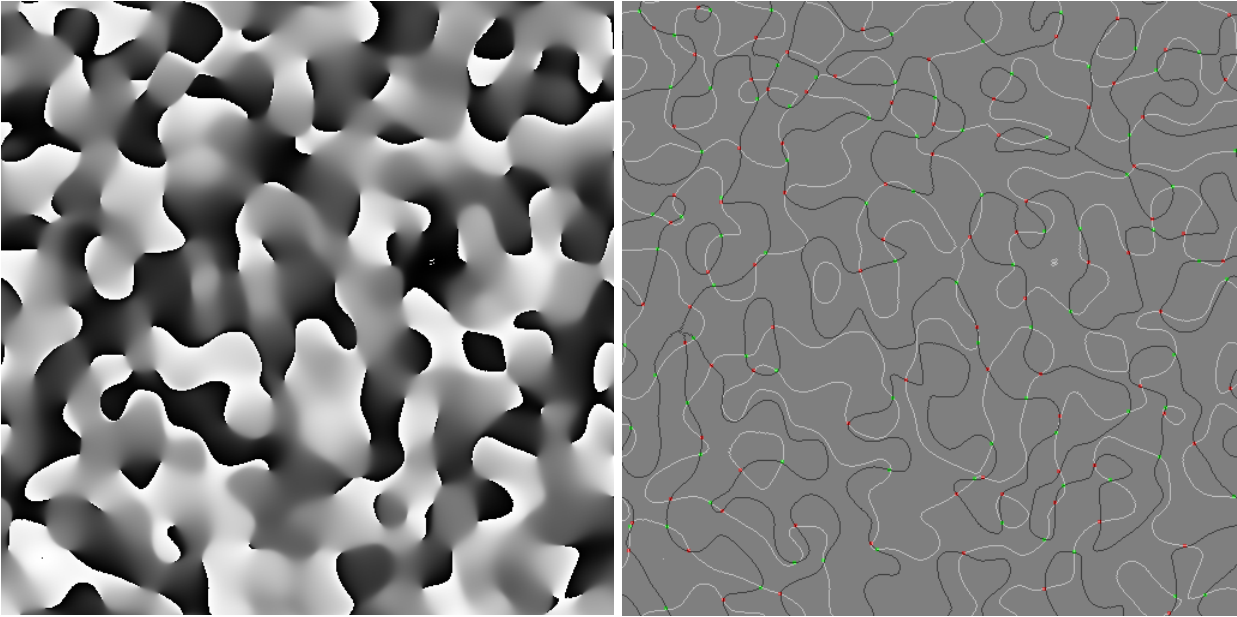


Fig. 2.17: Left: phase distribution of sample speckle field;  $[-\pi, \pi)$  represented as grey shades from black to white. Right: zero crossings of  $A_r(x, y)$ , black lines, and of  $A_i(x, y)$ , white lines. Red dots: positive, green dots: negative singularities.

The figure shows that the zero-crossings of  $A_r(x, y)$  and  $A_i(x, y)$  intersect at all angles between  $0$  and  $90^\circ$  [Fre94a], and also explains easily why dislocations always appear and vanish pairwise: it is impossible for the closed zero contours of  $A_r(x, y)$  and  $A_i(x, y)$  to generate only one new intersection. This is also the reason why they alternate in sign – also called topological charge – on paths along any zero-crossing contour [Shva94, Fre94b, Fre95d]. When the zero-crossings of  $A_r(x, y)$  and  $A_i(x, y)$  touch, they do so tangentially and generate a zero-amplitude line, or "edge" dislocation [Nye74, Bas95], of infinitesimal length in the  $x$ - $y$  plane, that instantly splits up into the two "screw" dislocations as the zero crossings of  $A_r(x, y)$  and  $A_i(x, y)$  intersect, i.e. as we shift our  $x$ - $y$ -plane in  $z$  direction and the wavefield evolves in space. The trajectories of the singularities can be thought of as dark lines that pierce the  $x$ - $y$ -plane and are orientated mostly in  $z$  direction [Ber78]. Their shape in space has been referred to as "snake-like" [Bar83]; the process of pair creation or annihilation therefore corresponds to turning points of these trajectories where the  $z$  component of their direction vector changes sign.

The abovementioned  $z$ -direction scan of the speckle field gives us the opportunity to track the loci of the dislocations slice by slice to see whether a pair of dislocations that has appeared together will also vanish together, and how one should imagine the zero-intensity trajectories in space. Fig. 2.18 presents the zero-intensity lines in the very centre of the sample phase field; the colouring helps to distinguish them. If they end, it means that they have moved out of the sample volume or that their tracking is discontinued for clarity of the representation.

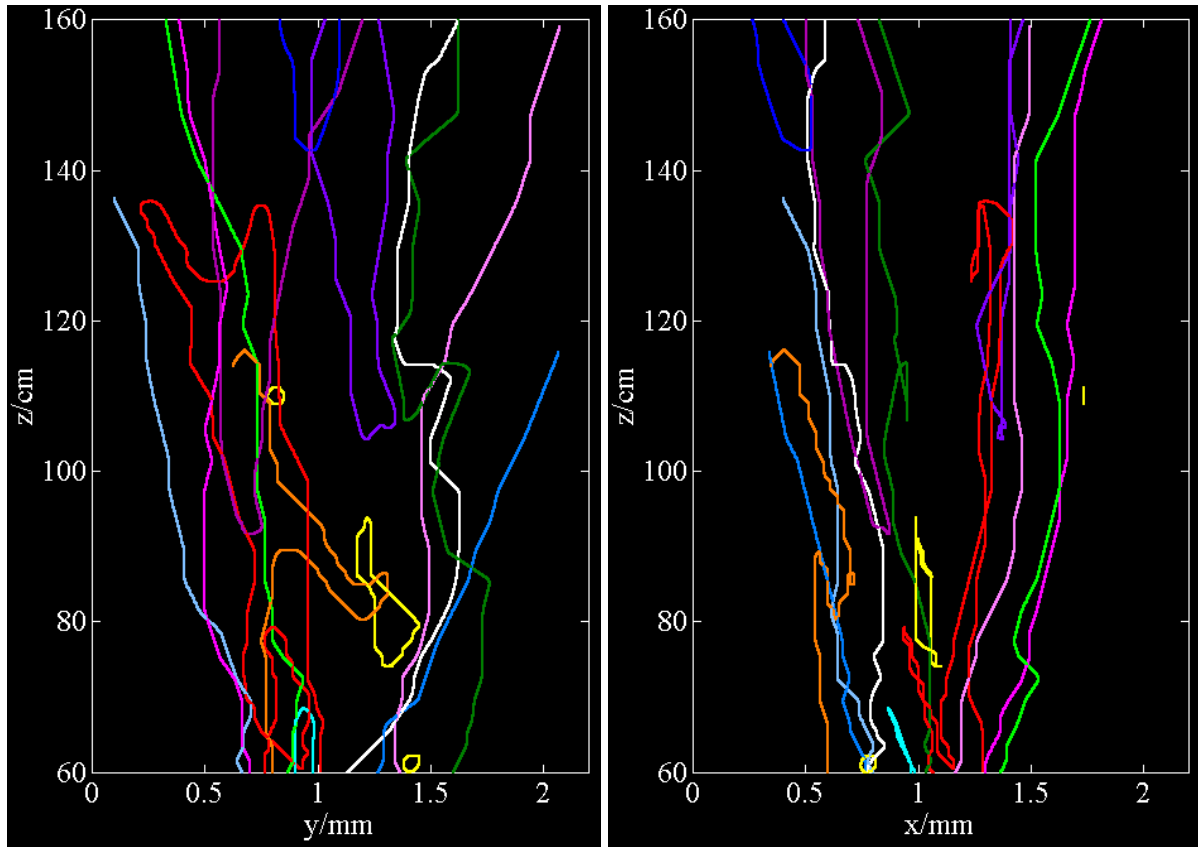


Fig. 2.18: Shape of some selected zero-intensity trajectories in a sample volume of  $(2 \text{ mm})^2 \times 100 \text{ cm}$ ; left: projection on the  $y$ - $z$  plane; right: projection on the  $x$ - $z$  plane. Positional data from 26  $x$ - $y$  slices with increasing spacing: 2 cm at the bottom, 6 cm at the top, and spline interpolated in between.

We will consider the meaning of these plots first by following the largest of the yellow structures: at  $z=73$  cm, a pair of dislocations is created. Initially, they quickly move away from each other until ( $z > 80$  cm) they approach again; finally they react and vanish at  $z=94$  cm. This is an example of a process in which the same dislocations appear and disappear together. All such events found are coloured yellow; and as to be seen, they are rather rare. The general case is the one we find when following the dark green line: it turns over at  $z=116$  cm, which means that the dislocation tracked thus far reacts with another one, from the pair that appeared at  $z=106$  cm. This in turn means that the latter pair does not vanish together: its remaining dislocation propagates without further interaction until  $z=160$  cm. Hence, every time a zero carrier bends back and forth again, a new pair of dislocations appears, and the short-lived dislocation of that pair changes its partner on vanishing. Extreme examples of this are the orange and the red lines, with a total of 5 pair reactions each. Of course, all the zero trajectories could be envisaged as separate sequences of lines, with alternately positive and negative  $z$ -components in their direction vectors, that are connected at their turning points with respect to  $z$ ; but their spatial structure is pointed out more clearly when we treat them as entities.

The trajectories without turning points correspond to singularities that persist at least throughout the sample volume, i.e. 1 m of depth. Since the speckle length  $l_s$  according to (2.45) is  $\cong 19$  cm for  $z=60$  cm and  $\cong 135$  cm for  $z=160$  cm, this poverty of events does not contradict the assertion that the zero lines' "longitudinal size of non-uniformity" is of the order of the speckle length [Bar83]. It is possible that some



of the non-interacting lines belong together and react at lower or higher  $z$  (especially the lines in magenta and green are very close at  $z=160$  cm); but this cannot be safely concluded from the available data.

The white line in the figure shows that the direction vectors of the zero trajectories can sometimes have a very small  $z$ -component, which means that its associated dislocations will move very fast in the  $x$ - $y$  plane as we change  $z$ . This raises the question whether an unambiguous assignment of zero-intensity lines to certain phase dislocations as in Fig. 2.18 is possible at all; but since the zero contours of  $A_r(x, y)$  and  $A_i(x, y)$  (cf. Fig. 2.17) evolve continuously with  $z$ , there is enough information about the singularities to always know which is which. It can, however, not be excluded that some minor zero-intensity loops between the recorded slices have gone unrecognised: the detection of new pairs of dislocations depends on the (3-D) resolution of the measurement.

Concerning the interaction and coupling of dislocation pairs, there are cases of dislocations appearing and vanishing together (the closed yellow loops within the measurement volume), but generally, the zero-intensity trajectories will turn over more than twice; and this results in swinging of relatively short-lived dislocations from and to different reaction partners. No statement can be made about the open zero-intensity lines: some might be large closed loops, some might extend to infinity.

From the statistics derived so far, also the average dislocation density  $\langle \rho_{disl} \rangle$  in the speckle field may be found [Ber78, Bar81]: setting  $A_r = A_i = 0$  in (2.1), one can come to an expression that counts the dislocations per area. We remark here that the derivation is based on the same formalism as that of (2.14); the details are given in Appendix A. For a circular scatterer, we get [Bar83, Fre93, Fre94a]

$$\langle \rho_{disl} \rangle = \frac{\pi}{8} \left( \frac{D}{\lambda z} \right)^2 \cong \frac{0.46}{A_s}, \quad (2.35)$$

where we have assumed circular speckles with an area

$$A_s = \frac{\pi}{4} \left( 1.22 \frac{\lambda z}{D} \right)^2 \cong 1.17 \left( \frac{\lambda z}{D} \right)^2; \quad (2.36)$$

$\langle \rho_{disl} \rangle$  is again the quantity that we have encountered as  $\rho(I_{zero})$  in (2.17), and as  $\rho(\varphi_{disl})$  in (2.34), and in perfect agreement with the experimental values quoted there. In [Fre93] the *ad hoc* argument is given that a speckle field contains equal amounts of bright and dark "grains" and that, therefore,  $\langle \rho_{disl} \rangle$  should equal  $1/(2A_s)$  independent of the scatterer's shape. The slight deviations in (2.35), and also for other scatterer shapes, are attributed to a somewhat inappropriate definition of the speckle area; this leads to the suggestion of referring the speckle area to  $\langle \rho_{disl} \rangle$  as an unambiguous quantity.

The constancy of  $\langle \rho_{disl} \rangle$  also delivers an argument to support the abovementioned assumption about the "longitudinal size of non-uniformity" of the zero-intensity trajectories. The speckle area depends on  $z^2$ , as does their length. Since  $\langle \rho_{disl} \rangle$  is constant, the number of dislocations per unit area should fall with a  $1/z^2$  dependence; but this is also the speckle "frequency" in  $z$  direction. Hence, one can think of each bright speckle as being accompanied by a zero line that "ends" (i.e. turns over) when the speckle "ends".

The  $z$ -direction scan of the expanding wavefield enables us to verify (2.35) by determining the number of dislocations,  $N_{dist}$ , in every recorded slice of  $512^2$  pixels: with

$$\langle \rho_{dist} \rangle \cong \frac{0.46}{A_s} \cong \frac{N_{dist}}{A_{sensor}}, \quad (2.37)$$

we can use (2.36) to establish

$$d_s \cong 2 \sqrt{\frac{A_{sensor} \cdot 0.46}{\pi}} \frac{1}{\sqrt{N_{dist}}}; \quad (2.38)$$

the speckle sizes thus obtained are plotted vs.  $z$  in Fig. 2.19.

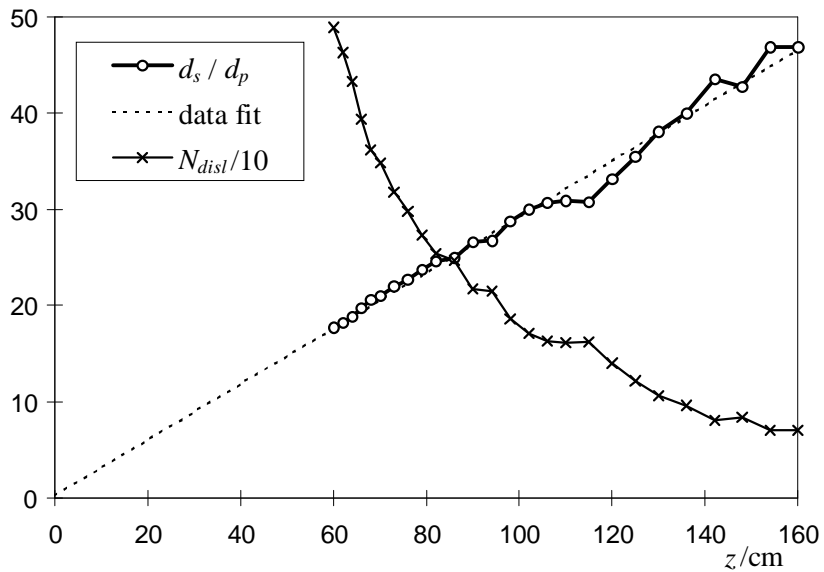


Fig. 2.19: Number of dislocations in sample area and corresponding speckle sizes for  $60 \text{ cm} < z < 160 \text{ cm}$ .

The expected dependence is confirmed by the measurement; not surprisingly, the determination of  $d_s$  from  $N_{dist}$  gets more and more precise as the latter rises. For this to function, the speckle field must of course be well resolved by the camera. The fitted straight line almost passes through the origin even though no data are available for  $z < 60 \text{ cm}$ . When comparing the  $d_s$  thus obtained with those from an evaluation of the speckle fields' autocorrelations, the values coincide within  $\pm 5\%$ . Since the number of speckles on the sensor is relatively small, the autocorrelation method is applied to a small ensemble, which does not match the spirit of the approach and explains the deviations. Apparently, the method of determining the speckle size from the dislocation density works quite well when the speckles are large. Other experimental results, confirming the linear dependence of  $\rho_{dist}$  and  $D$ , are given in [Bar83].

## 2.3 Second-order speckle statistics

In SPS, and in TPS with unresolved speckles, it occurs that the distances over which the spatial structure of the speckle field changes are not much larger – or even very much smaller – than the pixel size. Then one needs to know the spatial relation of speckle intensity and phase between two points  $P_1=(x_1, y_1)$  and  $P_2=(x_2, y_2)$  in the speckle field,  $p(I_1, I_2, \varphi_1, \varphi_2)$ , or simplifications thereof. We will proceed from the most general concept, the spatial autocorrelation of intensity and phase, to the somewhat more complicated topic of the relation between intensity and phase.

### 2.3.1 Intensity autocorrelation

Probably the most popular and indeed very useful second-order quantity is the concept of the mean speckle size in terms of intensity. We start with the autocorrelation of the complex amplitude,

$$R_{\mathbf{AA}^*}(x_1, y_1, x_2, y_2) = \left\langle \mathbf{A}(x_1, y_1) \mathbf{A}^*(x_2, y_2) \right\rangle, \quad (2.39)$$

which is also referred to as *mutual intensity* of the speckle field [Goo75, p. 36]. For our purposes, it may suffice to remember that this function is essentially the Fourier transform of the intensity distribution within the scattering spot or the aperture shape, depending on whether objective or subjective speckles are concerned. For the latter case however, the treatment is correct only if the imaging aperture contains a large number of speckles. Then the aperture may be thought of as another rough surface, whose shape plays the same role for the formation of subjective speckles as does the scattering spot in the case of objective speckles.

The mutual intensity is usually normalised to yield the complex coherence factor

$$\mu_A(x_1, y_1, x_2, y_2) := \frac{R_{\mathbf{AA}^*}(x_1, y_1, x_2, y_2)}{\sqrt{R_{\mathbf{AA}^*}(x_1, y_1, x_1, y_1) R_{\mathbf{AA}^*}(x_2, y_2, x_2, y_2)}}, \quad (2.40)$$

which is unity for  $x_1=x_2$  and  $y_1=y_2$  and decays as the points move away from each other; when it becomes zero, the points are said to be one spatial correlation length or speckle size apart.

It can be shown [Goo75, pp. 36-38] that the intensity autocorrelation  $R_I(x_1, y_1, x_2, y_2)$  is given by

$$R_I(\Delta x, \Delta y) = \langle I \rangle^2 \left( 1 + |\mu_A(\Delta x, \Delta y)|^2 \right) \quad (2.41)$$

with  $\Delta x = x_2 - x_1$  and  $\Delta y = y_2 - y_1$ . That is, the shape of the  $\mu_A$  curve determines that of a typical speckle area, or correlation cell, in the speckle field. If the scatterer or aperture is a uniformly bright circle, we get

$$\mu_A(\Delta x, \Delta y) = \frac{2J_1(\alpha)}{\alpha} \quad \text{with} \quad \alpha = \pi \frac{D}{\lambda z} \sqrt{\Delta x^2 + \Delta y^2}, \quad (2.42)$$

$J_1$  denoting the first-kind Bessel function of first order. This can very easily be generalised to the elliptical apertures that are also used in the experimental work. For circular apertures,  $\mu_A$  is the well-known Airy

function, which demonstrates that the speckle shape is closely related to the aperture's point spread function. It assumes its first zero at

$$\sqrt{\Delta x^2 + \Delta y^2} \cong 1.22 \frac{\lambda z}{D} = d_s, \quad (2.43)$$

which gives the mean speckle size. The shape of  $R_I(\Delta x, \Delta y)$  is given in Fig. 2.20. If we write the intensity correlation as  $R_I(x_1, y_1, x_2, y_2) = \langle I(x_1, y_1) I(x_2, y_2) \rangle$ , we can use the independence of  $P_1$  and  $P_2$  at  $\mu_A = 0$  to decompose it into  $\langle I(x_1, y_1) \rangle \langle I(x_2, y_2) \rangle = \langle I \rangle^2$ , while for  $\mu_A = 1$  we have  $P_1 = P_2$  and obtain  $\langle I(x_1, y_1) I(x_1, y_1) \rangle = 2 \langle I \rangle^2 = \langle I^2 \rangle$ . The "bias correlation" reflects the fact that the intensity is never negative, in contrast to the phase and its autocorrelation.

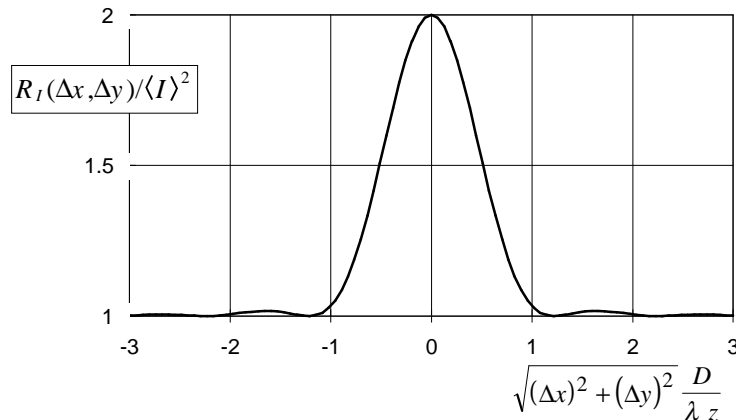


Fig. 2.20: Speckle intensity autocorrelation function for a circular scattering spot with uniform brightness.

This definition is merely statistical and does not imply anything about the true distribution of shapes and sizes of bright or dark regions. However, it has recently been found that the well-known and proven notion of "speckle size" is correct also with respect to the individual size of the bright spots [Fre96b]. Even the intensity profiles of individual speckles have been found to follow the course of  $R_I(\Delta x, \Delta y)$  quite well [Fre96b, Fre98a], which means that there is only a very small region of quasi-constant intensity within a bright speckle; the greater the peak intensity, the greater will be the intensity gradient *within* the speckle area.

The derivation of (2.41) is based on a two-dimensional treatment of the Kirchhoff-Fresnel diffraction integral. It is possible to extend the calculation to find the three-dimensional autocorrelation [Leu90]. The general result is rather difficult an expression; however considering the  $z$  direction only, one finds for a circular aperture [Leh98]

$$\mu_A(\Delta z) = \frac{\alpha}{2\pi i \Delta z} \exp\left(\frac{2\pi i \Delta z}{\alpha}\right) \quad \text{with} \quad \alpha = 8\lambda \frac{z^2}{D^2} \quad (2.44)$$

and  $|\mu_A(\Delta z)| = \left| \text{sinc}\left(\frac{\Delta z}{\alpha}\right) \right|$ ,

where  $\text{sinc}(x) = \sin(\pi x) / (\pi x)$ . The first zero of this expression, indicating the length of a correlation cell, is at

$$\Delta z = 8\lambda \left( \frac{z}{D} \right)^2 = l_s; \quad (2.45)$$

see also [Li 92, Yos93]. The quadratic relationship of  $l_s$  and  $z$  generates more and more elongated speckles – the aspect ratio is proportional to  $z$  – that are "cigars" only near the scatterer or aperture, and "worms" in most practical cases (cf. [Wei77]): for  $z/D=1.5$ ,  $l_s/d_s$  is already  $\cong 10$ .

### 2.3.2 Phase autocorrelation

It is clear that the phase structure of speckle patterns affects speckle interferometry as significantly as does the intensity structure. Again, especially for SPS it is useful to find out how the phase of a speckle pattern will fluctuate statistically, and over what distances we may expect to find some phase correlation. Unfortunately,  $\varphi$  is accessible modulo  $2\pi$  only, which is difficult to treat mathematically: if we map the phases onto  $[-\pi, \pi)$ , two points with  $\varphi_1(x_1, y_1) = -\pi + \varepsilon$  and  $\varphi_2(x_2, y_2) = \pi - \varepsilon$  would yield  $\Delta\varphi = \varphi_2 - \varphi_1 = 2\pi - 2\varepsilon$ , while the actual difference is only  $2\varepsilon$ .

Consequently, there are two ways to deal with  $\varphi$ . The first one regards  $\varphi$  as a continuous function without  $-\pi \leftrightarrow \pi$  jumps, which can lead to problems with path-dependence in complicated phase distributions with dislocations, such as speckle phase fields. The other confines  $\varphi$  to  $[-\pi, \pi)$ , which makes it a unique but discontinuous (wrapped) function.

For continuous phases, the phase autocorrelation function has been calculated long ago [Mid60] as that of a band-limited random signal, an example of which is speckle noise (as for the band limitation, see 3.3.1). If the primary phase interval is set to  $[-\pi, \pi)$ , the function reads

$$R_{\varphi, c}(\mu_A) = \pi \arcsin(|\mu_A|) - \arcsin^2(|\mu_A|) + \frac{1}{2} \sum_{n=1}^{\infty} \frac{|\mu_A|^{2n}}{n^2}, \quad (2.46)$$

with  $\mu_A$ , the complex degree of coherence, to be calculated from the scatterer's characteristics; the subscript  $c$  stands for "continuous". A primary phase interval of  $[0, 2\pi)$  would correspond to a "bias phase" of  $\pi$  and merely add a constant of  $\pi^2$  to the function.

For discontinuous phases, the decrease in correlation has particular properties because of the  $-\pi \leftrightarrow \pi$  transitions of the phase taken as real  $2\pi$  jumps; this function has been established only recently [Fre96a] and reads

$$R_{\varphi, d}(\mu_A) = \frac{1}{2} \left( \pi \arcsin(\operatorname{Re}(\mu_A)) + \arcsin^2(\operatorname{Re}(\mu_A)) - \frac{1}{2} \sum_{n=1}^{\infty} \frac{\operatorname{Re}(\mu_A)^{2n}}{n^2} \right), \quad (2.47)$$

where the subscript  $d$  denotes the discontinuous interpretation. Both of the functions are evaluated for  $n=1$  to 100, with  $\mu_A$  according to (2.42), and shown in Fig. 2.21. The scaling of the ordinate reflects the fact

that the phase variance in the speckle pattern is zero for  $|\mu_A|=1$ , and  $\pi^2/3$  for  $|\mu_A|=0$ , which corresponds to a uniform distribution.

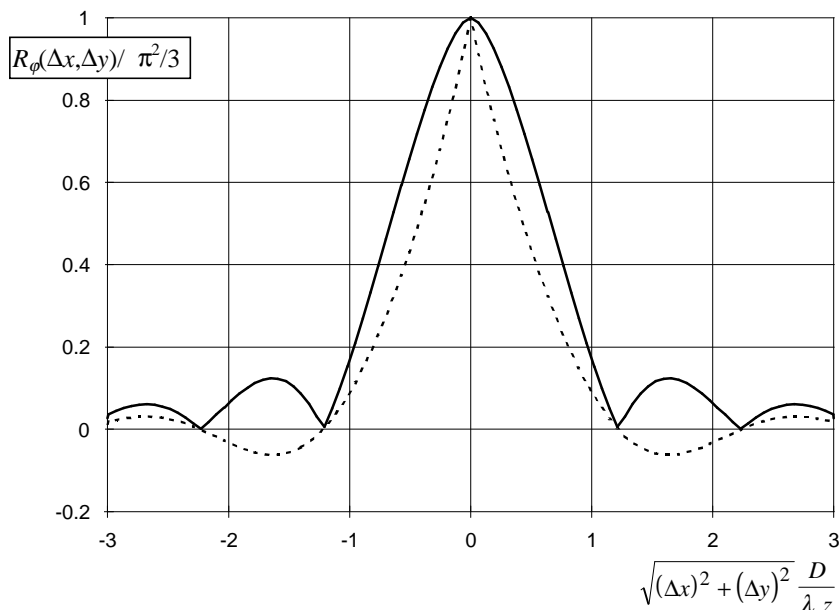


Fig. 2.21: Speckle phase autocorrelation function for a circular scattering spot with uniform brightness; solid line:  $R_{\phi,c}$ ; broken line:  $R_{\phi,d}$ .

Since  $R_{\phi}$  depends on  $\mu_A$ , as does  $R_I$ , its correlation length is exactly the same as for the intensity. The qualitative difference of the functions is due to the permissible ranges of phase differences between neighbouring points, which are  $(-\pi, \pi)$  for  $R_{\phi,c}$ , and  $(-2\pi, 2\pi)$  for  $R_{\phi,d}$ . Hence,  $R_{\phi,d}$  decays very quickly initially and even changes to anticorrelation after its first zero, which corresponds to an average phase change greater than  $\pm\pi$ ; for more details, see [Fre96a].

To clarify the interpretation of  $\phi$ , we consider Fig. 2.22, giving an example of the two methods applied to the familiar sample phase distribution, displayed in the middle of the top row. Of particular interest in this context are the so-called "branch cuts" [Fri92], the transitions from black to white where  $\phi$  crosses  $\pi$ . These jumps are related to the discontinuous interpretation of  $\phi$ ; it is hard to imagine a continuous representation. The outer images display the local phase correlation for  $\Delta x = 10$  pixels; to the left, continuous phases are assumed, and to the right, the discontinuity of  $\phi$  shows up distinctly wherever the direction vector of a branch cut has a non-zero y-component. In all correlation maps, white corresponds to complete correlation (no phase difference between  $(x_1, y)$  and  $(x_2, y)$ ), medium grey to zero correlation (phase difference of  $\pm\pi$ ), and black to complete anticorrelation (phase difference of  $\cong \pm 2\pi$ ). Remembering that the field's phase jumps by  $\pi$  while we are crossing points or lines where it vanishes, the identification of zero correlation with a phase offset of  $\pi$  seems quite reasonable.

It can be seen that  $R_{\phi,c}$  does not produce anticorrelations; as explained above, this is because phase differences greater/smaller than  $\pm\pi$  do not occur in this interpretation. In the map of  $R_{\phi,d}$ , we do find phase jumps of  $\pm 2\pi$  near the branch cuts of the speckle phase, giving rise to phase anticorrelation. However, the branch cuts are no physical reality, since they can be moved around in the image by adding

global phase shifts, as demonstrated in the bottom row. The phase distribution shown in the centre is exactly the same as in the top row, only a global phase shift of  $\pi$  has been added (or subtracted) modulo  $2\pi$ , as can be seen by the circulation of the branch cut in the black circle(s). The remaining correlation is unaltered when we assume continuous speckle phases – the images in the left column look exactly the same –, whereas the results from the discontinuous interpretation are rather different from each other.

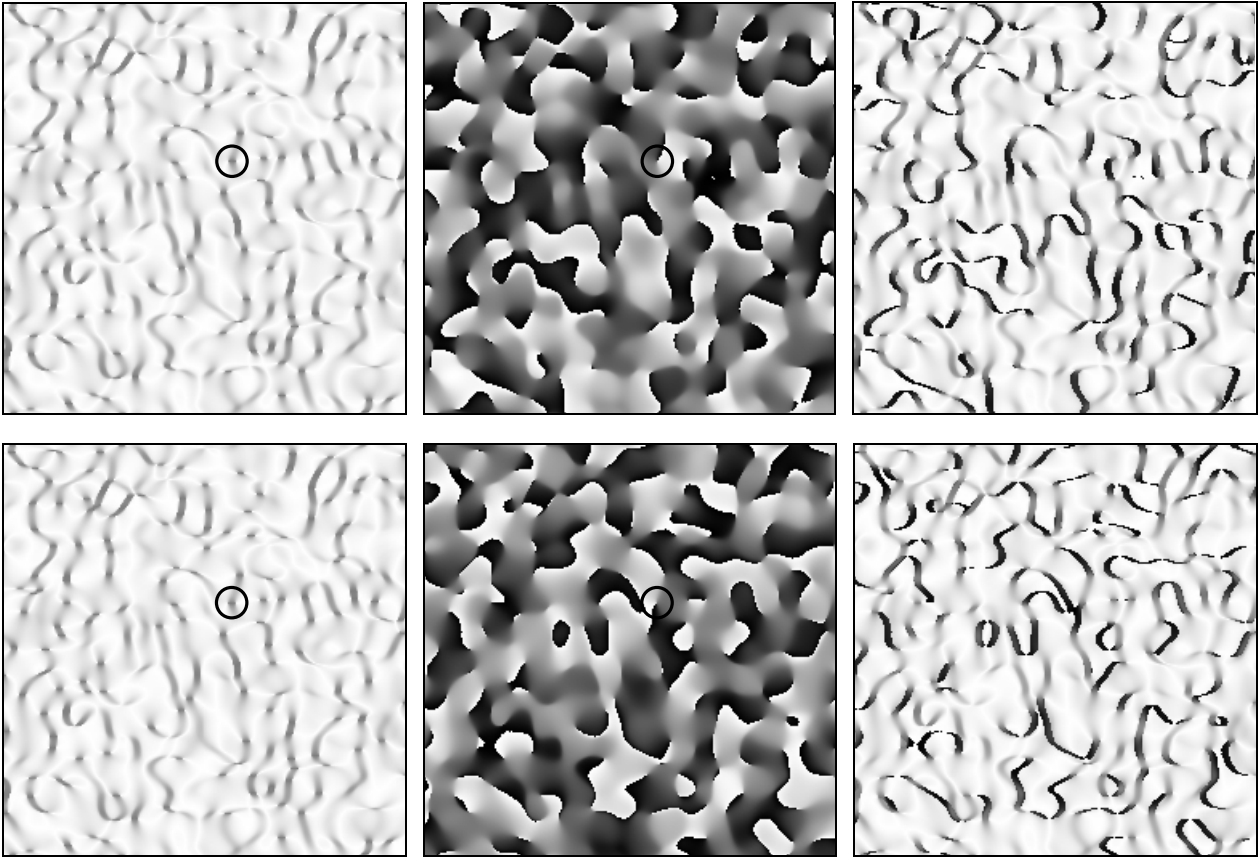


Fig. 2.22: Interpretations of phase fields leading to different phase correlations. Centre, speckle phase distribution; black circles: sample dislocation. Left,  $R_{\phi,c}$ ; black circles, example of decorrelation "spot"; right,  $R_{\phi,d}$ . Global phase shift of  $\pi$  between top and bottom row; see text.

Clearly, it is impossible for the phase decorrelation to depend on the global phase offset, which makes evident that the discontinuous interpretation is not suitable for our purpose. Moreover, when phase measurement errors in displacement images are evaluated, we will assume that they are in the range  $(-\pi, \pi)$  (see Chapter 4.2). The decorrelation "spot" enclosed by the black circles in the left column of Fig. 2.22 is an example of how phase singularities contribute some amount of complete phase decorrelation (cf. Fig. 2.15) even for small  $\Delta x$  and when branch cuts are ignored.

### 2.3.3 Second-order probability densities

As above, it proves easier to start with the amplitudes. The joint probability density of the complex amplitudes  $\mathbf{A}_1 = A_{1r} + iA_{1i}$  and  $\mathbf{A}_2 = A_{2r} + iA_{2i}$  at the points  $P_1$  and  $P_2$  is given by [Goo75, p. 42]

$$p(A_{1r}, A_{1i}, A_{2r}, A_{2i}) = \frac{1}{4\sigma^4 \pi^2 (1 - |\mu_A|^2)} \exp \left( - \frac{|\mathbf{A}_1|^2 + |\mathbf{A}_2|^2 - \mu_A \mathbf{A}_1 \mathbf{A}_2^* - \mu_A^* \mathbf{A}_1^* \mathbf{A}_2}{2\sigma^2 (1 - |\mu_A|^2)} \right); \quad (2.48)$$

the derivation relies on  $A_{1r}, A_{1i}, A_{2r}, A_{2i}$  being all jointly Gaussian variables, and  $\sigma$  is the same quantity as in (2.1). Using (2.3) again, the conversion to  $I$  and  $\varphi$  yields [Goo75, Vry86, Leh98]

$$p(I_1, I_2, \varphi_1, \varphi_2) = \frac{1}{\langle I \rangle^2 4\pi^2 (1 - |\mu_A|^2)} \exp \left( - \frac{I_1 + I_2 - 2\sqrt{I_1 I_2} |\mu_A| \cos(\varphi_1 - \varphi_2 + \psi)}{\langle I \rangle (1 - |\mu_A|^2)} \right), \quad (2.49)$$

with  $\|\mathbf{J}\|=1/4$  and  $\mu_A := |\mu_A| \exp(i\psi)$ . The phase factor  $\psi$  of the complex degree of coherence is deterministic and related to the phase distribution of the illumination and the scatterer's macroscopic geometry and symmetry; in general, it represents the non-speckled part of the wavefront. As we are considering a system that is symmetrical about the optical axis, we can set  $\psi=0$ ; to preserve generality however, we will continue including  $\psi$ , as it might play a role in other geometries. When  $|\mu_A|$  vanishes, (2.49) can be decomposed into  $p(I_1, \varphi_1) \cdot p(I_2, \varphi_2)$ , reflecting the statistical independence of the functions. As above, we will now derive some joint probability densities from this general expression.

Since the derivation of the presented expressions relies on jointly Gaussian variables, the extension to higher orders is in principle straightforward; the third-order pdf  $p(I_1, I_2, I_3, \varphi_1, \varphi_2, \varphi_3)$  has been calculated in [Rao91], also by starting with the complex amplitudes.

### 2.3.3.1 Intensity statistics

In a first step, we will put the phases aside by eliminating  $\varphi_1$  and  $\varphi_2$  and obtain [Goo75]

$$p(I_1, I_2) = \frac{1}{\langle I \rangle^2 (1 - |\mu_A|^2)} \exp \left( - \frac{I_1 + I_2}{\langle I \rangle (1 - |\mu_A|^2)} \right) I_0 \left( \frac{2\sqrt{I_1 I_2} |\mu_A|}{\langle I \rangle (1 - |\mu_A|^2)} \right), \quad (2.50)$$

where  $I_0$  – not to be confused with our intensities – is the modified Bessel function of first kind and zero order. The course of (2.50) is not too complicated, as Fig. 2.23 illustrates for  $I_1$  fixed to some arbitrary value. This plot already provides a complete interpretation of (2.50), as it is symmetrical in  $I_1$  and  $I_2$ .

The limiting case of  $|\mu_A|=1$  is not displayed because it corresponds to  $(x_1, y_1) = (x_2, y_2)$  and yields  $p(I_1, I_2)|_{|\mu_A|=1} = p(I_1) \cdot \delta(I_2, I_1)$ . For the other extreme,  $p(I_1, I_2)|_{|\mu_A|=0} = p(I_1)p(I_2)$ , with each of them as in (2.6). Hence, the distribution of  $I_2$  is initially free and assumes the well-known exponential form; as  $|\mu_A|$  increases, it is gradually being forced to centre on  $I_1$ .



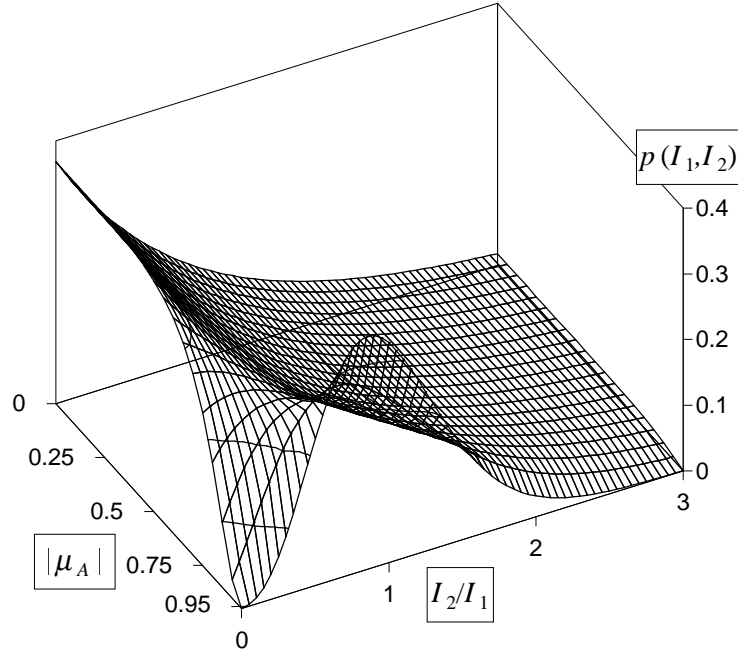


Fig. 2.23: Pseudo-3D plot of  $p(I_1, I_2)$ .

To find out the influence of a fixed  $I_1$ , we write down the pdf of  $I_2$  conditioned on  $I_1$ , which is

$$p(I_2|I_1) = \frac{p(I_1, I_2)}{p(I_1)} = \frac{1}{\langle I \rangle (1 - |\mu_A|^2)} \exp\left(-\frac{|\mu_A|^2 I_1 + I_2}{\langle I \rangle (1 - |\mu_A|^2)}\right) I_0\left(\frac{2\sqrt{I_1 I_2} |\mu_A|}{\langle I \rangle (1 - |\mu_A|^2)}\right). \quad (2.51)$$

As to be seen, the coupling between  $I_2$  and  $I_1$  depends on  $|\mu_A|$  and  $I_1$ . To understand the role of  $I_1$ , we visualise three cases with  $|\mu_A|=0.1, 0.6$ , and  $0.95$ , respectively.

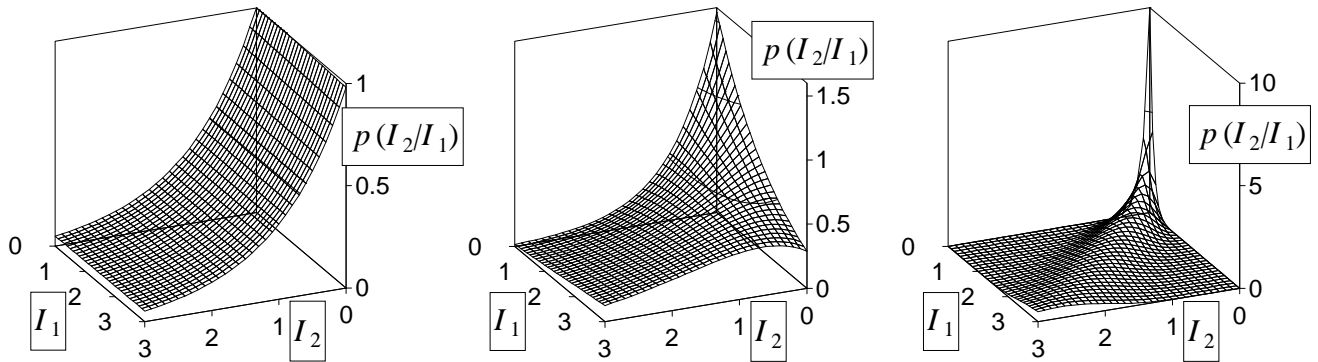


Fig. 2.24: Pseudo-3D plots of  $p(I_2|I_1)$  for  $\langle I \rangle=1$  and  $|\mu_A|=0.1$  (left),  $0.6$  (centre), and  $0.95$  (right).

While it is not surprising that  $I_2$  almost remains a negative exponential when  $|\mu_A|$  is small, we find an interesting behaviour for intermediate values of  $|\mu_A|$ . When  $I_1$  is small, the distribution of  $I_2$  is only slightly altered, which means that the dark portions of the speckle field are narrow structures: their influence does not reach very far. Then, at large  $I_1$ , the maximal probability of  $I_2$  reluctantly moves away from zero, but remains quite low. This means that bright spots do cause their surroundings to get brighter, but that the latter will nonetheless be considerably darker than the bright spots themselves, in agreement with the positive correlation of the intensity and its gradient that we found in 2.2.3.1. The last example

with  $|\mu_A|=0.95$  supports this further: while  $p(I_2|I_1)$  has its maximum almost at  $I_2$  when  $I_1$  is low, this maximum is shifted towards lower values for high  $I_1$ ; for instance, at  $I_1=3$ , the most probable value of  $I_2$  is  $\cong 2.7$ . This imbalance of properties of "dark" and "bright" structures is the reason why we can instantly tell a speckle image from its inverted counterpart.

It is clear that  $I_1$  also exerts a certain influence on mean value and standard deviations of  $I_2$  as compared to the "free" values given in (2.7). Also these calculations have been carried out [Don79], and we have

$$\begin{aligned} \langle I_2 \rangle | I_1 &= \langle I \rangle (1 - |\mu_A|^2) + |\mu_A|^2 \cdot I_1 \\ \sigma_{I_2}^2 | I_1 &= \langle I \rangle^2 (1 - |\mu_A|^2)^2 + |\mu_A|^2 |2\langle I \rangle (1 - |\mu_A|^2)| \cdot I_1, \end{aligned} \quad (2.52)$$

where we have written down the variance for convenience of notation. It is easy to see that we obtain the "free" values again for  $|\mu_A|=0$ . With growing  $|\mu_A|$ , the coupling of  $\langle I_2 \rangle$  to  $I_1$  gets stronger and reaches unity when  $(x_1, y_1)$  and  $(x_2, y_2)$  coincide. For the variance, we find the strongest influence of  $I_1$  at  $|\mu_A| \cong 0.71$ ; of course the variance eventually drops to zero when  $|\mu_A|=1$ . The functions are shown in Fig. 2.25.

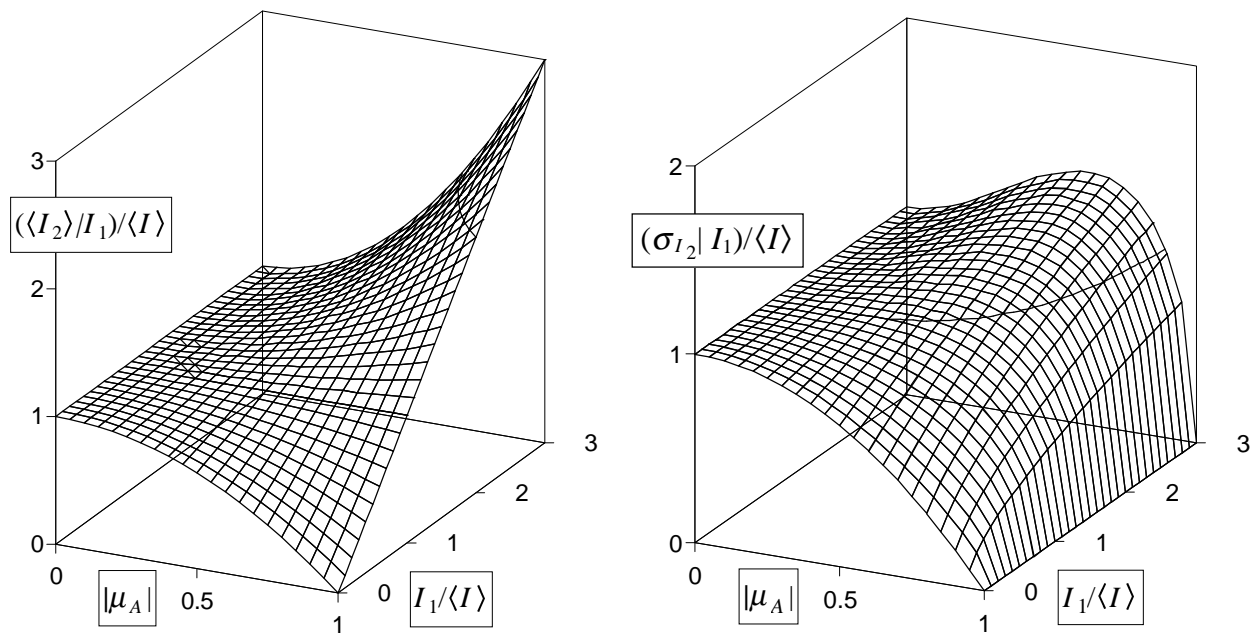


Fig. 2.25: Pseudo-3D plots of  $\langle I_2 \rangle | I_1$  (left) and  $\sigma_{I_2} | I_1$  (right), normalised by  $\langle I \rangle$ .

For  $\langle I_2 \rangle | I_1$ , the above interpretation of (2.52) suffices to understand the graph: the closer  $(x_2, y_2)$  is to  $(x_1, y_1)$  (i.e. the larger  $|\mu_A|$ ), the more are the intensities likely to be equal. When looking at  $\sigma_{I_2} | I_1$  however, we see that the standard deviation gets *larger* than the free value  $\sigma_{I_2} | I_1 |_{|\mu_A|=0} = \langle I \rangle$  when  $I_1$  is large and  $|\mu_A|$  takes on intermediate values. This again shows the tendency for rapid intensity fluctuations especially in the brighter regions of the speckle pattern. As shown in [Bar87], this remains valid for aperture-integrated speckle patterns as well.

## 2.3.3.2 Phase statistics

To obtain  $p(\varphi_1, \varphi_2)$ , we have to integrate (2.49) over  $I_1$  and  $I_2$ , which is rather complicated, but has fortunately been taken care of before [Mid60, Goo75]; the result is

$$p(\varphi_1, \varphi_2) = \frac{1 - |\mu_A|^2}{4\pi^2} (1 - \beta^2)^{-3/2} \left( \beta \arcsin \beta + \beta \frac{\pi}{2} + \sqrt{1 - \beta^2} \right), \quad (2.53)$$

where  $\beta = |\mu_A| \cos(\varphi_1 - \varphi_2 + \psi)$  and we deal with  $\psi$  as above. To look at the quantity of interest, namely the phase at  $(x_2, y_2)$  in relation to that at  $(x_1, y_1)$ , we can content ourselves with fixing  $\varphi_1$  to some arbitrary value and varying  $\varphi_2$  from  $-\pi$  to  $\pi$ . For convenience, we introduce the relative phase variable  $\vartheta := \varphi_1 - \varphi_2 + \psi$  and consider  $p(\vartheta)$ , which yields one plot for all  $\varphi_1$ . Repeating the procedure with swapped angles  $\varphi_1$  and  $\varphi_2$  would teach us nothing new, as  $\beta$  is symmetrical in  $\varphi_1$  and  $\varphi_2$ . The resulting probability distribution of  $\vartheta$  vs.  $|\mu_A|$  is shown in Fig. 2.26.

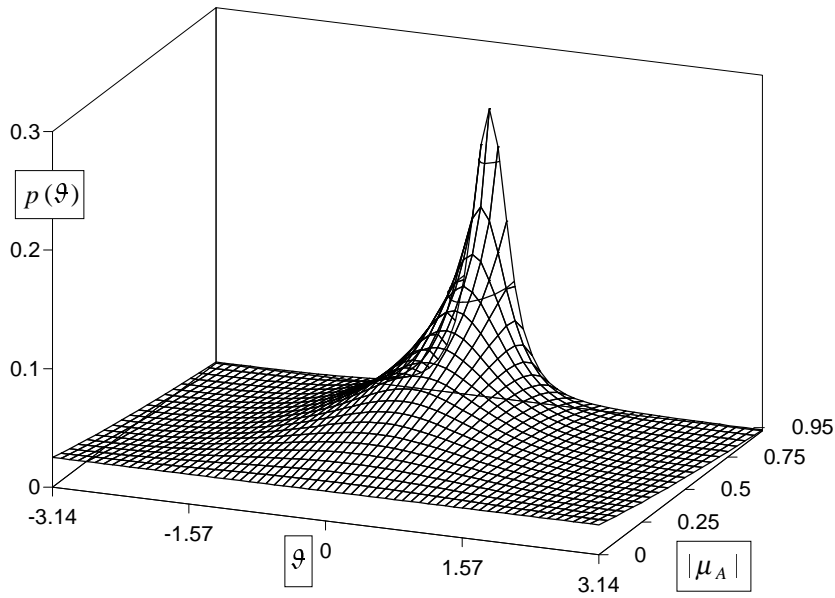


Fig. 2.26: Pseudo-3D plot of  $p(\vartheta)$  for  $0 \leq |\mu_A| < 1$ .

For high values of  $|\mu_A|$ ,  $\varphi_1$  and  $\varphi_2$  are indeed close together; as above, the case  $|\mu_A|=1$  corresponds to a  $\delta$  function because of  $\varphi_2|_{|\mu_A|=1} \equiv \varphi_1$ , and is not plotted. As we recede from  $(x_1, y_1)$ ,  $|\mu_A|$  decreases and the likely phase differences spread out, until we have a uniform distribution at  $|\mu_A|=0$ . This constant value at  $|\mu_A|=0$  has mistakenly been given as  $1/(2\pi)$  [Mid60, Goo75]; but as we have fixed  $\varphi_1$  to some value, we see only one of the two angular variables sweep its range in Fig. 2.26; therefore the value producing the correct normalisation is  $1/(4\pi^2)$ , which results immediately from (2.53) when  $\beta=0$ .

The conditional pdf for the phases is simply

$$p(\varphi_2|\varphi_1) = \frac{p(\varphi_1, \varphi_2)}{p(\varphi_1)} = \frac{1 - |\mu_A|^2}{2\pi} (1 - \beta^2)^{-3/2} \left( \beta \arcsin \beta + \beta \frac{\pi}{2} + \sqrt{1 - \beta^2} \right); \quad (2.54)$$

this is the function that we find in [Mid60, Goo75] and that looks qualitatively like in Fig. 2.26. When  $\beta < 0$ , the whole function is just shifted by  $\pi$  along the axis of  $\varphi_2$  because of  $-\cos(\varphi) = \cos(\varphi \pm \pi)$ .

For mean value and variance of  $\varphi_2$  conditioned on  $\varphi_1$ , we have [Don79]

$$\begin{aligned} \langle \varphi_2 \rangle | \varphi_1 &= \varphi_1 & \beta > 0 \\ &= \varphi_1 + \pi & \beta < 0 \\ \sigma_{\varphi_2}^2 | \varphi_1 &= \frac{\pi^2}{3} - \pi \arcsin |\mu_A| + \arcsin^2 |\mu_A| - \frac{1}{2} \sum_{n=1}^{\infty} \frac{|\mu_A|^{2n}}{n^2} \\ &\cong \frac{\pi^2}{3} (1 - |\mu_A|)^{0.84} ; \end{aligned} \quad (2.55)$$

the last line gives a useful approximation [Leh98]. The mean values instantly get plausible by the symmetry in Fig. 2.26; we avoid  $|\mu_A|=0$ , because then the statement of a mean value will be meaningless. The derivation of  $\sigma_{\varphi_2}^2 | \varphi_1$  is given in [Don79]; we omit the details here and just retain that the phase offset,  $\varphi_1$ , plays no role at all. Therefore we make use of  $\vartheta$  again and plot  $\sigma_{\vartheta}$  in Fig. 2.27.

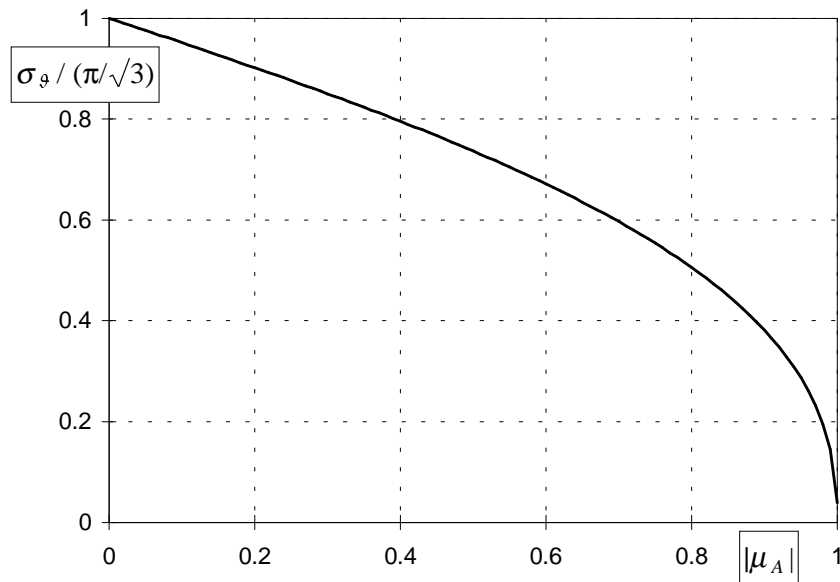


Fig. 2.27: Plot of  $\sigma_{\vartheta}$  vs.  $|\mu_A|$ .

For  $|\mu_A|=0$ , we obtain the "free" standard deviation of  $\pi/\sqrt{3}$ , corresponding to a uniform distribution of  $\varphi_2$ ; for  $|\mu_A|=1$ , the infinite sum in (2.55) is  $\pi^2/6$  [Bro87], and therefore the standard deviation becomes zero as expected. It is remarkable how quickly  $\varphi_2$  shakes off the influence of  $\varphi_1$ : for  $|\mu_A|=0.8$ , we have already  $\sigma_{\varphi_2} | \varphi_1 \cong \pi/(2\sqrt{3})$ . This is the reason why phase-measurement errors due to speckle decorrelation, i.e. the decrease of  $|\mu_A|$  due to lateral displacement or tilt of the object, increase rapidly initially [Hun95, Leh97b], while the fringes vanish only gradually as  $|\mu_A| \rightarrow 0$ . Many examples for this quasi-asymptotic course can be found in Chapter 5. Although  $|\mu_A|$  refers to one and the same stationary speckle field in our treatment thus far, (2.55) turns out to be a very universal description of phase errors due to fading speckle correlation [Cre85a, Vry86, Own91a, Hun95, Leh97b]; in fact, once  $|\mu_A|$  can be derived from the interferometer geometry, (2.55) applies likewise to image-plane decorrelation (lateral object displacement) and aperture-plane decorrelation (object tilt); moreover, it is almost independent of the ratio

of speckle size to pixel size. Hence, Fig. 2.27 gives the expected standard deviation of the error in many ESPI phase measurements, where  $\varphi_1(x,y)$  is the initial and  $\varphi_2(x,y)$  the final speckle phase distribution.

### 2.3.3.3 Interaction of intensities and phases

As already pointed out in [Don79], (2.49) is not separable into a product of marginal pdf's, which means that all of the involved quantities are mutually dependent. Hence we have dropped some information by eliminating intensities or phases from (2.49). Also, in 2.2 we have found that high speckle intensities are associated with low phase gradients, and vice versa. Therefore, we will now consider the interaction of intensities and phases more generally. This has been done in [Don79] as well; I list the results for completeness here and also give a simple qualitative interpretation for  $\vartheta \cong \pi$  that I think has not been mentioned before.

Since we are again interested in phase differences between two points instead of absolute phases, our relative phase variable  $\vartheta$  will be useful again. Then, we can investigate two general cases: (i), what influence do  $I_1$  and  $\vartheta$  have on  $I_2$ , and (ii) what does  $\vartheta$  do when we constrain  $I_1$  and  $I_2$ ? The pdf of  $I_2$  conditioned on the other quantities is [Don79]

$$p(I_2|I_1, \varphi_1, \varphi_2) = \frac{p(I_1, I_2, \varphi_1, \varphi_2)}{p(I_1, \varphi_1, \varphi_2)} = \frac{1}{\langle I \rangle (1 - |\mu_A|^2)} \exp \left( - \frac{I_2 - 2|\mu_A| \cos \vartheta \sqrt{I_1 I_2}}{\langle I \rangle (1 - |\mu_A|^2)} \right) D(\delta), \quad (2.56)$$

where we have abbreviated

$$\delta = |\mu_A| \cos \vartheta \sqrt{\frac{I_1}{\langle I \rangle (1 - |\mu_A|^2)}} \quad (2.57)$$

$$D(\delta) = \left( 1 + \sqrt{\pi} \delta \exp(\delta^2) (1 + \operatorname{erf} \delta) \right)^{-1}.$$

In contrast to the calculations in [Don79], we use  $|\mu_A|$  everywhere; since  $\vartheta$  appears as an argument of a cosine only, we can constrain  $0 \leq \vartheta \leq \pi$  and still explore  $-1 \leq |\mu_A| \cos \vartheta \leq 1$ ; thus, we need not deal with the ambiguity of  $\mu_A \cdot \cos \vartheta$  as was done in [Don79]. Unfortunately, it is still confusing to go through the many possible ways of plotting (2.56) with various fixed and running variables, so that we will resort to simpler functions. Indeed, it turns out that the statistical quantities

$$\begin{aligned} \langle I_2 \rangle | I_1, \vartheta &= \frac{\langle I \rangle}{2} (1 - |\mu_A|^2) (3 - D(\delta) + 2\delta^2) \\ \sigma_{I_2} | I_1, \vartheta &= \frac{\langle I \rangle}{2} (1 - |\mu_A|^2) \sqrt{6 - (1 - 2\delta^2) D(\delta) - D^2(\delta) + 8\delta^2} \end{aligned} \quad (2.58)$$

will provide sufficient insight. There are still three parameters to vary, namely  $|\mu_A|$ ,  $\vartheta$ , and  $I_1$ ; unlike [Don79], we do not use the composite parameter  $I_1 \cdot \cos^2 \vartheta / \langle I \rangle$ , but only  $I_1$ , which will allow us a direct interpretation and to see the effect of  $\vartheta$  more clearly. We normalise  $\langle I \rangle$  to unity and investigate

$I_1 \in \{0.3, 1, 3\}$ ; the corresponding plots are shown in Fig. 2.28. The limit  $|\mu_A|=1$  is difficult to treat, but of course it implies  $I_2 \equiv I_1$ ,  $\sigma_{I_2}|I_1, \vartheta \equiv 0$  and  $\vartheta \equiv 0$ . Therefore the maximum value of  $|\mu_A|$  in the plots is 0.995. These graphs show all combinations of  $|\mu_A|$  and  $\vartheta$ , although some are almost impossible in the underlying pdf (2.56).

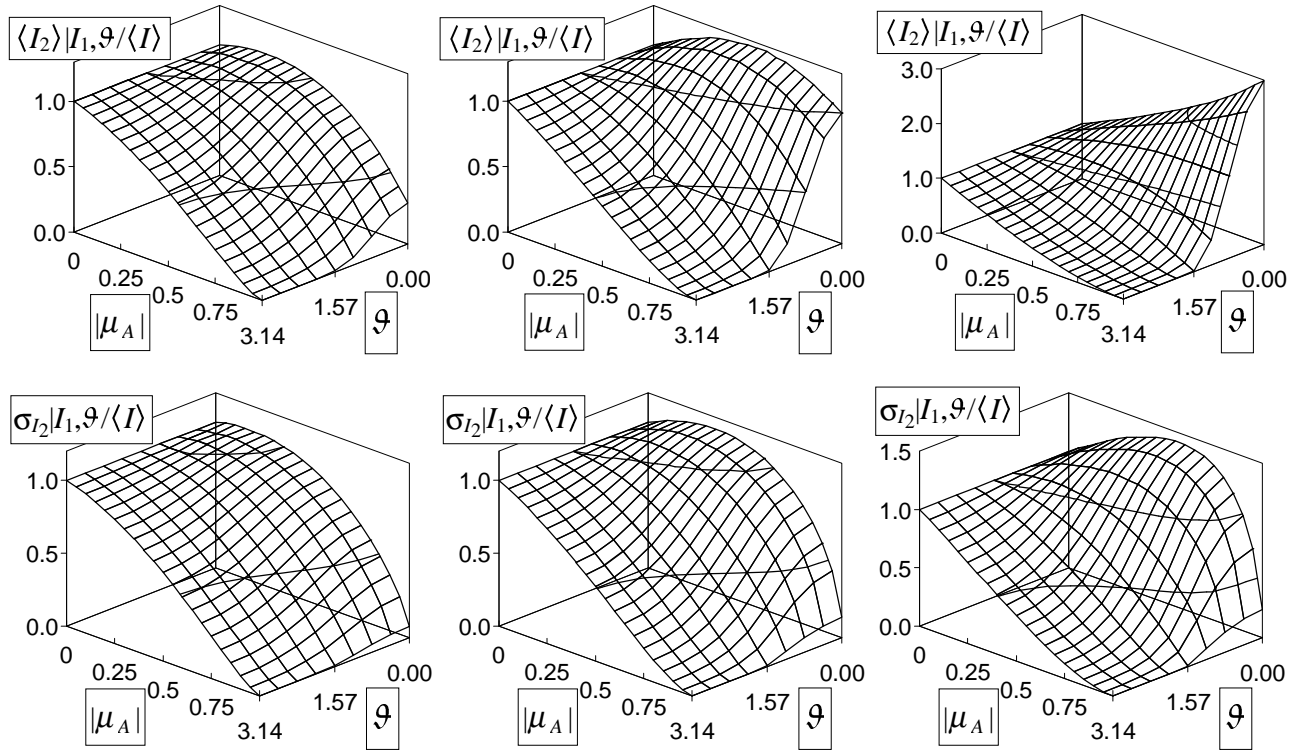


Fig. 2.28: Pseudo-3D plots of  $\langle I_2 \rangle |I_1, \vartheta$  (upper row) and  $\sigma_{I_2} |I_1, \vartheta$  (lower row) for  $I_1=0.3 \langle I \rangle$  (left),  $I_1=\langle I \rangle$  (centre),  $I_1=3.0 \langle I \rangle$  (right).

All the functions show a pronounced dependence on  $\vartheta$  that gets stronger as  $I_1$  increases; the curves for  $\vartheta=0$  correspond approximately to those in Fig. 2.25, while for  $\vartheta \geq \pi/2$ , both  $\langle I_2 \rangle |I_1, \vartheta$  and  $\sigma_{I_2} |I_1, \vartheta$  approach zero monotonically as we increase  $|\mu_A|$ . It is easy to see that the monotonic decrease sets in at  $\vartheta = \pm\pi/2$ , where  $\delta=0$  and

$$\langle I_2 \rangle |I_1, \vartheta = \sigma_{I_2} |I_1, \vartheta = \langle I \rangle (1 - |\mu_A|^2); \quad (2.59)$$

hence, for a phase difference of  $\geq \pi/2$  between  $(x_1, y_1)$  and  $(x_2, y_2)$ ,  $I_2$  is not only likely to be smaller than  $I_1$ , but will probably even be smaller than  $\langle I \rangle$ . This agrees with what we have found before: given a large phase difference between two points, we are the more certain to find a very low intensity at one of them the closer they are together. In particular, for  $\vartheta \cong \pi$  and  $|\mu_A| \cong 1$ , we are near a phase singularity, which interpretation is also helpful in understanding the asymmetry in the corresponding plots in [Don79]. Then of course a high value of  $I_1$  is very rare, but not completely impossible.

The second case we will consider is [Don79]

$$p(\varphi_2|I_1, I_2, \varphi_1) = \frac{p(I_1, I_2, \varphi_1, \varphi_2)}{p(I_1, I_2, \varphi_1)} = \frac{1}{4\pi^2} \frac{\exp(z \cos \vartheta)}{I_0(z)} \quad (2.60)$$

$$\text{with } z = \frac{2|\mu_A| \sqrt{I_1 I_2}}{\langle I \rangle (1 - |\mu_A|^2)};$$

as already shown in (2.53) and (2.54), one could eliminate  $\varphi_1$  simply by multiplying  $p(\varphi_2|I_1, I_2, \varphi_1)$  with  $2\pi$ , yielding  $p(\vartheta|I_1, I_2)$ . Like in 2.3.3.2, the symmetry in  $\vartheta$  gives immediately

$$\begin{aligned} \langle \varphi_2 \rangle | I_1, I_2, \varphi_1 = \varphi_1 & \quad \beta > 0 \\ & = \varphi_1 + \pi \quad \beta < 0 \end{aligned} \quad (2.61)$$

Therefore the variance again depends on  $|\mu_A|$  only, and we get [Don79]

$$\sigma_{\vartheta}^2 | I_1, I_2 = \frac{\pi^2}{3} + \frac{4}{I_0(z)} \cdot \sum_{n=1}^{\infty} \frac{(-1)^n}{n^2} I_n(z), \quad (2.62)$$

where  $I_n(\bullet)$  are the modified Bessel functions of first kind and  $n^{\text{th}}$  order. It is now instructive to compare this function with (2.55) for various speckle intensities. Since the intensities appear together in  $z$ , we can set  $\langle I \rangle = I_1 = 1$  and vary only  $I_2$ ; Fig. 2.29 covers the range of  $0.1 < \sqrt{I_1 I_2} < 10$ . As before, we plot the standard deviation rather than the variance.

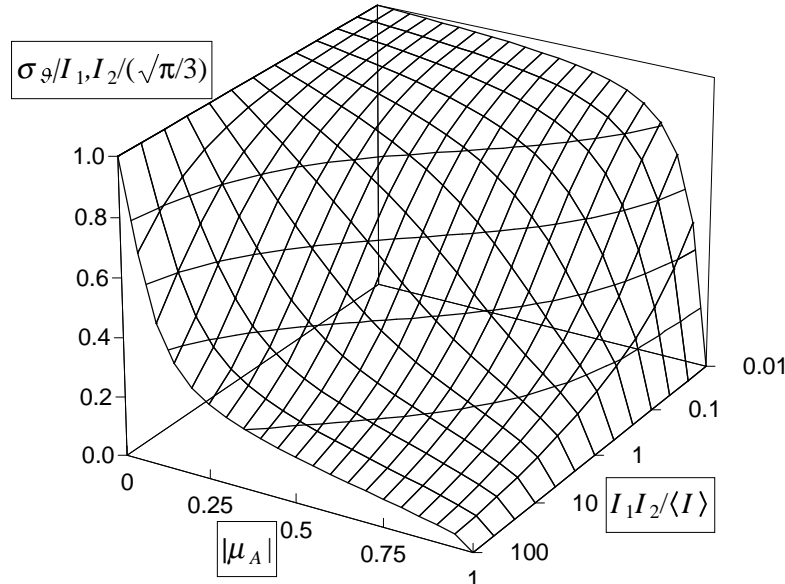


Fig. 2.29: Pseudo-3D plot of  $\sigma_{\vartheta}|I_1, I_2$  for a large range of speckle intensity ratios  $I_2/I_1$ .

For large values of  $I_1 I_2$ ,  $\sigma_{\vartheta}|I_1, I_2$  decreases rapidly as soon as  $|\mu_A| > 0$ , which means that in the very bright speckles, the phase indeed shows good constancy. At  $I_1 I_2 = \langle I \rangle$ , the standard deviation is still everywhere below the "free" (i.e. unconditioned) value of Fig. 2.27. As  $I_1 I_2$  decreases,  $\sigma_{\vartheta}|I_1, I_2$  grows and eventually

exceeds  $\sigma_{\phi}$  everywhere. Hence, most of the unconditioned standard deviation is due to those  $\cong 63\%$  ( $1-1/e$ ) of the speckle field that are darker than  $\langle I \rangle$ . As above, the application of (2.62) to interferometry with partially decorrelated speckle fields is possible [Leh97b], which immediately shows that phase measurements from bright speckles are more reliable than from darker regions of the field. Because of the low speckle intensity, the interferometric signal will be weak and susceptible to electronic noise, to which also a "decorrelation" parameter can be assigned [Hun97]. The remaining interference amplitude will be further diminished by integration of the rapid spatial phase fluctuations over the pixel area. Finally, the averaged phases will also strongly fluctuate from pixel to pixel, which makes the phase measurement by SPS more difficult. The best way to evade such problems would really be to retrieve all phase measurements from bright speckles; one step in that direction will be shown in Chapter 6.6.



### 3 Electronic or Digital Speckle Pattern Interferometry

The speckled wave scattered off an object bears a random intensity and phase structure that, in itself, will not reveal information about the object's macroscopic shape or deformation. By superposition with a reference wave, it becomes phase sensitive and the intensity modulation of each speckle is deterministic. It obeys the relationship

$$I(x, y) = O(x, y) + R(x, y) + 2\sqrt{O(x, y)R(x, y)} \cos(\varphi_O(x, y) - \varphi_R(x, y)) \quad (3.1)$$

where  $I$  denotes the interferogram intensity,  $O$  that of the object wave and  $R$  that of the reference wave, and  $\varphi_O$  and  $\varphi_R$  the respective phases;  $x$  and  $y$  are the co-ordinates of the image plane. While both  $O$  and  $\varphi_O$  fluctuate strongly with  $x$  and  $y$ , the spatial variations of  $R$  and  $\varphi_R$  are generally negligible. For the sake of readability, we will henceforth omit the spatial dependence of all variables. If two speckle interferograms are recorded, we have

$$\begin{aligned} I_i &= O_i + R_i + 2\sqrt{O_i R_i} \cos(\varphi_{O,i} - \varphi_{R,i}) \\ I_f &= O_f + R_f + 2\sqrt{O_f R_f} \cos(\varphi_{O,f} - \varphi_{R,f}) \end{aligned} \quad (3.2)$$

with subscript  $i$  for the initial and  $f$  for the final object state. On assuming that the intensities do not change during the experiment – which is easy to assure for  $R$  but requires the absence of speckle decorrelation for  $O$  –, we can reasonably rewrite this as

$$\begin{aligned} I_i &= O + R + 2\sqrt{OR} \cos(\varphi_O) \\ I_f &= O + R + 2\sqrt{OR} \cos(\varphi_O + \Delta\varphi) \end{aligned} \quad (3.3)$$

where we have set  $\varphi_{R,i}=0$  without loss of generality, and omitted the "initial" subscript for the speckle phase. The deterministic phase change  $\Delta\varphi$  is caused by object displacements, but includes possible global fluctuations of  $\varphi_{R,f}$  as well. From (3.3), the difference to classical interferometry is clear: for diffusely reflecting objects, no reference surface is available, and we need to compare it with itself. This can be done either by holography [Har94], where we have true interference of two object wavefronts, or by acquisition and subtraction of digitised interferogram intensity data [Løk87, Dov00]. The latter is commonly called digital or electronic speckle pattern interferometry (DSPI or ESPI), and the digital difference images are sometimes referred to as secondary interferograms, which is to distinguish them from direct, or primary, interferometric images.

Compared to holographic interferometry, the resolution of the pixel array-based digital method is poor, but with appropriate magnification of the object surface, still sufficient for many purposes. Among the advantages of an electronic system are versatility and very quick carrying out of experiments. Fig. 3.1 sketches the basic parts of an ESPI set-up.

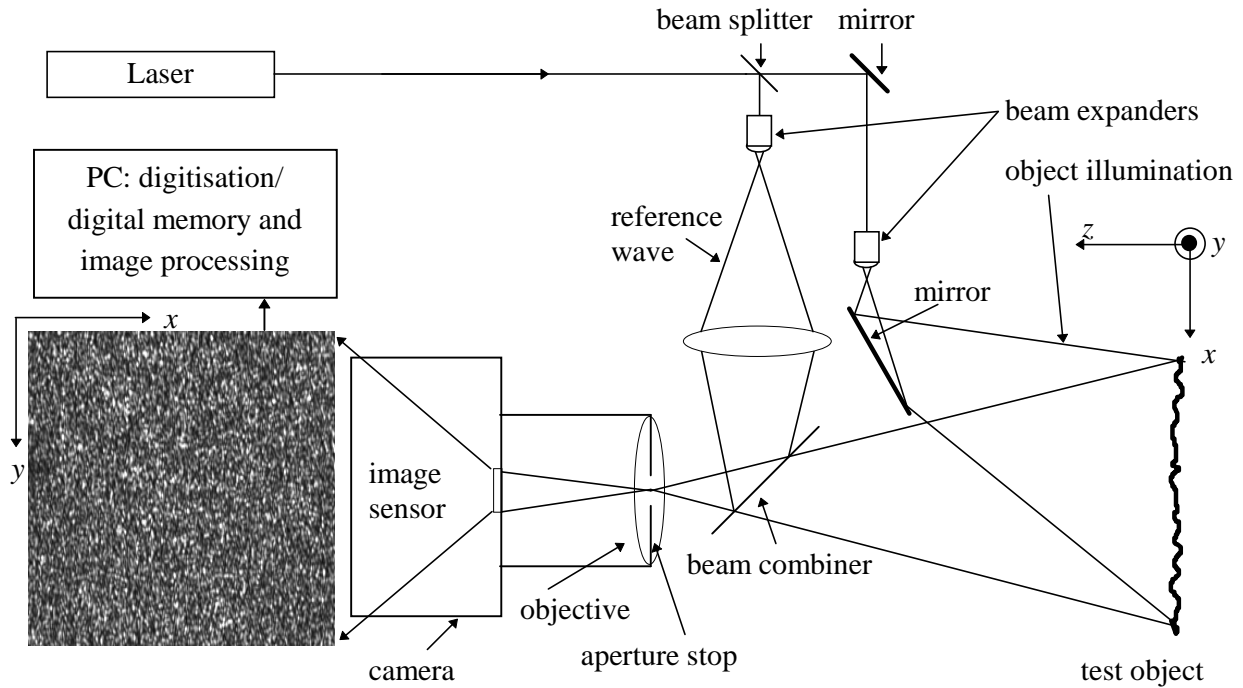


Fig. 3.1: Standard ESPI set-up.

The object is illuminated by a coherent wavefront, typically an expanded laser beam; its surface is imaged with an objective onto an electronic image converter (CCD or, more recently, also CMOS chip) where a subjective speckle pattern is observed. The reference wave is re-combined with the scattered object light by a beam splitter; it should be focused in the aperture plane so that its radius of curvature matches that of the object wave, the origin of which may be thought to lie in the centre of the aperture. Otherwise concentric interference fringes will be generated that decrease the contrast of the interference signal. The interferograms are digitised, most conveniently, but not necessarily, with one-byte resolution, and stored in the memory of the connected computer for whatever image processing is desired.

The aperture size is usually chosen to match the speckle size to the camera's pixel dimensions [Joh89], based on the *ad hoc* consideration that this ensures best spatial resolution and best fringe visibility. It has been shown however that resolving the speckles is not strictly necessary [Wyk87, Yos95, Maa97] and that even a speckle size of 1/8 pixel is sufficient to obtain a usable signal, which greatly improves light efficiency [Leh98]. On the other hand, adjusting too large a speckle size results in reduced spatial resolution, faster speckle decorrelation and waste of light efficiency because of the small aperture.

By appropriate choice of illumination direction(s) and wavefront form(s), the assembly can be made sensitive for displacements normal or parallel to the object's surface, or mixtures thereof. The former is called out-of-plane set-up, the latter is referred to as in-plane geometry. Examples and sketches of the different types can be found in Chapter 5.

The applicability of ESPI is mainly limited by speckle decorrelation, caused by large object displacements or changes in the object's microstructure, which can lead to severe signal degradation. The sensitivity of the ESPI system to these effects depends on, e.g., the speckle size and the dimensions of the image field. Also, for the secondary displacement fringes to be well resolved, their width should exceed

some 4 speckle sizes. This value was given in [Tan68] for holography; in ESPI however, the detector's pixel size plays a role as well.

### 3.1 Subtraction-mode ESPI

On subtraction of the interferograms obtained from the initial and final object state, we have

$$\begin{aligned} I_f - I_i &= 2\sqrt{OR}(\cos(\varphi_o + \Delta\varphi) - \cos(\varphi_o)) \\ &= -4\sqrt{OR}\left(\sin\left(\varphi_o + \frac{\Delta\varphi}{2}\right)\sin\left(\frac{\Delta\varphi}{2}\right)\right), \end{aligned} \quad (3.4)$$

with the second sine term representing the signal fringe profile and the first sine term the multiplicative speckle noise on it. Thus, one obtains a – secondary – fringe profile from the subtraction of two – primary – speckle interferograms. To give these fringes the familiar appearance of interferometric fringes on, e.g., a monitor, the negative values in the difference image have to be converted into positive ones. In DSPI, it is easy and customary to use the modulus of the difference,

$$|I_f - I_i| = 4\sqrt{OR}\left|\sin\left(\varphi_o + \frac{\Delta\varphi}{2}\right)\sin\left(\frac{\Delta\varphi}{2}\right)\right|; \quad (3.5)$$

averaging over  $\varphi_o$  gives a mean fringe intensity of

$$\begin{aligned} \langle |I_f - I_i| \rangle &= 4\sqrt{OR}\left\langle \left|\sin\left(\varphi_o + \frac{\Delta\varphi}{2}\right)\right| \right\rangle \left|\sin\left(\frac{\Delta\varphi}{2}\right)\right| \\ &= \frac{8\sqrt{OR}}{\pi} \left|\sin\left(\frac{\Delta\varphi}{2}\right)\right| \\ &= \frac{4\sqrt{2}\sqrt{OR}}{\pi} \sqrt{1 - \cos(\Delta\varphi)} \end{aligned} \quad (3.6)$$

in the so-called correlation fringes (note that the fringe envelope is *not* cosinusoidal and only serves to visualise the object changes). If an initial speckle interferogram is stored and the difference between it and the current one is viewed, one gets darkness where the optical phase is the same in both the images (i.e. the optical path has changed by an integer multiple of the wavelength) and brightness where the difference is maximum (i.e. the path has changed by an odd multiple of half the wavelength). Thus the digital secondary interferograms are formed.

Another way to generate the output is to square the fringe signal, in which case the fringe profile is given by

$$(I_f - I_i)^2 = 16OR \sin^2\left(\varphi_o + \frac{\Delta\varphi}{2}\right) \sin^2\left(\frac{\Delta\varphi}{2}\right) \quad (3.7)$$

and, after averaging over all  $\varphi_o$ ,

$$\begin{aligned}
\left\langle \left( I_f - I_i \right)^2 \right\rangle &= 16OR \left\langle \sin^2 \left( \varphi_O + \frac{\Delta\varphi}{2} \right) \right\rangle \sin^2 \left( \frac{\Delta\varphi}{2} \right) \\
&= 8OR \sin^2 \left( \frac{\Delta\varphi}{2} \right) \\
&= 4OR(1 - \cos(\Delta\varphi)).
\end{aligned} \tag{3.8}$$

This method yields a cosine profile and should be more suitable to generate correlation fringe images as an input for phase-shifting methods; but in the face of the drawbacks of the correlation fringe method discussed below, the performance gain will be negligible.

The dark regions of the images are noise-free, while the quality of the bright fringes is degraded by speckle noise: the visibility of the primary interferometric intensity modulation depends on the individual speckle brightness and hence fluctuates from point to point. Moreover, there are points where, due to unfavourable  $\varphi_O$ , the subsequent phase change does not effect a brightness change:

$$\cos(\varphi_O) = \cos(\varphi_O + \Delta\varphi) \Leftrightarrow \varphi_O = -\frac{\Delta\varphi}{2}, \tag{3.9}$$

which just means that  $\varphi_O$  and  $\varphi_O + \Delta\varphi$  are symmetrical about a – primary, cf. (3.3) – intensity extremum; and there are many more points coming close to this condition. While (3.9) is true for every interferometric measurement, it is – besides the fluctuations of  $O(x,y)$  – the randomness of the  $\varphi_O$  that prevents a spatially uniform detection of  $\Delta\varphi$ . It is worth noting that in the averages over  $\varphi_O$  in (3.6) and (3.8), this loss of signal leads to the factors  $2/\pi$  and  $1/2$ , respectively.

If, however, another pair of interferograms were available with phase offsets of, say,  $\pi/2$  each, we would have

$$\begin{aligned}
I_{f\pi/2} - I_{i\pi/2} &= 2\sqrt{OR} \left( \cos \left( \varphi_O + \Delta\varphi + \frac{\pi}{2} \right) - \cos \left( \varphi_O + \frac{\pi}{2} \right) \right) \\
&= 2\sqrt{OR} (\sin(\varphi_O) - \sin(\varphi_O + \Delta\varphi)) \\
&= -4\sqrt{OR} \left( \cos \left( \varphi_O + \frac{\Delta\varphi}{2} \right) \sin \left( \frac{\Delta\varphi}{2} \right) \right)
\end{aligned} \tag{3.10}$$

and could average the two secondary interferograms to obtain brighter correlation fringes:

$$\begin{aligned}
\frac{|I_f - I_i| + |I_{f\pi/2} - I_{i\pi/2}|}{2} &= 4\sqrt{OR} \left| \sin \left( \frac{\Delta\varphi}{2} \right) \left( \sin \left( \varphi_O + \frac{\Delta\varphi}{2} \right) + \cos \left( \varphi_O + \frac{\Delta\varphi}{2} \right) \right) \right| \\
&= 4\sqrt{OR} \left| \sqrt{2} \sin \left( \varphi_O + \frac{\Delta\varphi}{2} + \frac{\pi}{4} \right) \sin \left( \frac{\Delta\varphi}{2} \right) \right|.
\end{aligned} \tag{3.11}$$

The improvement of using (3.11) over (3.5) is demonstrated in Fig. 3.2, where on the left-hand side an image according to (3.5) is shown, and on the right, a superposition according to (3.11); the increase in brightness should be  $\sqrt{2}$  and is in fact 1.38. In simple words, the disadvantageous points of one image are

filled up by well-modulated data from its  $\pm\pi/2$ -complement. But of course, controlled phase shifts are not automatically available in an ESPI system.

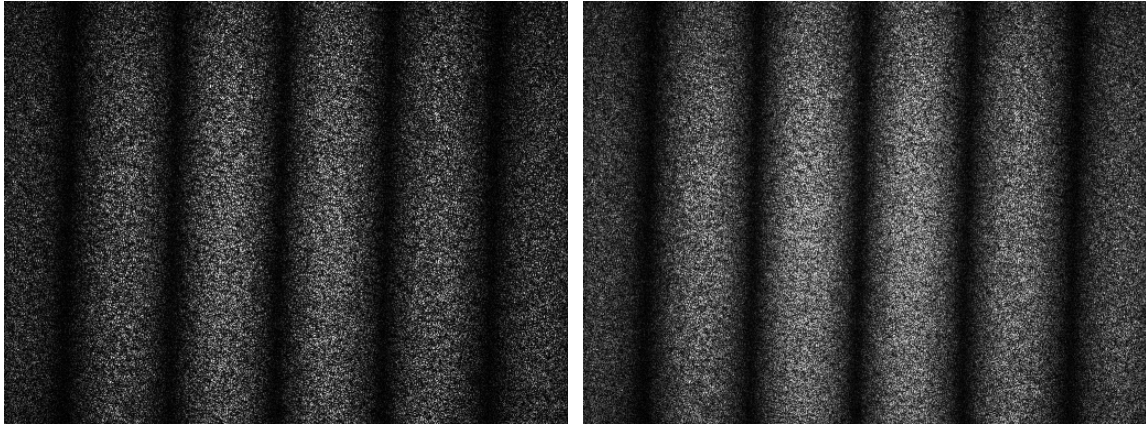


Fig. 3.2: Left: ESPI correlation fringes from subtraction of two primary speckle interferograms; right: average of two correlation fringe images with phase offsets of  $\pi/2$  in the underlying primary interferograms  $I_i$ ,  $I_{i\pi/2}$  and  $I_f$ ,  $I_{f\pi/2}$  (see text).

Although the optimisation of speckle size and fringe contrast has been the subject of numerous studies [Tan68, Sle79, Wyk87], the overly – in the sense of (3.9) – speckled appearance of the correlation fringes still limits the accuracy of ESPI measurements to about 1/10 fringe. Moreover, the fringe profile is an even function of  $\Delta\phi$ , which makes it impossible to determine the sign of the measured displacement gradient. To get rid of this ambiguity, *a-priori* information has to be used: either a pre-set bias fringe pattern with known phase gradient reveals the relative fringe orders when it changes, or the load is applied in such a way that only one direction of deformation gradient is possible [Wya82, Mat88].

A far more elegant method to retrieve quantitative displacement data is to convert the cosine into a tangent by means of several phase samples and then to extract the phase mod  $2\pi$  by a four-quadrant arctangent. This approach has become very popular under the name of phase sampling – although it relies on intensity sampling –, or phase shifting. It eliminates completely the difficulties described by (3.9), which is an important reason for its superior performance.

### 3.2 Phase-shifting ESPI

The technique of phase sampling or quasi-heterodyning has long been known in information theory and has first been used in classical interferometry to enhance accuracy [Car66, Bru74, Wya75]. After the application of phase shifting to holographic interferometry [Har82, Cha85], it was the merit of [Nak85, Cre85b, Ste85, Rob86] to have realised that also a digital speckle interferogram is an array of independent "micro-interferometers" that work like classical ones – although some of them suffer from too faint an object wave.

Hence, the phase information of a speckled wave front, although random *per se*, nevertheless responds deterministically to phase changes due to displacement or deformation of the test object, and digital subtraction of two speckle phase fields yields a difference phase field. The use of phase shifting has

greatly extended the possibilities of ESPI and enhanced the attainable accuracy of phase measurements by a factor of about 10. Whereas quantitative evaluation of correlation fringes requires sophisticated automation algorithms (see Chapter 4.1) or laborious interactive procedures, the phase shifting method automatically yields complete phase maps, so that today the correlation fringe methods have mostly been superseded by phase-shifting ESPI.

To introduce temporal phase sampling, or stepping, we establish the expression

$$I_n(x, y, t_n) = I_b(x, y) + M_I(x, y) \cdot \cos(\varphi_O(x, y, t_n) + \alpha_n(x, y, t_n)) \quad (3.12)$$

with

$n$ : number of phase sample

$I_n$ : measured intensity in the  $n^{\text{th}}$  frame

$I_b$ : bias intensity; corresponds to  $O+R$

$M_I$ : intensity modulation; corresponds to  $2 \cdot \sqrt{OR}$

$\varphi_O$ : speckle phase

$\alpha_n$ : additional (known) shift of  $\varphi_R$ ; generally,  $\alpha_n = n \cdot \alpha$  and  $n \in \{0, \dots, N-1\}$ .

For now, we restrict ourselves to static phase shifts, since a distinction between temporal and spatial phase ramping must be made that will be described in 3.3 and 3.4.4, respectively. Also,  $\varphi_R$  has been set to zero as above. All quantities depend on  $x$  and  $y$  due to the underlying speckle field. The phase shift  $\alpha_n(x, y, t_n)$  may be, but in practice seldom is, spatially uniform; various numbers  $N$  of phase samples can be used. Assuming  $O(x, y)$  and  $R(x, y)$  to remain temporally quasi-stable, we still have to account for possible temporal fluctuations of  $\varphi_O$  and  $\varphi_R$ . For convenience we put them all into  $\varphi_O$ .

The set of equations given by (3.12) can easily be linearised; the principle is outlined in Appendix C. It contains three unknowns, namely  $I_b$ ,  $M_I$ , and  $\varphi_O$ , and hence we need at least three linearly independent measurements of the  $I_n$  ( $N \geq 3$ ), with pairwise different  $\alpha_n$ , to solve unambiguously for  $\varphi_O$ . This can be done by generating an expression that gives  $\tan(\varphi_O) = \sin(\varphi_O) / \cos(\varphi_O)$ ; i.e. one needs a numerator proportional to the sine and a denominator proportional to the cosine of  $\varphi_O$ . To achieve this, the  $I_n$  are put together as

$$\varphi_O \bmod \pi = \arctan \frac{\sum_{n=0}^{N-1} a_n I_n}{\sum_{n=0}^{N-1} b_n I_n} \quad \text{with} \quad \sum_n a_n = \sum_n b_n = 0, \quad (3.13)$$

which is valid for any phase-sampling scheme. In all of such formulae, the coefficients in numerator and denominator add up to zero, which cancels the contribution from  $I_b$ . The simplest expression to evaluate the recorded data relies on equally spaced  $\alpha_n$  that are uniformly distributed in the interval  $[0, 2\pi)$ ; it is well

known since decades [Bru74] and has recently been referred to as DFT (digital Fourier transform) formula [Sur96]:

$$\varphi_O \bmod 2\pi = \arctan \frac{-\sum_{n=0}^{N-1} I_n \sin \alpha_n}{\sum_{n=0}^{N-1} I_n \cos \alpha_n} \quad \text{with } \alpha_n = n \cdot \frac{2\pi}{N}. \quad (3.14)$$

With this choice of the  $a_n$  and  $b_n$ , numerator/denominator represent the digital implementation of a Fourier sine/cosine transform [Bra87, p.17], where  $\alpha(x,y,t)$  has an angular frequency of  $2\pi/(N \text{ samples})$  and the sample interval is in time or space units; the Fourier aspect of phase sampling will be treated in greater detail in 3.2.2. The signs of numerator and denominator are used to generate a  $0-2\pi$  arctan, in contrast to its mathematical definition used in Chapter 2, where it ranges from  $-\pi/2$  to  $\pi/2$ . This is more convenient when converting the phases to grey levels.

For 3-step formulae, one can also choose  $n \in \{-1, 0, 1\}$ , thus assume phase shifts of  $\{-\alpha, 0, \alpha\}$  and write down the generally valid expression [Cre88, Schwi90, Gre92]

$$\varphi_O \bmod 2\pi = \arctan \left( \frac{1 - \cos \alpha}{\sin \alpha} \frac{I_{-1} - I_1}{2I_0 - I_{-1} - I_1} \right) = \arctan \left( \tan \left( \frac{\alpha}{2} \right) \frac{I_{-1} - I_1}{2I_0 - I_{-1} - I_1} \right). \quad (3.15)$$

Much work has been done to improve these simple approaches to very sophisticated sampling schemes, frequently at the expense of increased  $N$ . These are often called algorithms, although their flow diagrams are trivial; to distinguish them from another class of phase-retrieval methods that are truly algorithms [Ger72, Fie82, Rav99], I will avoid the term "algorithm" henceforth. Today, there are not only tailored formulae with excellent rejection of various errors [Schwi83, Har87, Lar92b, Sur93, Schwi93, dGro95, Hib95, Mlo95, Schmi95a, dGro97, Hib97, Kuch97, Ser97b, Sto97, Zha99], but also, the properties of phase-shifting formulae are by now so well understood [Fre90a, Lar92a, Rat95, Sur96, Phi97, Sur97b, Sur98c, Dor99] that for many purposes phase-extraction schemes can be tailored to adapt to the particular task. Good measurements reach an accuracy of about  $\lambda/100$  [Schwi83, Har87].

But the basic approaches with  $N=3$  to 5 have survived in ESPI because superb theoretical accuracy would remain theoretical where speckle noise and decorrelation set the limits. Also, since ESPI is obviously not concerned with precision surfaces, the requirements are often lower.

Moreover, a small  $N$  helps to determine phases very quickly: since the most time-consuming step in phase calculation is the arctangent operation, it is advantageous to map all possible values of numerator and denominator in two-dimensional look-up tables (LUTs).

The size of these LUTs depends on the digital resolution as well as on the respective number of samples involved. In the case of (3.15) with 8-bit digitisation, the LUT would have  $511 \times 1021$  entries, because the numerator can range from  $-255$  to  $255$  and the denominator from  $-510$  to  $510$ . These integers then serve as matrix indices to retrieve the associated phase value, which is often represented by an 8-bit integer as

well. This has been successfully applied in practice (cf. Chapter 6.7) and simplifies the account of [Nak95], where a 3-D phase LUT was used. But in general, the LUT approach works only if all the coefficients  $a_n$ ,  $b_n$  can be integrated in the LUT; hence the requirement is that the coefficients, or at least their ratios, be expressible by integers; an example is given in Appendix B.

For all these practical reasons, we will restrict ourselves to standard three- or four-sample formulae in this work. From (3.14), we get the widespread four-step formula for  $\alpha=90^\circ$ ,

$$\varphi_O \bmod 2\pi = \arctan \frac{I_3 - I_1}{I_0 - I_2} \quad (3.16)$$

and the three-step formula for  $\alpha=120^\circ$ ,

$$\varphi_O \bmod 2\pi = \arctan \sqrt{3} \frac{I_2 - I_1}{2I_0 - I_1 - I_2}, \quad (3.17)$$

where a factor of  $\frac{1}{2}$  has been cancelled from the fraction. Note that this formula follows likewise from (3.15) because, for  $\alpha=120^\circ$ ,  $I_{-1} \cong I_2$ . If however  $\alpha=90^\circ$ , (3.15) delivers the three-step (non-DFT) formula

$$\varphi_O \bmod 2\pi = \arctan \frac{I_{-1} - I_1}{2I_0 - I_{-1} - I_1}. \quad (3.18)$$

To simplify (3.18), it is usual to accept a phase offset – which is hardly relevant in classical, and less so in speckle interferometry – and choose a representation in which the coefficients are equal for all intensity samples:

$$(\varphi_O - 45^\circ) \bmod 2\pi = \arctan \frac{I_2 - I_1}{I_0 - I_1} \quad (3.19)$$

As mentioned above, the phases obtained from such calculations can be mapped onto a grey scale of, say, 256 steps. When  $\varphi_O$  crosses a  $2\pi$  boundary, it jumps back to zero, and so do the associated grey levels; this is why the images thus generated are known as sawtooth images. Since speckle interferometry is about comparing phases, we will dedicate the following subsection to finding out the best way to do so.

### 3.2.1 Calculation of phase changes in ESPI

There are several ways to come from interferograms to  $\Delta\varphi(x,y)$ , the displacement phase map which is represented in a sawtooth image; and since the accuracy in measuring  $\Delta\varphi(x,y)$  is the pivotal issue in this work, it is certainly worthwhile to investigate the different strategies in detail.

In what follows, we will refer to the first two approaches by the handy terms "phase of difference" and "difference of phase"; this nomenclature follows [Moo94], one of the relatively few papers on ESPI concerned with quantitative performance issues. For the third method, I propose the term "complex division". All of the methods have been introduced together with phase-shifting ESPI [Nak85, Cre85b, Ste85]. First of all, the treatment concerns temporal phase shifting, i.e. we shift the phase in time,



$\alpha_n = \alpha(t_n)$ , to obtain a temporal sequence of phase-shifted interferograms  $I_n(x, y, t_n)$ ; but once we have clarified the different methods, the transfer to spatial phase shifting is very simple.

### 3.2.1.1 Phase-of-differences method

The first approach to think of when processing secondary interferograms is to determine their phases as familiar from primary interferometric fringes. Given a set of images  $I_{n,i}$  of the initial object state, one then needs only one frame  $I_{0,f}$  of the final state, so four or five images are sufficient to use the phase-shifting methods of (3.16) or (3.17), respectively. As only one frame of the final object state is involved, we shall call the  $I_{n,i}$  plus  $I_{0,f}$  a "reduced" data set. The phase-shifted secondary correlation fringes  $I_{n,c}$  are formed according to

$$\begin{aligned}
 I_{n,c} &= (I_f - I_{n,i})^2 \\
 &= 4OR \left( \cos(\varphi_O + \Delta\varphi) - \cos(\varphi_O + \alpha_n) \right)^2 \\
 &= 16OR \sin^2 \left( \varphi_O + \frac{\Delta\varphi + \alpha_n}{2} \right) \sin^2 \left( \frac{\Delta\varphi - \alpha_n}{2} \right) \\
 &= 4OR (1 - \cos(2\varphi_O + \Delta\varphi + \alpha_n)) (1 - \cos(\Delta\varphi - \alpha_n)),
 \end{aligned} \tag{3.20}$$

where the first cosine describes the speckle noise in the correlation fringes and the second cosine is the envelope, phase shifted by  $\alpha_n$ . This approach offers one significant advantage: if the object under test can initially be observed at rest, the capturing of one interferogram suffices later on to obtain phase-shifted correlation fringes.

There is another important consequence of (3.20) that has, as far as I know, not been emphasised before: the first cosine depends on  $2\varphi_O$ . This is of course owing to the squaring operation – and would not look very different if we were dealing with the modulus –, but it means that we cannot distinguish between positive and negative speckle intensity changes anymore. Thus, half the information delivered by the intensity changes is discarded, with important consequences for the measured  $\Delta\varphi$ . The situation is represented in Fig. 3.3: the black curves show the result of using squared correlation fringes as in (3.20) for the standard four-sample phase calculation of (3.16).

To the left, a simulation result is shown: for each pre-set  $\Delta\varphi$ , 64 different  $\varphi_O$ , uniformly distributed over  $[0, 2\pi)$ , were inserted into (3.20) to form the corresponding sets of  $I_{n,c}$ , where  $\alpha = 90^\circ$ . These 64 sets of  $I_{n,c}$  were inserted as the  $I_n$  in (3.16) to yield 64 values for  $\Delta\varphi$ , whose average appears as calculated  $\Delta\varphi$ . The average over all  $\varphi_O$  thus gives the expectation value of the calculated vs. the true displacement phase. On the right, the measured  $\Delta\varphi \cong \Delta\varphi(x)$ , i.e. for vertical sawtooth fringes (cf. Fig. 3.4), averaged over 200 rows and represented as grey values, confirms that indeed the extraction of  $\Delta\varphi$  is almost impossible after the squaring or rectification process. The white curves refer to the difference-of-phases method and will be discussed below in 3.2.1.2.

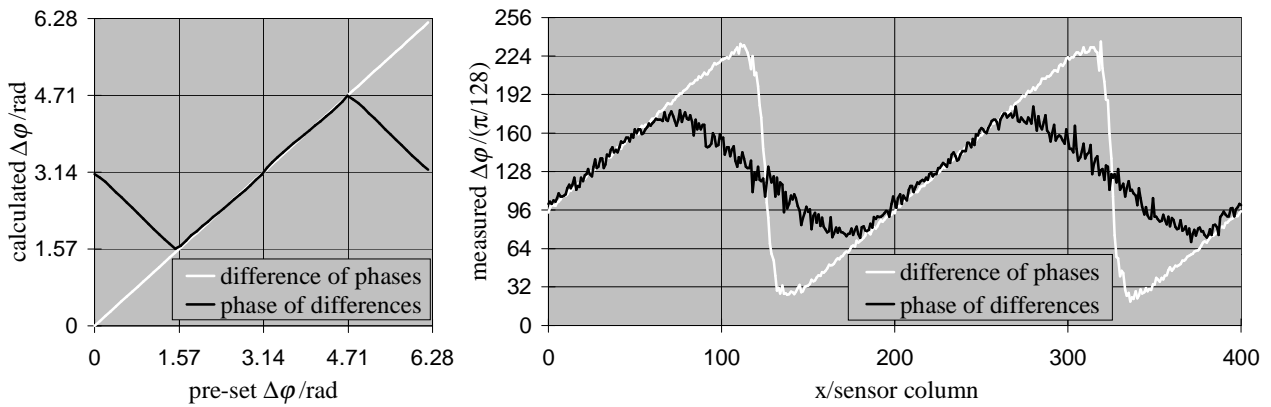


Fig. 3.3: Left: calculated  $\Delta\phi$ , averaged over  $\varphi_0$ , vs. pre-set  $\Delta\phi$ , for the methods to be compared in this subsection. Right: measured profiles of vertical sawtooth fringes, averaged over 200 rows.

Evidently, the phase-shifting method is not directly applicable to speckle correlation fringes. It will only work acceptably if the individual speckle phases are suppressed, i.e. the secondary interferograms must be smoothed to approximate the cosinusoidal envelope of (3.20) as closely as possible. This is usually done by a low-pass filter and reduces the spatial resolution.

The left-hand part of Fig. 3.4 shows the fringe profile plotted in Fig. 3.3 on the right: surprisingly, the image does yield direction information, although the averaged fringes do not. The reason is that for  $\pi/4 < \Delta\phi < 3\pi/4$ , the average is actually made up of intermediate grey values; for the other  $\Delta\phi$ , black and white occur more frequently. The standard deviation of the difference between the calculated  $\Delta\phi$  and the best fit of a noise-free sawtooth image (cf. Chapter 4),  $\sigma_{\Delta\phi}$ , is  $62.1^\circ$ , and the pdf of the calculated  $\Delta\phi$  shows four pronounced maxima, as depicted in the grey-level histogram. All the histograms in this subsection have been generated from 5.0 fringes, so that the measured phases ought to be uniformly distributed. On the right side of Fig. 3.4, the sawtooth image was calculated from correlation fringes previously smoothed by a  $9 \times 9$  averaging filter, which reduces  $\sigma_{\Delta\phi}$  to  $7.7^\circ$ . Although this is quite large a filter, the speckle structure has not disappeared; and since the spectral power density of a speckle pattern keeps increasing toward the spatial frequency of zero, it is not possible at all to remove the speckle noise in the correlation fringes by low-pass filtering. Therefore, the measured phases are still not uniformly distributed: this effect cannot be suppressed either.

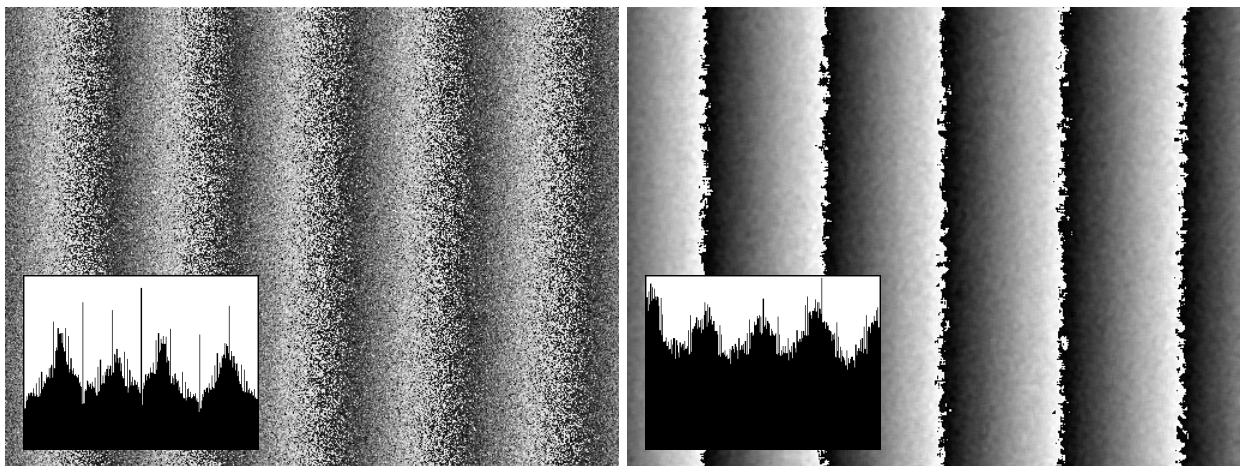


Fig. 3.4: Results of calculating  $\Delta\phi$  from raw (left) and  $9 \times 9$  low-pass filtered correlation fringes (right). Inserted histograms show relative pixel counts of grey levels from 0 to 255.

But remembering that we have initially been enforcing positive intensity values only to display them conveniently on a screen, one might argue that there is no real need to do so. Therefore we have to settle the question whether a kind of "signed" correlation fringes exists that circumvents the problems associated with squaring or rectification. If we form fringes according to

$$I_{n,s} = I_f - I_{n,i} = 2\sqrt{OR}(\cos(\varphi_O + \Delta\varphi) - \cos(\varphi_O + \alpha_n)), \quad (3.21)$$

with the subscript  $s$  for "signed", all of the information is being preserved. Unfortunately, when we insert these  $I_{n,s}$  into a phase-shifting formula like (3.13), we cannot measure  $\Delta\varphi$ : because of  $\sum a_n = \sum b_n = 0$ , the contributions from the first cosine are cancelled, and what we then measure by phase shifting is just the speckle phase. This has been verified experimentally and demonstrates that really some information is lacking from our reduced set of images  $I_{n,i}$  and  $I_{0,f}$ .

Nonetheless, some specialised methods exist that can determine both  $\Delta\varphi$  and  $\varphi_O$ , correct for  $\varphi_O$  and thus generate acceptable sawtooth images from unfiltered correlation fringes. In [Kuj89] a so-called "speckle phase correlation method" is derived for  $\alpha=120^\circ$  that indeed uses  $I_{\{0,1,2\},i}$  and  $I_{0,f}^*$  without filtering. The same is done in [Moo94] for  $\alpha=90^\circ$  and  $I_{\{0,1,2,3\},i}$  and  $I_{0,f}$ . However, none of these methods can find the correct speckle phase without help: the equations involve an arccosine and a square root and have four solutions, which again reflects the loss of information brought about by the rectification. This problem is solved by initially generating a smoothed phase map  $\Delta\varphi_{filt}$  in the usual way (Fig. 3.4, right side), which serves as a reference: that solution for  $\varphi_O$  which brings  $\Delta\varphi - \varphi_O$  closest to  $\Delta\varphi_{filt}$  is selected as the correct speckle phase and subtracted. In this way, the phase measurement from raw correlation fringes can be significantly improved, as shown in Fig. 3.5.

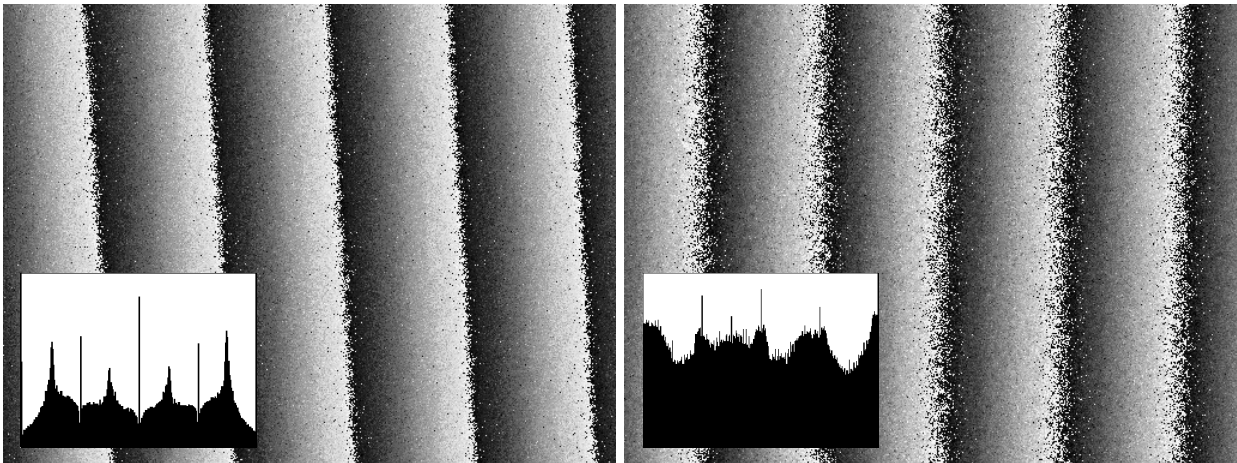


Fig. 3.5: Results of calculating  $\Delta\varphi$  with the method of [Kuj89] (left) and [Moo94] (right); the underlying sets of interferograms come from two different experiments with  $\alpha=120^\circ$  and  $90^\circ$ , respectively.

---

\*With a misprint in one of the expressions, which should read  $c = \frac{I_1 + I_2 + I_3}{3} - I_4$  in the nomenclature used.

The left image in Fig. 3.5 was calculated according to [Kuj89] from a data set with  $\alpha=120^\circ$ , which reduced  $\sigma_{\Delta\varphi} = 62.6^\circ$  as obtained from raw correlation fringes (image not shown) to  $\sigma_{\Delta\varphi} = 24.0^\circ$ . To the right, the method of [Moo94] was applied to the previous data set with  $\alpha=90^\circ$  that led to the results in Fig. 3.4, and  $\sigma_{\Delta\varphi}$  dropped to  $27.2^\circ$ . In both cases, the accuracy is more than doubled and most of the initial spatial resolution is maintained. The price for this is increased computational effort: a reference phase map must be generated first, whose lower resolution may influence the choices for  $\varphi_0$  somewhat, and one out of four phase values must be selected for every pixel. Since generally no ideal reference image will be available, the errors in it will also influence the choice of  $\varphi_0$  and propagate into  $\Delta\varphi$ . Finally, the histogram distortion can in neither case be removed.

Another method that uses  $I_{\{0,1\},i}$  and  $I_{\{0,1\},f}$  with  $\alpha=90^\circ$  has been proposed in [Own88]; while it is obviously not suitable for highly dynamic phenomena, it does find  $\Delta\varphi$  unambiguously. The result of this calculation can be seen in Fig. 3.6. Both the phase map ( $\sigma_{\Delta\varphi} = 53.2^\circ$ ) and the histogram of the phase distribution show that this method is rather susceptible to noise; therefore it has been used in [Own88, Own91b] with smoothing the sine and cosine terms before calculating  $\Delta\varphi$ . The argument of calculation speed that led to the development of this method is not important anymore; but interestingly, the very same scheme has meanwhile been applied in temporal phase unwrapping, again for reasons of, *inter alia*, speed [vBru98, vBru99].

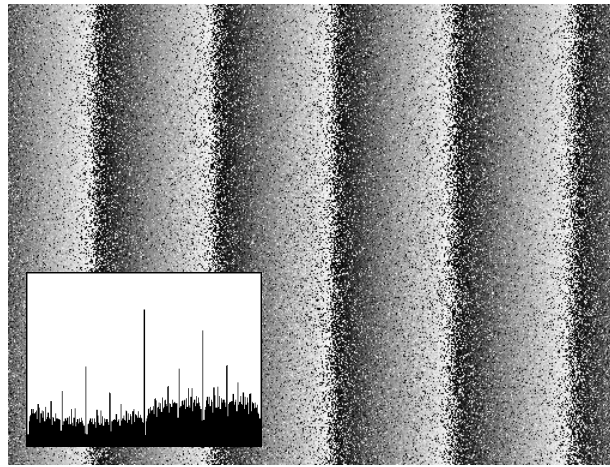


Fig. 3.6: Result of calculating  $\Delta\varphi$  with the method of [Own88].

As these considerations have shown, the use of ESPI correlation fringes for phase-shifting purposes is problematic when we are considering raw, i.e. unfiltered, phase data. This is because one uses only one set of phase-shifted data to determine  $\Delta\varphi$ . Nevertheless, this approach may sometimes be a good way to perform phase measurements when dynamic objects are studied.

### 3.2.1.2 Difference-of-phases method

Provided it is possible to record two sets of phase-shifted interferograms  $I_{n,i}$  and  $I_{n,f}$  for both object states, one can calculate two speckle phase maps by, e.g., (3.16):

$$\begin{aligned}\varphi_{O,i}(x,y) \bmod 2\pi &= \arctan \frac{I_{3i}(x,y) - I_{1i}(x,y)}{I_{0i}(x,y) - I_{2i}(x,y)} \\ \varphi_{O,f}(x,y) \bmod 2\pi &= \arctan \frac{I_{3f}(x,y) - I_{1f}(x,y)}{I_{0f}(x,y) - I_{2f}(x,y)},\end{aligned}\quad (3.22)$$

and then determine the phase change

$$\Delta\varphi(x,y) \bmod 2\pi = \left( \varphi_{O,f}(x,y) \bmod 2\pi - \varphi_{O,i}(x,y) \bmod 2\pi \right) \bmod 2\pi. \quad (3.23)$$

Admittedly, this requires more information than the phase-of-difference approach – 8 images with (3.16), and 6 with (3.17) –, but eliminates all the problems brought about by the ambiguity of intensity differences. Also, the pixels are truly regarded as independent entities, which accounts appropriately for the speckle nature of the wavefront to determine. In this case, the phase calculation reproduces the expected fringe profile rather well, as the white curves in Fig. 3.3 demonstrate. The displayed sawtooth edges are somewhat blurred by the averaging over the residual speckle noise; but the corresponding measured phase map, shown in Fig. 3.7, is of excellent quality when we compare it with the other unfiltered results obtained so far. In that case,  $\sigma_{\Delta\varphi} = 18.2^\circ$  without any low-pass filtering. Also, the pdf of measured phases is now uniform, which shows that computational biases are negligible for this method.

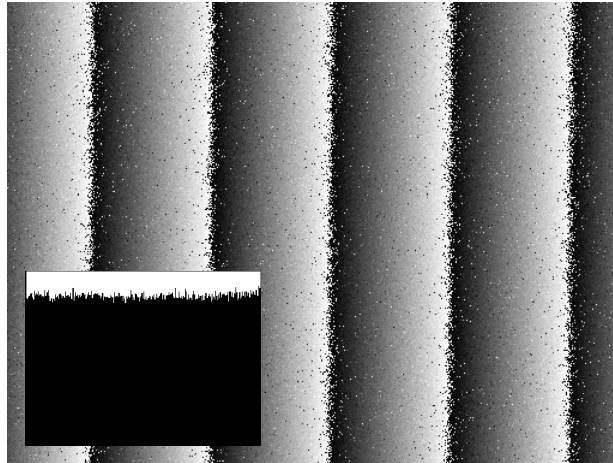


Fig. 3.7: Result of calculating  $\Delta\varphi$  with the difference-of-phases method.

This confrontation clearly indicates that it is necessary to genuinely measure the speckle phases twice to get the best sawtooth image. While an approximate recovery of information from reduced data sets is possible, the performance of this approach remains restricted. Therefore, the performance data given in chapters 5 and 6 are based on sawtooth images from the difference-of-phases method without exception. A practical merit of keeping ready the speckle phase distributions for every recorded object state is that one need not compare all data to the initial state anymore. In other words, it becomes possible to track phase differences incrementally even if the first and last state show decorrelated speckle patterns [Flo93]. We will come back to this issue in Chapter 6.7.

### 3.2.1.3 Complex-division method

Both of the methods discussed thus far have in common that they require one phase calculation and one subtraction, and differ in the order of these operations. There are however also methods to calculate  $\varphi_O$  in only one computation step. They require two complete phase-shifted data sets and combine the steps of phase calculation and difference formation in one formula. Examples of such calculations have been given before [Ste85, Ste90, Fac93, Hun93a, Sal96]; however the somewhat laborious derivation of the formulae can be generalised and greatly simplified when treated by the formalism of complex division [Bur98b]. As mentioned above, the numerator in phase-shifting formulae should correspond to the sine and the denominator to the cosine of the phase angle to be found, so that we can switch to complex notation and write:

$$\begin{aligned}\varphi_{O,i} \bmod 2\pi &= \arctan \frac{\sin \varphi_{O,i}}{\cos \varphi_{O,i}} = \arg(\cos \varphi_{O,i} + i \sin \varphi_{O,i}) := \arg(z_i) \\ \varphi_{O,f} \bmod 2\pi &= \arctan \frac{\sin \varphi_{O,f}}{\cos \varphi_{O,f}} = \arg(\cos \varphi_{O,f} + i \sin \varphi_{O,f}) := \arg(z_f)\end{aligned}\quad (3.24)$$

Now  $\Delta\varphi$  can be determined according to

$$\Delta\varphi \bmod 2\pi = \varphi_{O,f} - \varphi_{O,i} = \arg(z_f) - \arg(z_i) = \arg\left(\frac{z_f}{z_i}\right) \bmod 2\pi, \quad (3.25)$$

where

$$\frac{z_f}{z_i} = \frac{\sin \varphi_{O,i} \sin \varphi_{O,f} + \cos \varphi_{O,i} \cos \varphi_{O,f}}{\cos^2 \varphi_{O,i} + \sin^2 \varphi_{O,i}} + i \frac{\sin \varphi_{O,f} \cos \varphi_{O,i} - \sin \varphi_{O,i} \cos \varphi_{O,f}}{\cos^2 \varphi_{O,i} + \sin^2 \varphi_{O,i}}. \quad (3.26)$$

Eventually we combine these expressions to get

$$\Delta\varphi \bmod 2\pi = \arg\left(\frac{z_f}{z_i}\right) = \arctan \frac{\sin \varphi_{O,f} \cos \varphi_{O,i} - \sin \varphi_{O,i} \cos \varphi_{O,f}}{\cos \varphi_{O,i} \cos \varphi_{O,f} + \sin \varphi_{O,i} \sin \varphi_{O,f}} \bmod 2\pi, \quad (3.27)$$

which provides a generally valid instruction on how to compose the expressions of phase-shifting formulae; of course, the same result follows from the trigonometric relationship for the difference of arctangents [Cre94]. Now we can instantly establish one-step calculations; for instance, from (3.16),

$$\Delta\varphi \bmod 2\pi = \arctan \frac{(I_{3f} - I_{1f})(I_{0i} - I_{2i}) - (I_{3i} - I_{1i})(I_{0f} - I_{2f})}{(I_{0i} - I_{2i})(I_{0f} - I_{2f}) + (I_{3i} - I_{1i})(I_{3f} - I_{1f})}, \quad (3.28)$$

and (3.17) changes to

$$\Delta\varphi \bmod 2\pi = \arctan \sqrt{3} \frac{(I_{2f} - I_{1f})(2I_{0i} - I_{1i} - I_{2i}) - (I_{2i} - I_{1i})(2I_{0f} - I_{1f} - I_{2f})}{(2I_{0i} - I_{1i} - I_{2i})(2I_{0f} - I_{1f} - I_{2f}) + 3(I_{2i} - I_{1i})(I_{2f} - I_{1f})}. \quad (3.29)$$

These formulae help to save processing time, since (i) no intermediate images are formed, and (ii) only one arctangent calculation per pixel is required. But due to the involved multiplications, this method can be accelerated by LUTs only if enormous storage space or substantial data reduction in the LUT are acceptable.

As the complex-division method is mathematically equivalent to the difference-of-phases approach, the performance in terms of  $\sigma_{\Delta\phi}$  is exactly the same for both of them. It has however been demonstrated in [Vik93] that phase differences can be determined from six intensity samples even with an unknown phase shift.

### 3.2.2 Spectral transfer properties of few-sample phase shifting formulae

In our context of spatial phase shifting, the number of phase samples must be as small as possible, e.g. three or four; at the same time, the phase extraction method should possess the best possible tolerance of speckle intensity and phase gradients. The latter cause deviations of the phase shift from its nominal value. A valuable tool to investigate the behaviour of phase-sampling formulae under linear phase-shift miscalibrations (also called "detuning") is the so-called "Fourier description" of phase-shifting formulae. It was begun in [Ohy86, Ohy88], developed to its full potential in [Fre90a] and is nowadays a common tool to assess the performance of phase-sampling formulae [Lar92a, Hib95, Mlo95, Schmi95a, Hib97, Zha99, Mal00]. We will restrict the discussion to linear miscalibration sensitivity here, for which the Fourier description is particularly suitable. Moreover, it will provide a means to quantify how the signal sidebands in the frequency spectra of SPS interferograms (cf. Fig. 3.29) will be used and/or altered by the phase calculation.

To understand the behaviour of some few-sample methods in the frequency domain, we will briefly review the underlying principles. Some emphasis is put on the spatial version of phase extraction; but the phase-shift parameter  $x$ , denoting one spatial co-ordinate, can be replaced by  $t$  as well. As (3.14) indicates, the general task in phase determination is to generate signals that are proportional to sine and cosine of the phase of an unknown signal, say,  $I(x)$ , and then extract its phase  $\phi$  by an arctangent operation. We start with the continuous (analogue) description of the process, which will help to clarify the properties of the discrete (digital) version. An extensive overview of the formalism, and also of the spectral characteristics of many phase-shifting formulae besides the ones that we will examine here, can be found in [Mal98, pp. 113-245].

#### 3.2.2.1 Analogue synchronous detection

When  $I(x)$  is modulated with a so-called carrier frequency  $\nu_x$ , we can write

$$I(x) = I_b(x) + M_I(x) \cdot \cos(\phi(x) + 2\pi\nu_x x) \quad (3.30)$$

and use the well-known method of "synchronous detection" to extract the phase  $\phi(x)$  in (3.30). An early application of this method to spatial fringe analysis has been given in [Ich72]; moreover, it is the principle upon which lock-in amplifiers are based. The first step of synchronous detection is to multiply the input

signal  $I(x)$  with suitable "filter functions" of the frequency  $\nu_{0x}$ , where generally  $\nu_{0x} \cong \nu_x$  is assumed. It is however essential to note that we will later be concerned with the effects of  $\nu_x \neq \nu_{0x}$ . To measure the phase, we define the filter functions as

$$\begin{aligned} S(x) &= -\sin 2\pi\nu_{0x}x \\ C(x) &= \cos 2\pi\nu_{0x}x, \end{aligned} \quad (3.31)$$

and the multiplications yield the signals

$$\begin{aligned} &I(x)S(x) \\ &= -I_b(x) \sin 2\pi\nu_{0x}x + \frac{M_I(x)}{2} \left( \sin(\varphi(x) + 2\pi(\nu_x - \nu_{0x})x) - \sin(\varphi(x) + 2\pi(\nu_x + \nu_{0x})x) \right) \\ &I(x)C(x) \\ &= I_b(x) \cos 2\pi\nu_{0x}x + \frac{M_I(x)}{2} \left( \cos(\varphi(x) + 2\pi(\nu_x - \nu_{0x})x) + \cos(\varphi(x) + 2\pi(\nu_x + \nu_{0x})x) \right). \end{aligned} \quad (3.32)$$

Both of the equations contain contributions from the pure carrier frequency and from difference and sum frequencies. Since  $\nu_x \cong \nu_{0x}$ , the difference frequencies are low; in the ideal case,  $\nu_x - \nu_{0x} = 0$ , and the low-frequency contribution is determined by  $\varphi(x)$  alone. One can think of the fringes resulting from the multiplication as a moiré effect [Wom84, Ara97, Kat97]. The second step of synchronous detection is to remove, or "filter out", the high-frequency terms by integrating the product functions, which gives the so-called "filter outputs". This integration, or filtering, is achieved by the cross-correlation functions

$$\begin{aligned} S'(x') &= \int_{-\infty}^{\infty} I(x)S(x-x')dx \\ C'(x') &= \int_{-\infty}^{\infty} I(x)C(x-x')dx \end{aligned} \quad (3.33)$$

if we calculate them for  $x'=0$ . The "filter outputs" therefore are

$$\begin{aligned} S'(0) &= \int_{-\infty}^{\infty} I(x)S(x)dx \propto \sin \varphi(x) \\ C'(0) &= \int_{-\infty}^{\infty} I(x)C(x)dx \propto \cos \varphi(x). \end{aligned} \quad (3.34)$$

Using the central ordinate theorem [Bra87, p. 136] together with the convolution theorem [Bra87, p. 110], we can replace  $I(x)$ ,  $S(x)$  and  $C(x)$  by their Fourier transforms\* [Fre90a; Mal98, p.134] and rewrite (3.34) as

---

\*To apply the convolution theorem, we must use  $S(x'-x)$  and  $C(x'-x)$  in (3.33), which changes the correlation into a convolution. The sign change in (3.33) then simply leads to a complex conjugation in (3.35). This is possible since  $S(x)$  and  $C(x)$  are real functions, which means that their Fourier transforms are Hermitian. This is, their real parts are even and remain unaffected by the sign change, while their imaginary parts are odd and must be inverted after the integrations in (3.33), although their contributions vanish anyway.



$$\begin{aligned}
S'(0) &= \int_{-\infty}^{\infty} \tilde{I}(v_x) \tilde{S}^*(v_x) dv_x \\
C'(0) &= \int_{-\infty}^{\infty} \tilde{I}(v_x) \tilde{C}^*(v_x) dv_x ,
\end{aligned} \tag{3.35}$$

where tilde denotes the Fourier transforms and the sign convention [Bro87]

$$\tilde{f}(v_x) := \int_{-\infty}^{\infty} f(x) \exp(+2\pi i v_x x) dx \tag{3.36}$$

is adopted, i.e. the phase runs forward in the Fourier transform.

It is seen from (3.35) that the spectrum of  $I(x)$  is weighted, or filtered, by the spectra of  $S(x)$  and  $C(x)$ , which is why we have called them filter functions. We will therefore refer to  $\tilde{S}(v_x)$  and  $\tilde{C}(v_x)$  as filter spectra. Since  $I(x)$ ,  $S(x)$  and  $C(x)$  are real functions with Hermitian Fourier transforms, we can simplify the integrals (3.35) to [Fre90a]

$$\begin{aligned}
S'(0) &= 2 \operatorname{Re} \int_0^{\infty} \tilde{I}(v_x) \tilde{S}^*(v_x) dv_x \\
C'(0) &= 2 \operatorname{Re} \int_0^{\infty} \tilde{I}(v_x) \tilde{C}^*(v_x) dv_x .
\end{aligned} \tag{3.37}$$

This is, the filter outputs are indeed composed of all input spatial frequencies that may be present in  $I(x)$ , with weights determined by the moduli of the filter spectra,  $|\tilde{S}(v_x)|$  and  $|\tilde{C}(v_x)|$ ; we will refer to these latter also as filter responses. With our initial choice of  $S(x)$  and  $C(x)$ , we have

$$\begin{aligned}
S'(0) &= \int_{-\infty}^{\infty} I(x) \cdot -\sin 2\pi v_{0x} x dx \\
C'(0) &= \int_{-\infty}^{\infty} I(x) \cos 2\pi v_{0x} x dx ,
\end{aligned} \tag{3.38}$$

being proportional to the Fourier sine and cosine transforms [Bra87, p. 17] of  $I(x)$  at the frequency  $v_{0x}$ , and the spectral descriptions read:

$$\begin{aligned}
S'(0) &= 2 \operatorname{Re} \int_0^{\infty} \tilde{I}(v_x) i \delta(v_x - v_{0x}) dv_x \\
C'(0) &= 2 \operatorname{Re} \int_0^{\infty} \tilde{I}(v_x) \delta(v_x - v_{0x}) dv_x .
\end{aligned} \tag{3.39}$$

This models the ideal case that we can evaluate the signal over an infinite amount of space, which leads to unity filter responses at the nominal frequency  $v_{0x}$  and perfect suppression of all other  $v_x$ .

Finally the third step of synchronous detection is the extraction of  $\varphi(x)$ , using (3.34) and (3.39), by means of

$$\tan \varphi(x) = \frac{2 \operatorname{Re} \int_0^{\infty} \tilde{I}(v_x) i \delta(v_x - v_{0x}) dv_x}{2 \operatorname{Re} \int_0^{\infty} \tilde{I}(v_x) \delta(v_x - v_{0x}) dv_x} \propto \frac{\sin \varphi(x)}{\cos \varphi(x)}. \quad (3.40)$$

It was shown in [Fre90a] that a correct phase determination requires

$$\begin{aligned} |\tilde{S}^*(v_x)| &= |\tilde{C}^*(v_x)| & \Leftrightarrow & \quad |\tilde{S}(v_x)| = |\tilde{C}(v_x)| \\ \tilde{S}^*(v_x) &= i \tilde{C}^*(v_x) & & \quad \tilde{S}(v_x) = -i \tilde{C}(v_x), \end{aligned} \quad (3.41)$$

this is, the filter spectra must have equal magnitudes (also called "responses") and be  $90^\circ$  out of phase (also called "in quadrature"), so that  $S'(0)$  represents the sine and  $C'(0)$  the cosine of  $\varphi(x)$ . As a summary of the involved operations, the whole procedure has been given the name of "quadrature multiplicative moiré" [Wom84].

In (3.40), (3.41) need only hold for  $v_{0x}$ , since nothing is detected at other  $v_x$ ; but when we confine the integration to a finite interval  $(-X, X)$  instead of  $(-\infty, \infty)$ , the filter responses will broaden around  $v_{0x}$ . This need not be a disadvantage, because more signal energy – if present – may be utilised in this way; and as long as (3.41) remains valid,  $\varphi(x)$  can still be correctly determined also for  $v_x \neq v_{0x}$ . The objective of phase sampling is now to satisfy (3.41) with only a short sequence of digitised samples of  $I(x)$ .

### 3.2.2.2 Digital synchronous detection

Let us now assume that we are working on a discrete pixel grid, where the pixels are assumed to be point detectors with distance  $d_p$ . Let  $M$  be the number of pixels in  $x$  direction and  $k$  their individual numbers. Using the "filter property" of the  $\delta$  function, the filter outputs are now – with an appropriate choice of the origin of the co-ordinate system – given by

$$\begin{aligned} S'(0) &= \int_{-\infty}^{\infty} I(x) S(x) \sum_{k=1}^M \delta(x - kd_p) dx = \sum_{k=1}^M I(kd_p) S(kd_p) \\ C'(0) &= \int_{-\infty}^{\infty} I(x) C(x) \sum_{k=1}^M \delta(x - kd_p) dx = \sum_{k=1}^M I(kd_p) C(kd_p) \end{aligned} \quad (3.42)$$

i.e. the signal is being sampled by a sequence of  $\delta$  functions only. For convenience we retain the assumption of infinite spatial extent of the signal. To measure  $\varphi(x)$  at a given pixel  $k_0$  and thus introduce the spatial resolution of the phase measurement, the sampling pulse sequence must be "windowed" by selecting only a few intensity samples at  $(k_0+n)d_p$ , with  $n \in \{0, \dots, N-1\}$ , so that, in the simplest case of using a rectangle function as a window,

$$\begin{aligned}
S'_{k_0} &= \int_{-\infty}^{\infty} I(x)S(x) \cdot \left( \sum_{k=1}^M \text{rect}\left(\frac{x - k_0 d_p}{N d_p}\right) \delta(x - k d_p) \right) dx = \sum_{n=0}^{N-1} I\left((k_0 + n)d_p\right) S\left((k_0 + n)d_p\right) \\
C'_{k_0} &= \int_{-\infty}^{\infty} I(x)C(x) \cdot \left( \sum_{k=1}^M \text{rect}\left(\frac{x - k_0 d_p}{N d_p}\right) \delta(x - k d_p) \right) dx = \sum_{n=0}^{N-1} I\left((k_0 + n)d_p\right) C\left((k_0 + n)d_p\right)
\end{aligned} \tag{3.43}$$

where, following [Bra87, p. 52],  $\text{rect}(x)=1$  for  $0 \leq x < 1$ , and zero elsewhere.

Considering the spectra  $\tilde{S}(v_x)$  and  $\tilde{C}(v_x)$  of the expressions under the integrals in (3.43), we see that the sharp responses of (3.39) are still present but will undergo convolutions with the spectrum of the sampling window. This spectrum is continuous for any finite window, so that  $S'(x)$  and  $C'(x)$  acquire a significant sensitivity to signal frequencies  $v_x \neq v_{0x}$ . Recalling that  $S(x)$  and  $C(x)$  have been designed for, or "tuned" to,  $v_{0x}$ , we now have found the reason for the "de-tuning" sensitivity of short sequences of sampling pulses.

Due to the uncertainty relation between the spatial and the spectral domain, the spectral "response peak" of phase-shifting formulae will generally be the broader the smaller  $N$  gets, and vice versa. However, to obtain a narrower sampling-window spectrum, it is possible to replace the rectangle window by triangle or bell-shaped functions [dGro95, Schmi96, Sur98c]. An extreme example with  $N=101$  and a bell-shaped window function has been studied in [dGro97]; but its response peak is still broadened about the nominal signal frequency. Besides, it is certainly not applicable to spatial fringe analysis because of the mere number of samples involved; and as discussed below in 3.4.4, we would be ill-advised with too sharp a filter response for spatial phase shifting on speckle fields. With practical choices of  $N=3$  or  $4$ , the suppression of frequencies  $v_x \neq v_{0x}$  indeed is poor, and it is important to observe the validity of (3.41) over a larger range of  $v_x$ .

With  $S(x)$  and  $C(x)$  according to (3.31), and  $v_{0x}=1/N$ , we arrive at the truncated digital equivalent of (3.33),

$$\begin{aligned}
S'_{k_0} &= - \sum_{n=0}^{N-1} I\left((k_0 + n)d_p\right) \sin \frac{2\pi}{N} \cdot n := I(x_{k_0}) \otimes S(n) \propto \sin \varphi(x) \\
C'_{k_0} &= \sum_{n=0}^{N-1} I\left((k_0 + n)d_p\right) \cos \frac{2\pi}{N} \cdot n := I(x_{k_0}) \otimes C(n) \propto \cos \varphi(x) \\
\text{and} \quad \varphi(x) \bmod 2\pi &= \arctan \frac{I(x_{k_0}) \otimes S(n)}{I(x_{k_0}) \otimes C(n)}
\end{aligned} \tag{3.44}$$

where  $\otimes$  denotes the correlation. Note here that (3.44) is just (3.14) rewritten for spatial phase sampling. We call the  $S(n)$  and  $C(n)$  the sampling functions, bearing in mind that they are sequences of weighted  $\delta$  pulses. These sampling functions constitute a pair of digital filters; they act upon both amplitude and phase of the input signal  $I(x_k)$ , depending on  $v_x$ . As suggested in [Mer83, Vla94, Sur96], one can also regard the two processing "channels" (sine and cosine part) as one complex digital correlation:

$$\begin{aligned} Z(x_{k_0}) &= I(x_{k_0}) \otimes (C(n) + iS(n)) \\ \text{with } \varphi(x) \bmod 2\pi &= \arg(Z(x_{k_0})) \end{aligned} \quad (3.45)$$

where  $\arg(\bullet)$  is the polar angle of a complex number; this corresponds to a notation  $c_n = b_n + ia_n$  in (3.13) and is the starting point for the description of phase-shifting formulae by complex polynomials [Sur96].

To illustrate the significance of the facts compiled thus far, we rewrite (3.16) as

$$\varphi_o \bmod 2\pi = \arctan \frac{I\left(\frac{3P_{0x}}{4}\right) - I\left(\frac{P_{0x}}{4}\right)}{I(0) - I\left(\frac{P_{0x}}{2}\right)}, \quad (3.46)$$

where  $P_{0x} = 4 d_p$  is the period of the carrier fringes, and  $\alpha = 2\pi/P_{0x} = 90^\circ/d_p$ . (This denotes the phase shift per pixel, not the phase gradient in  $^\circ/\text{m}$ .) The filter functions are

$$\begin{aligned} S(x) &= \delta\left(x - \frac{3P_{0x}}{4}\right) - \delta\left(x - \frac{P_{0x}}{4}\right) \\ C(x) &= \delta(x) - \delta\left(x - \frac{P_{0x}}{2}\right) \end{aligned} \quad (3.47)$$

and the corresponding spectra read

$$\begin{aligned} \tilde{S}(v_x) &= \exp\left(2\pi i \frac{3}{4v_{0x}} v_x\right) - \exp\left(2\pi i \frac{1}{4v_{0x}} v_x\right) = 2 \sin\left(\frac{\pi}{2} \frac{v_x}{v_{0x}}\right) \exp\left(i\pi \left(\frac{1}{2} + \frac{v_x}{v_{0x}}\right)\right) \\ \tilde{C}(v_x) &= 1 - \exp\left(2\pi i \frac{1}{2v_{0x}} v_x\right) = 2 \sin\left(\frac{\pi}{2} \frac{v_x}{v_{0x}}\right) \exp\left(i\pi \left(-\frac{1}{2} + \frac{v_x}{2v_{0x}}\right)\right) \end{aligned} \quad (3.48)$$

with  $v_{0x} = 1/P_{0x}$ . In these expressions, the sine terms represent the amplitudes and the exponentials represent the phases of the filter spectra, so that the behaviour of  $\tilde{S}(v_x)$  and  $\tilde{C}(v_x)$  can be read off directly. Whenever we get a pure phase term, it is possible to plot the rest of the expressions as real amplitudes, which we will denote by  $\text{amp}(\bullet)$ . For more complicated formulae, it is not always possible to arrive at separable expressions; but once  $\tilde{S}(v_x)$  and  $\tilde{C}(v_x)$  are established, one can obtain at least their moduli and arguments separately.

This now gives us a means to explore the transfer characteristics of phase-shifting formulae by plotting their spectra. Extending the common practice of plotting only the amplitude spectra, we will consider the phase spectra as well. In all our spectra plots that follow, the frequencies will be normalised by  $v_{0x}$  and the range of frequencies will be from 0 to  $2v_N$ , where  $v_N$  is the Nyquist frequency  $1/(2 d_p)$ , corresponding to  $\alpha = 180^\circ/d_p$ . Consequently, when  $v_{0x} = 90^\circ/d_p$ ,  $2v_N = 4v_{0x}$ ; and for  $v_{0x} = 120^\circ/d_p$ ,  $2v_N = 3v_{0x}$ . The ordinates of the amplitude plots are dimensionless and scale with the  $a_n$  and  $b_n$  in the underlying sampling functions; the phases are shown in radians.

The spectral transfer properties of (3.48) are shown in Fig. 3.8: while the amplitudes of  $\tilde{S}(v_x)$  and  $\tilde{C}(v_x)$  are seen to be the same throughout the frequency spectrum, the phases are in quadrature only at  $v_x/v_{0x}=1$  and  $v_x/v_{0x}=3$ , which corresponds to  $\alpha=90^\circ$  and  $270^\circ/d_p$  (aliased as  $-90^\circ/d_p$ ), respectively. Also,  $S'(x)$  will represent  $\sin(\varphi_O)$  in the former and  $\sin(-\varphi_O)$  in the latter case: if we reverse the phase shift, the calculated phase must change its sign too. It can also be seen from the phase spectrum that (3.16) measures  $\varphi_O$  without offset: at  $v_{0x}$ ,  $\arg(\tilde{C}(v_x)) = 0^\circ$  and  $\arg(\tilde{S}(v_x)) = -90^\circ$ , as (3.41) requires.

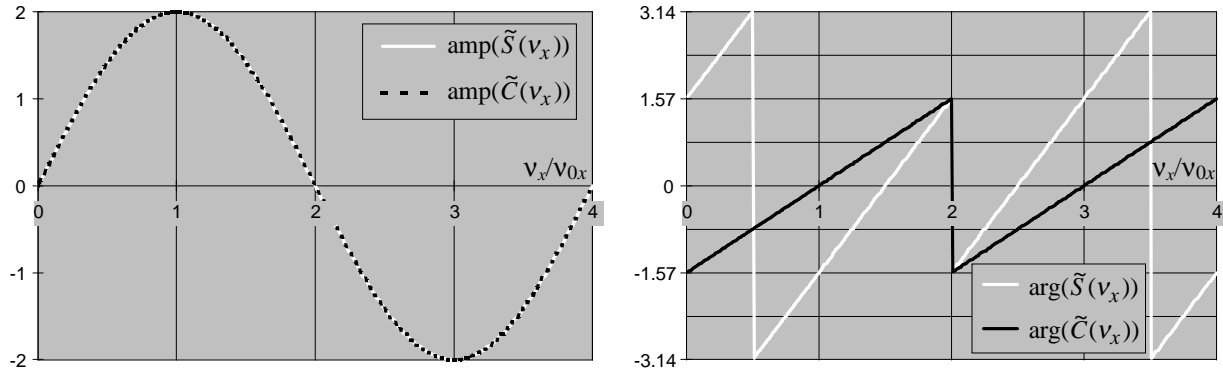


Fig. 3.8: Filter spectrum for 4-step- $90^\circ$  phase-sampling formula (3.16); left: amplitudes, right: phases.

The zero transitions of  $\text{amp}(\tilde{S}(v_x))$  and  $\text{amp}(\tilde{C}(v_x))$  at  $v_x = n \cdot v_N$ ,  $n \in \{0,1,2\}$ , cause the phases to jump by  $\pi$ ; this corresponds to the "singular" cases of  $\alpha=0^\circ, 180^\circ, 360^\circ/d_p$ , in which situations the differences of phase-shifted intensity samples record only  $I_b$ , with no intensity modulation, and a phase measurement is impossible. The filter outputs then must vanish because of the requirement that  $I_b$  be suppressed.

The spectral responses of simple sampling functions can sometimes be qualitatively understood without Fourier analysis. For instance, a difference of two samples will be maximal in the average over all  $\varphi_O$  when they are  $180^\circ$  out of phase. This behaviour is reflected in Fig. 3.8: since in (3.16) the nominal phase difference of the intensity samples in  $S(n)$  and  $C(n)$  is  $180^\circ$ , their responses peak at the nominal frequency  $v_{0x}$ . After this example, we now investigate the transfer properties of some phase-extraction methods that recommend themselves for SPS because of their small number of samples.

### 3.2.2.3 Three-sample formulae

When we consider (3.18), we obtain

$$\begin{aligned} \tilde{S}(v_x) &= 4 \sin\left(\frac{\pi v_x}{4 v_{0x}}\right) \cos\left(\frac{\pi v_x}{4 v_{0x}}\right) \exp\left(i\pi\left(-\frac{1}{2} + \frac{1}{2} \frac{v_x}{v_{0x}}\right)\right) \\ \tilde{C}(v_x) &= 4 \sin^2\left(\frac{\pi v_x}{4 v_{0x}}\right) \cdot \exp\left(i\pi\left(\frac{1}{2} \frac{v_x}{v_{0x}}\right)\right) ; \end{aligned} \quad (3.49)$$

this time the phase factor associated with  $v_{0x}$  is the same in both expressions, which means that the phases always remain in quadrature; but in turn, the amplitudes depend on  $v_{0x}$  as shown in Fig. 3.9. The samples for  $C(n)$  are now nominally  $90^\circ$  apart, but by the argument used above, the maximum average response

for that arrangement occurs when they are  $180^\circ$  apart, i.e. at  $v_x=2v_{0x}$ . Also, (3.18) measures  $\varphi_0+\pi/2$  instead of  $\varphi_0$  (cf. Fig. 3.8). Therefore, in [Fre90a] we find  $S(n)$  and  $C(n)$  swapped, and the new  $S(n)$  inverted, which cancels the offset. An example of how this works is given below in (3.53) and (3.54).

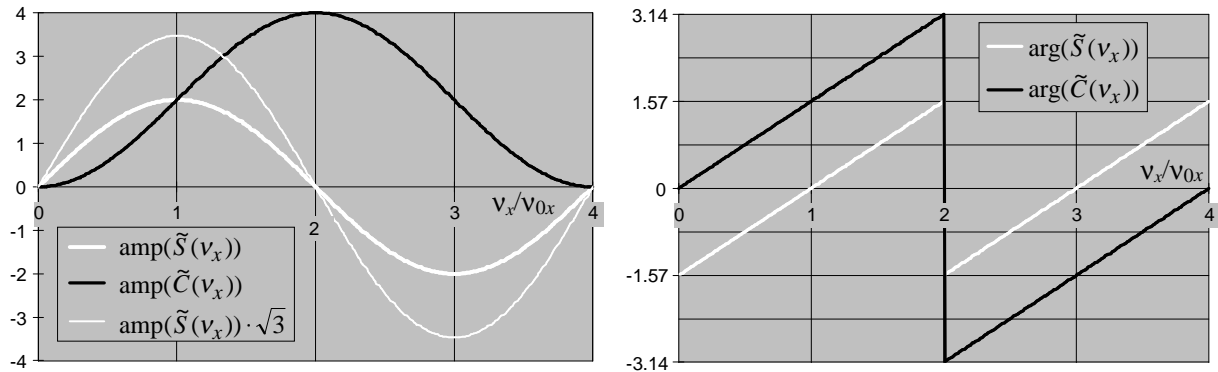


Fig. 3.9: Filter spectrum for 3-step- $90^\circ$  phase-sampling formula (3.18); left: amplitudes, right: phases.

As to be seen from Fig. 3.9, reliable operation of (3.18), i.e. validity of (3.41), is assured only within small deviations of  $v_x$  from  $v_{0x}$ : while  $d\tilde{S}(v_x)/dv_x|_{v_{0x}} = 0$ , a maximum of  $d\tilde{C}(v_x)/dv_x$  occurs at  $v_{0x}$ . A low influence of phase-shift errors would require both gradients to be equal or at least close to each other; then the phase reconstruction would tolerate some miscalibration. The graphs shown in Fig. 3.9 are also qualitatively valid for phase calculation with (3.17), and more generally with (3.15), since  $S(n)$  and  $C(n)$  are just scaled to shift up or down that  $v_x$  which fulfils  $\text{amp}(\tilde{S}(v_x)) = \text{amp}(\tilde{C}(v_x))$ . This is indicated by the curve labelled " $\text{amp}(\tilde{S}(v_x)) \cdot \sqrt{3}$ ", which would suffice to change (3.18) to (3.17). The phase spectra are indeed the same in either case.

With 3 phase steps of  $90^\circ$ , it is more common to use the representation (3.19), which formula has the transfer properties depicted in Fig. 3.10; in this case, the amplitudes are equal for all  $v_x$ , while again  $\tilde{S}(v_x)$  and  $\tilde{C}(v_x)$  are in quadrature only at  $\alpha=90^\circ$  and  $-90^\circ/\text{sample}$ ; also, the inherent phase offset of  $-\pi/4$  is clearly revealed by the graphs.

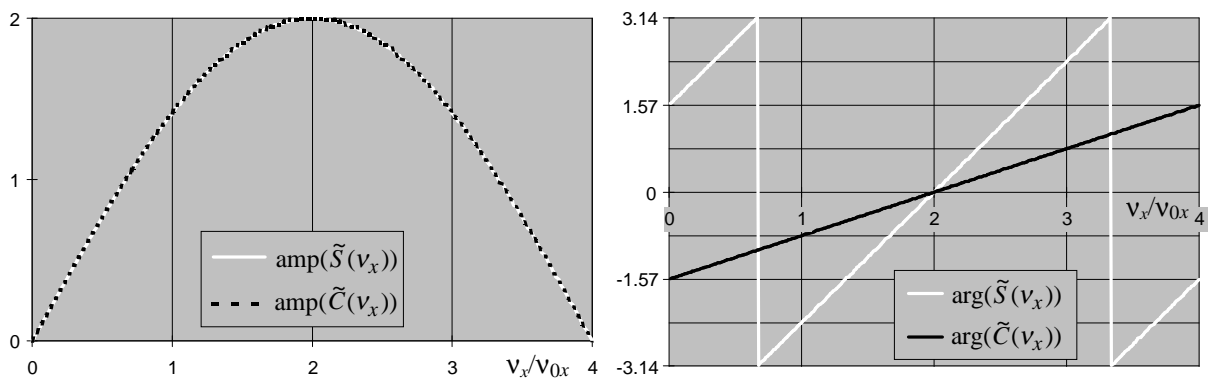


Fig. 3.10: Filter spectrum for 3-step- $90^\circ$  phase-sampling formula (3.19); left: amplitudes, right: phases.

It is possible to balance  $\text{amp}(\tilde{S}(v_x))$  and  $\text{amp}(\tilde{C}(v_x))$  for  $\alpha=120^\circ$  as well, yet at the sacrifice of integer coefficients. From (3.14), one can easily derive

$$(\varphi_O - 15^\circ) \bmod 2\pi = \arctan \frac{-0.259I_0 - 0.707I_1 + 0.966I_2}{0.966I_0 - 0.707I_1 - 0.259I_2} \quad (3.50)$$

with the transfer characteristics shown in Fig. 3.11, which are indeed very similar to those of Fig. 3.10. Note the different normalisation of the frequency axis; here,  $2v_N = 3v_{0x}$ , and  $-(\varphi_O - 15^\circ)$  is detected at  $2v_{0x} \cong \alpha = 240^\circ/d_p$  (aliased to  $-120^\circ/d_p$ ).

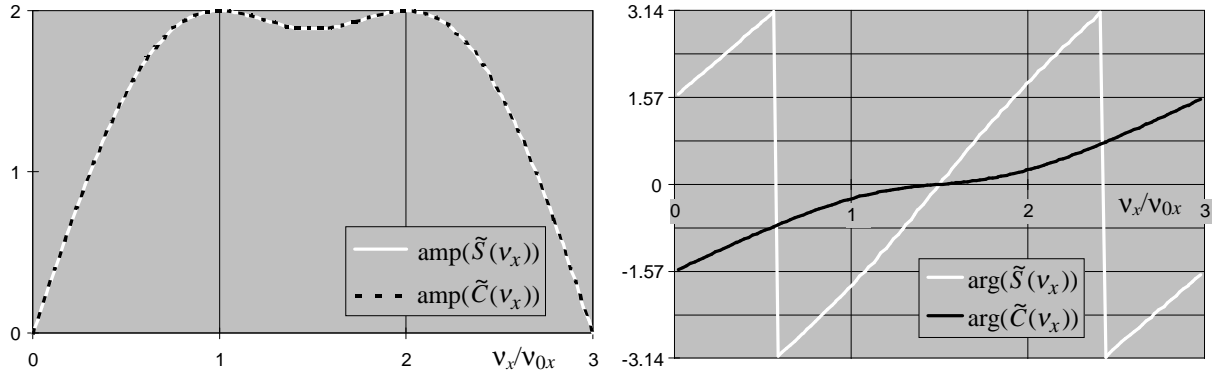


Fig. 3.11: Filter spectrum for 3-step-120° phase-sampling formula (3.50); left: amplitudes, right: phases.

But also for cyclical permutations of the intensity samples, which is equivalent to changing the offset by integer multiples of  $\alpha$  [Schmi95b], the transfer functions of our formulae change considerably. This brings up the question whether a formula really can benefit from such an operation: generally speaking, improving the matching of  $\text{amp}(\tilde{S}(v))$  and  $\text{amp}(\tilde{C}(v))$  worsens the quadrature properties, and vice versa, so that we are in need of a method to account for both aspects simultaneously.

An interpretation of  $\tilde{S}(v_x)$  and  $\tilde{C}(v_x)$  as complex phasors, also suggested in [Mal97], is very helpful to reach conclusions about this point. Therefore we introduce the auxiliary function

$$bsc(v_x) := \arg(\tilde{C}(v_x) + \tilde{S}(v_x)) - \arg(\tilde{C}(v_x)), \quad (3.51)$$

where  $bsc$  stands for the bisector between  $\tilde{S}(v_x)$  and  $\tilde{C}(v_x)$ . Of course, it is the bisector only when the moduli of  $\tilde{S}(v_x)$  and  $\tilde{C}(v_x)$  are equal; its general range is  $-\pi/2 \leq bsc(v_x) \leq \pi/2$ . At  $v_x = v_0$ ,  $\tilde{S}(v_x)$  and  $\tilde{C}(v_x)$  are in quadrature, and  $bsc(v_{0x}) = -45^\circ$ , which is the value indicating correct phase calculation. This is valid for all  $v_x$ , since  $\arg(\tilde{C}(v_x))$  is being subtracted, so that the angle between the phasors always has one side on the real axis. The advantage of  $bsc(v_x)$  is that it responds to changes in both modulus and phase of  $\tilde{S}(v_x)$  and  $\tilde{C}(v_x)$ . The ideal situation is sketched in Fig. 3.12 on the left, being the graphical representation of (3.41).

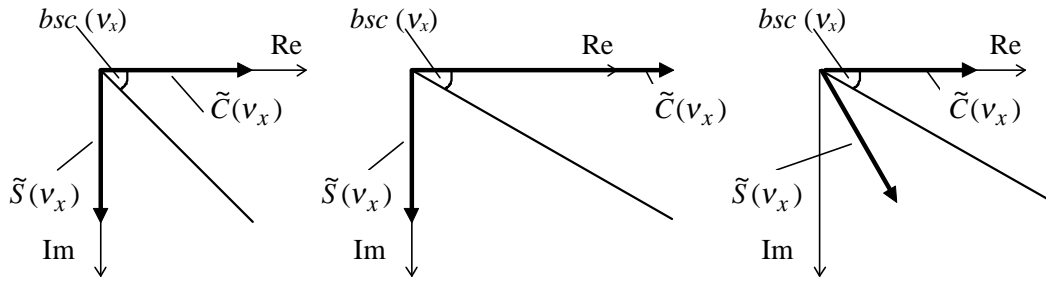


Fig. 3.12: Graphical representation of  $bsc(v_x)$ . Left: ideal case, centre:  $|\tilde{C}(v_x)| = \sqrt{3}|\tilde{S}(v_x)|$ , right: quadrature lost; see text.

In the centre of the drawing,  $|\tilde{C}(v_x)|$  is too large by a factor of  $\sqrt{3}$  due to some error, which changes  $bsc(v_x)$  to  $-30^\circ$ : the calculated phase will oscillate around the true value with a p-v amplitude of  $\cong 15^\circ$  (see Fig. 3.14). The same effect is produced when, e.g.,  $\arg(\tilde{S}(v_x))$  deviates from its nominal value by  $30^\circ$ , as depicted in Fig. 3.12 on the right: although the phasors for  $\tilde{S}(v_x)$  and  $\tilde{C}(v_x)$  have the same length,  $bsc(v_x) = -30^\circ$ . The – normally irrelevant – overall offsets of  $\varphi_0$  (see 3.2.2.4) that the two types of errors produce are not the same, however. Also, it must be stressed that the purpose and capability of  $bsc(v_x)$  is to analyse, not to design phase-shifting formulae.

A vector representation of filter spectra has already been used in [Mal97] to customise phase-shifting formulae; however the influence of detuning had to be treated for amplitudes and phases separately. With the help of  $bsc(v_x)$ , we can now evaluate amplitude and phase spectra of our phase-shifting formulae simultaneously, and it can be seen from Fig. 3.13 that this approach is indeed able to greatly clarify the situation.

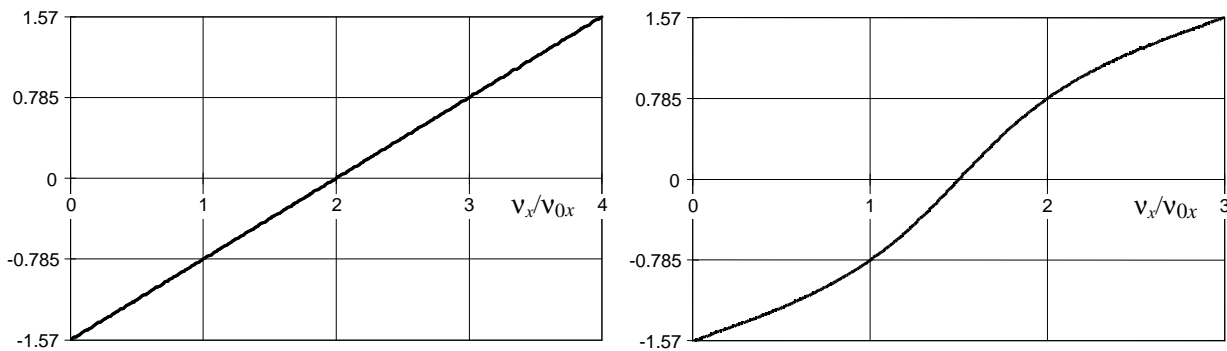


Fig. 3.13: Left:  $bsc(v_x)$  for phase-sampling formulae (3.16), (3.18) and (3.19); right:  $bsc(v_x)$  for phase-sampling formulae (3.17) and (3.50).

One finds that  $bsc(v_x)$  produced by linear detuning is the same for the  $90^\circ$ -formulae (3.16), (3.18) and (3.19)\*, and for the  $120^\circ$ -formulae (3.17) and (3.50), respectively. The interpretation of the values for

\*  $bsc(v_x)$  also reveals some redundancy in [Fre90a]: the reported "case examples" 1 through 4 for  $90^\circ$ -phase-shifting formulae are indeed identical (with respect to p-v detuning errors, cf. Fig. 3.14). Also,  $bsc(v_x)$  solves the quadrature problems with cases 2, 3 and 5 that have been addressed on p. 547.



$v_x \cong 0$  is that  $\tilde{S}(v_x)$  and  $\tilde{C}(v_x)$  point in almost opposite directions, while they have nearly the same argument at  $v_x \cong v_N$ . As mentioned above, for  $v_x=0$  and  $v_x=v_N$ , no phase information at all can be retrieved. The correct value of  $b_{sc}(v_x)$  appears at  $v_x=v_{0x}$  for  $\alpha=90^\circ$  or  $120^\circ$ , respectively. It is interesting to note that the p-v phase errors increase symmetrically for  $v_x \neq v_{0x}$  when  $\alpha=90^\circ$ , while for  $\alpha=120^\circ$ , they rise more steeply for  $v_x > v_{0x}$  than for  $v_x < v_{0x}$ . Also, the slope of  $b_{sc}(v_{0x})$  is greater for  $\alpha=120^\circ$  than for  $\alpha=90^\circ$ , which immediately explains the observation that  $120^\circ$ -formulae are somewhat less tolerant of phase-shift deviations than  $90^\circ$ -formulae [Cre96].

On the whole, this treatment shows that, except for convenience of computer implementation, no advantage or disadvantage is to be expected from different representations of phase-sampling schemes. This has been found by quite a different approach in [Lóp00] and also agrees with the findings in [Sur00], where the characteristic polynomial theory [Sur96] was applied to show that different representations of a given formula can be identified with constant phase factors that do not alter the formula's properties. However, this invariance need not hold for speckle interferometry, since different selections of samples (here: pixels) to include in the calculation result in different utilisation of the spatial information in the speckle interferogram. Therefore, we will check the validity of our findings experimentally in 3.4.5.

#### 3.2.2.4 Four-sample formulae

As discussed, the choice of the  $a_n$  and  $b_n$  is dictated by the necessity to get one sine and one cosine term with no bias intensity, which is a significant restriction for only three intensity samples. Sophisticated averaging or windowing approaches [Schmi95a, Zha99], or the characteristic polynomial theory [Sur96], are not helpful here: the three-step formulae are minimalistic in that they do not contain any redundancy, so they need a correct signal to deliver the correct phase.

Therefore we take into account one more sample, which will give us a certain freedom to customise our formulae. The largest impact on accuracy is to be expected from the sensitivity to linear phase-shift miscalibrations. Recalling our finding of Chapter 2.2.5 that phase extrema are very rare in speckle fields, it follows that the speckle phase fluctuations over a few adjacent pixels will almost always contain a linear contribution; hence it really makes sense to consider its effect. Possibilities to suppress the influence of linear phase-shift deviations have been thoroughly investigated in phase-shifting research and there are many formulae to cope with them. While there are even methods for exact compensation that use three [Ran86, Ser95], four [Car66] or five [Lar96, Sto97] samples, they involve higher computational load, and fail to work as well as predicted on speckle fields, so that we will instead consider again the minimalistic approaches, for  $90^\circ$  and  $120^\circ$  of nominal phase shift.

A linear phase-shift miscalibration causes  $\delta\varphi_O = \varphi_{O,real} - \varphi_{O,calc}$  to oscillate with half the period of  $\varphi_O$  itself [Schwi83, Che85, Lar92c], as depicted in Fig. 3.14 for phase calculation with (3.19) and  $\alpha=95^\circ$ . These  $5^\circ (\cong 0.087 \text{ rad})$  of miscalibration are propagated as p-v error to  $\varphi_{O,calc}$ ; additionally,  $\varphi_{O,calc}$  acquires an overall offset, which is irrelevant unless absolute phases are desired. Under small miscalibration,  $\delta\varphi_O$  has

a quasi-sinusoidal dependence on  $\varphi_0$ ; however it has been shown [Lóp00] that this dependence approaches a sawtooth profile when the detuning error is large.

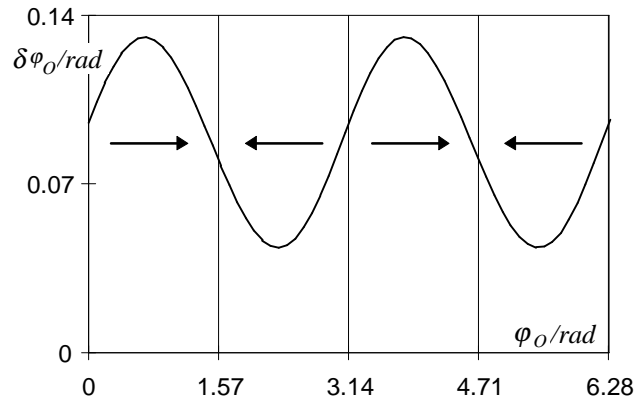


Fig. 3.14: Deviation  $\delta\varphi_0$  of calculated phase from true phase  $\varphi_0$  when  $\alpha=95^\circ$  instead of  $90^\circ$ . Arrows: alteration of phase measurements due to  $\delta\varphi_0$  (see 3.4.6).

There is a simple intuitive way to understand these phenomena: when the sample spacing is incorrect, errors periodical in  $\varphi_0$  will arise in the sine and cosine terms of the phase-sampling formulae; their relative phase lag introduces a double( $2\nu_{0x}$ )- and a zero-frequency (offset) error [Lar92c] in their quotient, which then propagates into the calculated phase.

The fact that  $\delta\varphi_0 \cong -\delta(\varphi_0+90^\circ)$  allows for a very simple approach of error suppression. If the nominal phase shift is set to  $\alpha=90^\circ/\text{sample}$ , we can use (3.19) and construct two consecutive phase measurements with an offset of  $90^\circ$ ,

$$\begin{aligned}\varphi'_{O_0} \bmod 2\pi &= \arctan \frac{I_2 - I_1}{I_0 - I_1} := \frac{N_0}{D_0} = \frac{\sin \varphi'_O}{\cos \varphi'_O} \\ \varphi'_{O_1} \bmod 2\pi &= \arctan \frac{I_3 - I_2}{I_1 - I_2} = \frac{\sin(\varphi'_O + 90^\circ)}{\cos(\varphi'_O + 90^\circ)},\end{aligned}\quad (3.52)$$

where we abbreviate  $\varphi_0-45^\circ$  by  $\varphi'_O$ , cf. (3.19). In these two sampling sequences, we have  $\delta\varphi'_{O_0} \cong -\delta\varphi'_{O_1}$ , which allows us to cancel the error by averaging the results. But for this to function, we must modify the second formula to yield  $\varphi'_O$  instead of  $\varphi'_O+90^\circ$ :

$$\varphi'_{O_1} \bmod 2\pi = \arctan \frac{I_2 - I_1}{I_3 - I_2} = \frac{\sin \varphi'_O}{\cos \varphi'_O} := \frac{N_1}{D_1}, \quad (3.53)$$

where we have used

$$\begin{aligned}\sin \varphi &= -\cos(\varphi + 90^\circ) \\ \cos \varphi &= \sin(\varphi + 90^\circ) .\end{aligned}\quad (3.54)$$

Then, when constructing the phase average, it is better to average the  $N_n$  and  $D_n$  terms before executing the arctangent operation, as opposed to averaging  $\varphi'_{O_0}$  and  $\varphi'_{O_1}$  after separate arctangent operations. This can be justified theoretically and has been done in [Hun97]; to understand the basic idea, it is very helpful

to think of adding weighted and unweighted phasors, respectively, as detailed in [Stroe96]. Therefore, the  $N$  and  $D$  terms are averaged according to [Schwi83, Har87, Schwi93]

$$\bar{\varphi}'_O \bmod 2\pi = \arctan \frac{N_0 + N_1}{D_0 + D_1}, \quad (3.55)$$

which results in

$$\bar{\varphi}'_O \bmod 2\pi = \arctan \frac{2 \sin \varphi'_O}{2 \cos \varphi'_O} = \arctan \frac{2(I_2 - I_1)}{I_0 - I_1 - I_2 + I_3}; \quad (3.56)$$

and this is the formula given in [Schwi93], subsequently referred to as 3+3 averaging formula. Its transfer properties are shown in Fig. 3.15.

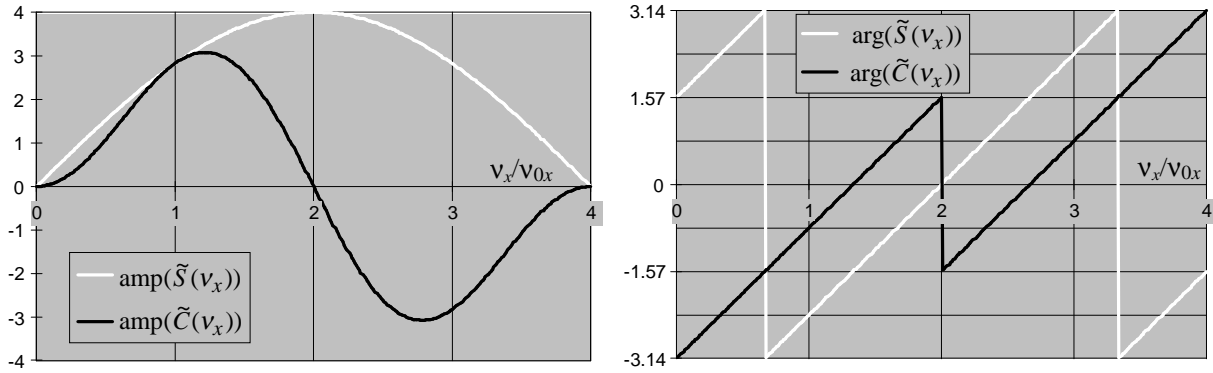


Fig. 3.15: Filter spectrum for 3+3-step-90° phase-sampling formula (3.56); left: amplitudes, right: phases.

As in (3.19), the offset of the reconstructed phase is  $-45^\circ$ ; but the phases of  $\tilde{S}(v_x)$  and  $\tilde{C}(v_x)$  are in quadrature for all  $v_x$ , and also the gradients of  $\tilde{S}(v_x)$  and  $\tilde{C}(v_x)$  are matched:  $d\tilde{S}(v_x)/dv_x|_{v_{0x}} = d\tilde{C}(v_x)/dv_x|_{v_{0x}}$ . This assures stable performance for a larger range of deviations, because  $\tilde{S}(v_x)$  and  $\tilde{C}(v_x)$  are nearly equal for a broader range of  $v_x$ . In [Ser97b], an iterative search for smallest miscalibration sensitivity showed that (3.56) is an almost optimal solution. The offset-free version of the 3+3 formula, also given in [Schwi93], is

$$\bar{\varphi}_O \bmod 2\pi = \arctan \frac{-I_0 + 3I_1 - I_2 - I_3}{I_0 + I_1 - 3I_2 + I_3}; \quad (3.57)$$

this formula shows equal amplitudes for  $\tilde{S}(v)$  and  $\tilde{C}(v)$ , similar to (3.19), but much better quadrature stability than (3.19), as to be seen in Fig. 3.16.

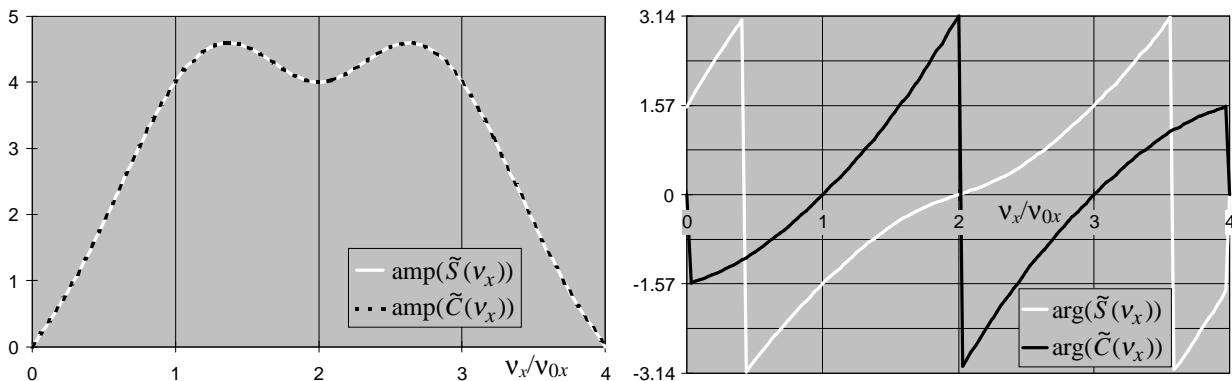


Fig. 3.16: Filter spectrum for 3+3-step-90° phase-sampling formula (3.57); left: amplitudes, right: phases.

It is also possible to average two 4-step formulae [Schwi83, Har87], which yields a 4+1 formula, or to extend the averaging approach to even more samples [Schmi95a, Zha99]. Particularly the 4+1 formula is very frequently used in ESPI; but we ignore it here because it requires 5 samples already; we will briefly discuss 5-sample formulae in Appendix D.

While formulae with  $\alpha=90^\circ$  are most effective against detuning due to the error frequency having twice the signal frequency, it is also possible to design compensating formulae with  $\alpha=120^\circ$ . A recipe to do so has been given in [Lar92b]; it is based on arranging the  $a_n$  and  $b_n$  (anti)symmetrically over the sampling sequence (which results in frequency-independent quadrature) and matching the gradients of  $\tilde{S}(v)$  and  $\tilde{C}(v)$  at  $v_0$ . (At this point, we note that also (3.56) fulfils these criteria; in fact, all the formulae with stable quadrature presented thus far have (anti)symmetrically arranged coefficients. This so-called Hermitian symmetry of the coefficients is a necessary and sufficient condition for the frequency independence of the quadrature, and it has been shown in [Sur98a, Hib98] how to symmetrise phase-shifting formulae.)

The error-compensating symmetrical 3+1-sample formula for  $\alpha=120^\circ$  reads [Lar99]

$$\bar{\varphi}_O \bmod 2\pi = \arctan \frac{I_0 + 3(I_1 - I_2) - I_3}{\sqrt{3}(-I_0 + I_1 + I_2 - I_3)}; \quad (3.58)$$

its spectral characteristics, shown in Fig. 3.17, demonstrate that (3.58) also has reduced sensitivity to linear phase-shift miscalibration.

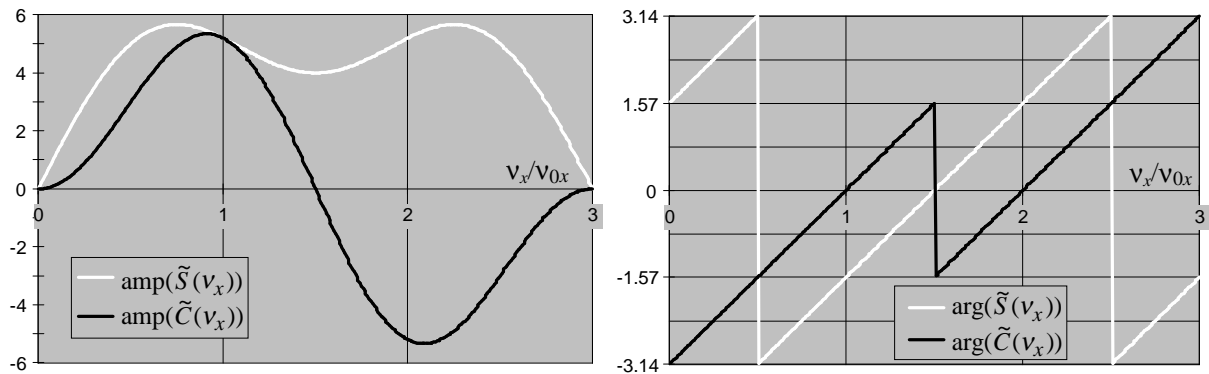


Fig. 3.17: Filter spectrum for 3+1-step- $120^\circ$  phase-sampling formula (3.58); left: amplitudes, right: phases.

Since we have been dealing with different offsets of the reconstructed phase in (3.56) and (3.57), we will again make use of  $bsc(v_x)$  to find out more general properties of the methods. Fig. 3.18 presents the corresponding plots for (3.56)-(3.58).

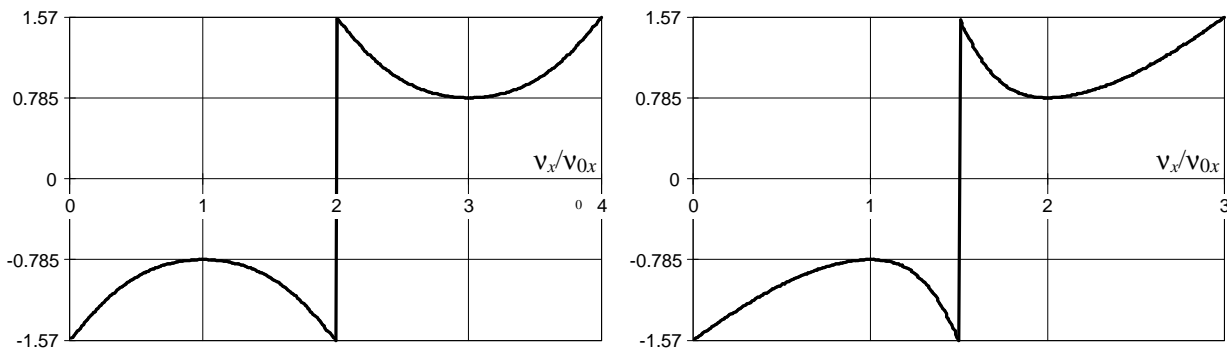


Fig. 3.18: Left:  $bsc(v)$  for phase-sampling formulae (3.56) and (3.57); right:  $bsc(v)$  for formula (3.58).

Again, we find errors increasing symmetrically on both sides of  $v_{0x}$  when  $\alpha$  is nominally  $90^\circ$ ; the key to error suppression is the vanishing slope of  $b_{sc}(v_{0x})$ . The same is true for  $\alpha=120^\circ$ ; but as above in Fig. 3.13, we find a steep increase of errors for  $v_x > v_{0x}$ , simply because  $v_{0x}$  is not centred between  $v_{0x}=0$  and  $v_{0x}=2v_N$  and hence the  $b_{sc}(v_x)$  curve cannot be symmetrical.

Generally, the error compensation cancels the oscillating error only; the zero-order error (phase offset) persists, as can also be seen from the phase spectra of (3.56) and (3.58): while the difference of  $\arg(\tilde{S}(v_x))$  and  $\arg(\tilde{C}(v_x))$  remains constant, the reconstructed phase will depend on the phase-shift deviation, as gets obvious from the progression of  $\arg(\tilde{S}(v_x))$  and  $\arg(\tilde{C}(v_x))$  with  $v_x$ . Hence, in ESPI the correct absolute phase difference  $\Delta\varphi$  is only obtained when the phase-shift error is the same in both sets of samples. In TPS, this is generally not the case, but as long as the error is spatially uniform, the determination of phase *gradients* will not suffer: a fringe offset in the sawtooth image is irrelevant. In SPS, the offsets fluctuate locally with the speckle phase gradients; but since the speckle field is supposed to remain correlated during the measurement, the errors cancel on subtraction of the speckle phase maps.

As mentioned above, these theoretical considerations do not account for the spatial coherence present or not present within the sampling pixel window. For instance, a 3+3 formula need not automatically reduce the measurement errors, because its error compensation might be superseded by low spatial correlation of the sampling points. Therefore we will subject also the compensating formulae to an experimental check in 3.4.5.

### 3.3 Temporal phase shifting

Many of the peculiarities of TPS have already been treated implicitly in 3.2.1.1, so that we now address only two more subjects: first, we consider the loss of modulation associated with phase ramping instead of stepping, and second, we take a look at the power spectrum of a speckle interferogram and consider a very simple method to determine the average speckle size.

While the phase-shifted interferograms are recorded sequentially in time, the different  $\alpha_n$  are adjusted by means of a phase shifter such as a mirror on a piezoelectric crystal in the reference arm. While it is possible to set the  $\alpha_n$  statically, i.e. no change takes place during the exposure of each frame, it is more convenient and has become popular to shift the phase linearly during the recording sequence, so that each measurement becomes an integral over a phase interval. This changes (3.12) to

$$\begin{aligned}
 I_n &= \frac{1}{\alpha} \cdot \int_{\alpha_n - \frac{\alpha}{2}}^{\alpha_n + \frac{\alpha}{2}} I_b + M_I \cdot \cos(\varphi_O + \alpha_n + \alpha') d\alpha' \\
 &= I_b + M_I \cdot \frac{2\sin(\frac{\alpha}{2})}{\alpha} \cdot \cos(\varphi_O + \alpha_n) \quad ;
 \end{aligned}
 \tag{3.59}$$

the additional factor is 0.9 when  $\alpha=90^\circ$ , and 0.83 for  $\alpha=120^\circ$ , so that the overall effect of the ramping approach is a slight decrease in the modulation of the data; however, the measured  $\varphi_O$  remains the same

whenever the integration interval is symmetrical. The static method is referred to as the step method and the dynamically phase shifting approach is known as integrating-bucket or simply bucket method [Wya75].

The equation system (3.12) or (3.59) is set up under the assumption that the unknowns do not change from frame to frame, i.e. are temporally constant. While this is very likely to be correct for  $I_b$  and  $M_I$ , it is difficult to assure for  $\varphi_0$ , which is why vibration-isolating optical tables, phase stabilisation facilities and/or short exposure times are very common with this method. The interferograms  $I_n(x,y,t_n)$  must be recorded as quickly as possible to diminish influences by object changes or phase fluctuations in the interferometer, and the possibilities to carry out TPS measurements of rapidly moving objects or under external disturbances are limited. Fig. 3.19 presents sawtooth phase maps from experiments under various conditions. While TPS delivers good phase measurements under temporally stable conditions, a vibrating interferometer (here: table without air cushion) can cause wrong phase shifts and thus loss of direction information. With locally different phase shifts, as caused by turbulent air in the beam paths, also the qualitative correctness of the image may get lost.

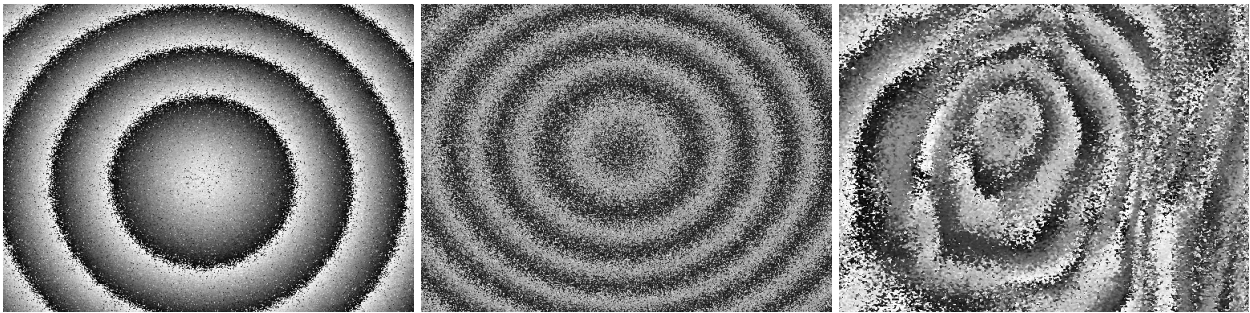


Fig. 3.19: Sawtooth phase maps as results of deformation measurement with TPS under: stable experimental conditions (left), vibrations (centre), and air turbulences (right).

Much work has been done to cope with the various error sources: phase-shift miscalibrations [Moo80, Schwi83, Che85, Joe94, Sla95, Och98], vibrations [dGro96, Dec96, Dec98, Hun98], unequal and/or uncalibrated phase steps [Gre84, Oka91, Far94, Ryu97, Wei99], nonsinusoidal intensity profile [Hib95], and in a wider context, variable bias intensity [Ono96, Sur97b], or variable fringe visibility [Lar96]. There have also been attempts to reduce the data acquisition time by 2+1-frame methods [Ker90, Col92, Fac93, Ng 96] or high-speed devices [Cog99, Hun99]. Many of these efforts are concerned with the sensitivity of TPS to time-dependent phase fluctuations, which shows that these are indeed a major obstacle.

### 3.3.1 Speckle "size" in interferograms

The experimental determination of the mean speckle size is usually done by calculating the autocorrelation function of the speckle intensity field and determining the full or half width of its central peak. As the speckles get smaller, this digital method grows imprecise because the peak is then only a few pixels wide and requires fitting a curve to it to estimate its width with subpixel accuracy. When dealing with speckle interferograms however, there is a simpler method: one can conveniently determine the speckle size from the power spectrum of an interferogram, in which the speckle size is "doubled" by

adding a reference wave [Enn75, Maa98]. To understand how this is meant, we first consider briefly the power spectrum of a speckle pattern. The situation is depicted in Fig. 3.20.

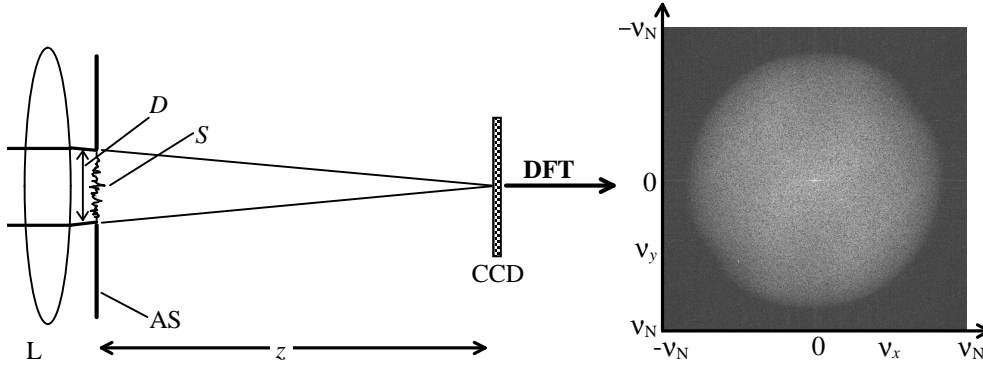


Fig. 3.20: Left: Imaging of a speckle pattern: L, lens; S, speckle field; AS, aperture stop;  $z$ , distance of AS from CCD sensor. Right: power spectrum of speckle pattern in log display;  $v_x=v_y=0$  is in the centre of the image and the positive and negative  $v_N$  at its borders.

The aperture stop AS has a transmission function  $T_{AS}$  (here a circle of diameter  $D$ ) with which the speckle pattern  $S$  is multiplied on passing the aperture plane. For simplicity, we assume that  $z \cong f$ , whereby we have the far field of  $S \cdot T_{AS}$  in the image plane. The field on the CCD chip is therefore  $FT(S \cdot T_{AS}) = \tilde{S} * \tilde{T}_{AS}$ , where FT stands for the Fourier transform,  $*$  for convolution, tilde denotes the transformed variables, and we omit proportionality constants. The speckle intensity detected by the CCD is given by  $|\tilde{S} * \tilde{T}_{AS}|^2$ , and using the Wiener-Khintchine theorem, we can write its Fourier transform as  $FT(|\tilde{S} * \tilde{T}_{AS}|^2) = ACF(S \cdot T_{AS})$  – ACF denoting the autocorrelation function –, which is simply a speckle halo, as shown in Fig. 3.20 in logarithmic scaling. The size of this speckle halo in the frequency plane is proportional to  $D$  and therefore inversely proportional to  $d_s$ .

The maximal spatial frequency in the speckle pattern on the CCD is determined by the interference of the outermost rays that pass the aperture, i.e.

$$v_{max,s} = \frac{D}{\lambda f}, \quad (3.60)$$

which is of course only valid if  $T_{AS}$  really reaches zero at the edges of the aperture. This is the "band limit" mentioned in Chapter 2.3.2. For circular apertures, the speckle size is, cf. (2.43),

$$d_s = 1.22 \frac{\lambda f}{D}, \quad (3.61)$$

which links to (3.60) to yield the simple formula

$$d_s = \frac{1.22}{v_{max,s}}, \quad (3.62)$$

so that e.g. a speckle halo just fitting in the DFT's frequency plane, with  $v_{max,s} = \pm v_N = \pm 1/(2 d_p)$ , is seen to come from a speckle pattern with  $d_s = 2.44 d_p$ . In Fig. 3.20, we have  $d_s = 3 d_p$ .

If we assume that a reference wave  $R$  of amplitude  $R$  is added as a point source in the centre of AS, which is drawn in Fig. 3.21, the field on the CCD chip will be  $FT(S \cdot T_{AS} + R\delta(0,0)) = \tilde{S} * \tilde{T}_{AS} + \tilde{R}$ . The intensity on the sensor is  $|\tilde{S} * \tilde{T}_{AS} + \tilde{R}|^2$ , and its Fourier spectrum is  $FT(|\tilde{S} * \tilde{T}_{AS} + \tilde{R}|^2) = ACF(S \cdot T_{AS}) + |R|^2 \delta(0,0) + (S^* \cdot T_{AS}^*) * R\delta(0,0) + (S \cdot T_{AS}) * R^* \delta(0,0)$ . The first term is again the speckle halo, the second term is a central peak due to the uniform reference wave; these are often called the self-interference terms. On inspecting the mixed or cross-interference terms, we find that they reproduce the speckle field's amplitudes, with an envelope that is the aperture function again. The convolution with the  $\delta$  function of the reference wave reproduces this distribution and multiplies it with  $R$ . The power spectrum of a speckle interferogram therefore looks as in Fig. 3.21 on the right; again, the scale is logarithmic and  $d_s = 3 d_p$ .

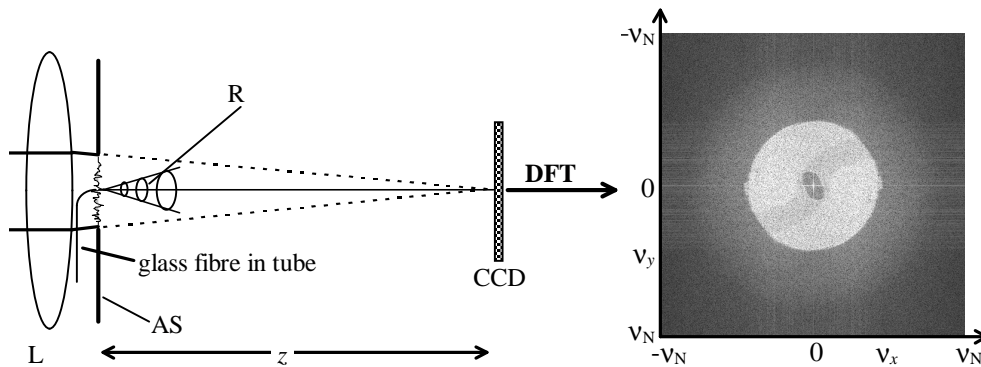


Fig. 3.21: Left: Imaging geometry for ESPI;  $R$ , reference wave; other abbreviations as above in Fig. 3.20. Right: power spectrum of speckle interferogram in log display; frequency plane as above.

The interference terms overlap in the centre and are point-symmetrical with respect to each other; hence the shadow of the fibre guide, being an undesired but here instructive part of  $T_{AS}$ , is visible in each of them. The speckle halo is still the same as in Fig. 3.21, but the extent of the spectra or "bands" of the interference terms,  $(S^* \cdot T_{AS}^*) * R\delta(0,0) + (S \cdot T_{AS}) * R^* \delta(0,0)$ , in the frequency plane is exactly half that of the speckle halo. This is the "doubling of speckle size" mentioned above. It occurs only when  $R$  is large enough to suppress the speckle halo; the influence of  $R$  will play an important role later on.

As Fig. 3.21 indicates, the maximal spatial frequencies of the interference bands are given by interference of  $R$  with the outermost rays passing the aperture. With

$$v_{max,i} = \frac{D}{2\lambda f}, \quad (3.63)$$

where the subscript  $i$  stands for interference, we arrive at

$$d_s = \frac{0.61}{v_{max,i}}, \quad (3.64)$$



which allows for a very convenient determination of the speckle size from the power spectrum of the interferogram. When the interference bands are centred on each other (i.e. the source point of R is placed in the exact centre of AS), the edges of the frequency plane are reached when  $d_s=1.22 d_p$ , but using its corners, we can accurately determine speckle sizes down to  $0.86 d_p$ .

The advantage of using interferogram power spectra gets clear when we consider Fig. 3.22: determining the speckle size from this image is very easy, while it is problematic to apply the autocorrelation technique for so small a speckle size.

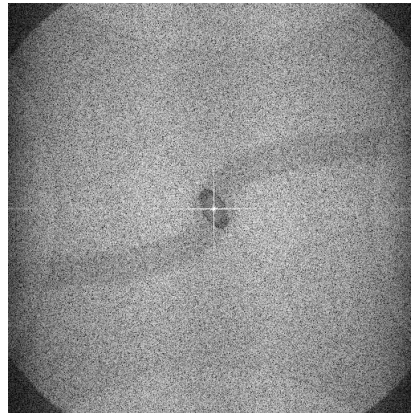


Fig. 3.22: Power spectrum of interferogram with  $d_s=1 d_p$ ; spatial frequency axes as in Fig. 3.20.

Finally, if the source point of R is not in the plane of AS, the  $\delta$  function above will broaden; then, on convolution with  $S \cdot T_{AS}$ , the sharp edges of the cross-interference spectra will smear out. This behaviour provides us with a very accurate means to match the curvatures of the two wave fields.

### 3.4 Spatial phase shifting

An elegant way to get rid of the problems associated with inter-frame temporal parameter fluctuations is to acquire the phase-shifted data simultaneously. Since the phase shift then has to take place in space instead of time, this approach is quite generally called spatial phase shifting (SPS) [Schwi90, Tak90b, Kuj93, Vla94]; the underlying principle has been known for a long time [Lei62]. With SPS, phase-measuring methods gain access to unstable environments and transient events. For very rapid phenomena, the use of pulsed illumination represents an effective way to suppress even the intra-frame fluctuations and freeze virtually anything. In principle, it gets possible to track the object phase at the frame rate of the camera, with the additional benefit that any frame of the series can be appointed the new reference image.

The increased temporal resolution of this approach has, however, to be paid for in terms of spatial resolution, since it is of course necessary to spatially separate the  $I_n$ . In analogy to TPS, we can distinguish between phase stepping and phase ramping. The former is implemented by generating several images of the same object and recording them simultaneously on several sensors, or different parts of the same sensor. The necessary phase shift between the images can be generated by polarisation optics [Smy84, Kuj93, vHaa94], diffraction gratings [Kwo84, Kuj88], CGHs [Bar99] or combinations of these [Kra98, Kem99, Het00]. For the phase retrieval to work properly, the  $I_n$  must be aligned with subpixel accuracy

and all have the same  $I_b$  and  $M_I$ , which is difficult to achieve [Kuj91a, Het00]. If parts of one and the same sensor are used for the sub-images, resolution is lost; if several full-chip images are taken, they will have to share the light energy available. High expense on the components, great adjustment effort and high sensitivity to misalignment are to be expected when working with set-ups of this type.

The phase-ramping or bucket method of SPS works with one detector, on which a dense additional fringe pattern is generated to function as a so-called spatial phase bias or, in the Fourier terminology, carrier frequency. The – low-frequency – signal of interest distorts the carrier pattern and can be retrieved from it by a number of methods [Wom84]. This approach has first been implemented with vertical carrier fringes in [Ich72, Mer83] as analogue real-time processing of TV line signals. (Note here that only SPS lends itself to this technique: TPS requires digital processing since separate TV frames are involved.) The first studies were soon followed by digital implementations [Toy84, Toy86, Sho90, Fre90b,c, Kuch90, Kuch91, Kuj91b], allowing for arbitrary directions of the carrier fringes. Also, it was demonstrated in [Tak82] that the signal can conveniently be retrieved in the frequency plane by a Fourier-transform method; we defer details to Chapter 6.5. Other methods to retrieve phase from images with a spatial carrier are the phase-locked-loop method [Ser93] and the frequency demodulation technique [Ara96].

Later it was realised that this approach could be applied to speckle interferometry as well [Ste91, Wil91, Gut93]. A standard ESPI set-up is very easily changed to an SPS system; it is sufficient to laterally displace the focus, or source point, of the reference wave to introduce the fringe carrier. Fig. 3.23 shows the modification, with a magnified portion of a speckle interferogram: the fine fringes on the speckles are clearly discernible.

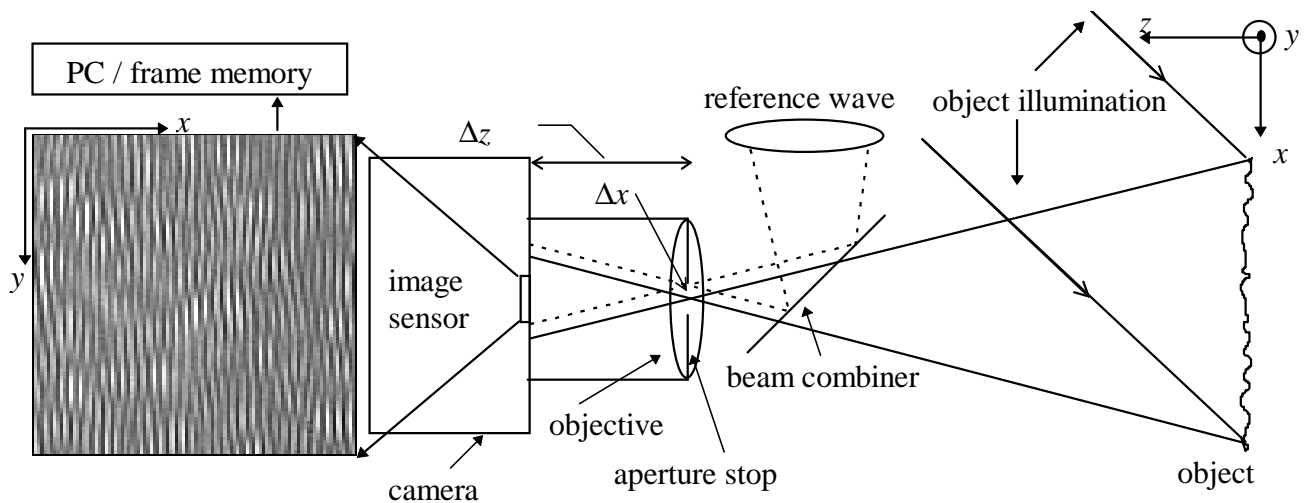


Fig. 3.23: ESPI set-up slightly modified (cf. standard configuration in Fig. 3.1) for spatial phase shifting.

In the following subsections, we will go through some details pertaining especially to SPS to get an overview of the quality criteria for interferograms with a spatial carrier.

## 3.4.1 Geometrical description of spatial phase shift

The lateral offset  $\Delta x$  of the reference wave's origin generates a quasi-linear geometric path and hence phase difference between the object wave O and the reference wave R over the sensor. Fig. 3.24 sketches the principle.

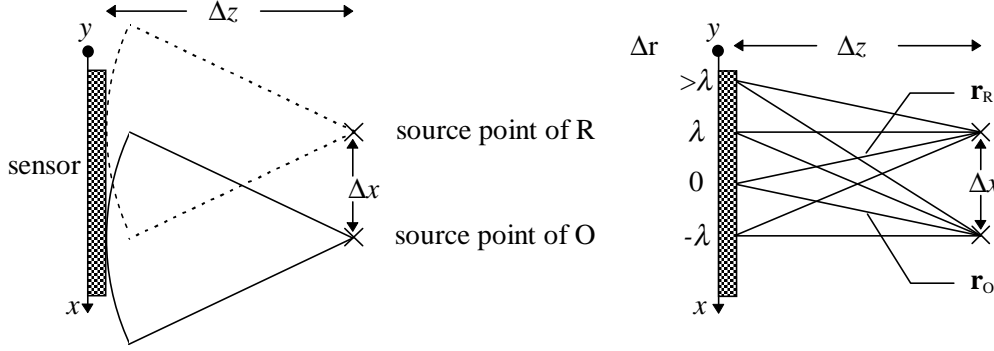


Fig. 3.24: Left: incidence of two spherical waves with origins displaced by  $\Delta x$ ; right: construction of corresponding pathlength differences  $\Delta r = |\mathbf{r}_O| - |\mathbf{r}_R|$ .

While a phase shift in the sensor's  $y$ -direction may be added by a displacement  $\Delta y$ , this case is still one-dimensional in the appropriate co-ordinate system. Hence it is sufficient to consider the phase difference  $\alpha(x)$ , given by

$$\alpha(x) = |\mathbf{r}_O| - |\mathbf{r}_R| = \frac{2\pi}{\lambda} \left( \sqrt{\left(x + \frac{\Delta x}{2}\right)^2 + y^2 + \Delta z^2} - \sqrt{\left(x - \frac{\Delta x}{2}\right)^2 + y^2 + \Delta z^2} \right) \quad (3.65)$$

where  $x = 0$  is defined to be the  $y$  axis in the middle between the waves' source points. This is not generally the central sensor column: since the centre of the aperture should lie on the optical axis over the centre of the sensor, the object wave's origin cannot be shifted from there. However,  $y = 0$  does lie on the central row of the sensor. The corresponding phase gradient in  $x$ -direction,

$$\alpha_x(x, y) = \frac{2\pi}{\lambda} \left( \frac{x + \frac{\Delta x}{2}}{\sqrt{\left(x + \frac{\Delta x}{2}\right)^2 + y^2 + \Delta z^2}} - \frac{x - \frac{\Delta x}{2}}{\sqrt{\left(x - \frac{\Delta x}{2}\right)^2 + y^2 + \Delta z^2}} \right), \quad (3.66)$$

is quasi-constant when  $\Delta z$  is much larger than everything else, which is quite reasonable to assume when using common imaging optics. Then  $\Delta z$  will be on the cm scale, whilst the other quantities are on the mm scale. It turns out that the  $y$  co-ordinate also has a weak influence on  $\alpha_x$ ; hence the carrier fringes are not exactly straight. In fact, they have hyperbolic shape, which also follows from the definition of a hyperbola as the set of points for which  $|\mathbf{r}_O| - |\mathbf{r}_R|$  is constant. Fig. 3.25 depicts the situation for an average nominal phase gradient of  $\alpha_x(x, y) = 120^\circ$  per sensor column and the optical configuration of Fig. 5.1. The spatial dimensions refer to sensor of the camera that was used throughout the work to follow, ADIMEC MX12P with  $1024 \times 768$  pixels of size  $(7.5 \mu\text{m})^2$ .

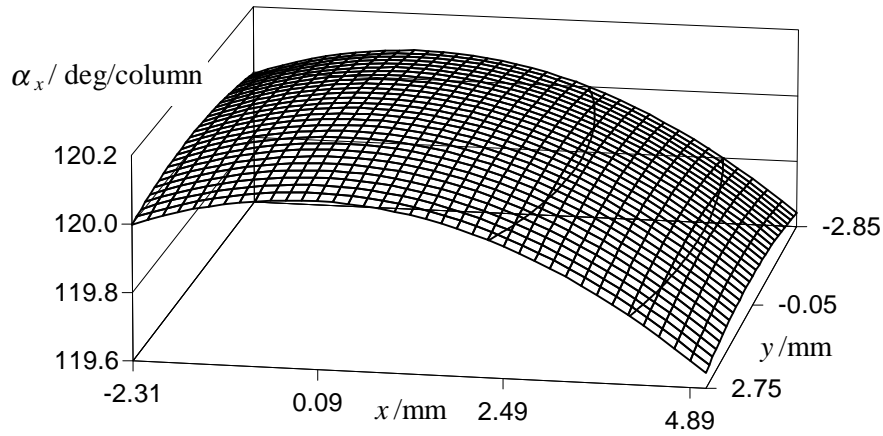


Fig. 3.25: Spatial distribution of  $\alpha_x(x,y)$  on the CCD sensor area for  $z = 10.2$  cm and  $\Delta x = 2.9$  mm.

Clearly, the continuous phase progression over the sensor leads to an integration over the pixels, so that this is an integrating-bucket method. When the phase runs along columns or rows only, the recorded  $I_n$  are described by (3.59), since also the camera pixels are rectangular integration windows, only in space instead of time. The factors given in 3.3 for the decrease of  $M_I$  remain valid in this case.

If, however, the carrier fringes are slanted with respect to the Cartesian sensor axes, the situation is different: for instance, if  $\Delta x = \Delta y$ , the slant is  $45^\circ$  and the function over which the phase progression is "windowed" becomes a triangle; for values below  $45^\circ$ , it acquires trapezoidal shape. Fortunately, the windows remain symmetrical in any case, from which it follows that the detected phase angles will remain correct [Wom84]. To determine the loss of  $M_I$  due to a "composite" phase ramp (i.e. for phase shift in  $x$  and  $y$  direction), it is easiest to integrate over its components separately, which gives

$$I_n = I_b + M_I \cdot \frac{2\sin(\frac{\alpha_x}{2})}{\alpha_x} \cdot \frac{2\sin(\frac{\alpha_y}{2})}{\alpha_y} \cdot \cos(\varphi_O + \alpha_n); \quad (3.67)$$

not surprisingly, this reflects the theoretical 2D-MTF for square pixels. For  $\alpha_x = \alpha_y$ , and hence a triangular envelope of the phase integration, the factor becomes  $4 \sin^2(\alpha_x/2)/\alpha_x^2$  and is indeed the transfer function of a triangle. We will be concerned with such a case in Chapter 6.3.

The choice of the carrier frequency is influenced by contradictory requirements: on the one hand, it should be as high as possible to allow a broad range of signal frequencies to be measured. On the other hand, aliasing of too high frequencies must be avoided. In general,  $\alpha_x$  must have the same sign in the whole measuring field to keep the phase extraction unambiguous: a reversed, or aliased, phase shift leads to the wrong sign of the calculated phase, cf. 3.2.2. In classical interferometry, this means that closed interferometric fringes are not allowed, and the complete fringe pattern must be properly sampled; in speckle interferometry, the requirements are different and we will discuss them in 3.4.4.

Since the  $I_n$  are arranged as adjacent pixels on the sensor, it is clear that the speckles must be enlarged to obtain sufficient spatial correlation of speckle intensity and phase within the sampling pixel cluster, so that the modulation detected by a phase-extraction formula comes more from the phase shift than from

crossing speckle "boundaries". The ideal case is sketched in Fig. 3.26 for  $d_s=3 d_p$ . Depending on the orientation and density of the carrier fringe pattern, various phase-extraction formulae can be applied.

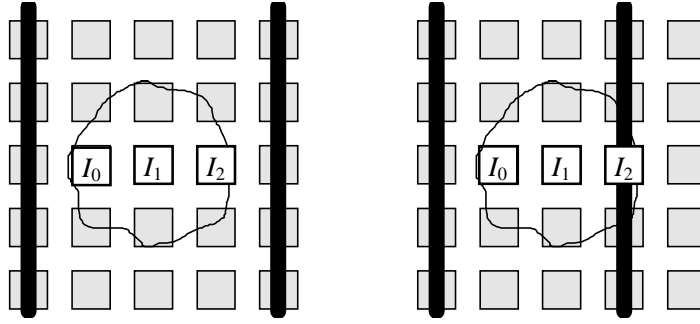


Fig. 3.26: Acquisition of three intensity samples  $I_0, I_1, I_2$  for SPS. Small squares: sensor pixels, irregular outlines: speckles. Direction and spacing of the carrier fringes are indicated by the vertical black bars; left:  $\alpha=90^\circ/d_p$ , right:  $\alpha=120^\circ/d_p$ .

The speckles, and also the sampling pixel cluster, should be as small as possible for the sake of spatial resolution; on the other hand, a somewhat larger pixel cluster can lead to more reliable phase measurements even when the speckle size is not increased. We will consider this point in detail in Chapter 6.2.2.

In any case, the aperture must be smaller than in TPS; a first guess for the minimal speckle size would be  $d_s=3 d_p$ , because in (3.12), we need  $n \geq 3$ . So small an aperture entails some drawbacks: first, significantly less object light is available; and second,  $\Delta x$  can usually not be chosen freely, since for R to reach the sensor,  $\Delta x$  must not exceed  $D/2$  (cf. Fig. 3.21). The latter problem can be solved with customised imaging optics: a narrow slit beside the diaphragm hole, allowing the focus of R to pass, will broaden the possible range of  $\Delta x$  (cf. Fig. Fig. 5.1). Finally, when the test surface undergoes a tilt, the decorrelation of the speckle field proceeds faster with narrow than with wide apertures: that portion of the speckle field which is collected by the aperture is being panned "out of view" sooner when  $D$  is small.

Once these problems are overcome, it becomes possible to study dynamic phenomena; using (double-)pulsed illumination, even very rapid transients can be frozen [Ped93, Ped94, Sched97, Ped97c, Pet98, Pet99]. Moreover, the decrease in spatial resolution is in practice more than offset by the low data storage requirements, since mostly the sawtooth images are smoothed anyway during data processing.

### 3.4.2 Evaluation of SPS interferograms

The intensity samples for the phase calculation are picked from an interferogram in analogy to (3.12) which we rewrite as a spatial version (restricting ourselves to  $\alpha=\alpha(x)$ , i.e. the phase changes from column to column of the image):

$$I_n(x_{k+n}, y, t) = I_b(x_{k+n}, y) + M_I(x_{k+n}, y) \cdot \cos(\varphi_O(x_{k+n}, y, t) + \alpha_n(x_{k+n}, y)), \quad (3.68)$$

this is, to find the phase at a pixel in column  $k$  of the image, some neighbouring pixels are needed to provide the phase-shifted interference data. The equation system expressed by (3.68) then imposes the

restriction that  $\varphi_O(x_k, y) \cong \varphi_O(x_{k+n}, y)$  for all  $n$ , and the same applies to  $I_b(x_k, y)$  and  $M_I(x_k, y)$ ; this is, spatial fluctuations of these quantities should be as small as possible. The time dependence of  $\varphi_O$  can be neglected unless  $\varphi_O$  fluctuates substantially within the integration time for the camera frames;  $\alpha_n$  has no time dependence at all, because the phase shift is determined by the stable geometry depicted in Fig. 3.24.

The  $I_n$  are then processed as described in 3.2; however, when working spatially, it is reasonable to use evaluation formulae with  $n \in \{-1, 0, 1\}$  or  $n \in \{-1, 0, 1, 2\}$  because, as Fig. 3.26 shows, the central pixel of the cluster will be the one that has best spatial correlation with its neighbours and to which the resulting  $\varphi_O$  should be assigned. From this it follows that  $1 < k < M$  or  $1 < k < M-1$ , i.e. no values for  $\varphi_O$  can be obtained for the first and the last, or the last two, image columns; but considering the large numbers of pixels on modern sensors (here: 1024 columns  $\times$  768 rows), this restriction is negligible.

The natural way to determine deformations from a pair of interferograms,  $I_i(x, y)$  and  $I_f(x, y)$ , is the difference-of-phases method, since two frames, each one subjected to (3.68), suffice to generate two speckle phase maps. However, with three-sample methods one can also obtain correlation fringes from SPS interferograms according to

$$I_{n,c}(x_k, y_l) = \left| I_f(x_{k+n}, y_l) - I_i(x_k, y_l) \right|, \quad (3.69)$$

where the subscript  $c$  denotes correlation fringes and  $n \in \{-1, 0, 1\}$ ; this is, we shift  $I_f$  by one column to the right and subtract  $I_i$ , then subtract the unshifted images, and finally shift  $I_f$  one column to the left and subtract  $I_i$  [Ped93, Ped94]. But the lateral image shift of course causes lower speckle correlation between  $I_f(x_{k\pm 1}, y)$  and  $I_i(x_k, y)$  than between  $I_f(x_k, y)$  and  $I_i(x_k, y)$ , resulting in non-constant fringe contrast within the set of the  $I_{n,c}(x_k, y)$ , and consequently, unnecessary errors in the phase calculation. Hence it is easy to understand why apparently this method has not been used with four-sample formulae and  $n \in \{-1, 0, 1, 2\}$ : an offset of two columns would lead to very faint correlation fringes in  $|I_f(x_{k+2}, y) - I_i(x_k, y)|$ , unless the speckles are larger than  $3 d_p$ . Therefore, correlation fringes from SPS are even less suitable for the phase-of-differences method than are those from TPS.

When SPS is tested under the same disturbances as the TPS measurements shown above in Fig. 3.19, the difference-of-phases method leads to the example results presented in Fig. 3.27. While the experiment under good conditions yields slightly higher noise than for TPS, vibrations do not alter the phase shift, since it is determined geometrically here, and the quality of the measurement is preserved. Of course, when the frequency and/or amplitude of the vibrations gets too high, the modulation in the speckle interferogram may be washed out; but as mentioned, pulsed illumination solves this problem. Under turbulences, there is no simple way to avoid warping of the phase front; but the image from SPS is far easier to interpret than that from TPS. As long as the sawtooth fringes remain resolvable, they should lead to a usable result, and possibly reveal the nature of the turbulence in addition.

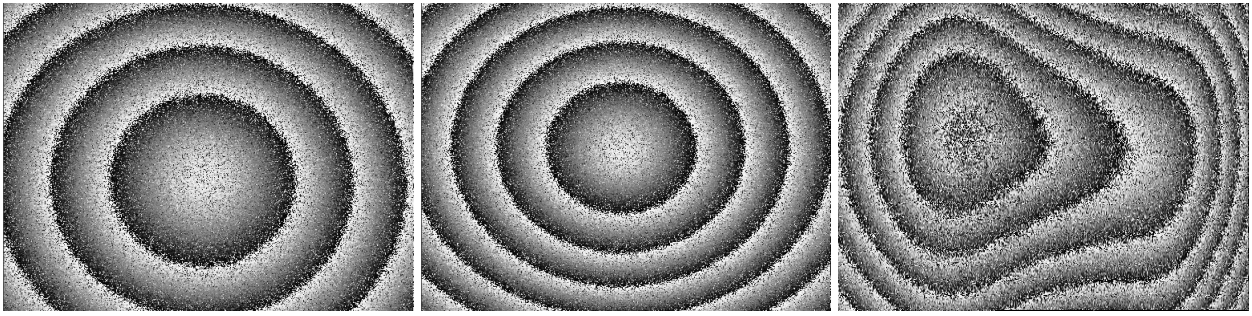


Fig. 3.27: Sawtooth phase maps as results of deformation measurement with SPS under: stable experimental conditions (left), vibrations (centre), and air turbulences (right).

### 3.4.3 Relation of speckle size and magnification

For usual imaging optics,  $f\# = f/D$  is confined to a maximum of 22 or 32, which may prevent reaching the desired  $d_s$  in some cases. Considering

$$d_s = 1.22\lambda(M+1)f\# \quad (3.70)$$

where  $M$  is the magnification (image size : object size), we can immediately see that the maximum object size that can be imaged gets smaller when  $d_s$  is to be increased, and vice versa. Fig. 3.28 gives an overview of the necessary  $f$ -numbers when a certain magnification is required. The plots are scaled for the pixel size of  $7.5 \mu\text{m}$  of the MX12P camera.

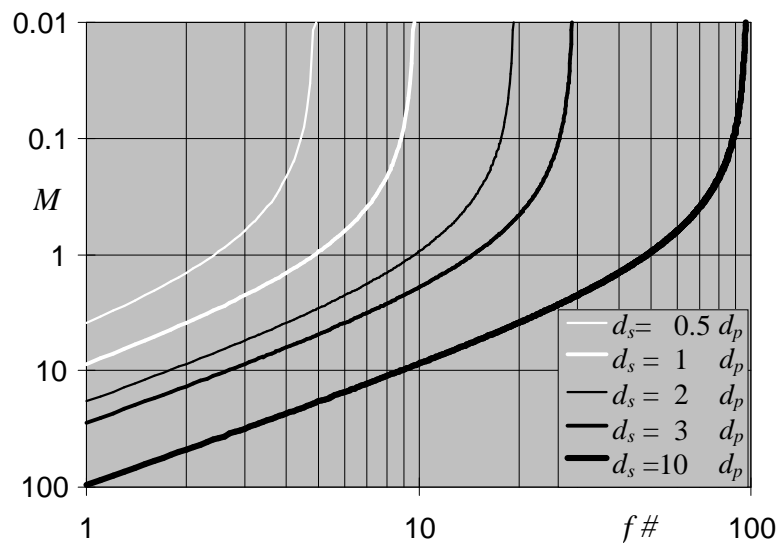


Fig. 3.28: Double-logarithmic plot of magnification  $M$  vs.  $f$ -number for various pre-set speckle sizes.

Let us consider a practical example: with a sensor of  $1024 \times 1024$  pixels, we would need  $M=0.02$  in order to image  $(37.5 \text{ cm})^2$  on the chip; for  $d_s=1$  pixel,  $f\# \cong 10$ ; but for  $d_s=3 d_p$ ,  $f\# \cong 28$ , which may not be possible with standard imaging optics. It also follows from (3.70) that the speckles tend to get very large when  $M > 1$ , even for low  $f\#$  [Løk97, Aebi97]. This is the reason why SPS is applicable at no expense in microscopic ESPI [ElJa99]: the speckles are large enough in any case.

### 3.4.4 Spatial phase shifting on speckle fields

We have seen in Fig. 3.21 and Fig. 3.22 that the positive and negative interference bands overlap exactly in the spatial frequency plane when the source point of the reference wave coincides with the centre of the aperture. As the origin of the reference wave is laterally displaced, the overlap of the interference spectra gets smaller; ideally they can be fully separated in the frequency plane, as shown in Fig. 3.29 for two different settings of phase shift and speckle size. In the Fourier formalism, the carrier frequency manifests itself as a constant phase factor, which shifts the interference spectra by  $\pm v_c$ , with  $v_c$  being the spatial carrier frequency, and thus turns them into the so-called signal sidebands. We defer a more detailed discussion to Chapter 6.5.

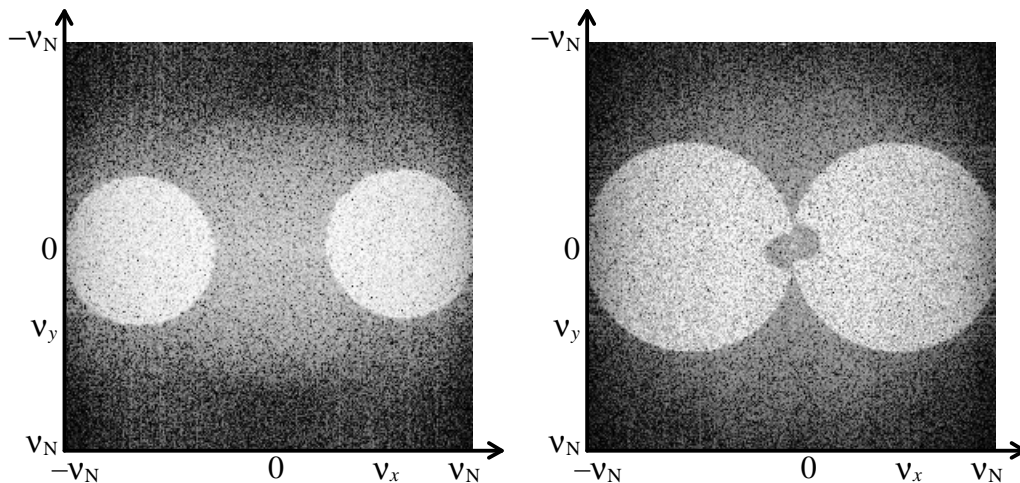


Fig. 3.29: Power spectra (log scale) of speckle interferograms with carrier frequency; left:  $\alpha_x=120^\circ/\text{column}$  ( $v_{c,x}=1/(3 d_p)$ ),  $d_s=3.5 d_p$ ; right:  $\alpha_x=90^\circ/\text{column}$  ( $v_{c,x}=1/(4 d_p)$ ),  $d_s=2.5 d_p$ . To allow for sufficient  $\Delta x$  to obtain  $\alpha_x=120^\circ/\text{column}$ , the fibre end is in a slit beside the aperture (cf. Fig. 5.1); to the right,  $\Delta x \cong D/2$ , and the fibre guide obscures part of the aperture. The contrast of the images has been enhanced to make the speckle halo visible.

The width of the side bands in an interferogram's power spectrum indicates the range of speckle phase gradients that distort the carrier fringes. As already hinted in 2.2.3.2, these distortions are equivalent to local miscalibrations of the phase shift, which makes great demands on the miscalibration tolerance of the phase-reconstruction formula. Also, its spectral response should utilise as much of the signal as possible; but as we have seen in 3.2.2, neither is easy to be had.

Complete separation of the interference bands is desirable because then all frequency components of the signal will be unambiguous. If  $\alpha_x$  is to have the same sign throughout the interferogram, one has to demand that the positive/negative signal frequencies occupy no more than the positive/negative half-plane,  $(v_{x+}, v_y)$  and  $(v_{x-}, v_y)$ , in the frequency spectrum. If these boundaries are crossed, the signal bands will overlap around  $v_x = 0$ , or with aliasing (see below) around  $v_x = \pm v_N$ , or both. We will consider examples of such power spectra in Chapter 5.5.3.

However, it is possible to permit sidebands larger than in Fig. 3.29 on the right and still avoid their mixing when we record information in the  $v_y$  co-ordinates as well and thus truly utilise the 2-D nature of the measurement. Depending on the speckle size and shape, there may then be various solutions to



arrange the signal bands advantageously in the spatial frequency plane. An example of how to obtain very large, "clean" (i.e. non-overlapping) sidebands will be given in Chapter 6.5.

The speckle size is determined from power spectra with a spatial phase shift by

$$d_s = \frac{1.22}{|v_+| - |v_-|} = \frac{0.61}{|v_c| - |v_-|}, \quad (3.71)$$

where  $|v_+|$  is the largest and  $|v_-|$  the smallest spatial frequency of a sideband and  $|v_c| = (|v_+| + |v_-|)/2$ . This of course needs to be modified when  $|v_+| > |v_N|$ : due to aliasing,  $\pm(v_N + v_a)$ , where subscript  $a$  denotes the aliased contributions above  $v_N$ , will appear in the Fourier plane at  $\mp(v_N - v_a)$ . To find the minimum permissible speckle size when  $|v_c|$  is given and no aliasing is to occur, we find

$$|v_N| \leq |v_c| + \frac{0.61}{d_s}; \quad (3.72)$$

considering the examples of Fig. 3.29, we have  $v_c = 1/(3 d_p)$  for  $\alpha_x = 120^\circ/\text{column}$ ; therefore,  $0.61/d_s \leq 1/(6 d_p)$ , which gives the condition that  $d_s \geq 3.66 d_p$ . Similarly, for  $v_c = 1/(2 d_p)$ ,  $d_s \geq 2.44 d_p$ .

For real sensors, the merely geometrical notion of  $v_c$  is a more or less accurate approximation: the higher spatial frequencies will usually be attenuated by the falling pixel MTF and the read-out electronics. This is not visible in Fig. 3.29 due to the logarithmic display; examples may be found in Fig. 3.31 and Fig. 3.34. This "low-pass" behaviour shifts the actual  $\langle v_c \rangle$ , or the "centre of gravity" of the sidebands' detected power, below their geometrical centre,  $v_{c,geom}$ . This raises the question whether an advantage can be gained by calibrating the phase shift on  $\langle v_c \rangle$ , which minimises the actual phase-shift deviations. However we retain the geometrical definition for three reasons: (i) With respect to the high spatial frequencies, it is indispensable to operate the camera with its pixel clock activated. Unfortunately, this damps  $v_x$  much more strongly than  $v_y$  (for the camera used, the pixels are read out in  $x$  direction at a rate of 20 MHz as independent video lines, whose frequency is only 15.625 kHz), which would greatly complicate the treatment of composite  $x$ - $y$ -phase shifts if we used  $\langle v_{c,x} \rangle$  and  $\langle v_{c,y} \rangle$  for calibration. (ii) Shifting a sideband outward, until the measured  $\langle v_{c,x} \rangle$  reaches its nominal value, is a waste of signal energy, because more and more of the sideband then comes to lie in the low-MTF regions of the frequency plane. (iii) The problem affects the methods for  $v_{c,x} = 1/(3 d_p)$  more than those with  $v_{c,x} = 1/(4 d_p)$ ; but we have seen from Fig. 3.13 and Fig. 3.18 that phase-shifting errors are less severe for  $v_x < 1/(3 d_p)$ , so that one may even obtain a slightly increased performance when  $\langle v_{c,x} \rangle < 1/(3 d_p)$ .

Despite these considerations, an overlap of the sidebands at the edges or in the centre of the frequency plane may be permissible and even advisable from the standpoint of light economy (remember that this is associated with smaller speckles and larger apertures). This need not upset the phase calculation: as seen before, any phase-extraction formula has its characteristic frequency response and will therefore select only a part of the interferogram's spatial frequency content anyway. One could therefore say that phase maps from SPS are being smoothed intrinsically by convolution with the phase-calculation pixel cluster. Hence, the spatial resolution of SPS is not governed by the speckle size alone.

### 3.4.5 Spectral side-effects of spatial phase calculation

As mentioned above, the findings of 3.2.2 require some experimental inspection because they were derived, so to speak, in the absence of speckle. In particular, the spatial phase calculation in SPS is influenced by the spatial correlation of the pixels selected for processing, as demonstrated in Fig. 3.30 for intensity sampling by (3.18) and (3.19), respectively.

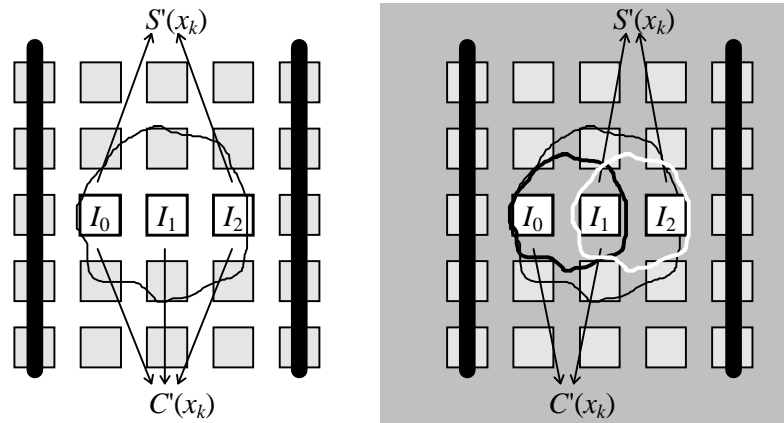


Fig. 3.30: Processing of intensity samples by (3.18) (left) and (3.19) (right), where the smaller outlines in white and black indicate the smaller coherence areas required for  $S'(x_k)$  and  $C'(x_k)$  alone.

In (3.18), the first and last intensity sample are used for  $S'(x_k)$  and all three samples for  $C'(x_k)$ ; the terms are balanced with respect to the central pixel, being the target pixel of both calculations. In (3.19), both  $S'(x_k)$  and  $C'(x_k)$  are constructed from only two consecutive samples; hence they make lower demands on the spatial coherence of the pixels. Of course, the complete sampling window is still three pixels wide, and  $S'(x_k)$  and  $C'(x_k)$  are associated with slightly different portions of the speckle field, so that their spatial correlation may suffer. The same line of argument applies to all other phase-shifting formulae, where different  $a_n$  and/or  $b_n$  are large, small, or vanish, in different representations of the formulae.

To find out the significance of this consideration, we study  $\tilde{S}(v_x, v_y)$  and  $\tilde{C}(v_x, v_y)$  experimentally. First, we generate two separate arrays  $I(x,y) \otimes S_x(n)$  and  $I(x,y) \otimes C_x(n)$ , this is, we use (3.68) to process 2-D images with a 1-D phase shift. The results, when visualised as images, should yield two fringe patterns that look very much like the speckle interferogram, but have a phase lag of  $90^\circ$  and hence deserve the names of "sine" and "cosine" image. This processing method has been used in [Sin94] in the context of phase demodulation.

The power spectra of the "sine" and "cosine" images,  $|\tilde{I}(v_x, v_y) \cdot \tilde{S}(v_x)|^2$  and  $|\tilde{I}(v_x, v_y) \cdot \tilde{C}(v_x)|^2$ , can be compared with that of the original interferogram,  $|\tilde{I}(v_x, v_y)|^2$ , to reveal the changes\*. This yields

---

\* Realising that the phase-shift is one-dimensional, it would suffice to investigate the  $v_x$  only; but since we will be concerned with full 2-D information in Chapter 6.3, we include the  $v_y$  here already, bearing in mind that they contribute little information now.

information about the actual manipulation of the interferogram's frequency content by the phase calculation.

The phase lag between the "sine" and "cosine" fringe patterns may be estimated when we determine their phases as if they were interferograms and then subtract these phase maps as if we wanted to measure a deformation. The "double" phase determination of course leads to a circular argument, which we must avoid by using the Fourier-transform method (cf. Chapter 6.5).

To evaluate the spectral transfer characteristics of phase-shifting formulae, we could simply choose white noise, e.g. a random distribution of grey values, as a dummy interferogram for input; but since our objective here is an experimental check of the findings in 3.2.2, we use actual interferograms. Starting with  $\alpha=90^\circ$ , we choose the interferogram with the spectrum of Fig. 3.29 (right side) as input, which indeed accounts for the whole range of interest,  $v_x=0$  up to  $v_x=v_N$ . The power spectra that we compare are scaled linearly this time to fit the expected deviations; the low-frequency part of the spectra then has to be masked out. The first example is the phase calculation by (3.18), whose outputs are compiled in Fig. 3.31. The images of the power spectra have been spatially smoothed to make differences more easily discernible.

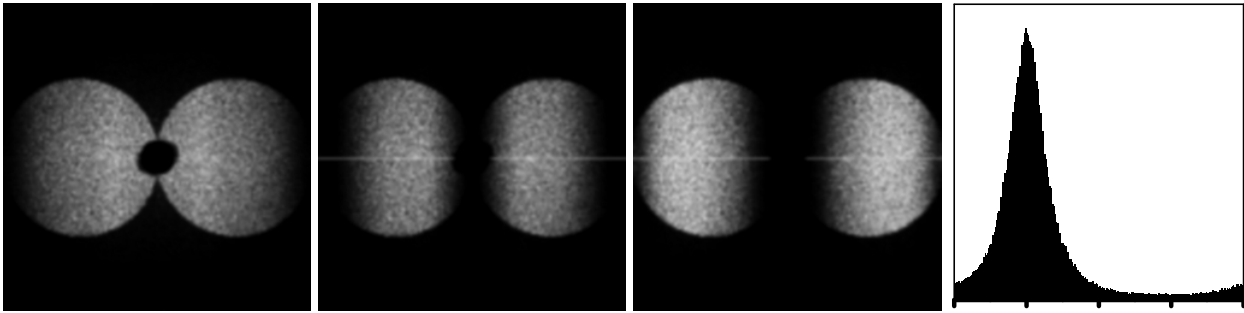


Fig. 3.31: From left to right:  $|\tilde{I}(v_x, v_y)|^2$ ;  $|\tilde{I}(v_x, v_y) \cdot \tilde{S}(v_x)|^2$  of (3.18);  $|\tilde{I}(v_x, v_y) \cdot \tilde{C}(v_x)|^2$  of (3.18); pixel histogram of phase lag between  $I(x,y) \otimes S_x(n)$  and  $I(x,y) \otimes C_x(n)$  of (3.18); the range of the abscissa is  $0-2\pi$ . The spatial frequency axes of the power spectra are as in Fig. 3.29.

As discussed in 3.4.4, the measured power spectrum shows significant attenuation of high  $v_x$  already in the interferogram, which is now clearly visible on the linear scale. This appears to be quite common with pixel-clocked CCD cameras, cf. the power spectra reproduced in [Sal96, Ped97a,b]; hence, when looking at  $|\tilde{I}(v_x, v_y) \cdot \tilde{S}(v_x)|^2$  and  $|\tilde{I}(v_x, v_y) \cdot \tilde{C}(v_x)|^2$ , we must bear in mind that even a maximal response at  $v_N$  will fail to produce a high output when the corresponding frequencies are already weak in the input data; but differences of the two spectra will remain discernible. Comparing now the spectra of  $I(x,y)$  modified by  $S_x(n)$  and  $C_x(n)$  with what Fig. 3.9 predicts, we see that indeed  $|\tilde{I}(v_x, v_y) \cdot \tilde{S}(v_x)|^2$  peaks at  $v_x=v_N/2$ , while the maximum of  $|\tilde{I}(v_x, v_y) \cdot \tilde{C}(v_x)|^2$  is shifted towards  $v_N$ . Hence, the values  $I(x,y) \otimes S_x(n)$  and  $I(x,y) \otimes C_x(n)$  will not generally represent  $\sin \varphi_O(x,y)$  and  $\cos \varphi_O(x,y)$ . This affects the quadrature properties

predicted by Fig. 3.9, as the histogram of the phase lag demonstrates: the peak is centred at  $89.6^\circ$  but is broadened considerably ( $\sigma \cong 19^\circ$ ).

On the other hand, we can expect from Fig. 3.10 that (3.19) will filter the interferogram's frequencies equally by  $\tilde{S}(v_x)$  and  $\tilde{C}(v_x)$ , and indeed this is what we find in Fig. 3.32, with the same input interferogram as above.

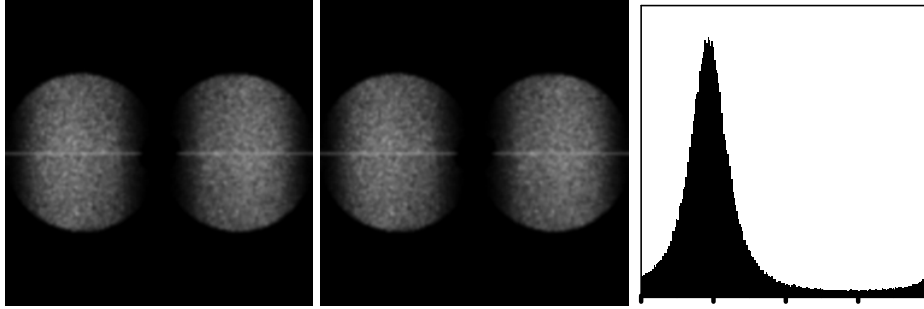


Fig. 3.32: From left to right:  $|\tilde{I}(v_x, v_y) \cdot \tilde{S}(v_x)|^2$  of (3.19);  $|\tilde{I}(v_x, v_y) \cdot \tilde{C}(v_x)|^2$  of (3.19); pixel histogram of phase lag between  $I(x,y) \otimes S_x(n)$  and  $I(x,y) \otimes C_x(n)$  of (3.19).

In contrast to what Fig. 3.10 suggests, the mean phase lag shows reasonable stability: the peak is at  $83.4^\circ$ . Thanks to the matching responses of  $S_x(n)$  and  $C_x(n)$ , the peak is somewhat narrower than in Fig. 3.31 ( $\sigma \cong 17.3^\circ$ ). From these findings, we may expect that both formulae should be almost equally suitable to evaluate SPS interferograms with  $v_{0x} = 1/(4 d_p)$ .

To verify this, we consider the Fourier spectra  $\tilde{I}(v_x, v_y) \cdot \tilde{S}(v_x)$  and  $\tilde{I}(v_x, v_y) \cdot \tilde{C}(v_x)$ , from which we can obtain  $b_{sc}(v_x, v_y)$  experimentally by (cf. 3.2.1.3)

$$\begin{aligned} b_{sc}(v_x, v_y) &= \arg\left(\tilde{I}(v_x, v_y) \cdot \tilde{C}(v_x) + \tilde{I}(v_x, v_y) \cdot \tilde{S}(v_x)\right) - \arg\left(\tilde{I}(v_x, v_y) \cdot \tilde{C}(v_x)\right) \\ &= \arg\left(1 + \frac{\tilde{S}(v_x)}{\tilde{C}(v_x)}\right), \end{aligned} \quad (3.73)$$

which is again  $-45^\circ$  when (3.41) is valid. This gives us an idea of how well the "sine" and "cosine" images correspond to their theoretical descriptions. Applying the above calculations to these images, we eventually obtain a phasor map in the frequency plane that should range from  $-\pi/2$  to  $\pi/2$ . As usual in DFT, we can use the equivalence  $[-v_N, 0] \Leftrightarrow [v_N, 2v_N]$  to come from the image to our familiar plot of  $b_{sc}(v_x)$ . A first example of this is presented in Fig. 3.33; the power spectrum of the input interferogram is again that of Fig. 3.29.

On the left, we find the distribution of  $b_{sc}(v_x, v_y)$  for (3.18); the one for (3.19) would be indistinguishable from it in this size, which confirms that the performance of (3.18) and (3.19) is almost equal despite the differences explained above. It is only at first glance surprising that the signal sidebands are almost invisible in  $b_{sc}(v_x, v_y)$ : the phase calculation of (3.73) does not distinguish between signal and noise

frequencies. The difference is solely that those regions of the frequency plane where there is no signal, and hence relatively little spectral power, are quite a bit more noisy.

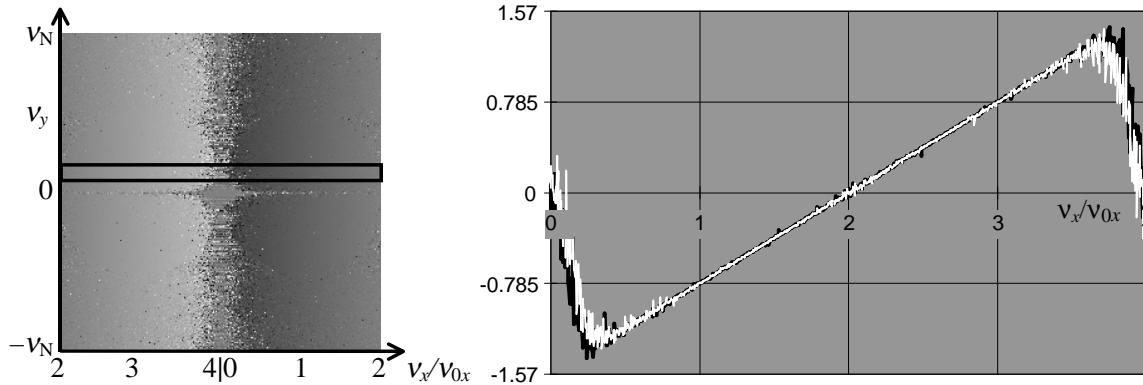


Fig. 3.33: Left:  $bsc(v_x, v_y)$  for (3.18) as calculated from (3.73), with  $0 \triangleq$  black and  $2\pi \triangleq$  white; note that  $v_x=v_y=0$  is in the centre of the image. Right:  $bsc(v_x)$  for (3.18) (black) and (3.19) (white); average of 50 rows from the small black frame on the left.

To the right, the plot of  $bsc(v_x)$  as output by (3.18) (black) and (3.19) (white) does indeed show that both compare quite well with the corresponding graph in Fig. 3.13. The high noise around  $v_x=0$  and  $v_x=2v_N$  reflects the suppression of  $I_b$ , i.e. the fact that  $\tilde{S}(0) = \tilde{C}(0) = 0$ . It is interesting to note that, in agreement with the larger absolute filter output of (3.18), the susceptibility to noise is indeed somewhat lower than for (3.19); but this affects a frequency range that produces large errors anyway, so that the difference in performance will be very small. For this case of  $\alpha=90^\circ$ , we therefore conclude that the utilisation of different sets of pixels for different representations of the 3-sample  $90^\circ$  formula does not invalidate the theoretical considerations in 3.2.2.3.

For  $\alpha=120^\circ$ , we use an interferogram with a power spectrum as in Fig. 3.29 on the left; this time, the signal sidebands cover a smaller part of the frequency plane. When this interferogram is processed with (3.17), we can expect a qualitative behaviour resembling that in Fig. 3.31 because the sampling formulae are both derived from (3.15). As to be seen from Fig. 3.34, this is indeed the case; again the high-frequency preference of  $\tilde{C}(v_x)$  is clearly visible. The distribution of the phase lag has a mean of  $89.6^\circ$  and a standard deviation of  $22.0^\circ$ .

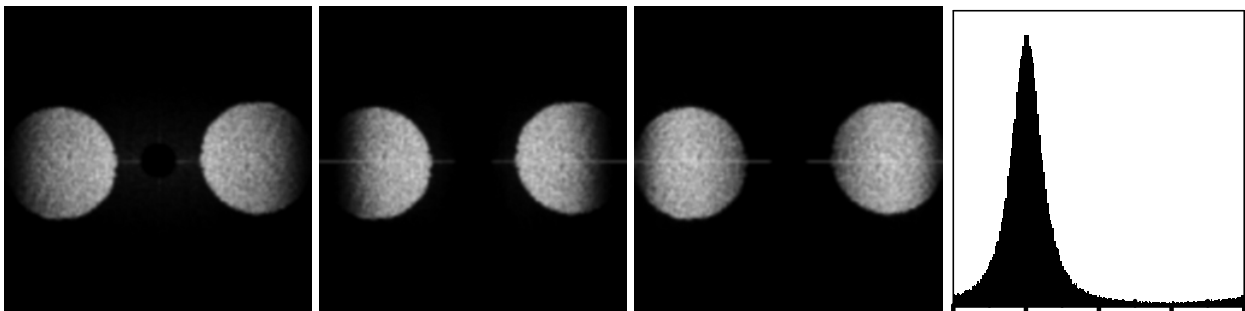


Fig. 3.34: From left to right:  $|\tilde{I}(v_x, v_y)|^2$ ;  $|\tilde{I}(v_x, v_y) \cdot \tilde{S}(v_x)|^2$  of (3.17);  $|\tilde{I}(v_x, v_y) \cdot \tilde{C}(v_x)|^2$  of (3.17); pixel histogram of phase lag between  $I(x,y) \otimes S_x(n)$  and  $I(x,y) \otimes C_x(n)$  of (3.17).

Investigating (3.50) with its equal spectral responses of  $S_x(n)$  and  $C_x(n)$ , the output spectra from processing the same interferogram as above are indeed equal, as to be compared in Fig. 3.35; but this time the phase quadrature is disturbed (centre at  $104.9^\circ$ , and  $\sigma=26.4^\circ$ ).

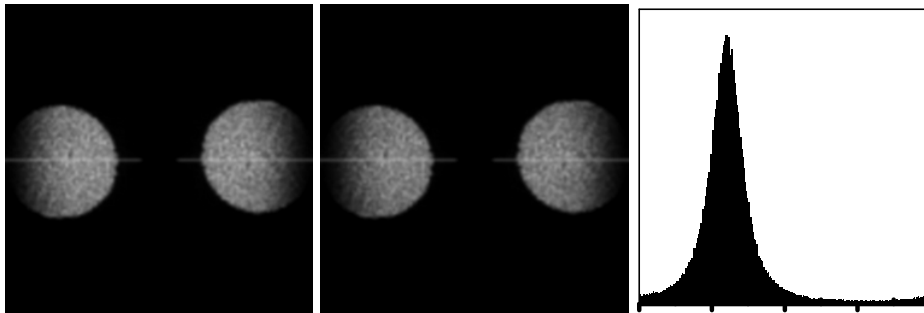


Fig. 3.35: From left to right:  $|\tilde{I}(v_x, v_y) \cdot \tilde{S}(v_x)|^2$  of (3.50);  $|\tilde{I}(v_x, v_y) \cdot \tilde{C}(v_x)|^2$  of (3.50); pixel histogram of phase lag between  $I(x,y) \otimes S_x(n)$  and  $I(x,y) \otimes C_x(n)$  of (3.50).

From Fig. 3.13, we should expect equal performance from (3.17) and (3.50), but the quadrature deficiency of (3.50) raises doubts in this respect. Therefore we use the help of  $bsc(v_x)$  again; Fig. 3.36 gives a comparison of the two methods.

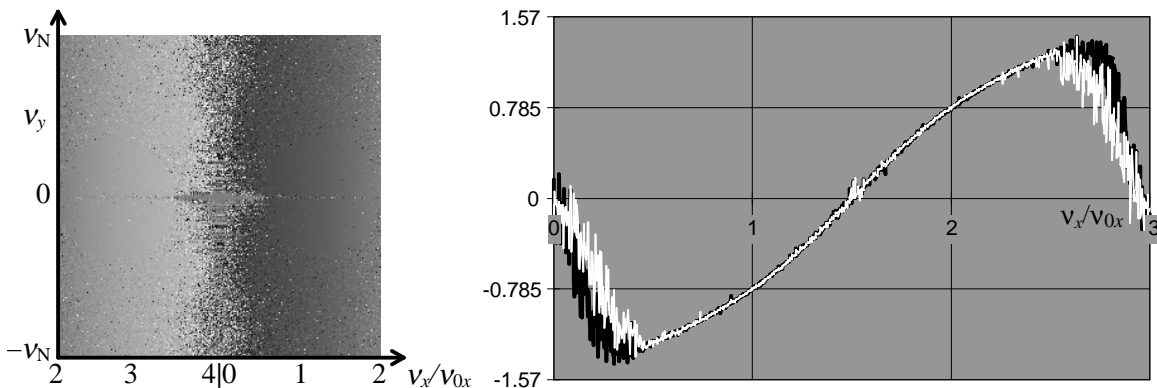


Fig. 3.36: Left:  $bsc(v_x, v_y)$  for (3.17); right:  $bsc(v_x)$  for (3.17) (black) and (3.50) (white); average calculated from same image region as in Fig. 3.33.

Again, we find good agreement with the theoretical curve of Fig. 3.13, except for the slightly higher noise of (3.50) as we leave the signal sideband. However, this difference does not lead to a detectable performance loss, since there is comparatively little power outside the sidebands, which in addition is greatly attenuated by the filter functions.

Since (3.17) is a DFT formula, it was possible to check the performance of 120 different  $120^\circ$  formulae, where the phase offsets of the sine and cosine weighting functions were varied in  $3^\circ$  steps, with coefficients according to (3.14); two out of these are (3.17) and (3.50). A pair of interferograms from an object tilt was processed to a sawtooth image with the 120 different formulae, and each of them was evaluated for  $\sigma_{\Delta\phi}$ ; the result was that indeed all the formulae gave performances equal to within 0.4%. Therefore, when  $\alpha=120^\circ$ , it is best to choose the representation with the simplest coefficients; and

although such a test is not possible with the three-step  $90^\circ$  formulae, the findings thus far strongly indicate a similar behaviour.

In the error-compensating formula (3.56),  $S(n)$  requires only two samples but  $C(n)$  uses four, whilst in (3.57), both terms include four samples; but also for these methods, the performances are virtually identical. Therefore we will not compare these in detail, but we do investigate the performance of (3.56) against that of (3.58); these results are shown in Fig. 3.37.

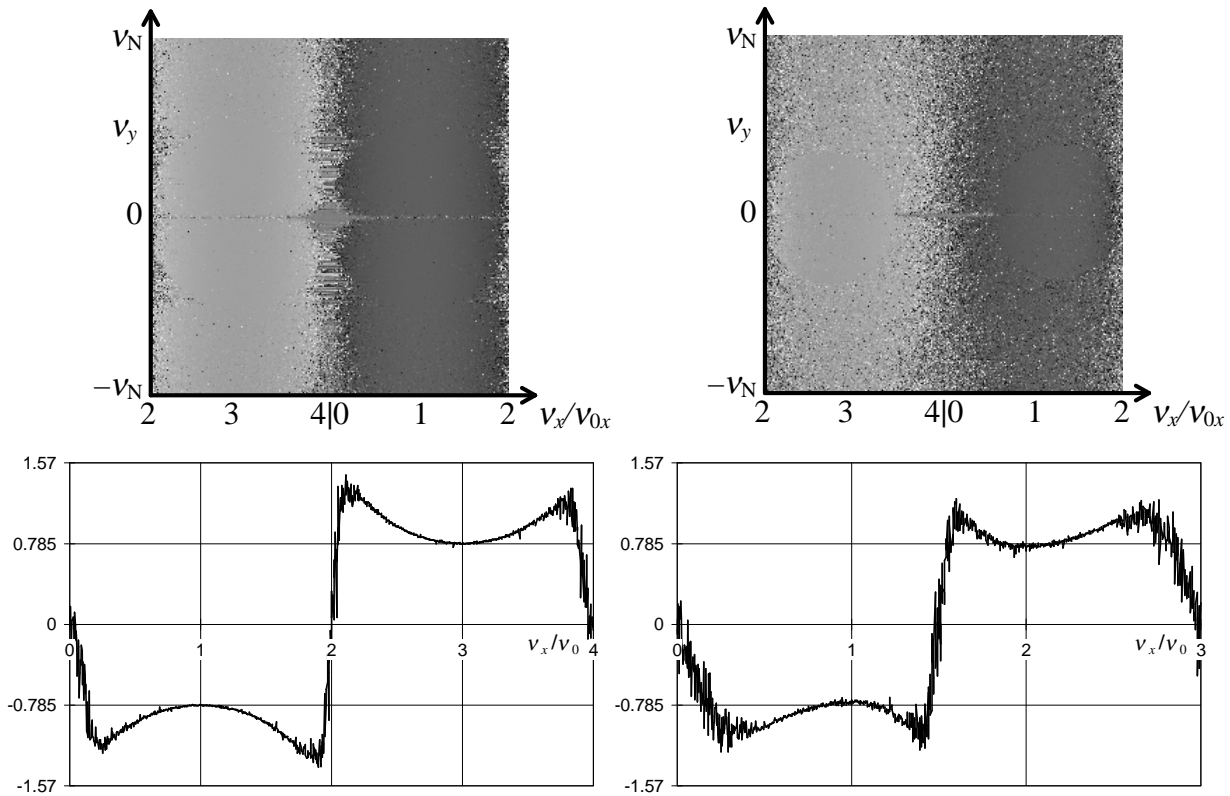


Fig. 3.37: Top row:  $bsc(v_x, v_y)$  for (3.56) (left) and (3.58) (right); bottom row:  $bsc(v_x)$  for (3.56) (left) and (3.58) (right).

From the images as well as from the plots, we can see that (3.56) operates with greater stability in the whole spatial frequency range, including the signal regions. Also for the 3-sample formulae investigated before, the tendency was recognisable that  $\alpha=90^\circ$  gives slightly safer phase determination than  $\alpha=120^\circ$ . For the reasons mentioned above in 3.2.2.4, this difference is even more pronounced when we attempt to correct phase-shifting errors. After our numerous considerations of spatial frequencies, the reasons for this are clear: setting  $v_{c,geom}$  to  $v_N/2$  assures best utilisation of the frequency plane and best suppression of detuning errors.

Our scrutiny of the effect of different sampling pixel clusters yields the interesting result that the representation of the used formula can be chosen at convenience. This facilitates a simple general strategy for placing the signal sidebands optimally: given the invariant course of  $bsc(v_x)$ , or  $bsc(v_x, v_y)$  for composite  $x$ - and  $y$ -phase shift, one can refer to that representation of the phase-extraction formula which gives equal frequency responses of  $S(n)$  and  $C(n)$ , and maximise the signal utilisation (in which the system MTF will also play a role) while minimising the phase-shifting errors. Once this is done, one can

go back to a simple representation of the formula, which, as we have seen, will not affect its performance. For the case of  $d_s=3 d_p$ , it was indeed found that the best  $v_{c,geom}$  for, say, (3.19) was  $\alpha \cong 75^\circ/\text{sample}$ , and for, e.g., (3.17), the minimal error occurred around  $\alpha \cong 100^\circ/\text{sample}$ . But the difference in performance was only 2-3%; and since also these values may change with the sensor and electronics used, we do not further pursue this detail.

### 3.4.6 Distorted phase distributions due to miscalibrated phase shift

None of the formulae investigated, including the error-compensating ones, will perfectly suppress the oscillating phase errors sketched in Fig. 3.14. This has important consequences for the statistics of the measured phases. In the presence of a systematic phase-shift deviation, the uniform distribution of the speckle phases (cf. (2.6)) will be modified by the faulty measurements, as pointed out in [Kad91]. The arrows in Fig. 3.14 indicate the direction to which the true  $\varphi_0$  values are biased by measuring  $\varphi_0 + \delta\varphi_0$  under excessive phase shift: phase readings of  $0 < \varphi_0 < \pi/2$  are increased by  $\delta\varphi_0$ , and those of  $\pi/2 < \varphi_0 < \pi$  are decreased. The same thing happens between  $\pi$  and  $2\pi$ , so that the measured values will be more or less concentrated at  $\cong \pi/2$  and  $\cong 3\pi/2$ . Hence, the histograms of measured speckle phases will show characteristic fluctuations. For phase shifts that are too small,  $\delta\varphi_0$  changes its sign, whereby phase measurements cumulate at  $\cong 0$  and  $\cong \pi$ . This is demonstrated by Fig. 3.38, where histograms of measured speckle phases are compared for different phase shifts.

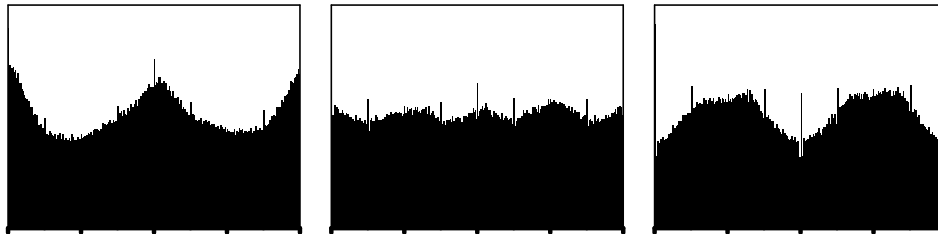


Fig. 3.38: Influence of real phase shift on measured speckle phase pdf when reconstructed by (3.19) ( $\alpha_{ideal}=90^\circ/\text{sample}$ ) with  $d_s=3 d_p$ . Left,  $\langle \alpha_{real} \rangle < 90^\circ$ ; centre,  $\langle \alpha_{real} \rangle = 90^\circ$ , right,  $\langle \alpha_{real} \rangle > 90^\circ$ . Abscissae range from 0 to  $2\pi$ ; ordinates give relative frequencies.

This effect has been used in [Kad91, Bot97, Dob97] to calibrate the phase shift. In SPS however, this calibration is different from the Fourier method because it optimises the centre of gravity of the sideband instead of its geometrical centre. As explained above, this involves the sensor MTF and the transfer spectrum of the phase-extraction formula. Therefore  $\alpha_{geom}$  will rarely coincide with  $\langle \alpha \rangle$ ; I judge the calibration on  $\alpha_{geom}$  to be more reliable, accurate and advisable from the standpoint of signal utilisation, and in what follows,  $\alpha$  will denote  $\alpha_{geom}$ .

Moreover, Fig. 3.38 teaches us that even with the correct  $\langle \alpha \rangle$ , the deviations will not vanish. This is of course owing to the speckle phase gradients that inevitably cause local detuning; the smaller the speckles, the larger the deviations will get. This is partly due to increasing phase gradients on the camera pixels as the speckles get smaller, and for smaller speckles, the  $I_{k+n}$  will not even lie within one statistical coherence area anymore. Hence, we have an oscillating measurement error regardless of the adjusted phase shift. Since the phase offset  $k \cdot \alpha$  in a spatially phase-shifted interferogram varies by  $\alpha$  from sample to sample, also  $\delta\varphi_0$  will vary cyclically. This effect has been given the name "high-frequency fringe



error"; in classical interferometry, it causes a fine ripple in the measured phase map [Cre96]. In speckle interferometry, where sawtooth images  $\Delta\varphi(x,y)$  are generated by subtracting speckle phases  $\varphi_{O,i}(x,y)$  and  $\varphi_{O,f}(x,y)$ ,  $\delta\varphi_0$  alternately cancels and doubles, depending on  $\Delta\varphi(x,y)$ . Independent of the miscalibration's sign,  $\delta(\varphi_0) = \delta(\varphi_0 + \pi) \cong -\delta(\varphi_0 + \pi/2)$  (cf. Fig. 3.14); therefore  $\delta\varphi_0$  cancels when  $\Delta\varphi(x,y)$  is 0 or  $\pi$ , and doubles in between. This is in contrast to (3.55), where  $\delta\varphi_0$  is averaged out by addition of two sampling sequences offset by  $\pi/2$ ; the  $\Delta\varphi(x,y)$  maps however are formed by subtraction. The effect of this can be seen in Fig. 3.39 for  $d_s=3 d_p$ : the phase-measurement error depends on the phase to be found. The error images on the right are the absolute differences between the actual phase maps and their least-squares-fitted noise-free counterparts (see Chapter 4.2). The inserted white error curves allow a quantitative comparison of  $\delta\varphi_0$  vs.  $\Delta\varphi(x,y)$ .

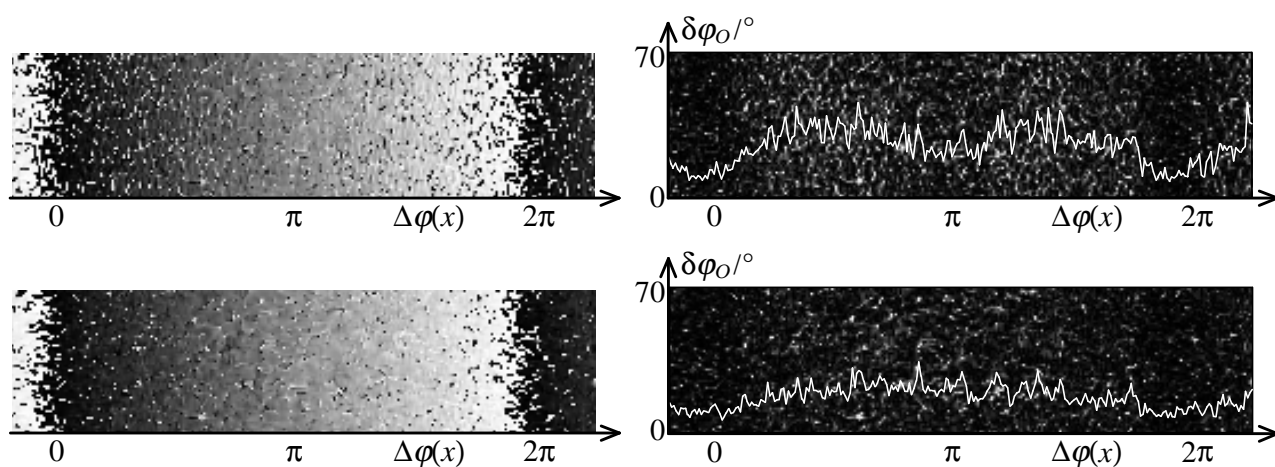


Fig. 3.39: Fringe profiles (left) and corresponding  $\delta\varphi_0$  (right) from a displacement measurement with  $\alpha=90^\circ/\text{column}$  and various phase-extraction formulae: top, (3.19); bottom, (3.57). All images come from the same region of interest and have  $256 \times 64$  pixels; the error curves on the right are vertically averaged.

When the phase is calculated by (3.19) (upper row), a significant ripple is produced around  $\Delta\varphi(x)=\pi/2$  and  $\Delta\varphi(x)=3\pi/2$  that also leads to a higher average error. In the lower row, the error compensation of (3.57) does not remove the ripple completely, but is good enough to suppress it to approximately the level of the speckle noise: almost no high-frequency oscillations can be seen in the sawtooth image. The remaining profile of  $\delta\varphi_0$  is still periodical but the frequency is halved to  $1/(2\pi)$ . The importance of phase-shift deviations and their correction is clearly emphasised by Fig. 3.39.

Moreover, we observe that in both of the error graphs,  $\delta\varphi_0$  is higher for  $\Delta\varphi(x)=\pi$  than for  $\Delta\varphi(x)=0$ . This reminds of correlation fringes, which also have low noise for  $\Delta\varphi=0$ , and also the reason is similar: a phase difference of zero is always measured reliably because both interferograms simply look the same in this case. It is then unimportant what formula is used: the error minima are almost identical in both  $\delta\varphi_0$  images. At  $\Delta\varphi=\pi$ , the carrier fringe pattern is "inverted" from the first to the second interferogram, so that phase-calculation errors with a period of  $2\pi$  will change their sign and introduce the largest deviations upon subtraction of the speckle phase maps.

It is now interesting to see what fringe profiles we can obtain with our  $120^\circ$  formulae. The error suppression by (3.58) is theoretically somewhat inferior to (3.57); the ratio of remaining errors of the

methods should be  $4/3$  [Lar99]. For Fig. 3.40, a pair of interferograms with  $d_s=3 d_p$  and  $\alpha=120^\circ$  was processed with various corresponding formulae.

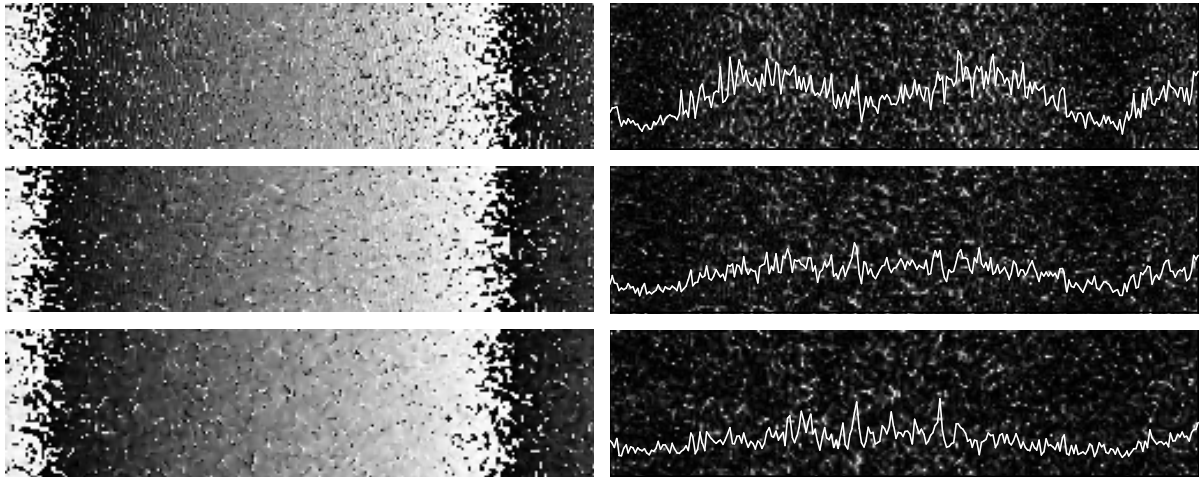


Fig. 3.40: Fringe profiles (left) and corresponding phase errors (right) from a displacement measurement with  $\alpha=120^\circ$ /column and various phase-extraction methods: top, (3.17); middle, (3.58); bottom, Fourier method. Scales are as in Fig. 3.39.

The error profile produced by (3.17) is very similar to that from (3.19) (Fig. 3.39, upper row) both qualitatively and quantitatively. From the graphs presented here, it is hard to tell which is better, so that we defer the answer to Chapters 5 and 5. As could be presumed, (3.58) leaves a faint ripple that is only just discernible in Fig. 3.40; in this case, only the Fourier transform approach (cf. Chapter 6.5) is capable of suppressing the oscillations below the speckle noise.

There is yet another consequence of this phase-dependent error: in a similar way as above for miscalibrated  $\alpha$ , the measurements of  $\Delta\phi$  tend to concentrate at  $0$  and  $\pi$ : they "leak" most strongly from  $\Delta\phi = \pi/2$  and  $3\pi/2$ , which are therefore the least frequent values in the sawtooth image, but also from all  $\Delta\phi$  other than  $0$  or  $\pi$ . When detuning correction is present, the relative frequency of  $\Delta\phi=0$  will increase at the expense of  $\Delta\phi = \pi$ , where the largest errors occur and which is consequently the rarest entry in the map of  $\Delta\phi(x,y)$ . The relative frequencies of  $\Delta\phi$  values in our full-size ( $1024 \times 768$  pixels) test sawtooth images, not just the portions shown before, are summarised in Fig. 3.41.

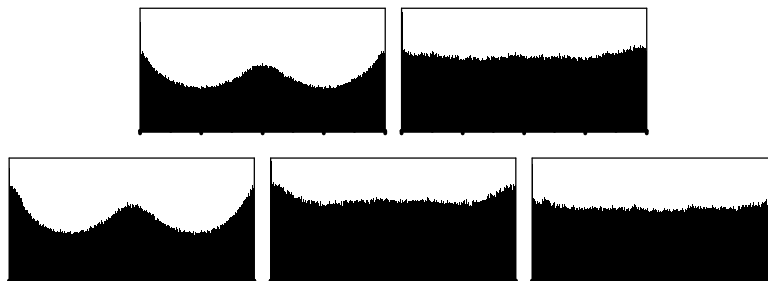


Fig. 3.41: Pixel histograms of phase values in sawtooth images calculated by various phase-sampling formulae. Upper row refers to Fig. 3.39; left: result from (3.19); right: results from (3.57). Lower row refers to Fig. 3.40; left, (3.17); centre, (3.58); right, Fourier method. The abscissae range from  $0$  to  $2\pi$ ; the ordinates give relative frequencies.

Since the displacement's phase gradient is constant in the test images and the histograms were generated from an integer number of fringes (5.0), the true phase distribution is uniform as in Fig. 3.7; but depending on the amount and type of  $\delta\varphi_0$ , various distortions are present. For  $\alpha=90^\circ/\text{sample}$ , (3.57) (upper row, right histogram) yields the most realistic phase statistics with only a small preference for  $\Delta\varphi \cong 0$ . In the centre of the lower row of Fig. 3.41, one can recognise the residual ripple in the phase map from (3.58) by a small increase of the distribution at  $\Delta\varphi \cong \pi$ ; generally speaking, the amount of detuning sensitivity may be seen from the height of that peak. Finally, the Fourier method (lower row, right histogram) suppresses this deviation as well and leads to almost uniform phase statistics.

While these effects exert a smaller influence on the measuring accuracy than the histograms may suggest, they are characteristic of SPS. As seen above in Fig. 3.7, TPS yields perfectly uniform distributions when the phase shift is well calibrated; but in SPS the speckle phase gradients always cause systematic distortions. These even allow one to tell from the histogram of a sawtooth image whether it is from TPS or SPS, and in the latter case, what type of phase-extraction formula was used.



## 4 Quantification of displacement-measurement errors

Since a major part of this work deals with the "quality" of displacement phase maps, it is vital to have a numerical figure of merit at hand that allows to compare measurements accurately enough. While the human brain's image processing allows to tell a "bad" sawtooth image  $\Delta\varphi(x,y)$  from a "good" one at just a glance, it runs into problems when small quality differences have to be found or even quantified. Therefore, we must find a reliable and standardised method to determine noise levels numerically.

The general problem when determining the noise in measured displacement phase maps  $\Delta\varphi_{meas}(x,y)$  is: what does the noise-free reference phase map  $\Delta\varphi_{ref}(x,y)$  look like, and how can one obtain it? In practice, unless excellently calibrated displacements are available, one has to fall back upon the actual measurement. One common approach is to generate  $\Delta\varphi_{ref}(x,y)$  by spatially smoothing the noisy phase map  $\Delta\varphi_{meas}(x,y)$  as much as possible and to obtain an average displacement phase-measurement error  $\langle\delta\varphi\rangle=\langle|\Delta\varphi_{meas}(x,y)-\Delta\varphi_{ref}(x,y)|\rangle$  or a so-called root-mean-square (r.m.s.) displacement phase-measurement error  $\sigma_{\Delta\varphi}=\sqrt{\langle(\Delta\varphi_{meas}(x,y)-\Delta\varphi_{ref}(x,y))^2\rangle}$  from a comparison of the "raw" and the smoothed data. Such approaches are widely used and give reasonable results, but the best way to reduce the noise in a sawtooth image will most likely depend on the input image; this is, the smoothing filter's parameters and/or the number of iterations remain a matter of user judgement. Since we intend to compare TPS and SPS, and to find improved phase-extraction methods for SPS later on, we need comparable performance data throughout a very wide range of fringe densities and noise levels, so that smoothing images "by hand" does not seem to be universal and accurate enough. Therefore, to generalise the process of finding the best-matching  $\Delta\varphi_{ref}(x,y)$ , I felt the need to develop an almost fully automatic procedure.

### 4.1 Previous methods

We start with a brief survey of some existing noise reduction methods; while their objective has seldom been an accurate quantification of experimental errors, their purpose is certainly to improve the reliability of experimental data, which happens by approximating  $\Delta\varphi_{ref}(x,y)$ , the true phase map, as closely as possible. Although we are aiming at a method to evaluate sawtooth images, we also include some achievements of noise handling in secondary interferograms. We will, however, put some emphasis on the processing of sawtooth images and point out specific difficulties with various filtering schemes.

#### 4.1.1 Processing of correlation fringes

There is a wealth of smoothing and filtering methods to generate clearer fringes from ESPI subtraction images that can then be used for the phase-of-difference method, or possibly for direct evaluation. It is important to realise that the design of filters for correlation fringes must take into account that the speckle noise is multiplicative in secondary interferograms. This is not a generic property of the speckle effect

[Tur82]; however when correlation fringes are formed as described in Chapter 3.1, this is valid, as can instantly be seen from (3.4) and related expressions.

The general problem is to smooth the correlation fringes as much as possible while preserving details of the image, which is a demanding task in image processing. A helpful tool to quantify speckle noise is the so-called speckle index [Cri85], here defined for a  $3 \times 3$  neighbourhood of pixel  $(k, l)$  as

$$s = \frac{1}{(N-2)^2} \sum_{k=1, l=1}^{N-1} \frac{\Delta_{kl}}{\langle I_{kl} \rangle} \quad \text{with} \quad (4.1)$$

$$\Delta_{kl} := \max(I_{k+i, l+j}) - \min(I_{k+i, l+j}), \quad \langle I_{kl} \rangle := \frac{1}{9} \sum_{i=-1}^1 \sum_{j=-1}^1 I_{k+i, l+j},$$

where  $-1 \leq i, j \leq 1$  in an image of  $N^2$  pixels, and the normalisation accounts for the exclusion of the image edges. Depending on the specific application, a larger neighbourhood ( $|i_{max}|, |j_{max}| > 1$ ) may be chosen. The quantity  $s$  can be regarded as a measure of the noise-to-signal ratio and is useful to assess the performance of specially designed filters.

When the reference data are known (typically in computer simulations), it is possible to employ a quantity called image fidelity, defined as [Dáv94]

$$F = 1 - \frac{\sum_{k=1, l=1}^N (I_{kl}^{ref} - I_{kl}^{meas})^2}{\sum_{k=1, l=1}^N (I_{kl}^{ref})^2} \quad (4.2)$$

and indicating the similarity of a real image to the ideal one; as in (4.1), the error is weighted by the bias intensity to obtain a noise-to-signal figure.

Many types of specialised routines, partly involving considerable computational or experimental effort, have been developed. These are, *inter alia*, low-pass filtering with contrast enhancement, polynomial fitting [Var82], binarising and XOR processing [Nak83], geometric filtering [Cri85], image segmentation, fringe thinning with phase interpolation [Yat82, Ost87, Eich88], variance algorithm [Cre87], averaging over different speckle pattern realisations, either in the image plane [Cre85c, Fre92] or in the Fourier-transform plane [Hun92, Hun93b], scale-space filter [Dáv96], wavelet analysis [Kau96, Ber97] and direct correlations [Schmi97].

The simple approach of discarding the high spatial frequencies of the speckles in the Fourier plane has been shown to require considerable user interaction [Ker89], unless the fringe patterns are very simple, or to blur image details, e.g. holes or edges [Dáv96]. This can be circumvented by recording the frequency content of the speckle pattern separately and dividing it out from that of the correlation fringe image [Bie89]. Equivalently, it can be subtracted on a logarithmic scale, which accounts for the multiplicative nature of the noise.

All of these methods have led to substantial improvement in the fringe evaluation while simultaneously minimising interaction and arbitrariness; but the advent of phase-shifting in ESPI has greatly superseded their application. However, phase shifting is still not fully available in double-pulse addition fringes [Kau94, Pou95], so that the need continues to analyse correlation fringes. Today there are specialised fringe-fitting procedures [Yu 98, Schmi98] that rely on *a priori* information such as the sign of deformation and the power spectra of signal and noise, which leads to results that can easily compete with the accuracy of standard phase shifting. Also, the use of Bayesian inference [Mar97, Schmi97, Lir99] has proven helpful to restore low-noise data from correlation fringes. A promising class of fringe filters is known as regularisation functionals [Ser97a, Mar97], which are essentially narrow bandpass filters that adapt automatically to the local fringe frequency and thus evade the problems associated with fixed filter sizes. While the listed methods are very powerful, their main drawback remains that they require the operator's careful choice of filter parameters to obtain the "best" results.

#### 4.1.2 Processing of sawtooth fringes

In Chapter 3.2.1, we have seen that the difference-of-phases method is more suitable for our purpose, so that we need not prepare perfect correlation fringes for the phase calculation, nor even try to obtain phase data from only one secondary interferogram. Unfortunately, the figures of merit (4.1) and (4.2), normalised by the local speckle intensity, fail in our intended application to phase maps because in  $\Delta\varphi_{meas}(x,y)$ , the information about the underlying speckle intensities is discarded.\* In what follows, we will therefore simply regard the phase noise as additive [Cap97] and investigate some standard filtering procedures for phase maps.

Generally, low-pass filtering of sawtooth images is very efficient to suppress the "salt-and-pepper" noise spikes, and consequently, even a filter size of  $3\times 3$  pixels effects a significant reduction of the residual noise. The issue of image blurring is very much the same as above, however the additional difficulty arises that the  $0\leftrightarrow 2\pi$  phase jumps or, equivalently, the  $0\leftrightarrow 255$  grey-level jumps, need to be preserved as faithfully as possible by the smoothing operation.

##### 4.1.2.1 Smoothing the arctangent

The edge-preserving property of the median filter has made it the common choice for smoothing sawtooth images for a long time. However, this type of filter does not perfectly retain the  $0\leftrightarrow 255$  jumps. If the ideal grey value for a pixel is 0 or 255, the median filter will not be able to reproduce it because it will never find values below 0 or above 255, which would be necessary if 0 or 255 were to be the median of a

---

\* However, it has been shown that the reliability of  $\Delta\varphi_{meas}(x,y)$  is proportional to  $M_{I_i}(x,y) \cdot M_{I_f}(x,y)$  [Hun97, Leh98], where  $i$  denotes the first and  $f$  the final object state; this has been used for optimised filtering [Hun97, Cog99] and could also serve as a normalisation to obtain a signal-to-noise figure for phase maps. While this way of generating  $\Delta\varphi_{ref}(x,y)$  leads to good results, it would of course not eliminate the noise.

particular pixel array. Fig. 4.1 illustrates the effect of median filtering by data from a measurement of a mere out-of-plane tilt that should give a linear phase profile.

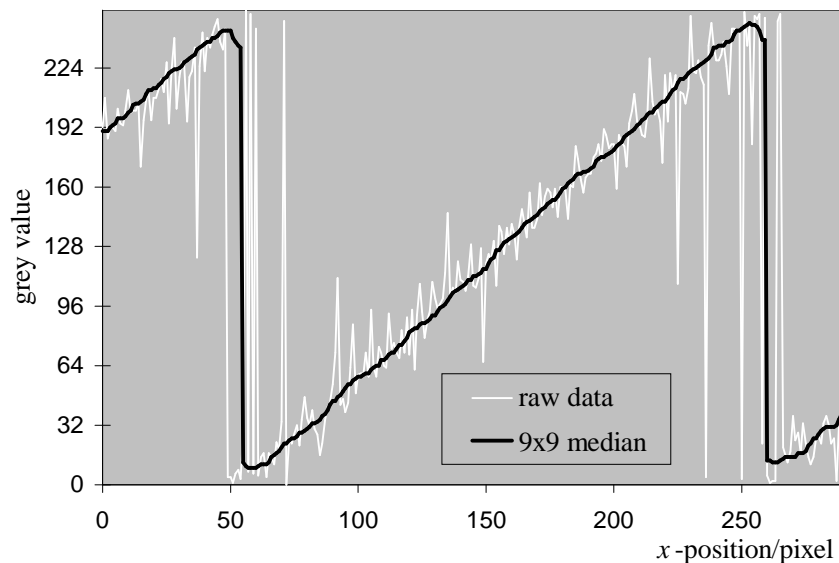


Fig. 4.1: Effect of image smoothing by a median window. A single image row is displayed for both raw and filtered data, but the median filtering was done, as usual, in 2D.

While the spikes in the raw data could be removed with a  $3 \times 3$  pixel filter, the distortions of the fringe profile continued to distinctly calm down until the filter kernel size of  $9 \times 9$  was reached. Even with so large a filter window, there are significant deviations from the expected linear course of the phase. The  $0 \leftrightarrow 255$  transitions where the phase is "wrapped" (white-black edges in the image) remain sharp, but the fringe profile nearby gets rounded off. Hence the raw data set will in fact be more accurate in those regions despite the higher noise. With fringe densities as low as in the figure (some 5 fringes over 1024 pixels), it would be possible and desirable to use very large median windows; but due to the edge falsification, this must be ruled out.

There have been successful attempts to eliminate the edge falsification by generating a second sawtooth image  $\Delta\varphi_{meas}(x,y)+\pi$ , where the wrap edges are shifted *a posteriori* by half a fringe width. Then both  $\Delta\varphi_{meas}(x,y)$  and  $\Delta\varphi_{meas}(x,y)+\pi$  are filtered and only the wrap-free regions from both images reassembled, where, of course, the phase shift by  $\pi$  must be undone in the second image [Vik90]; this is perfectly permissible because the fringe offset in sawtooth images is arbitrary. It was found that the edge degradation is very efficiently suppressed by this technique.

The so-called classification filtering method described in [Own91c] exceeds the performance of the median filter: it is edge-preserving, much faster than the median processing – that almost always involves pixel sorting – and also yields the best noise tolerance of all filtering routines studied in [Own91c].

Another high-performance sawtooth-image filter is the partially recursive window described in [Pfi93]; it proceeds line by line and stores the smoothed data back to their original addresses, so that the filter window will operate on both smoothed and raw data in subsequent image lines. The performance of this filter has been compared with other filters recently in [Aebi99].



### 4.1.2.2 Smoothing sine and cosine

To cope with the problem of edges, it has also been adopted to work on, in the mathematical sense, continuous data: the sawtooth image (signifying the optical phase) can be decomposed *a posteriori* into the sine and the cosine part from which it was originally generated [Lüh93] (cf. 3.4.5); this step has recently been given the name of "trigonometric transform" [Sea98]. This gives two edge-free fringe profiles that can be filtered with considerably larger filter windows, without affecting the  $0 \leftrightarrow 2\pi$  transitions that appear again when the phase is re-calculated. However, too large a filter will attenuate the contrast of the sine/cosine patterns or eliminate them completely, depending on their spatial frequency; therefore the proper choice of filter size requires some care as well. Fig. 4.2 shows the improvement brought about by this strategy when the same filter size as above is used.

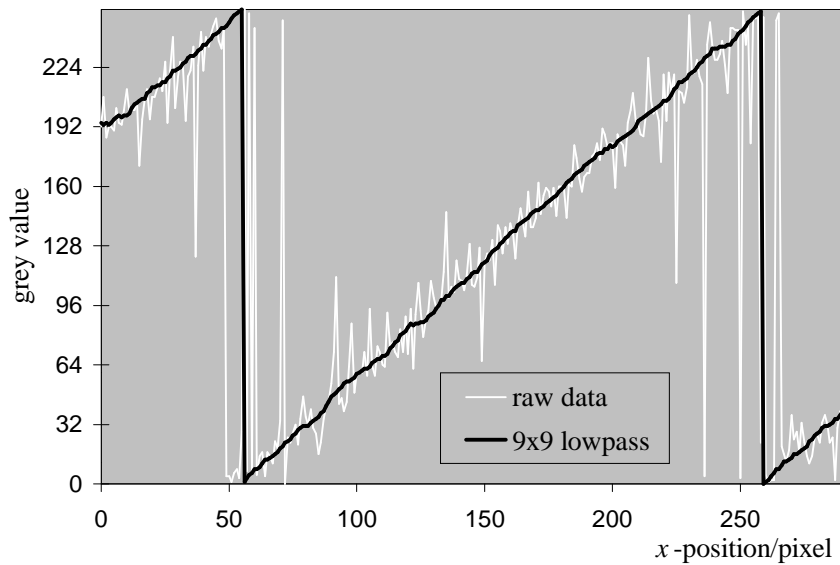


Fig. 4.2: Effect of image smoothing by decomposing into sine and cosine part, low-pass filtering each of them and re-calculating the phase. As above, single image lines are shown, and the filtering was done in 2D.

Obviously, the edges and their heights are preserved in this case; but the fringe shape still remains noisy. It improves a little when a median filter is used for the sine and cosine images: unlike the low-pass filter that is simply an average formation, the median filter really eliminates outliers. Yet it is clear that the ideal fringe profile will still not be restored by this type of filtering operation. Moreover, it is definitely inappropriate for the case of deterministic large-scale distortions of the fringe profile, as Fig. 4.3 shows.

In this case, a severe phase-shift miscalibration resulted in a concentration of calculated phase values around 0 and  $180^\circ$  (see Chapter 3.4.6), and the filtering does not even approximately restore the expected fringe profile. While this is certainly an extreme example, it shows that filtering does not automatically generate an ideal reference phase map  $\Delta\phi_{ref}(x,y)$  where both random and deterministic errors ought to be small or absent. Therefore,  $\sigma_{\Delta\phi}$  will be underestimated when calculated with the black curve in Fig. 4.3 as a reference.

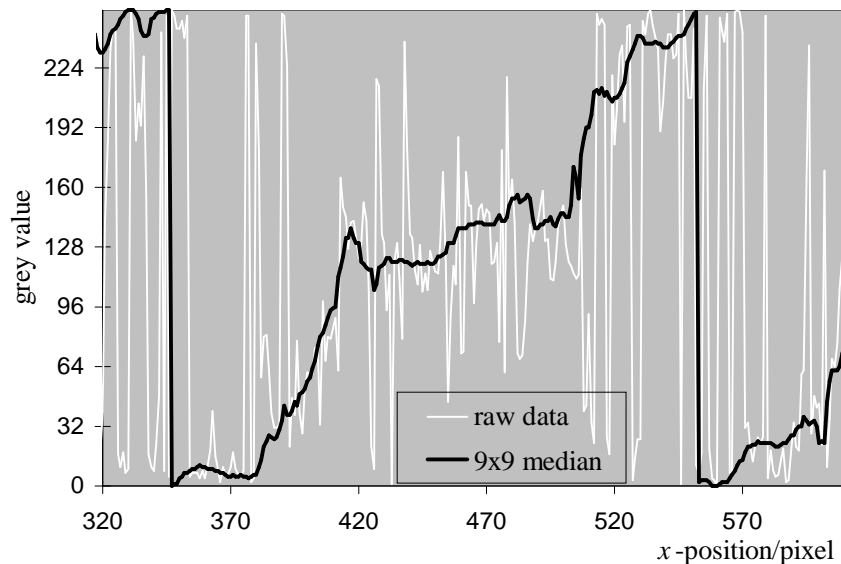


Fig. 4.3: Deterministically distorted fringe profile due to wrong phase shift; filtering in 2D by the sine-cosine method with  $9 \times 9$ -median windows.

From this, it gets clear that filtering sawtooth images to obtain reference data is always only an approximation. This should perform well enough in most cases but seems inappropriate for us since there are some extreme fringe densities and noise levels to be explored. And finally, the filter size cannot be standardised, the best choice would change from image to image and still remain a matter of judgement.

#### 4.1.2.3 Composite method

Recently it has been demonstrated that a very good filter can be implemented by using the sine-cosine method with a small filter size together with a large number of iterations [Aebi99]; the peculiarity of this algorithm is that the phase is always re-calculated between the iterations. Once again, the phasor interpretation assists in understanding this qualitatively: by determining the phases and re-deriving sine and cosine from them, the length of the phasors is re-set to unity in each iteration, which counteracts the contrast attenuation mentioned above and preserves any phase detail in the image that survives a single run of the filter kernel. Hence, one can in principle use arbitrarily many iterations and therefore eliminate the speckle noise almost completely. This seems to be a promising method to generate near-ideal reference data from whatever input fringe pattern. But still the restriction is that the filter size must be optimised by the operator; and also, depending on the accuracy required, the number of iterations may become very large. It was also observed that at the borders of the image and/or at phase discontinuities in the image, the phase profile gets more and more distorted with increasing number of iterations.

#### 4.1.2.4 Comparing unwrapped data

The problem of white-black edges in the image can also be circumvented by unwrapping the phase before comparing raw and smoothed data. Clearly, the raw image must not be filtered before unwrapping, which restricts the application of this method to rather good results with low to medium noise and moderate fringe density. Even then, the result will not be a direct conversion of phase to displacement, since almost

all unwrapping algorithms substitute "bad" pixels by some "better" estimate and hence tend to suppress errors without the user's request.

The attractive feature of this method is that, if the – continuous – theoretical displacement function is qualitatively known, one can generate completely noise-free reference data, e.g. a best-fit plane. The parameters for the displacement function are adjusted to match the measured values best, which will be done by an iterative fitting process. An example of this is presented in Fig. 4.4: the sawtooth image  $\Delta\varphi(x,y)$  whose fringe profile has been shown in Fig. 4.1 and Fig. 4.2 was unwrapped – without prior filtering –, and a best-fit plane was subtracted from the resulting height data  $\Delta d(x,y)$ . Hence, the residual displacement deviations  $\delta d(x,y)$  – scaled back to grey levels to allow a comparison with the previous figures – could be directly evaluated for their rms,  $\sigma_{\delta d}$ .

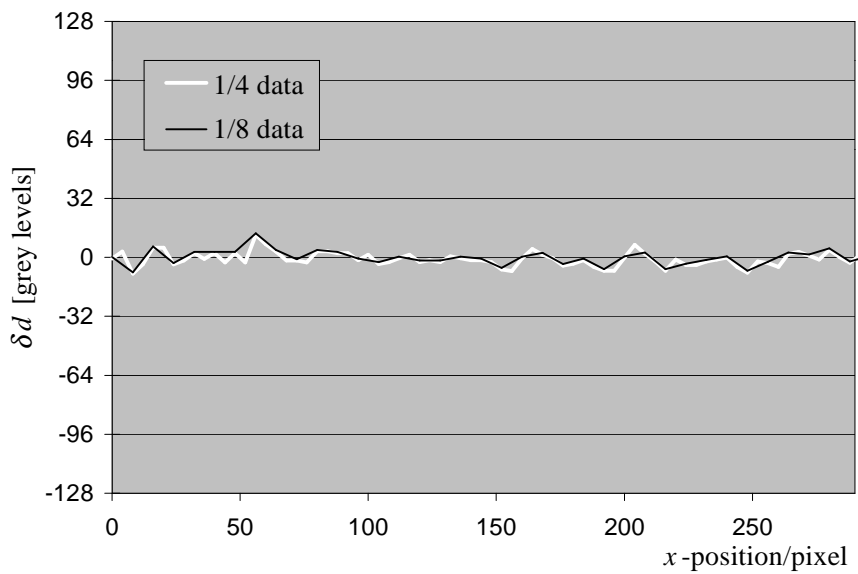


Fig. 4.4: Deviation  $\delta d$  between unwrapped sawtooth image and best-fit plane ( $\delta d=0$ ). "1/4 data": average of 4 lines of input image; "1/8 data": average of 8 lines of input image; see text.

Comparing the deviations  $\delta d$  in Fig. 4.4 with the deviations of the white curves in Fig. 4.1-Fig. 4.3 from the expected linear fringe profile, it is evident that a substantial unintentional smoothing has occurred: the spikes have been removed. This is in part due to the abovementioned pixel replacement during the conversion of  $\Delta\varphi$  to  $\Delta d$  by the unwrapping algorithm; but the more important contribution comes from the data reduction that could not be switched off [Ett97]: on unwrapping with the highest choosable resolution, an image with, e.g.,  $1024 \times 768$  pixels will be shrunk to  $256 \times 192$  averaged height values, which, as known, reduces the spatial resolution and the noise. On testing a two times lower output resolution, one finds however that the values for  $\sigma_{\delta d}$  are almost the same for the corresponding image lines out of a  $256 \times 192$  entry field (denoted by "1/4 data" in Fig. 4.4) and out of a  $128 \times 96$  entry field (denoted by "1/8 data" in Fig. 4.4), respectively; this is, little further data smoothing takes place after the unwrapping step. While the automatic noise suppression during unwrapping is certainly useful for practical tasks, it runs counter to our intentions of quantitative error determination, and is therefore not considered further.

## 4.2 Noise quantification in this work

For a quantitative comparison of TPS and SPS, we will have to test different speckle sizes, fringe densities, and experimental set-ups, which means that a universal method is needed to find the reference data from which to calculate  $\sigma_d$ . From the preceding discussion, it appears desirable to avoid estimating  $\Delta\varphi_{ref}(x,y)$  from the experiment, which means that the theoretical displacement function should be known. Furthermore, unwrapping should be avoided because it involves additional, and sometimes unknown, image processing by the unwrapping algorithm.

A concept fulfilling these requirements is fitting a synthetic, noise-free sawtooth image to the completely unprocessed original one. This of course requires that we know very well what type of fringe pattern the experiment should generate. We choose a linear phase course in  $x$ - and/or  $y$ -direction as displacement function, which gives straight and equidistant sawtooth fringes with arbitrary density and direction. This approach is sufficiently general for our purpose: provided the field of sensitivity is quasi-uniform, it adapts to out-of-plane tilts, and in-plane rotations.

Since the global phase is not controlled in most of the experiments, the positions of the white-black edges can vary considerably for otherwise identical displacements; therefore the synthetic fringe pattern has to be given the correct phase offset as well.

Together, we have three parameters to optimise in order to obtain the best-matching synthetic image: (i) the number of fringes per image width (1024 pixels) in  $x$ -direction,  $N_x$ ; (ii) the number of fringes per image height (768 pixels) in  $y$ -direction,  $N'_y$ ; and (iii) the phase offset  $N_0$  at some arbitrary point. For the latter, a practical choice is the upper left corner of the images that is interpreted as (0,0) by computer graphics.

In the plots that follow in Chapters 5 and 5,  $N'_y$  is multiplied by 4/3 to yield  $N_y \triangleq$  "fringes per 1024 pixels", so that the fringe *densities*, not the actual fringe *numbers* in the image, are equal when  $N_x=N_y$ . Since we are evaluating phase maps, the signs of  $N_x$  and  $N_y$  must match the respective phase gradient in the image. Every triple  $(N_x, N_y, N_0)$  is a point in  $\mathbb{R}^3$  from which a noise-free sawtooth image can be generated. Since we are interested in the rms of the displacement-measurement error,  $\sigma_d$ , first a least-squares fit must be run to find that  $\Delta\varphi_{ref}(x,y)$  which minimises  $\sigma_{\Delta\varphi}$ , and then  $\sigma_{\Delta\varphi}$  must be converted to  $\sigma_d$  via the interferometric sensitivity vector. The quantity actually used for the fit are the pixels' grey values in the 8-bit phase map representations.

In multidimensional parameter spaces, it is generally not easy to implement fitting algorithms; most of them are extensions of one-dimensional strategies. They tend to be mathematically complicated and require some care to make them reasonably fail-safe. Apparently, there is only one genuinely multidimensional fitting strategy, namely the "downhill simplex method" that is described in detail in [Pre88]. It is easy to code and extend to more degrees of freedom, which is presumably why several mathematics programs also include a "simplex" module. Although the simplex method is comparatively slow, it has a high inherent robustness (indeed, it never failed to terminate correctly in thousands of runs for this work).

A simplex in  $\mathbb{R}^n$  is a (hyper-)body set up by  $n+1$  vertices; it is the simplest body one can create in the respective dimensionality. In  $\mathbb{R}^3$ , a simplex is a tetrahedron. Because this is the parameter space that we are in with our type of sawtooth images, we consider this example to clarify how the strategy works. Initially, the routine is passed a starting vertex, which is the user guess for  $(N_x, N_y, N_0)$ . From this, the noise-free fringe system  $\Delta\varphi_{ref}(x,y)$  is calculated to compare it with  $\Delta\varphi_{meas}(x,y)$ . The resulting  $\sigma_{\Delta\varphi}$  is assigned to the first vertex. Then, the three other vertices are established by simply varying each one of the parameter co-ordinates a little; this 3-bein ensures that a volume is generated instead of a plane or a line. Each of the vertices defines a slightly different  $\Delta\varphi_{ref}(x,y)$  and thus leads to its corresponding  $\sigma_{\Delta\varphi}$ , so that we have a set of four different  $\sigma_{\Delta\varphi}$ . The vertex that has generated  $\sigma_{\Delta\varphi,max}$  is the worst-fitting point, and hence the one to move through the  $\mathbb{R}^3$  to find a location closer to the minimum for it. (There are many local minima, but with an accuracy of  $1/4$  fringe for the starting values, the absolute minimum is safely found.) This is done by means of the geometrical operations sketched in Fig. 4.5.

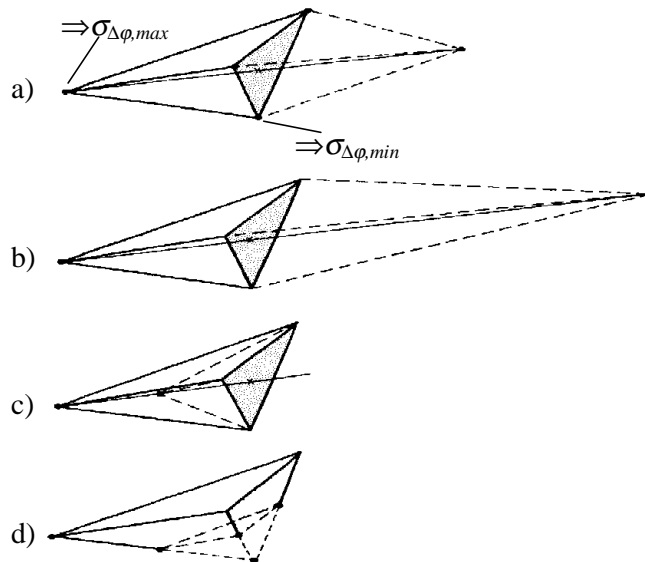


Fig. 4.5: Downhill simplex data fitting strategy in 3 dimensions (see text). Figure taken from [Pre88].

During the fitting process, the simplex must remain non-degenerate, i.e. truly 3-dimensional, which is guaranteed by the shown sequence of trials. Assumed the "worst" and "best" vertices are as in Fig. 4.5 at the beginning – or any other stage – of the fitting process, the first trial is step a), a reflection of the worst point through its opposite – here shaded – surface (generally, through the centre of gravity of all other vertices). If the new  $\sigma_{\Delta\varphi}$  is then found to have decreased, an expansion as in step b) will be tested. If  $\sigma_{\Delta\varphi}$  decreases further, this larger step toward the minimum is done. If no improvement comes about by step a), step c) is executed: the tetrahedron just shrinks away from the worst point. If this does not reduce  $\sigma_{\Delta\varphi}$  either, the tetrahedron is simply contracted towards the best-fit point, as in step d): only the "best" vertex is fixed, and all three other points are moved towards it, so that the resulting tetrahedron will be the dashed outline. Then the process repeats with a new worst point, and if we are lucky, the former worst point could be the new best one. In each iteration, the currently worst estimate of  $(N_x, N_y, N_0)$  is subjected to the trial sequence, whereby the tetrahedron creeps through the  $\mathbb{R}^3$  to enclose the minimum, and then to

contract until the desired relative accuracy of the rms values is reached. As an example, Fig. 4.6 presents a comparison of ideal and measured phase map at the final iteration of the fitting procedure. In this case, the iterations terminated at  $(\sigma_{\Delta\phi,max} - \sigma_{\Delta\phi,min})/\sigma_{\Delta\phi,min} = 10^{-5}$ . The ideal data have been digitised for visualisation only, but the fitting routine uses the C language's `long double` numerical format.

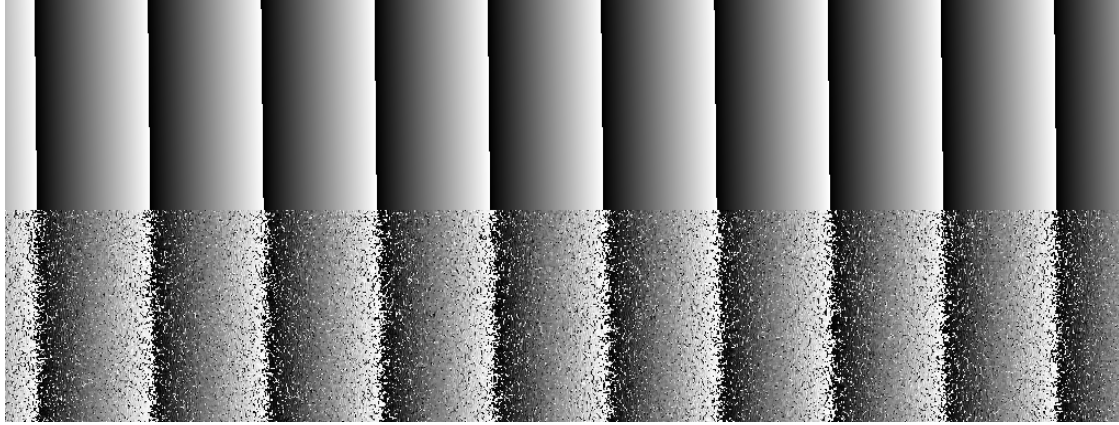


Fig. 4.6: Downhill simplex algorithm at work, just executing the last iteration. Upper half, best-fit  $\Delta\phi_{ref}(x,y)$ , laid over  $\Delta\phi_{meas}(x,y)$  still visible in lower half.

The disadvantage of the method is that every iteration involves the generation of  $1024 \times 768$  synthetic phase values and the comparison to their measured counterparts. This took  $\cong 4$  s on the Pentium-233 system used. Consequently, one determination of  $\sigma_{\Delta\phi}$  with 40 to 50 iterations took some 3 minutes, so that most of the results of Chapters 5 and 5 come from batch-fit sequences that ran overnight. An advantage of this expensive approach is that the output is an average over the whole image and therefore statistically very reliable.

The method was tested by synthetic fringe patterns with various known amounts of random noise, and it was verified that with the termination threshold given above, the pre-set  $N_x$ ,  $N_y$  and  $N_0$  could be found with an accuracy of 0.01 fringes even at very high  $\sigma_{\Delta\phi}$ . Re-starts of the routine always led to the same results within this accuracy.

The least possible  $\sigma_{\Delta\phi}$  for non-constant phases is (by digitisation of measured data) 0.29 grey values or  $0.41^\circ$ ; the largest detectable  $\sigma_{\Delta\phi}$  (trying to find a fringe system in random noise, e.g. a speckle phase map) amounts to 73.9 grey values or  $103.9^\circ$  (see also [Own91c]). This is the rms of a uniform distribution within the range  $[-128,128)$ , corresponding to phases in the range  $[-180^\circ,180^\circ)$ . The error is confined to  $[-180^\circ,180^\circ)$  because phase errors larger than  $180^\circ$ , i.e. of  $\pm(180^\circ + \epsilon)$ ,  $0 < \epsilon < 180^\circ$ , are wrapped back onto  $\mp(180^\circ - \epsilon)$  due to the cyclic nature of the phase. As an example, consider Fig. 4.1 and Fig. 4.2: the noise spikes are highest near the black-white edges, but this of course does not mean that the noise also is. The pronounced "salt-and-pepper" noise near the sawtooth edges is only a characteristic of the visual phase representation. These merely visual problems with the representation of a non-unique phase have also been discussed in Chapter 2.3.2.

As mentioned before, the fitting method can be easily extended to greater dimensionality. If, for instance, a correlation fringe pattern is to be evaluated, two degrees of freedom, namely  $I_b$  and  $M_I$ , are added and the algorithm can determine the fringe visibility in  $\mathbb{R}^5$ . More complicated fringe structures could also be treated. But every new variable increases the number of iteration steps as well as the time for a single iteration, so that the issue of speed gains importance in such applications.

Since the resulting measurements of  $\sigma_{\Delta\phi}$  will mostly appear converted to graphs of  $\sigma_d$  in the following chapters, it may be helpful at this point to provide the reader with a pictorial representation of the various amounts of noise. The image parts grouped in Fig. 4.7 are taken from an out-of-plane TPS measurement series with decreasing object illumination.

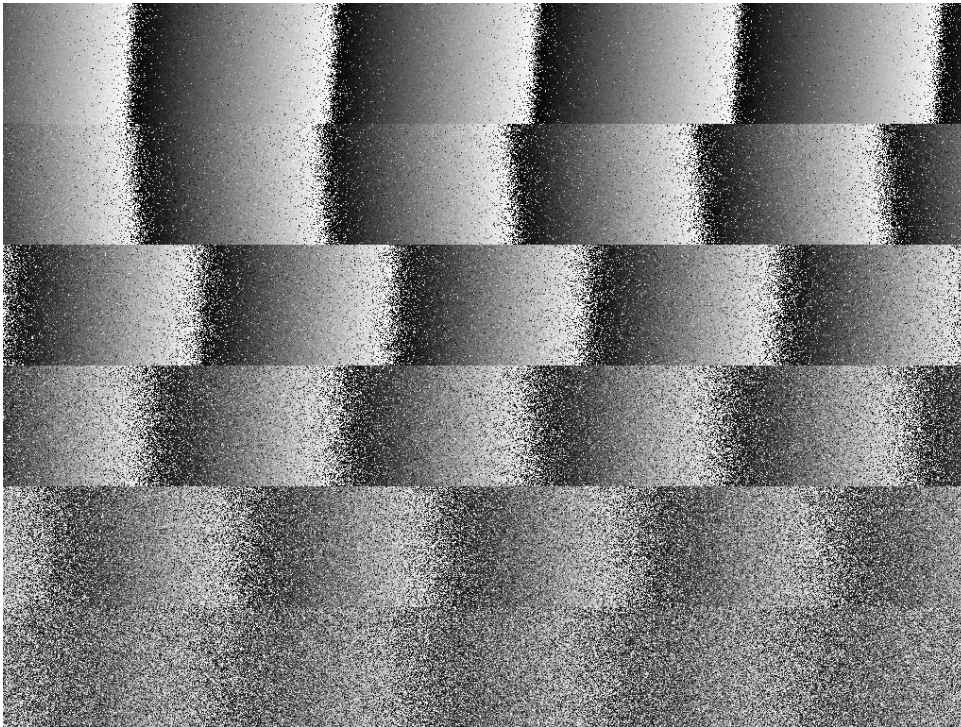


Fig. 4.7: Image segments from results of deformation measurements using TPS with varying, and rather weak, object illumination.  $\sigma_{\Delta\phi}$  as grey values: 13.3, 21.2, 28.0, 40.3, 51.9 and 63.1; as phase: 18.8°, 30.0°, 39.5°, 56.9°, 73.3° and 89.0°, in obvious order.

The last sawtooth image in the figure is hardly discernible as such and therefore raises the question whether results like this are of any use at all. It turned out, however, that the filtering procedure described in section 4.1.2.2 still improved the image sufficiently to enable correct unwrapping; but as explained above, the phase error could be determined without doing so. Other examples of sawtooth images severely degraded by synthetic Gaussian noise have been presented in [Kad97].

From the preceding overview of methods, it is clear that the approach to noise quantification presented here is new only in that it avoids unwrapping before the best-plane fit; however, it is the only strategy known to me that can generate noise-free data with no user interaction – except for the input of starting parameters – even from the worst of results, and is hence free of arbitrariness. While this may not always be necessary, it is desirable from a methodological point of view.





## 5 Comparison of noise in phase maps from TPS and SPS

Over the years, TPS has become a well-established technique that is confidently used in many applications; SPS is far less frequently used in ESPI and seldom considered as an alternative despite its ease of use and immunity to instabilities. And there are indeed reasons to doubt whether SPS can compete with TPS in ESPI: the small aperture needed to generate speckles large enough for SPS leads to decreased light efficiency, reduced spatial resolution, and also accelerates aperture-plane speckle decorrelation. Moreover, the spatial intensity and phase variations of the speckle field obstruct an accurate phase calculation, all the more as the number of available phase samples is very limited.

But also in TPS, where almost any error-compensating phase extraction with any number of intensity readings could be employed, it is customary to use Carré's [Car66] or Schwider's [Schwi83] formula. This is because not even the most sophisticated of formulae will help against speckle decorrelation and pixels with too low modulation  $M_I$ . Therefore, the uncertainty estimates have not changed much over the years; they range from  $\lambda/15$  [Nak85] to  $\lambda/30$  [Rob86, Ker88] or even  $\lambda/50$  [Vik91, vHaa94], depending on whether correlation fringes or speckle phase maps are evaluated, and in the latter case, also on the fringe density.

As yet, there are no corresponding data available for SPS, so that the decision which method to use remains a matter of presumptions. The present chapter is intended as an attempt to fill this gap [Bur00a]. Although it must be borne in mind that the data presented here are, strictly speaking, only valid for the interferometer and test object used, they do allow a comparison of TPS and SPS.

There are many parameters to be tested in such a study. The most essential ones are the phase shift and the reference-to-object intensity ratio to use. Speckle size and shape can be expected to play a special role for the fringe quality in SPS; and by varying the fringe densities, we will get an idea whether the reduced spatial resolution of SPS matters in practice. Moreover, we will test the performance of TPS and SPS under very low illumination levels to learn what restrictions the smaller aperture for SPS effects.

Although we will of course use imaging optics, we will determine the speckle size as if we were dealing with objective speckles; this is owing to the slightly modified objective shown in Fig. 5.1. When we take  $D$  as the diameter of the aperture and  $z$  as its distance to the camera chip, (2.43) remains perfectly valid, although there is no "free" scattering after the lens anymore; but  $z$  is large enough for this simple geometrical formula to function correctly, as was also confirmed by accurate measurements of the speckle size as described in 3.3.1.

While the out-of-plane measurements can be carried out with the same interferometer geometry for both methods, the symmetrical-illumination in-plane layout for TPS [Lee70] cannot be reproduced for SPS. Therefore we will test two different approaches of in-plane displacement measurements with SPS to gain a "three-dimensional" insight.

In order to obtain comparable data, it is essential to carry out both TPS and SPS measurements under experimental conditions as similar as possible. Therefore I built a speckle interferometer suitable for TPS and SPS measurements; especially for the out-of-plane set-up, only a minor change is necessary to switch from one method to the other. For the other configurations, changes of rather different extent are necessary. While it was possible to maintain the imaging geometry for the mixed in-plane/out-of-plane configurations and also for the pure in-plane TPS set-up, the pure in-plane SPS assembly has little in common with the "standard" set-up.

### 5.1 The experimental set-up

The out-of-plane arrangement is shown in Fig. 5.1. The basic layout is similar throughout Chapters 5 and 5, and the front-end changes of the set-up for the other geometries are described later in the context of the corresponding measurements.

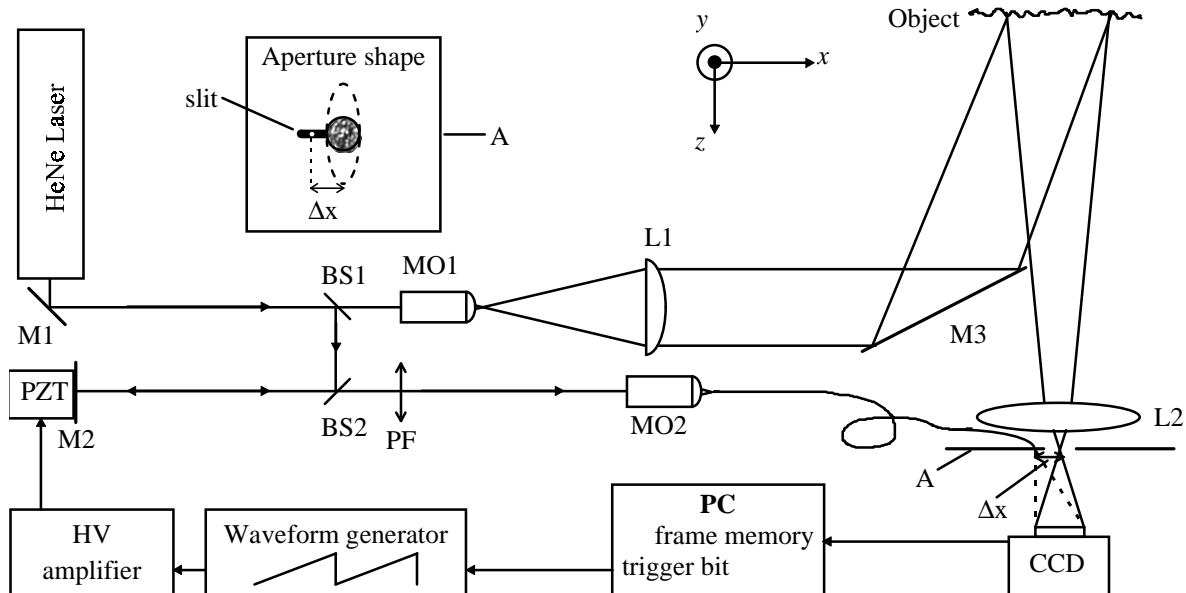


Fig. 5.1: Optical set-up used for TPS and SPS. Abbreviations: M, mirrors, BS, beam splitters, L, lenses, MO, microscope objectives, PF, polarisation filter, PZT, piezo actuator, A, aperture stop; upper left: detailed view of A as seen from the direction of the camera.

The light from a 50-mW HeNe laser ( $\lambda \cong 633$  nm) is split by BS1. The object light is expanded by MO1 and collimated by a large lens of 250 mm focal length, L1. This serves to obtain an almost uniform field of sensitivity [dVeu97]. The mirror M3 directs the light onto the object at an angle of  $\cong 11.5^\circ$  to the surface normal, which gives a quasi-out-of-plane sensitivity. The light spot on the object has a diameter of some 10 cm, of which only  $28.5 \times 21.5$  mm<sup>2</sup> are imaged onto  $1024 \times 768$  pixels of the CCD sensor by L2 ( $f=100$  mm) with a magnification of  $M \cong 0.26$ . For a perfectly uniform field of sensitivity, the object would have to be imaged telecentrically; but thanks to the small field of view, the error introduced by the conventional imaging geometry is negligible.

The object, a flat aluminium plate, can be tilted about all three spatial axes; however the  $x$  and  $y$  rotation axes lie 4.5 cm behind the plate's surface, which gives rise to lateral speckle displacement during

out-of-plane tilts. The axis of in-plane rotation coincides with the optical axis. The aluminium plate is coated with a white chalk spray that causes complete depolarisation. Thereby an incoherent background is present in all of the measurements, which is a realistic scenario.

A second beamsplitter BS2 together with mirror M2 guides the reference light path close to the one of the object. The mirror M2 can be displaced by means of the piezo-electric translator PZT (PI-170) and thus adds the possibility to use TPS. The polarisation filter PF attenuates the reference light to the extent required. By MO2 the reference wave is coupled into a single-mode fibre that is held in place by a bent syringe needle. The reference wavefront that leaves the fibre end (cut with blunt scissors) is very smooth.

The aperture stops A are laser-cut aluminium plates of 0.2 mm thickness with circular or elliptic holes of various diameters to generate different speckle sizes. The distance  $\Delta x$  of the fibre end relative to the centre of the aperture stop determines the spatial phase shift  $\alpha_x(\Delta x)$ . It is set to zero ( $\Delta x = 0$ ) for the TPS measurements and to the desired  $\alpha_x(\Delta x)$  for SPS, and calibrated by the Fourier method [Bot97]. Since the necessary  $\Delta x$  is frequently larger than the radius of the aperture, there are slits adjacent to the holes through which the reference light can pass, which is also depicted in Fig. 5.1 as seen from the direction of the camera. To obtain "clean" power spectra of the interferograms, the rest of the slit is covered again once the fibre end is correctly positioned, which becomes very important for the smaller apertures. The aperture shape for elliptical speckles is indicated by the broken line; thus the speckles will be elongated in  $x$  direction.

For TPS, the slits are covered completely and the fibre end is brought to the centre of the aperture. The syringe needle then obscures a part of the aperture, which becomes the more important the smaller the aperture is. To remove the spatial phase shift, the Fourier method can assist as well: the interference sidebands in the frequency plane are shifted into each other (see Chapter 3.3.1).

To shift the phase temporally, a control bit from the PC triggers a digital sawtooth waveform generator (HP 33120A) that drives the PZT via an HV amplifier (built in-house). The voltage ramp is chosen so as to generate a nominal phase shift of  $\alpha_t$ , matching  $\alpha_x(\Delta x)$  to obtain comparable data. While the temporal phase shifting is in progress, a sequence of consecutive camera frames\* is stored, of which the first and the last one are subtracted. They have a nominal phase difference of  $2\pi$  and should look exactly the same. If their mean brightness difference exceeds a certain threshold, an external mechanical or thermal disturbance is presumably present, the frames are discarded and the sequence is repeated. Otherwise the phase shift of all recorded frames is assumed to be correct; additional tests\*\* confirmed  $\alpha_t$  to be accurate

---

\* It turned out that the frame grabber was not capable of recording a full-format sequence of  $1024^2$  pixel frames (frame frequency: 12.5 Hz) reliably, which is why only  $1024 \times 768$  pixels were used.

\*\* These rely on executing a temporal phase-shift sequence *without* removing the spatial phase shift. The global phase offsets between the recorded interferograms can then be determined by calculating their phase maps with SPS and subtracting them. In principle, the same was done in 5.3; see also [Lai91, Küch94, Win95].

within  $\pm 5\%$  when this technique was used. The subtraction method is known as „dark frame“ calibration method [Che85]. Note here that both SPS and TPS are implemented as integrating-bucket versions.

## 5.2 Preliminary investigations

To obtain the best performance for both of the methods, some experimental parameters have to be fixed. These are the phase shift to work with and the optimal reference-to-object intensity ratio. The latter will be treated in Chapter 6.1.1 in a wider context; for now, let us retain that the standard beam ratio  $B=R/\langle O \rangle$  is 10:1 in this chapter. Also, it is important to get to know the test object and to assess the reliability of the results. The preliminary steps are briefly described below.

### 5.2.1 Choice of phase shift

Since it is essential for light efficiency to keep the speckles as small as possible, the number of phase sampling points for SPS is restricted to the minimum, which is three (see Chapter 3.2). Therefore, we use a three-phase formula also in TPS. For this number of samples, the two common values for the phase shift to choose from are  $\alpha=90^\circ$  or  $\alpha=120^\circ$ . Theoretical results [Cre88, Sur97a] suggest that for TPS,  $120^\circ$  should be the better choice. For SPS however, the findings of Chapter 3.2.2 indicate an advantage for  $\alpha=90^\circ$ . The error quantification established in Chapter 4.2 now allows us to check these presumptions experimentally. For this purpose, I recorded a series of out-of-plane tilts with various sawtooth fringe densities for each of the phase shifts in question, by both TPS and SPS. The resulting  $\sigma_{\Delta\phi}$  in the sawtooth fringes was converted into  $\sigma_d$  and plotted over the number of fringes in the sawtooth image. This graph is Fig. 5.2.

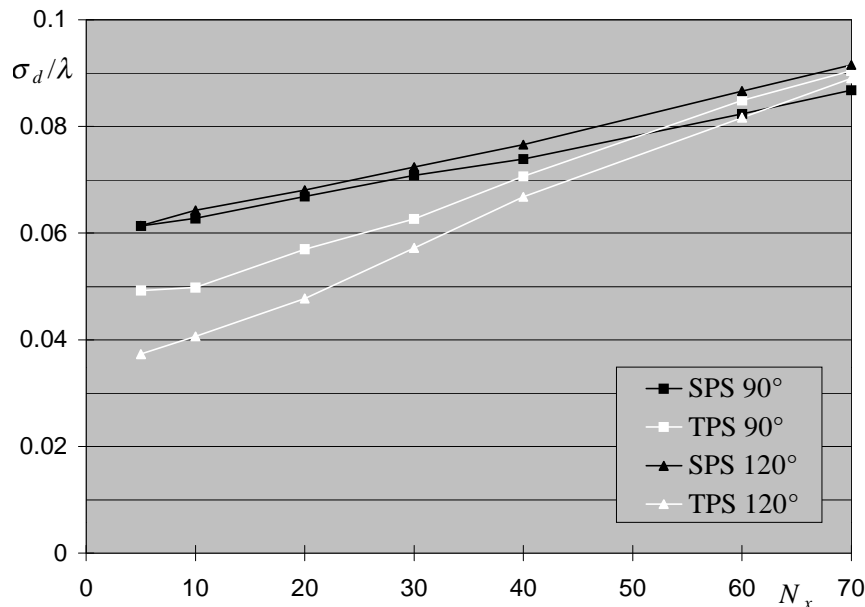


Fig. 5.2: Test of phase shifting angles for TPS and SPS:  $\sigma_d$  in wavelengths over fringe count  $N_x$ . For TPS,  $d_s=d_p$ , and for SPS,  $d_s=3d_p$ .

The  $\sigma_d$  measurements show that a phase shift of  $120^\circ$  is clearly the better alternative for TPS: particularly in the region of low fringe densities, the  $120^\circ$  method yields distinctly the lowest error. Apart from the

generally higher noise level, the accuracy of the SPS measurements shows a less pronounced dependence on the phase shift. Moreover, the  $90^\circ$  formula performs slightly better, in contrast to the theoretical findings in [Bot97], but in agreement with the more speckle-specific investigations in Chapter 3.2.2. The slight difference in performance does however not appear to discourage using  $120^\circ$  also for SPS in this study, and we will do so to maintain comparability, but will come back to  $\alpha=90^\circ$  in SPS in Chapter 6.1.2.

For higher fringe densities, TPS and SPS deliver similar performance; this is partly due to the aforementioned fact that significant speckle displacement occurs for larger tilts, which contributes the larger part to speckle decorrelation when the speckles are small.

### 5.2.2 Reproducibility of the $\sigma_d$ values

While the fitting algorithm described in Chapter 4.2 yields a very reliable average of phase errors in one sawtooth image, this tells us nothing about whether we will get the same error in a second experiment. This deserves particular attention because the test object had not been specially made: it was a large mirror mount onto which a rotation stage was fitted with the aluminium plate on it. The out-of-plane tilts were generated by manual setting via the fine-thread screws of the mirror mount, and the in-plane rotations by manual setting of the rotation stage via a reduction gear. While the latter yielded excellent reproducibility of the measured displacement errors, the former showed some fluctuations, which had to be investigated in more detail to learn how reliable the  $\sigma_d$  measurements are. Fig. 5.3 shows the results for a set of SPS experiments. For each of the speckle sizes  $1.5$ ,  $3$ , and  $6 d_p$ , the tilt sequence was repeated 10 times; the averages  $\langle \sigma_d \rangle$  with their respective standard deviations  $\sigma_{\sigma_d}$  are given in the figure. This was done for both vertical and horizontal sawtooth fringes.

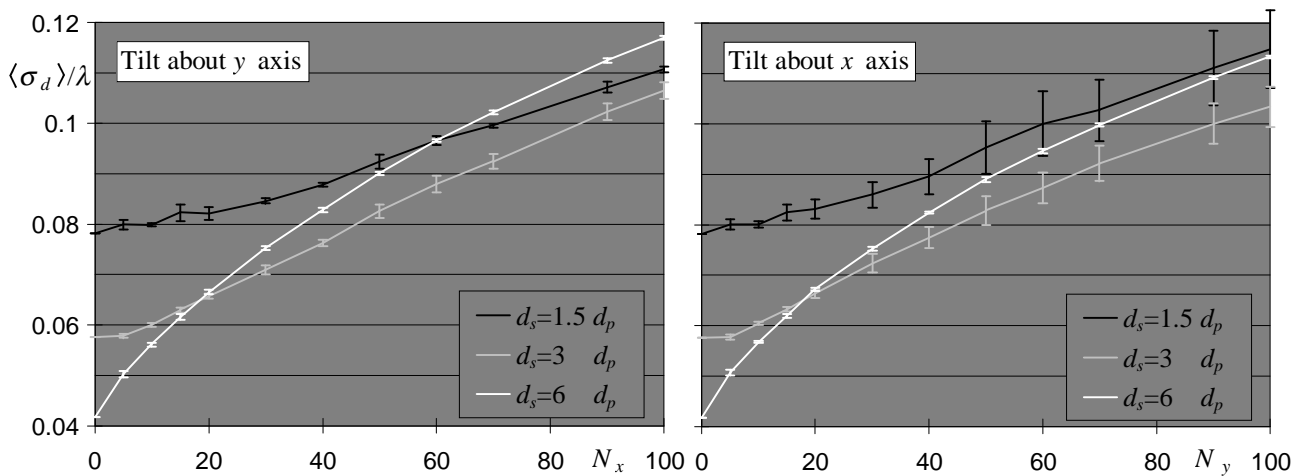


Fig. 5.3: Reproducibility of measurements of  $\sigma_d$  vs.  $N_x$  and  $N_y$  for out-of-plane tilts. Left: tilt about  $y$ -axis, vertical fringes; right: tilt about  $x$ -axis, horizontal fringes. Note that the ordinates begin at  $\sigma_d = 0.04 \lambda$  to expand the error bars.

For a speckle size of  $6 d_p$ , the reproducibility is excellent. At low fringe densities, the spatial phase measurement works well because of the low intensity and phase gradients in the speckles; but as the tilt increases, aperture-plane decorrelation impairs the accuracy. For  $d_s=6 d_p$ , the  $\sigma_d$  curves are very similar

for  $N_x$  and  $N_y$ . At lower speckle sizes, a higher bias noise is present (the curves start from higher values of  $\sigma_d|_{N_x, N_y=0}$ ), but in turn,  $\langle \sigma_d \rangle$  increases more slowly with the fringe density. Apparently, a reduction of  $d_s$  effects an increase of  $\sigma_{\sigma_d}$  particularly for tilts about the  $x$  axis. Hence, there are most likely random in-plane object shifts of some  $\mu\text{m}$ , and subsequent speckle pattern shifts on the sensor, when the object is tilted so as to produce horizontal fringes.

Therefore we will consider vertical fringes in most of the out-of-plane investigations; although the performance was also checked with horizontal fringes and found to essentially agree with Fig. 5.3, we would learn little from displaying those curves as well.

Since the tilts were adjusted by hand, there was also some fluctuation in the fringe densities given on the abscissae of the plots. The error amounts to  $\pm 1/4$  fringe for each "basic" displacement step of 5, 10, 20, 30 and 40 fringes; and for compositions of several of these (e.g. 100 fringes  $\cong 10+20+30+40$  fringes), the deviation sometimes accumulated to  $\pm 1$  fringe, which still seems negligible for plotting. Also, there was slight interaction between the axes, i.e. the fringes were rarely exactly vertical or horizontal; this deviation remained within  $\pm 1/4$  fringe per step as well and was not systematic. Although each curve for  $\langle \sigma_d \rangle$  consists of only 12 data points, i.e. 12 different fringe densities, the values are linked to "curves" for the sake of a better overview. This applies likewise to the  $\sigma_d$  plots to follow, and will prove useful there.

Finally, in the TPS experiments, also the stability of the interferometer plays a role for the accuracy of measurements. As mentioned before, I applied rather stringent a criterion to accept a phase-shifted frame sequence. Since the laboratory was in the 1<sup>st</sup> floor, with a railroad and a motorway nearby, it saved much time to do these experiments with the least possible building vibration – whose maximal power was at  $\cong 4.3$  Hz –, i.e. between midnight and 4 a.m.

### 5.3 Zero-displacement-gradient measurements

Of the results of phase measurements that will be presented here, those with zero displacement gradient are the most general ones, since they do not depend on the specific assembly's parameters but should be comparable for any set-up with only the speckle size as the relevant quantity. The way to obtain such measurements is to leave the object untouched and to compare two nominally identical object states, differing only by a controlled or random global phase offset  $\Delta\varphi$ . Unfortunately, in SPS the measured  $\sigma_d$  depends strongly on  $\Delta\varphi$ , which is due to the ample intensity and phase gradients in the object speckle field; this has been discussed in detail in Chapter 3.4.4.

Therefore, the evaluation of zero-displacement measurement errors in SPS is quite an elaborate procedure: one has to collect a set of phase maps with various  $\Delta\varphi$  that suffices to reconstruct the underlying continuous curve of  $\sigma_d$  vs.  $\Delta\varphi$  and then determine the mean of the errors. Since the interferometer was fortunately too stable to produce phase drifts and fluctuations uniform in  $[0, 2\pi)$ , the piezo-driven mirror assisted in generating the phase offsets. Of course, it has to move very slowly to generate quasi-stable interferograms; I used an amplitude-modulated triangle waveform that was

theoretically suitable to distribute the global phases uniformly over  $[0, 2\pi)$  when the interferograms were captured and stored at a fixed rate of 1/3 Hz. Fig. 5.4 shows results from this procedure for three different speckle sizes and 120 measurements of  $\sigma_d$  for each of them.

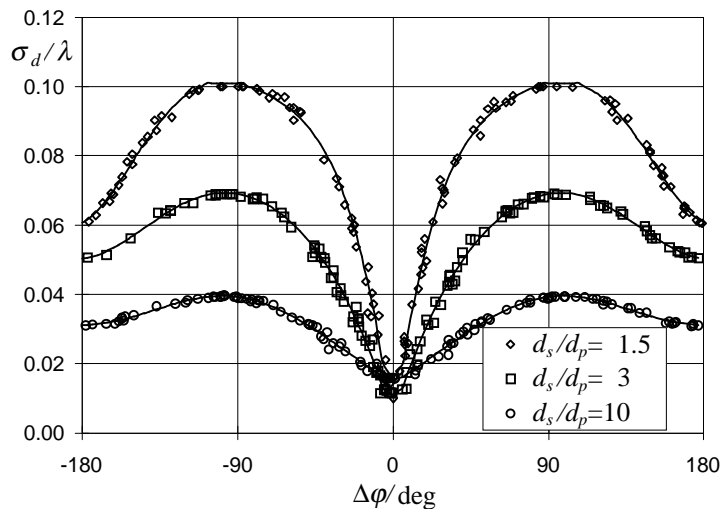


Fig. 5.4: Dependency of  $\sigma_d$  as determined by SPS on the phase offset  $\Delta\phi$  for various speckle sizes and  $N_x=N_y=0$ , cf. the error fringe profiles given in Fig. 3.39 and Fig. 3.40.

As in Chapter 3.4.6, the qualitative appearance of the graphs in Fig. 5.4 suggests that the underlying phenomenon could mainly be a linear miscalibration of the phase shift: when we subtract one phase map from another, the errors thus produced theoretically cancel at phase differences of  $\Delta\phi = 0$  and  $\pi$ , and add up in between these values. In particular, this explanation seems reasonable because the smaller the speckles, the higher their phase gradients in units of  $d_p$  and thus the larger  $\sigma_d$ . At  $\Delta\phi \cong \pi$ , however,  $\sigma_d$  does not reach the minimum at  $\phi_0 \cong 0$  again, which tells us that there are other error sources than wrong phase shift alone; this has been interpreted in Chapter 3.4.6.

The dependence of  $\sigma_d$  on  $\Delta\phi$  is also found within displacement fringes (in which  $\Delta\phi$  progresses deterministically from  $-\pi$  to  $\pi$ ), so that the  $\sigma_d$  which we assign to sawtooth images is in itself an average over all  $\Delta\phi$ . Examples of this behaviour are the white curves in Fig. 3.39 and Fig. 3.40.

As can be seen from Fig. 5.4, the distribution of the  $\Delta\phi$  is still too irregular to permit a direct calculation of the average; this effect does come from random phase fluctuations in the interferometer. Therefore it was necessary to fit suitable functions (given in the figure as well) to the data points and to determine the mean values of these instead. The values finally obtained constitute the entries for  $N_x=N_y=0$  appearing in the following plots.

With TPS, none of the described detours is necessary; the phase error does not depend on the global phase offset, provided the phase shift is calibrated exactly enough. Consequently, one measurement with  $N_x=N_y=0$  suffices to determine the corresponding  $\sigma_d$ . Furthermore,  $\sigma_d$  is uniformly distributed in sawtooth fringes from TPS, and there is no such thing as an error fringe profile in this case.

## 5.4 Out-of-plane displacements

The sequence of tilts described in 5.2.2 was carried out for both phase-shifting methods; the results for vertical fringes (varying  $N_x$ ) are graphed in Fig. 5.5. The conversion factor from phase to displacement is  $\lambda/713^\circ$ , or equivalently,  $\lambda/(507 \text{ grey levels})$ ; this means that one wavelength of displacement gives rise to almost two fringes in the sawtooth image. Hence, the maximal detectable  $\sigma_{d,max}$  in the sawtooth images (cf. Chapter 4.2) corresponds to  $104 \cdot \lambda/713 \cong 74 \cdot \lambda/507 \cong 0.146 \lambda$  for the out-of-plane geometry.

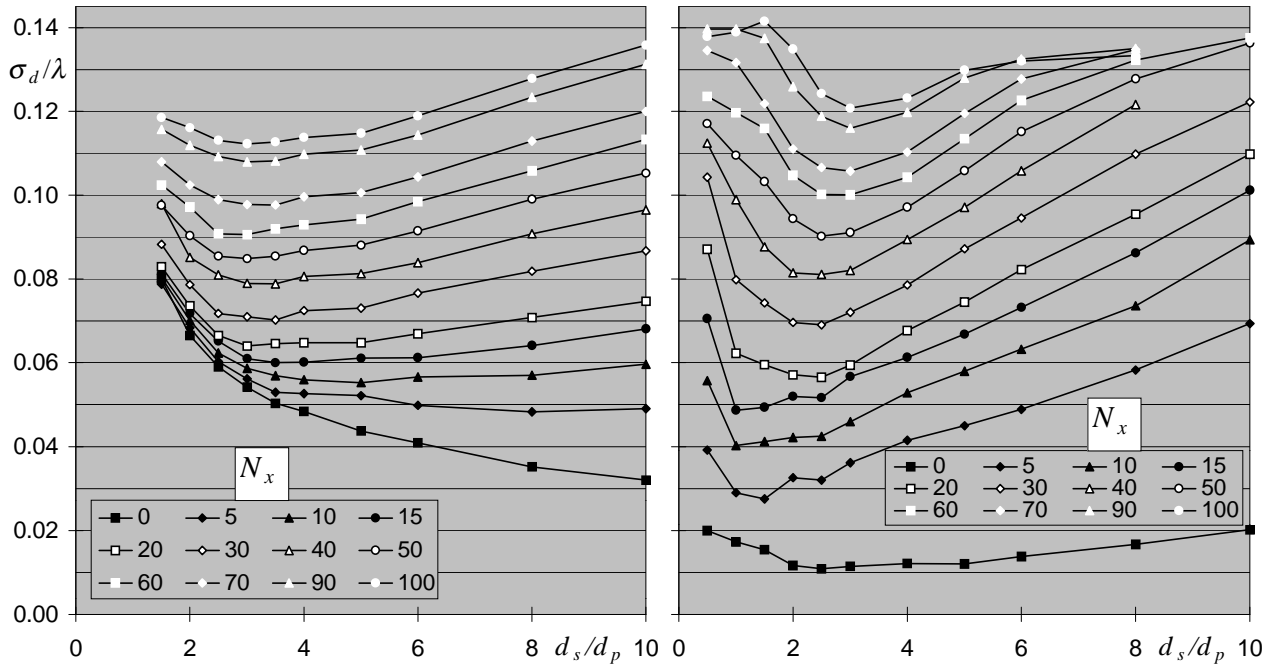


Fig. 5.5:  $\sigma_d$  for ESPI displacement measurements with SPS (left) and TPS (right) as a function of speckle size for out-of-plane displacements. The parameter for each curve is  $N_x$ , the number of vertical fringes per 1024 pixels, as indicated in the legend boxes.

In the interpretation of these plots, we will again have to bear in mind that we encounter both types of speckle decorrelation here: (i), *aperture-plane* decorrelation, which progresses faster for small apertures (large speckles) as we increase the tilt; (ii), *sensor-plane* decorrelation or speckle pattern displacement due to object tilt, which leads to an increasing pixel position mismatch between initial and final speckle pattern and affects the fringe quality more strongly for small speckles. It is true that the fringe quality could be partly restored by re-positioning the images to compensate the shift of the speckle pattern, as suggested in [Leh98]; but as this would frequently involve non-integer pixel shifts, we do not further pursue this approach. Despite this minor flaw in the set-up, we will be able to carry out the intended comparison.

Not surprisingly, the zero-displacement measurements with SPS turn out best with very large speckles, since this minimises the problems for the phase calculation. But the high sensitivity to aperture-plane decorrelation leads to a fast deterioration of the fringe quality as the tilt increases. Also, at  $N_x=100$ , one fringe would consist of only one speckle at  $d_s = 10 d_p$ , and this is clearly below the limit of 4 speckles given in [Tan68]. For  $d_s = 5 d_p$ , which corresponds to 2 speckles per fringe when  $N_x=100$ , we can already



observe a distinctly reduced error. Further reduction of the speckle size does not greatly improve the performance for this and other high  $N_x$ .

On the other end of the scale, at  $d_s = 1.5 d_p$ ,  $\sigma_d$  from SPS consists chiefly of bias noise (i.e.  $\sigma_d$  is already at  $\cong 0.08 \lambda$  for  $N_x=0$ ) until decorrelation sets in. At moderate fringe densities, i.e. up to some 30 fringes over the image width, we observe  $\sigma_d$  to increase steeply for a speckle size below some  $2.5 d_p$ , which shows that the SPS method is not very tolerant of low spatial coherence of the data points. In general, the SPS experiments confirm a speckle size of about  $3 d_p$  to be most suitable. Since the available amount of object light grows as  $1/d_s^2$ , we will not stop here and try to further reduce  $d_s$  without increasing  $\sigma_d$  in Chapter 6.4.

In the TPS experiments, a speckle size around  $1 d_p$  turns out to yield the best results for low fringe densities; yet at larger tilts, we obtain better measurements with larger speckles. This is due to image-plane speckle displacement: the same lateral speckle displacement introduces less noise when the speckles are larger, although the pattern in itself decorrelates faster.

With large speckles, the TPS measurements are worse than those from SPS as soon as the object is moved. For high fringe densities and  $d_s = 10 d_p$ , some entries are missing from the curves because decorrelation had advanced in such a way that no trace of fringes was left (of course, the fitting algorithm did find a minimum in the coarse random phase map; but it always does). In this case, reducing the speckle size brings about a larger improvement of performance.

For  $N_x \gtrsim 40$ , SPS performs better than TPS for any speckle size. This demonstrates a peculiarity of SPS: because of the spatially extended phase-sampling window (see 3.4.4), some smoothing of the phase values takes place as they are determined. The sampling window has an extent of 3 pixels in the  $x$  direction only, which could introduce anisotropy; but the errors from the  $N_y$  measurements agree with Fig. 5.5 quite well, so that the one-dimensional phase sampling has no detectable effect.

The drastic increase of  $\sigma_d$  for the speckle size of  $0.5 d_p$  is somewhat surprising, since it has been proven in [Leh98] that very good TPS measurements remain possible even with much smaller speckles. In our case however, there are also slight random in-plane shifts of the object that accompany the tilts. They do not show up in the left-hand graph of Fig. 5.3 because of the larger speckles used there; but at  $d_s = 0.5 d_p$ , the accuracy suffers noticeably from this minor effect.

To get an impression of what the obtained sawtooth images look like, Fig. 5.6 provides some example results; the corresponding  $\sigma_d$  values may be found from Fig. 5.5.

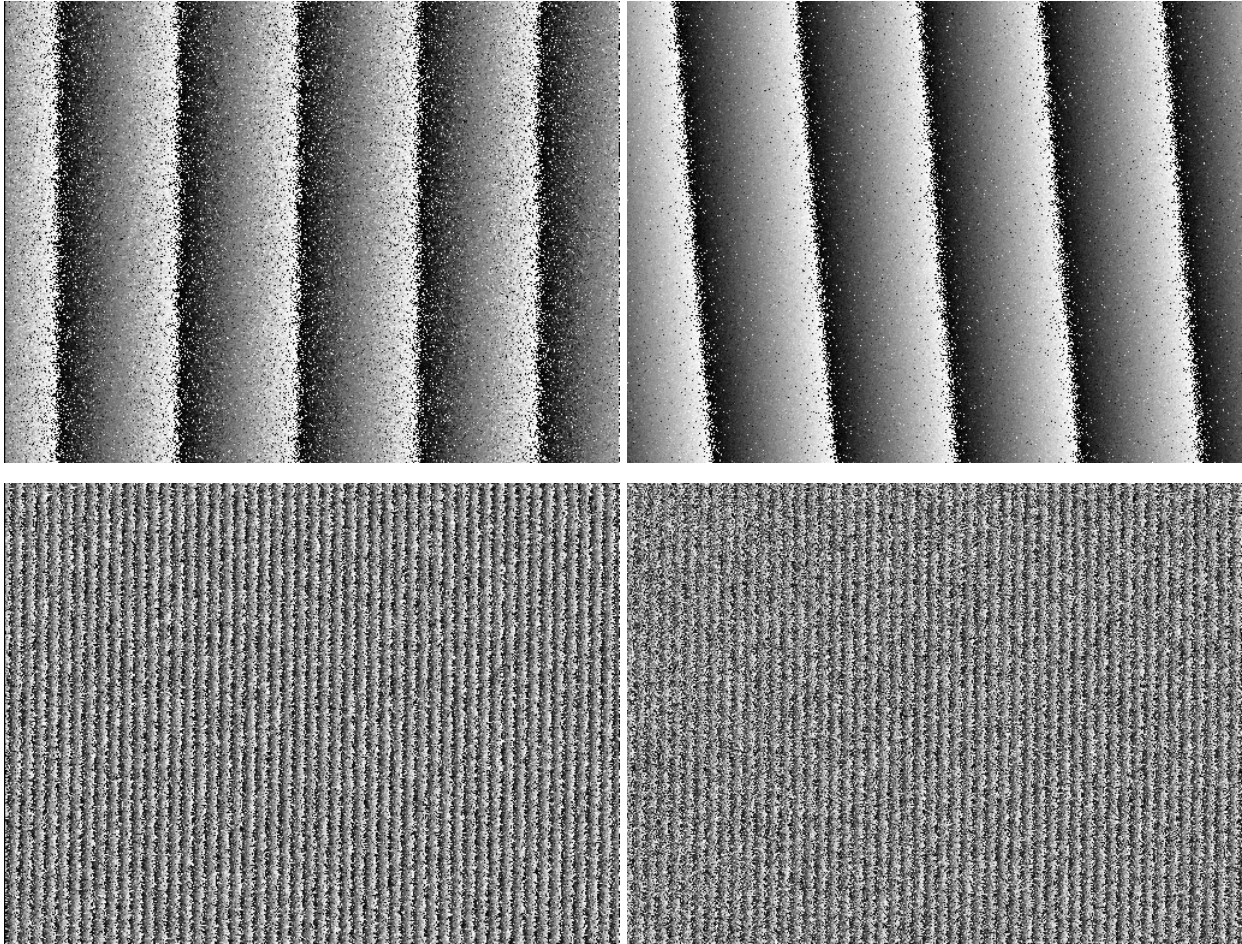


Fig. 5.6: Some examples of maps of  $\Delta\phi(x,y)$  that have been evaluated for  $\sigma_d$ . Upper row,  $N_x=5$ ; lower row,  $N_x=50$ ; left, SPS with  $d_s=3 d_p$ ; right, TPS with  $d_s=1.5 d_p$ .

Summarising this subsection, one can state that TPS is significantly more accurate than SPS at low fringe densities. For SPS, the best range of  $d_s$  is 2.5 to 3.5  $d_p$ , with  $\sigma_d \cong \lambda/15$  for moderate fringe densities; for TPS, we find  $d_s \cong d_p$  to give a typical  $\sigma_d$  of  $\cong \lambda/20$ . Imperfections of the test object prevented an extension of the TPS study towards smaller  $d_s$ . It turns out that in the presence of speckle decorrelation, SPS benefits from larger  $d_s$  and spatial phase sampling, so that the advantage of TPS fades quickly with increasing object displacement.

## 5.5 In-plane displacements

When carrying out in-plane displacement measurements using SPS and assessing its performance, the reference is the ingenious symmetrical pure-in-plane TPS configuration [Lee70] with its excellent sensitivity. A pure-in-plane SPS configuration using a double aperture has been established [Sir97a], and we will investigate its merits, but it also seems worthwhile to modify the set-up of Fig. 5.1 for more oblique object illumination and to gain in-plane sensitivity in this way, since this arrangement is by far easier to handle.

Therefore we start the investigation of in-plane measurement accuracy with a set-up that has a mixed in-plane/out-of-plane sensitivity (henceforth abbreviated by "mixed sensitivity") and again offers a

possibility to compare TPS and SPS under the same experimental parameters. As soon as pure in-plane sensitivity is demanded, the interferometer assemblies are rather different, also from each other; we will discuss these in the second part of this subsection.

### 5.5.1 Mixed-sensitivity interferometer

As mentioned earlier, the set-up of Fig. 5.1 need only be slightly changed to acquire a non-negligible in-plane sensitivity component, which is shown in Fig. 5.7.

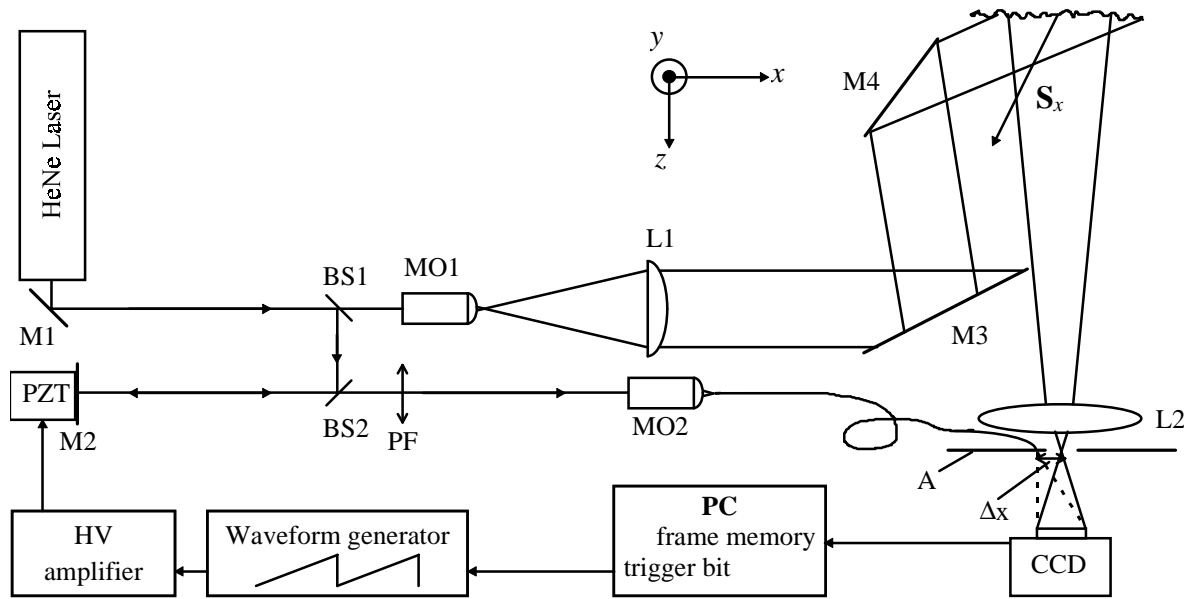


Fig. 5.7: Mixed-sensitivity set-up for detection of in-plane object displacements by TPS or SPS.

To obtain in-plane displacement sensitivity, the object is illuminated obliquely by means of the additional mirror M4, whose centre is placed at co-ordinates  $(-x_{M4}, 0, z_{M4})$ . The geometry is chosen to give an angle of incidence of  $\cong 53^\circ$  to the surface normal for the object illumination. Thus the sensitivity vector  $\mathbf{S}_x$  is inclined by  $26.6^\circ$  to the normal, and the in-plane sensitivity is half the out-of-plane sensitivity. The latter is not greatly reduced in comparison to the quasi-out-of-plane configuration, but of no concern here. The collimated illumination is particularly important for in-plane geometries, as was shown in [Kun97, Alb99].

M3 has to be rotated to illuminate M4, and since this lengthens the light path in the object arm, M2 is appropriately displaced to bring the temporal coherence back to its maximum. This is rather important because the laser is being operated without an etalon and its coherence length is therefore only  $\cong 10$  cm. This configuration detects in-plane displacements along the  $x$  axis; for  $y$ -sensitivity, there is another mirror M5 above the object (not shown here) with its centre at  $(0, x_{M4}, z_{M4})$ , so that the in-plane components of  $\mathbf{S}_x$  and  $\mathbf{S}_y$  are of equal modulus and orthogonal on the  $x$ - $y$ -plane. A rotation of the object about the  $z$  axis then yields horizontal (with  $\mathbf{S}_x$ ) or vertical (with  $\mathbf{S}_y$ ) fringe patterns that fulfil the conditions listed in Chapter 4.2. Thanks to the expensive bearing, the reproducibility of the measured  $\sigma_d$  was excellent for this type of displacement, also with smaller  $d_s$ .

The conversion factor from phase to displacement is  $\lambda/288^\circ$  or  $\lambda/(205 \text{ grey levels})$ , which means that one wavelength of in-plane displacement generates 0.8 sawtooth fringes. This has an important consequence: even "good" sawtooth images with low *phase*  $\sigma_{\Delta\phi}$  error yield a large *displacement* error  $\sigma_d$  after the conversion. Indeed, as Fig. 5.8 shows, the ordinate scale of previously  $0.146 \lambda$  for the out-of-plane measurements changes to  $\sigma_{d,max} \cong 0.36 \lambda$ .

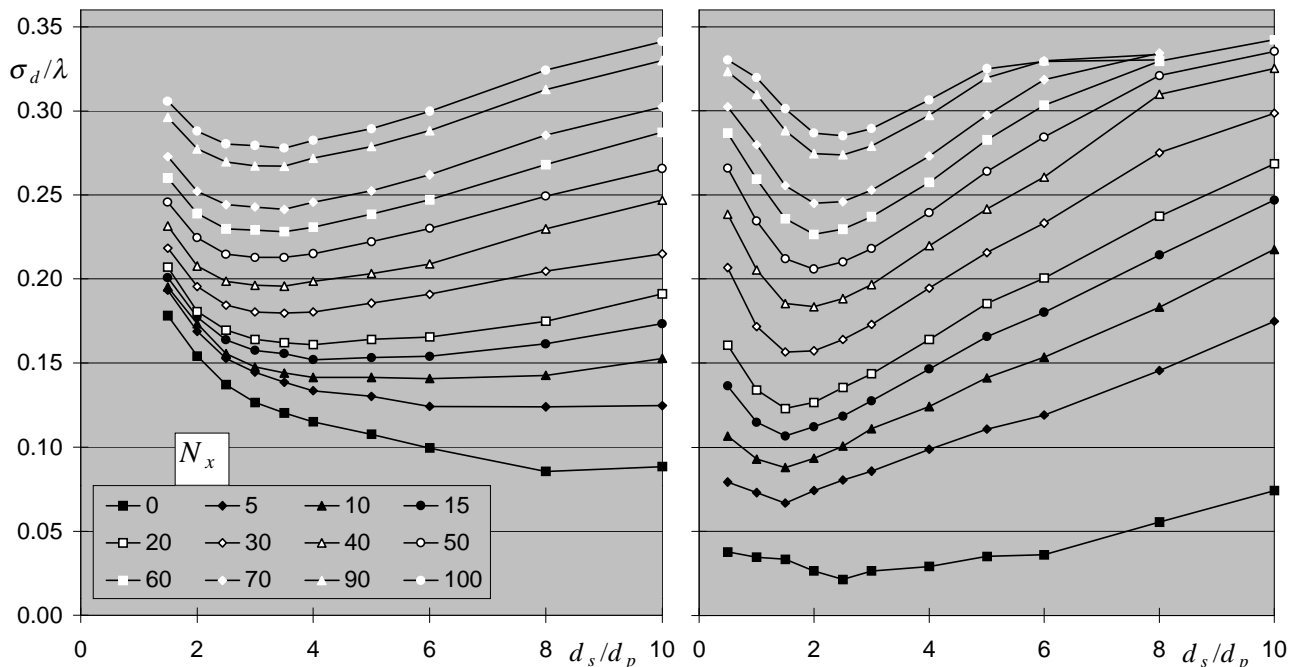


Fig. 5.8:  $\sigma_d$  for ESPI displacement measurements with SPS (left) and TPS (right) as a function of speckle size for in-plane displacements. The parameter for each curve is  $N_x$ , the number of vertical fringes per 1024 pixels, as indicated in the legend box.

Since no object tilts are involved here, the image decorrelation is exclusively of type (ii). Evidently, this does not change the qualitative course of the plots: they strongly resemble those of Fig. 5.5. Again, a speckle size between 2.5 and 4  $d_p$  is found to be a good choice for SPS and about 1  $d_p$  for TPS. The evaluation of  $\sigma_d$  with TPS and SPS, respectively, for various  $N_y$ , led to similar performance as for  $N_x$ .

On comparing the  $\sigma_d$  obtained here with those from Chapter 5.4, it turns out that here the  $\sigma_d$  are about 2.5 times as large as in 5.4, particularly for the SPS measurements, where the factor is nearly exact. This is a direct consequence of the reduced sensitivity ( $\cong 40\%$  that of the out-of-plane configuration) and tells us that the  $\sigma_{\Delta\phi}$  in the underlying sawtooth images are very similar in both cases. The displacement information is encoded in the interferograms in the same way, but by different displacements, for the out-of-plane and in-plane configurations. Hence it is not surprising that also the  $\sigma_{\Delta\phi}$  are on a comparable level. This result confirms that we now have reasonable performance data for smooth-reference ESPI setups with TPS and SPS at our disposal.

### 5.5.2 Purely in-plane sensitive interferometer for TPS

In the previous subsection we have seen the disadvantageous effects of a low sensitivity on the  $\sigma_d$  of displacement measurements. Besides, it is desirable from a practical point of view to measure the Cartesian components of displacement separately because this simplifies the evaluation greatly. The way to carry out pure in-plane displacement measurements is known since a long time [Lee70] and has become the common choice because of its ease of use and its high sensitivity that is hard to surpass [Sir93, Joe95].

The basic interferometer is modified for symmetrical oblique object illumination as sketched in Fig. 5.9. Component numbers skipped, or not starting from one, indicate that the "original" components are still in place, which helps restoring the former set-up accurately. In particular, the fibre assembly is disabled, but not removed.

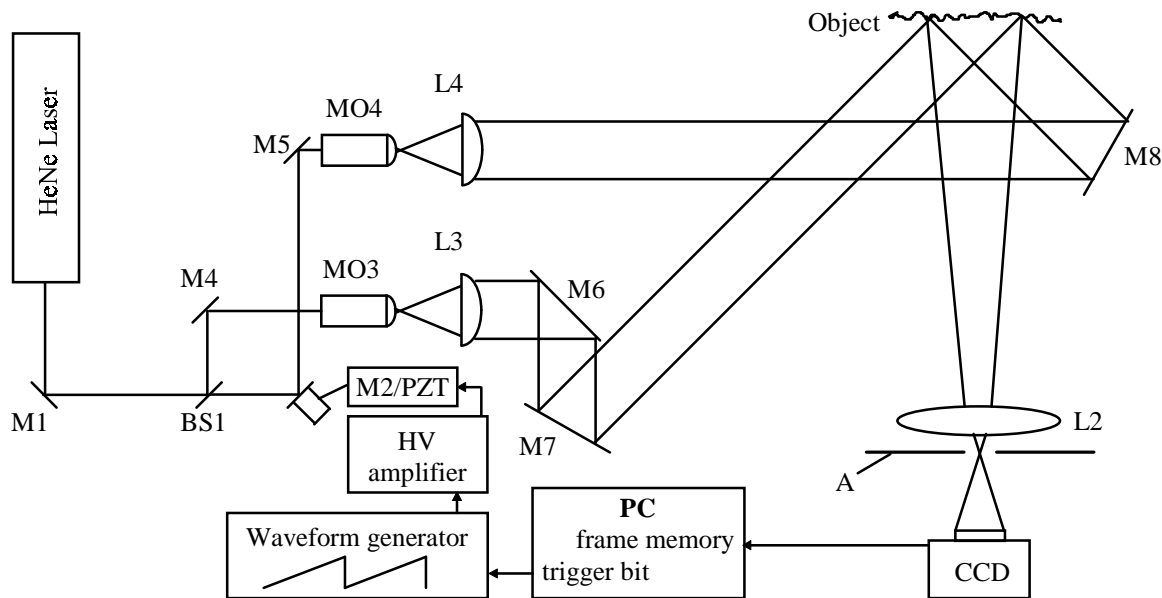


Fig. 5.9: Optical set-up used for pure in-plane TPS measurements. Abbreviations: M, mirrors, BS, beam splitter, L, lenses, MO, microscope objectives, PZT, piezo actuator, A, aperture stop.

By BS1, the light is divided into two beams of almost equal power; the "reference" beam is directed into MO4 via M2 and M5. Although there is no distinction of object and reference beam in speckle-reference set-ups, we declare this beam the reference because it is the one to undergo the temporal phase shift by means of the PZT that moves M2. Since M2 reflects the beam at  $45^\circ$ , the phase shift must be recalibrated. Theoretically, the voltage ramp used for normal incidence should be augmented by  $\sqrt{2}$ ; due to imperfections of the PZT, the true value was 1.33.

The "object" beam reaches M4 and then MO3, which is of the same type as MO4. Also the collimating lenses L3 and L4 are of the same type ( $f=140$  mm), and via several other mirrors each beam illuminates the object at an angle of  $45^\circ$ . In this configuration,  $B$  is very close to unity to maximise  $M_I$ .

The layout seems somewhat complicated, but is necessary to attain equal paths for both beams, and also facilitates leaving the imaging unit with L2 and A completely unchanged.

The sensitivity vector lies in the object's plane in horizontal direction; in this case, only  $x$ -displacements can be measured. The object rotation generates 1.4 horizontal sawtooth fringes per wavelength of in-plane displacement. Consequently, the conversion factor from phase to displacement is  $\lambda/509^\circ$  or  $\lambda/(362 \text{ grey levels})$ , which is approximately halfway between the out-of-plane and the in-plane sensitivity that we have previously been dealing with. (It would however be easy to increase this value: if both incidence angles were  $\cong 53^\circ$ , as in 5.5.1, we would get 1.6 sawtooth fringes per wavelength of displacement.) The measured  $\sigma_d$  are shown in Fig. 5.10.

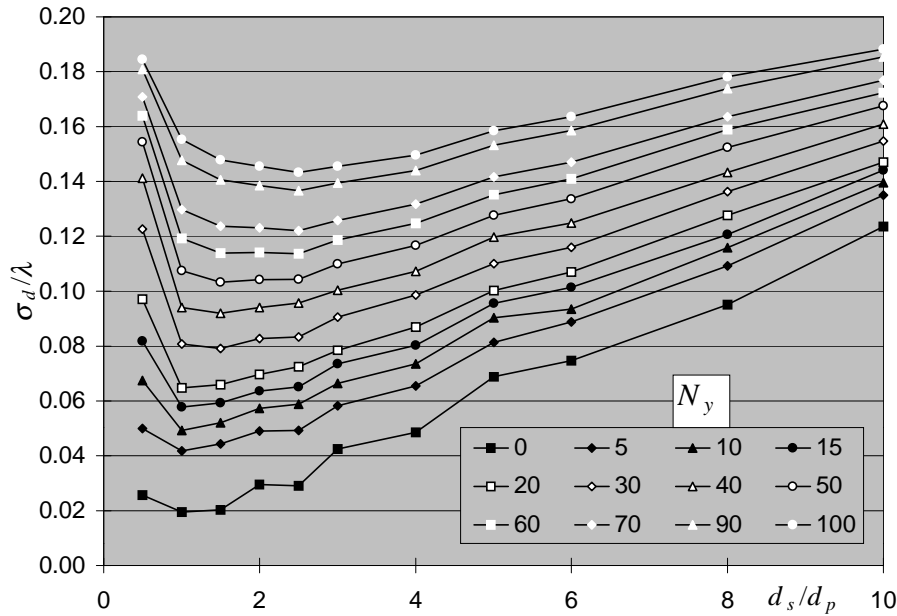


Fig. 5.10:  $\sigma_d$  for ESPI displacement measurements with pure in-plane TPS as a function of speckle size for in-plane displacements. The parameter for each curve is  $N_y$ , the number of horizontal fringes per 1024 pixels, as indicated in the legend box.

Again, the ordinate reflects the change in sensitivity:  $\sigma_{d,max} \cong 0.20 \lambda$  for this geometry. But since only 57% of the displacement of 5.5.1 are necessary to generate the same number of fringes, there is less speckle decorrelation present than in Fig. 5.8. This improves the performance significantly for higher fringe densities, although the optimum of the speckle size still wanders towards two or more pixels for larger rotations. Over the whole range of fringe densities, the accuracy is comparable to that obtained in the out-of-plane TPS study. Apart from the comparison with SPS that we are to continue, this shows that speckle-reference ESPI is not very much inferior to the smooth-reference configurations and that a 3-D TPS system with Cartesian sensitivities would have well-balanced systematic  $\sigma_d$  in each of the directions.

### 5.5.3 Purely in-plane sensitive interferometer for SPS

A set-up that facilitates exclusive in-plane displacement detection also with SPS has been described in [Sir97a]. Because the sensitivity of this configuration is also adjustable, we are able to compare the merits of SPS and TPS also with pure in-plane interferometers of equal sensitivity. Fig. 5.11 shows a schematic of the interferometer.

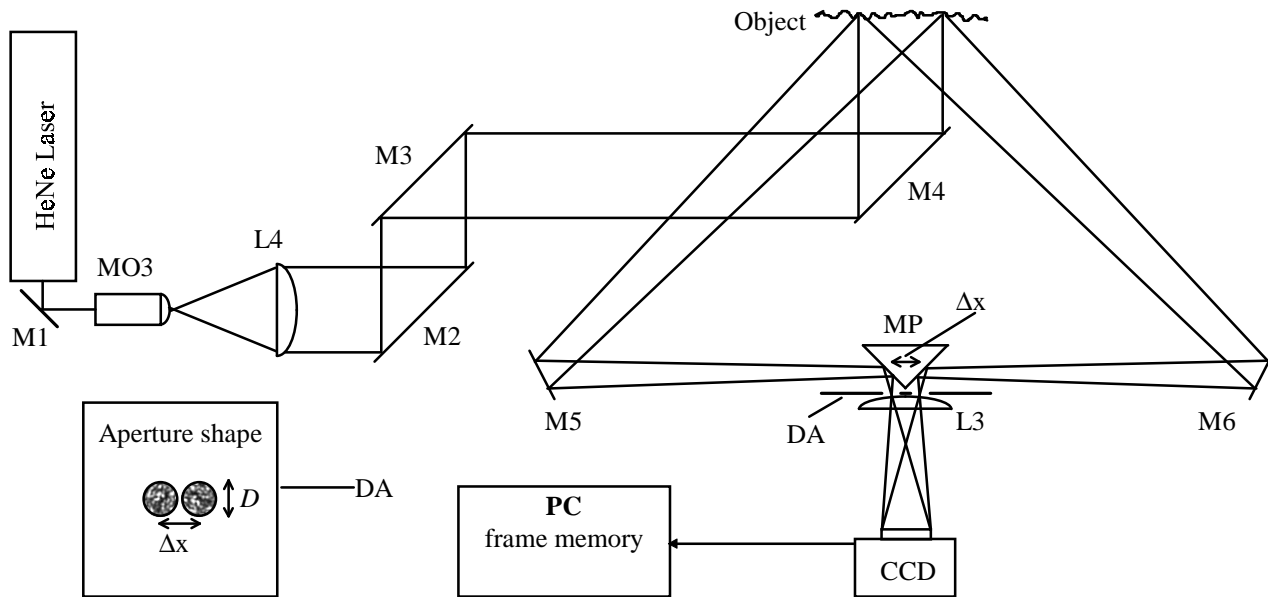


Fig. 5.11: Optical set-up used for pure in-plane SPS measurements. Abbreviations: M, mirrors, MP, mirror prism, L, lenses, MO, microscope objective, DA, double aperture; lower left: detailed view of DA as seen from the direction of the camera.

The laser beam is expanded, collimated and directed normally onto the object by M4, which is located so as to be out of the viewing paths. By M5 and M6, some of the scattered light is directed towards the aluminium coated prism MP. It is attached directly in front of the double aperture DA so that each "object beam" finds its own aperture to reach the sensor. In this case, the imaging lens ( $f=140$  mm) is located immediately *behind* the apertures, but still we can use the (equal) diameters of the apertures  $D$  for the determination of speckle sizes by means of (2.43). Like the set-up of 5.5.2, this in-plane configuration generates horizontal fringes only.

By means of the distance  $\Delta x$  between the centres of the apertures, each of diameter  $D$ , the two speckle fields interfere at an angle on the sensor, which introduces the spatial phase shift. Due to the spatial extent  $D$  of both the sources of "reference" and "object" light, the power spectrum of the interference sideband that carries the signal is twice as broad for a given speckle size as it is for the interferogram of one speckle field and a point source. In other words, there will be twice the phase shift miscalibrations and nearly twice the number of phase singularities disturbing the interferogram. Moreover,  $B$  is fixed to unity, which makes all the improvements for smooth-reference SPS (see Chapter 5) inapplicable. It is quite instructive to compare the power spectra of interferograms from the set-up in Fig. 5.11 with those from a smooth-reference configuration (see Chapter 3.4.4). Fig. 5.12 shows the spatial frequency content of speckle-reference SPS interferograms for two different speckle sizes.

The double aperture generates signal sidebands that are of the same extent as the speckle halo itself, and at least 50% of the spectral power is inevitably contained in the speckle halo, in contrast to smooth-reference interferograms. Hence, if the signal frequencies are to be well separated from the speckle noise and to remain below the Nyquist limit, the speckle size must be twice that which was derived for a point-source reference in Chapter 3.4.4.

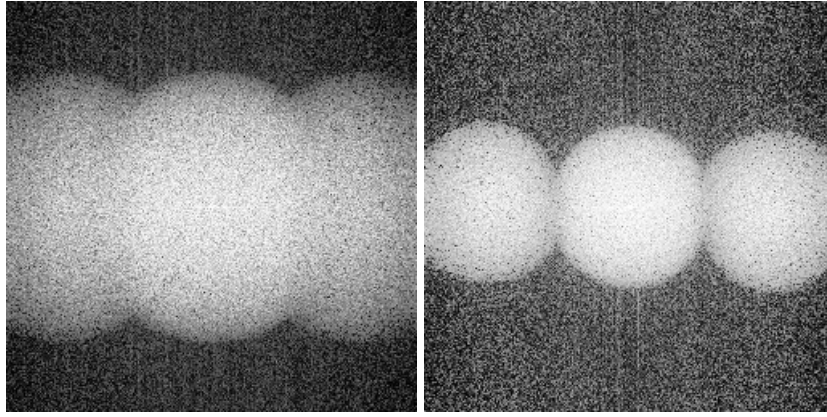


Fig. 5.12: Power spectra of interferograms from pure in-plane SPS set-up; left,  $d_s = 3.6 d_p$  ; right,  $d_s = 6.0 d_p$  . The scaling is logarithmic and contrast-enhanced.

In contrast to the TPS set-up, where the in-plane sensitivity is obtained by symmetrical oblique illumination, the SPS in-plane method relies on oblique viewing of the object. Unfortunately, the imaging geometry is now quite different from all the assemblies presented before, and also, the viewing under  $\pm 45^\circ$  introduces a considerable perspective error. In principle, this could be corrected by use of prisms as described in [Sir97b], but in order to evaluate the configuration in its basic version, this was not done here.

Owing to the perspective and the altered imaging geometry, the field of view is  $68.5 \times 36.5 \text{ mm}^2$ ; we will have to take the greater image height into account when comparing fringe densities. (We continue working with the familiar fringe counts because this keeps the quantity of "pixels per fringe" comparable.) Moreover, the apparent height of the object (size in  $y$ -direction) changes with the  $x$  co-ordinate: it ranges from 35 to 38 mm, so that the height statement is necessarily an average. Since the height changes have opposite sign for the two viewing directions, there is also a position mismatch between the superposed speckle images that is largest at the left and right edges of the field of view, and can vanish only on a vertical line in its centre. This causes a slight sensitivity to displacement gradients, as in shearing ESPI, but fortunately these do not affect displacements in  $x$ -direction. Furthermore, the quality of the mirror prism bears some relevancy: a pyramidal shape error (i.e. the prism is a segment of a high three-sided pyramid) will cause a rotation of the images against each other. Indeed, such an image rotation, of  $\cong 2^\circ$ , was present, that added to the position mismatch caused by perspective.

The perspective error plays a role in so far as the fringes are not exactly localised on the object surface. In white light-images of the object however, no significant defocusing was present over the width (size in  $x$ -direction) of the image, which is due to the large depth of focus by the small apertures.

Since the aperture sizes  $D$  can be no larger than the separation of their centres,  $\Delta x$ , we have

$$D \leq \Delta x \quad \Rightarrow \quad \frac{d_s}{1.22} = \frac{\lambda z}{D} \geq \frac{\lambda z}{\Delta x} = \frac{360^\circ}{\alpha_x}, \quad (5.1)$$

where  $z \cong f$  is the distance of the aperture to the camera sensor. Hence, if we adjust  $\alpha_x$  to  $120^\circ/\text{column}$  again, the smallest speckle size we can get is  $d_s \cong 3.7 d_p$ . This can be seen in Fig. 5.13, where this entry is



the first one on the abscissa. Nevertheless, the plots are scaled as in Fig. 5.10 to make the visual comparison easier. Because we have a symmetrical  $45^\circ$  set-up also here, the conversion factors and  $\sigma_{d,max}$  are the same as in 5.5.2.

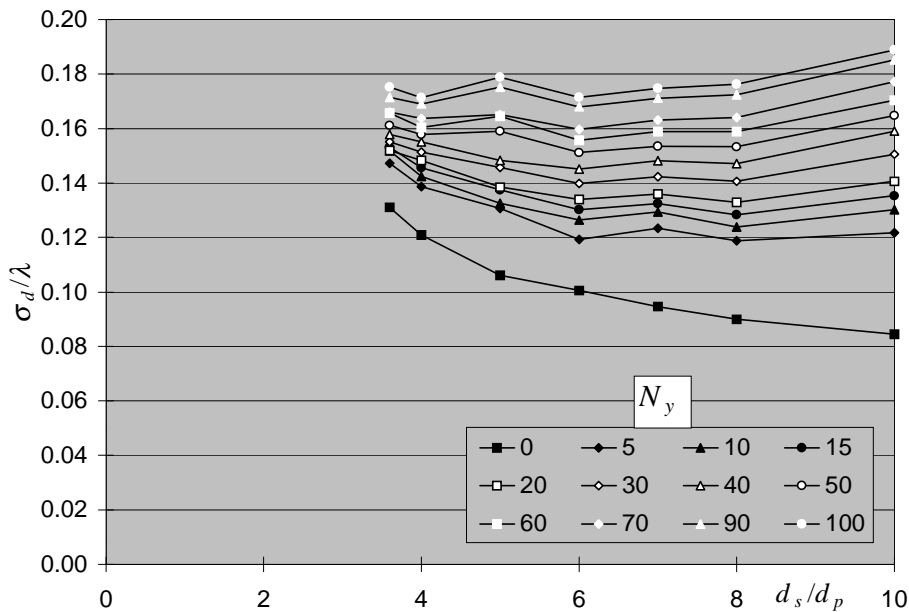


Fig. 5.13:  $\sigma_d$  for ESPI displacement measurements with pure in-plane SPS as a function of speckle size for in-plane displacements. The parameter for each curve is  $N_y$ , the number of horizontal fringes per 1024 pixels, as indicated in the legend box.

The first thing to notice is the large difference between the  $\sigma_d$  for zero and nonzero displacements, which shows that the imaging imperfections described above come into play as soon as the object is moved. From then on, however, the  $\sigma_d$  depend only weakly on the fringe density. This weak dependency has three reasons: (i) Due to the larger field of view, we need only 59% of the rotation used in 5.5.2 to generate equal fringe counts, so that there is less decorrelation owing to speckle displacement alone; (ii) the noise level generally rises more slowly as it approaches  $\sigma_{d,max}$ , as careful inspection of the preceding plots reveals. Hence, because we already start from a relatively poor fringe quality, there is less possibility for the measurements to deteriorate. And (iii), the long paths for the object beams and the oblique observation lead to problems with light efficiency, so that a certain noise floor is already due to the camera, especially for the larger speckle sizes.

According to the figure, the best speckle size is around  $6 d_p$ ; in this case, the spectral width of the signal sideband, or the extent of apparent phase-shift miscalibrations, corresponds to the case of  $d_s=3 d_p$  and a smooth reference. We have seen before that this was a reasonable choice, only now there is no way to suppress the speckle character of the interferogram by a bright reference wave, so that the signal cannot be made to stand out against the speckle noise. This leads to a displacement error that is much larger than in the case of pure in-plane TPS.

### 5.5.4 Direct comparison of the in-plane geometries

To summarise the findings from the in-plane experiments in a useful form, we shall re-consider them in a direct confrontation; this is done in Fig. 5.14 with some selected  $N_y$  for each set-up. The TPS mixed-sensitivity configuration does not appear here since the pure in-plane configuration outperforms it clearly; the  $\sigma_{d,max}$  for the pure in-plane set-ups are still at  $\cong 0.20\lambda$ , which is indicated by the dashed white grid line.

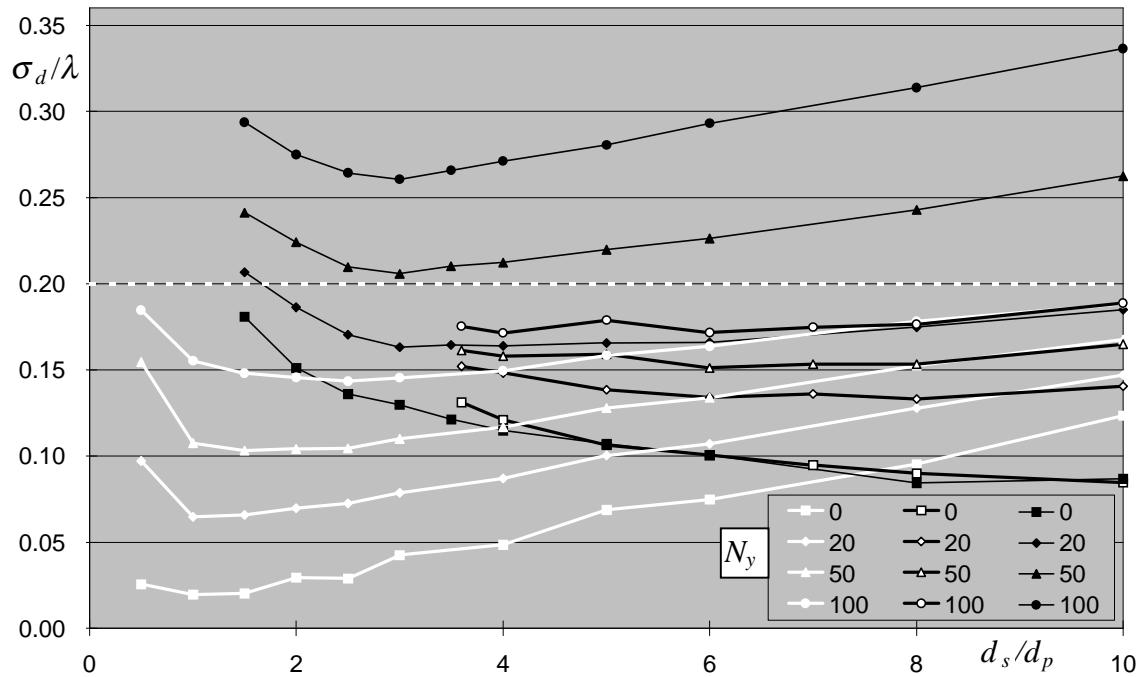


Fig. 5.14: Confrontation of  $\sigma_d$  for the different in-plane measurements. SPS mixed-sensitivity set-up: all black; pure in-plane symmetrical set-up for TPS: all white, bold lines; and for SPS: black bold lines, white filled symbols. The selected  $N_y$  are indicated in the legend box.

For  $N_y=0$ , the  $\sigma_d$  for both of the SPS methods are very similar. With increasing displacement, the pure in-plane configuration gains an advantage thanks to its high sensitivity, but also because the field of view is larger; the discussion given in 5.5.3 applies likewise here. But since the displacement data are output as sawtooth images first, it is also important how co-operative a sawtooth image will be in unwrapping. To understand this, Fig. 5.15 provides a visual demonstration of the best sawtooth images from each method for  $N_y=10$  (which corresponds to 7.5 fringes/768 pixels, cf. Chapter 4.2).

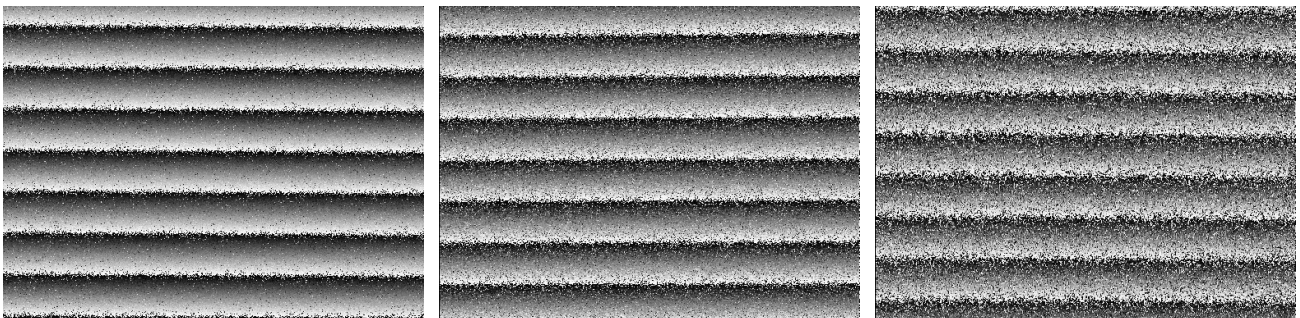


Fig. 5.15: Visual comparison of sawtooth images with  $N_y=10$  from the various pure in-plane set-ups. Left: TPS pure in-plane,  $d_s=1.5 d_p$ ; centre: SPS mixed-sensitivity,  $d_s=3 d_p$ ; right: SPS pure in-plane,  $d_s=6 d_p$ .

The images confirm that TPS delivers good phase maps ( $\sigma_{\Delta\varphi} \cong 25.7^\circ$ ) with good sensitivity. The result from the mixed-sensitivity SPS configuration has reasonable quality in terms of  $\sigma_{\Delta\varphi}$  ( $\cong 43.0^\circ$ ); but on converting to displacements, the  $\sigma_d$  value (cf. Fig. 5.14) suffers from the relatively low in-plane sensitivity. For the pure in-plane measurement by SPS, the  $\sigma_d$  value is lower; but as to be seen,  $\sigma_{\Delta\varphi}$  has the highest value of all the examples ( $\cong 64.3^\circ$ ). While this example does not present images that are difficult to unwrap, it does show that the  $\sigma_d$  figure of merit alone can be misleading when the quality of images is to be judged. In terms of  $\sigma_{\Delta\varphi}$ , the mixed-sensitivity method is preferable for SPS: for  $N_y=0$  its  $\sigma_{\Delta\varphi}$  is around one-half that of the pure in-plane SPS method, and it is still by some 14% better at  $N_y=100$ , which may then allow to skip some filtering before unwrapping can take place.

Moreover, the mixed-sensitivity SPS set-up has a great advantage in light efficiency over the pure in-plane SPS configuration; and in Chapter 5, we will explore methods to improve measurements with a smooth reference wave, so that the deficiency in  $\sigma_d$  is reduced. Finally, a 3-D SPS system with two pure in-plane assemblies is difficult to implement, while – at the sacrifice of orthogonal sensitivity vectors – it would not be difficult to use layouts with oblique illumination.

On the whole, the results presented here show an advantage for TPS when in-plane displacement measurements are concerned. For moderate fringe densities,  $\sigma_d \cong \lambda/20$  is realistic, while both of the SPS approaches yield  $\lambda/6$  to  $\lambda/7$ .

## 5.6 Impact of light efficiency

In the preceding subsections we have already mentioned the potential influence of the aperture size on the measurement in terms of light economy. During the investigations presented thus far, it was easy to collect sufficient object light: the laser was powerful and the image field was rather small. But it is not unusual in practice to have very little object light available. In these cases, TPS should be in favour because it will function with very small speckles, which in turn allows for large apertures to collect a greater amount of the scattered light. It is even stated that under conditions difficult in this respect, the aperture should be opened up as wide as possible [Leh97a, Leh98]. There is no way to do so in SPS: for phase shifting to make sense, a certain minimum speckle size in the direction of the phase shift, and hence sufficient spatial coherence over the spatial sampling window, is necessary.

This subsection presents some measurements of  $\sigma_d$  under shortage of object light for TPS and SPS, carried out with the out-of-plane configuration of Fig. 5.1. Aiming at getting an idea of the difference between the methods, we simply consider  $d_s=1 d_p$  for TPS and  $d_s=3 d_p$  for SPS, although both values could still be decreased. With this setting, the usable object wave intensity in SPS is smaller by almost an order of magnitude than in TPS when circular apertures are used.

This can be partly circumvented by enlarging the speckles only in the direction of the spatial phase shift, which is easy to achieve by using an elliptical or rectangular imaging aperture [Pfi93, Ped93, Sal96]. The idea is sketched in Fig. 5.16 for the example of  $\alpha_x=120^\circ/\text{column}$  (of course, the relevant parameter is the

number of samples and not  $\alpha_x$ ). The corresponding elliptical aperture shape was indicated in Fig. 5.1; its area, and hence the object intensity it transmits, is three times that of the circular aperture.

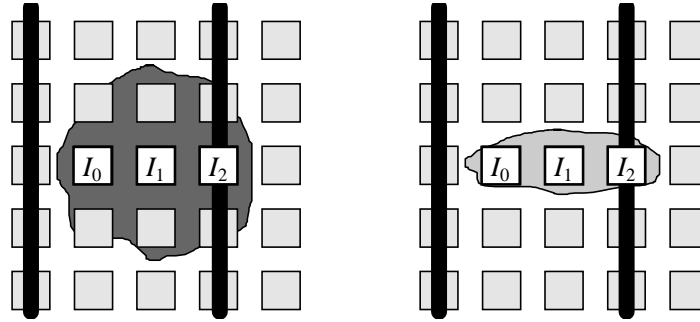


Fig. 5.16: Adjustment of speckle width suitable for SPS with optimal light economy. Black bars: orientation and spacing of carrier fringes, small squares: sensor pixels, irregular filled shapes: mean speckle size and orientation; grey values of the shading on the speckles indicate their relative brightness.

The situation depicted on the left is the result of using a circular aperture:  $2/3$  of the coherence area are superfluous for the phase calculation and the speckle field appears rather dark. But one can reduce the speckle size from  $d_{sx} \times d_{sy} = 3 \times 3 d_p^2$  to  $d_{sx} \times d_{sy} = 3 \times 1 d_p^2$ , where  $d_{sx}$  is the speckle width and  $d_{sy}$  the speckle height, to produce a brighter speckle image. On the right, an elliptical aperture generates speckles that are just large enough to allow for phase calculation; the speckle intensity is greater by a factor of three, indicated by the speckle outline in lighter grey. The question arises what improvement the change to elliptic speckles will bring about: the plus in object light gives better  $M_I$  or, optionally, allows to reduce the gain of the camera amplifier; on the other hand, the non-circular average speckle shape causes the measurement to become anisotropic with respect to displacement fringe orientations.

For TPS and SPS with circular and elliptic aperture, the behaviour of  $\sigma_d$  was studied with the out-of-plane set-up as in 5.1. To control the object illumination, I used a series of neutral density filters ( $D \in [1.0, 5.0]$ ) directly behind MO1. The basic laser power density of  $O_I = 1.1 \text{ mW/cm}^2$  on the object was thus attenuated to values between 110 and  $0.01 \text{ }\mu\text{W/cm}^2$ . The absolute value of sensor illumination could not be measured accurately enough, but since we are still dealing with the comparison of TPS and SPS, the given power scale will be sufficient for our purpose.

For each series, the chosen object intensities ranged from the first turning up of signal to the optimum where further increase of the illumination power did not improve the measurements anymore. At the lowest light level the interference was only just detectable in the speckle interferograms,<sup>\*</sup> whereas the speckle pattern alone was completely immersed in electronic noise. The reference light was always adjusted so as to obtain a high average brightness of the interferograms, which decreases the contrast  $M_I/I_b$  but maximises  $M_I$  and thus reduces the noise somewhat. Even so, we have high noise and low  $M_I$  due to beam ratios exceeding 1000:1. This corresponds to  $R \cong 190$  grey levels and  $\langle O \rangle \cong 0.2$  grey levels, which of course cannot be reliably measured; therefore the optical densities of the filter set served to determine

<sup>\*</sup> Also, the light scattered from the object was detectable only by dark-accommodated eyes.

$\langle O \rangle$ , and from this,  $R/\langle O \rangle = B$ , by extrapolation from measurable values. Fig. 5.17 shows the improvement attainable by switching to elliptical apertures.

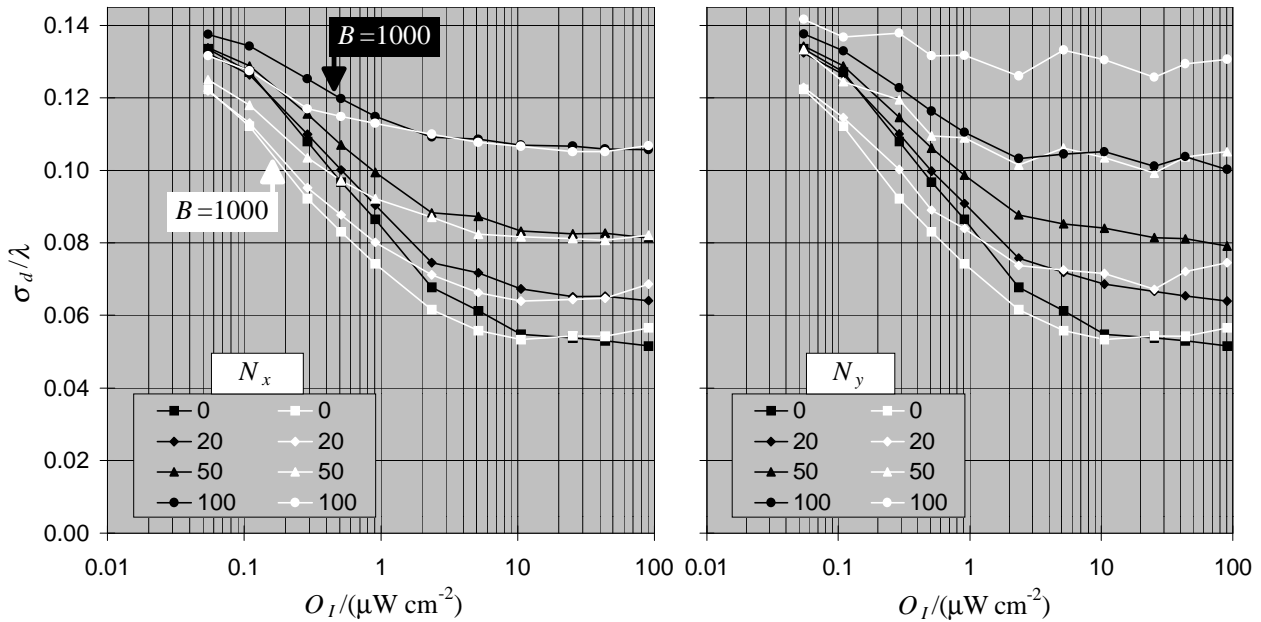


Fig. 5.17:  $\sigma_d$  for ESPI displacement measurements with SPS at low levels of  $O_I$ . "Dark"  $\triangleq$  black:  $d_{sx} \times d_{sy} = 3 \times 3 d_p^2$ ; "bright"  $\triangleq$  white:  $d_{sx} \times d_{sy} = 3 \times 1 d_p^2$ . Fringe densities  $N_x$  (left) and  $N_y$  (right) as indicated in the legend boxes.

At very low  $O_I$  (left-hand regions of the plots), electronic and digitisation noise are indeed the most significant error sources: the fringe density influences  $\sigma_d$  only weakly. With increasing  $O_I$  however, the familiar relationship of fringe density and error appears again. To the left,  $\sigma_d$  is plotted for various  $N_x$  as a function of  $O_I$ . The slope of the graphs is largest around  $B=1000$  (marked by the arrows for either aperture shape); the use of an elliptical aperture reduces  $\sigma_d$  by as much as 15% in these regions of  $O_I$ .

The  $\sigma_d$  measurements for various  $N_y$  are plotted on the right-hand side of Fig. 5.17. The black graphs for the circular aperture look very much like those on the left, which confirms the expectation that the values of  $\sigma_d$  vs.  $N_x$  and  $N_y$  are very similar when the circular aperture is used. The white curves reveal the drawback of switching to an elliptical aperture:  $\sigma_d$  rises more rapidly with  $N_y$  than with  $N_x$ , so that the advantage initially gained vanishes for  $N_y > 50$ . Again, this comes from the speckle pattern displacement which results in a larger  $\sigma_d$  for smaller  $d_s$ . Thus for object tilts resulting in horizontal fringes (associated with vertical speckle displacements and small speckle height  $d_{sy}$ ), this error source is more important than for tilts that generate vertical fringes, which are associated with horizontal speckle displacements and large speckle width  $d_{sx}$ .

While the quantitative impact of the aperture shape is of course specific of the interferometer, Fig. 5.17 does show that the anisotropy by an elliptical aperture is not negligible. On the whole, the greater amount of light is seen to be helpful; but of course, the improved SPS measurement must be set in relation to the performance of TPS at low  $O_I$ , of which Fig. 5.18 gives an overview.

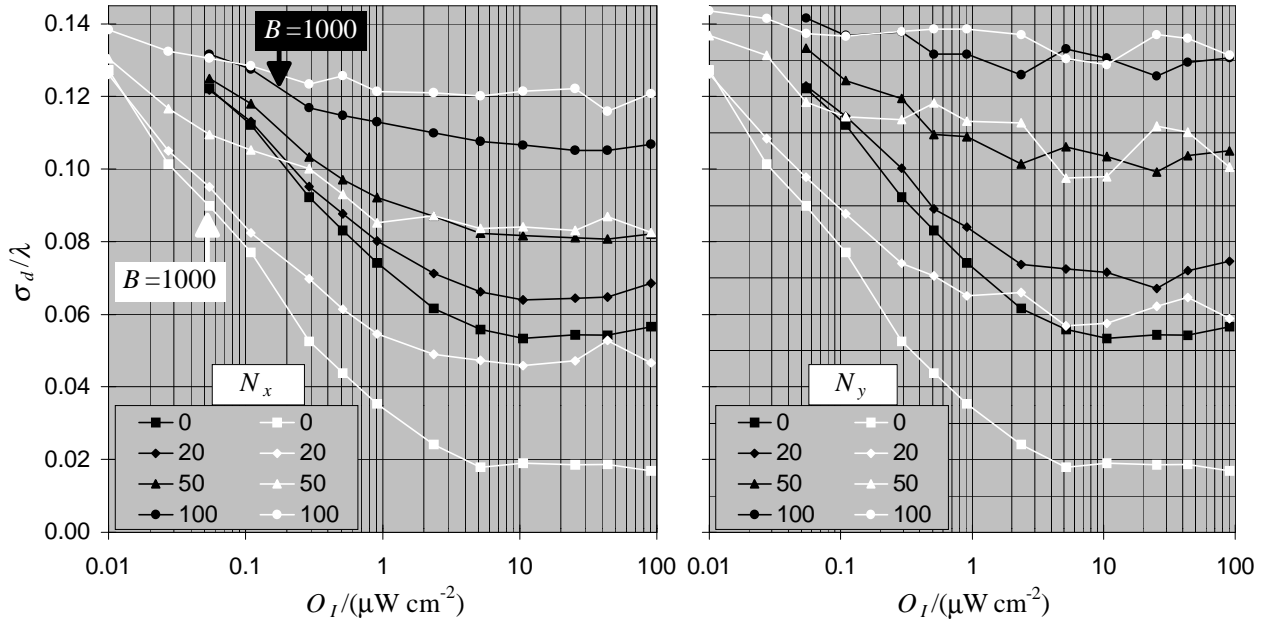


Fig. 5.18:  $\sigma_d$  for ESPI displacement measurements using SPS vs. TPS at low levels of  $O_I$ . "Dark"  $\triangleq$  black: SPS with  $d_{sx} \times d_{sy} = 3 \times 1 d_p^2$ ; "bright"  $\triangleq$  white: TPS with  $d_{sx} \times d_{sy} = 1 \times 1 d_p^2$ . Fringe densities  $N_x$  (left) and  $N_y$  (right) as indicated in the legend boxes.

The results from TPS are distinctly better, and  $O_I$  can even be lowered to  $0.01 \mu\text{W}/\text{cm}^2$ . The improvement by using TPS amounts to  $\cong 30\%$  for low densities of both horizontal and vertical fringes over quite a large range of  $O_I$ . This confirms that TPS is less problematic under critical illumination conditions, all the more since  $d_s$  can – and should – be further reduced in order to maximise the amount of light collected. The occasional crossing of the curves for  $N_y$  is due to the greater  $\sigma_{\sigma_d}$  for tilts about the  $x$  axis that was described in 5.2.2.

Surprisingly little power is necessary to reach the plateau of nearly constant errors; it turns out that a 0.5-mW laser would have been powerful enough for the out-of-plane experiments. Also, this experiment demonstrates impressively the advantage of the phase-shifting technique: even with 2-3 bits of signal resolution, it is possible to obtain usable results [Dör82, Ker88, Vro91, Hac00]. It may also be worth noting that both TPS and SPS reach their best performance at the same level of  $O_I$ , which is  $\cong 10 \mu\text{W}/\text{cm}^2$  in this case.

From the results in this subsection, it follows that the decision for or against elliptic speckle is not a general one: it depends on the expected result of the experiment, as well as on the amount of light actually available. We will briefly return to this issue in Chapter 6.1.3.

## 6 Improvements on SPS

The comparison of TPS and SPS has shown that TPS yields lower measurement errors especially in the region of low fringe densities. Since it is generally more preferable to record several sawtooth images with few fringes than one image with many fringes [Flo93, Her96], we shall therefore explore some ways to reduce the  $\sigma_d$  associated with SPS in this chapter. First of all, the beam ratio in the interferograms is shown to be of great importance; but there are also possibilities to reduce the measurement error by phase calculation formulae tailored for SPS. And lastly, we employ the "single-frame" measurement capability of SPS to introduce some improvements.

### 6.1 Optimisation of experimental parameters

#### 6.1.1 Beam ratio

Although the best intensity ratio of reference to object wave,  $B$ , has been thoroughly investigated [Sle86, Leh95, Maa97] in order to maximise the interferometric modulation, it has also been stated that the least permissible  $M_I$  can be set quite low, e.g. at some 8 grey levels or even less [Dör82, Ker88, Vro91, Hac00]. Consequently, phase shifting in ESPI yields reasonable results for quite a large range of  $B$ . In what concerns TPS, we can expect the errors to remain approximately constant as long as  $M_I$  is beyond its lower threshold. With growing intensity of the reference wave, the modulation drops and electronic noise and digitisation errors gradually gain the upper hand over the signal.

For SPS however, the speckle character of the object wave constitutes an error source that depends on the object intensity: the intensity readouts  $I_n$  (cf. (3.12)) from a set of adjacent pixels should have equal  $I_b$  and  $M_I$  if the phase calculation is to function correctly; but the brighter the speckles are, the greater become their intensity gradients and the worse is the mismatch of the interferometric parameters on adjacent pixels. It is clear that the *absolute* intensity errors drop when the beam ratio is increased; but this is of no consequence for the measurement, because the modulation goes down as well. An improvement comes about only by a decrease of the *relative* intensity errors, and it has been shown in a simple form in [Bur99a] that this is indeed the consequence of a brighter reference wave.

To describe the phenomenon, we first need to know how statistical intensity fluctuations are propagated to phase errors  $\sigma_{\varphi_0}$  by the phase calculation. Assuming a standard deviation of  $\sigma_I$  for the intensity readings, this relationship is described by Eq. (12) of [Bot97] in a general form for 3-bucket formulae. For  $\alpha_x=120^\circ/\text{sample}$ , it reads

$$\sigma_{\varphi_0} = \frac{\sigma_I}{2M_I} \cdot \sqrt{\frac{8}{3}}, \quad (6.1)$$

where  $\sigma_{\varphi_0}$  is the standard deviation of the calculated phase averaged over all  $\varphi_0$ , and  $\sigma_I$  that of the interferogram intensities. In a simple approximation,  $\sigma_I$  is composed mainly of the standard deviation of

intensity on adjacent pixels  $(x,y)$  and  $(x\pm 1,y)$ ,  $\sigma_{o_0,o_{\pm 1}}$ , and of that of the imaging system's electronic noise,  $\sigma_e$ .<sup>\*</sup> Hence we rewrite (6.1) as

$$\sigma_{\varphi_O} \cong \frac{\sqrt{\sigma_{o_0,o_{\pm 1}}^2 + \sigma_e^2}}{2 \cdot \sqrt{\langle O \rangle} \cdot R} \cdot \sqrt{\frac{8}{3}}. \quad (6.2)$$

In a speckle field,  $\sigma_{o_0,o_{\pm 1}}$  depends on the degree of spatial coherence [Goo75],  $\mu_A(x_0, x_{\pm 1})$ , of the points  $(k,l)$  and  $(k\pm 1,l)$ . For a circular aperture and  $d_s = 3d_p$ , we find  $\mu_A(x_0, x_{\pm 1}) \cong 0.81$ . Moreover,  $\sigma_{o_0,o_{\pm 1}}$  is conditioned on  $O_0$ , which relationship is analytically known [Don79]. We can generalise (2.52) to read

$$\sigma_{o_0,o_{\pm 1}}^2 = (\langle O \rangle (1 - \mu_A^2))^2 + 2\langle O \rangle^2 \mu_A^2 (1 - \mu_A^2), \quad (6.3)$$

and inserting (6.3) into (6.2), we can calculate  $\sigma_{\varphi_O}$ , which is the same for both object states:  $\sigma_{\varphi_O} = \sigma_{\varphi_{O,i}} = \sigma_{\varphi_{O,f}}$ . For the phase difference  $\Delta\varphi = \varphi_{O,f} - \varphi_{O,i}$  we therefore get  $\sigma_{\Delta\varphi} = \sqrt{2}\sigma_{\varphi_O}$  and from this the corresponding quantity for the displacement,  $\sigma_d$ , as a function of the beam ratio  $B = R/\langle O \rangle$ . These data can be compared with the experimental results.

Fig. 6.1 shows the performance of various evaluation methods for sawtooth images with  $N_x=10$ ,  $N_y=0$ ,  $d_s=3d_p$  and  $\alpha_x=120^\circ/\text{column}$  from an out-of-plane configuration with SPS; for TPS,  $d_s$  was set to  $1d_p$ . Curves in Fig. 6.1 that are not addressed here will be discussed later on.

The theoretical curve of  $\sigma_d$  vs.  $B$  for SPS is the bold white line and matches the measured data reasonably if we shift it vertically by adding a constant displacement deviation of  $\sigma_{d_0} = 0.05\lambda$ . This is not an arbitrary adjustment of data: since (6.2) does not account for spatial fluctuations of the phase  $\varphi_O$  between adjacent pixels, the predicted values of  $\sigma_d$  will be too small. Of course, adding a constant  $\sigma_{d_0}$  relies on the simple assumption that the influence of speckle phase gradients on  $\sigma_d$  does not depend on  $B$ .

From the figure we see that TPS works well from  $B \cong 1$  on, and  $\sigma_d$  only starts to increase from  $B \gtrsim 100$  on, where  $\langle O \rangle$  is already weaker than the electronic noise. The quasi-constancy of  $\sigma_d$  vs.  $B$  in TPS has also been reported in [Hun97] for a beam ratio between  $0.1 \leq B \leq 10$ . For SPS,  $\sigma_d$  first decreases as the reference wave gets stronger, and has its minimum around 30. With fading  $M_I$ , the influence of electronic noise grows and so does  $\sigma_d$ . This behaviour agrees reasonably with our theoretical prediction.

Hence, in SPS a proper choice of the beam ratio is far more important than it is in TPS. Fortunately the best SPS results turn up in a region of high beam ratio, which alleviates the problem of poor light efficiency somewhat. Based on these results, for most of the investigations in Chapter 5  $B$  was set to 10, at which setting both SPS and TPS operate with near-optimum performance.

---

<sup>\*</sup> With the imaging system used, a realistic value for  $\sigma_n$  was  $\cong 2.5$  grey levels; this corresponds to a resolution of only 6-7 true bits. With optimum intensity resolution, the usable beam ratios would have been even higher.



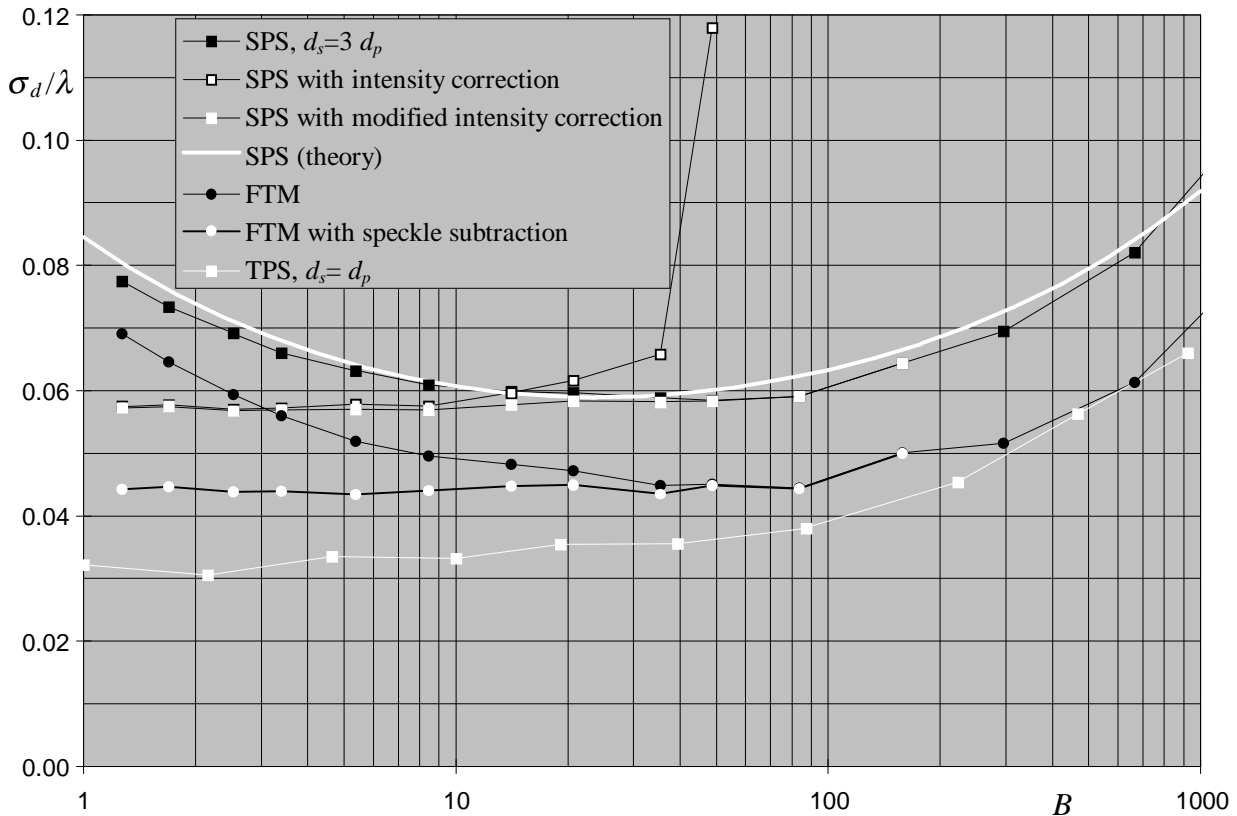


Fig. 6.1:  $\sigma_d$  for various ESPI measurements of out-of-plane displacements by SPS and TPS as a function of  $B$ . All measurements were done with  $N_x=10$  and  $N_y=0$ .

Besides the variation of the beam ratio, there is another possibility of reducing  $\sigma_d$ : the individual speckle intensities can be accounted for in a modified phase calculation formula. This approach is described in detail in 6.2.1, where also the curves for "SPS with (modified) intensity correction" in Fig. 6.1 will be explained. For a discussion of the Fourier transform method (FTM), see 6.5.

### 6.1.2 Phase shift

In Chapter 3.2.2 we have considered the spectral transfer properties of phase-shifting formulae and discussed some points that are relevant for their application to signals with a broad spectrum. In Chapter 5.2.1, we collected some preliminary evidence that  $\alpha_x=90^\circ/\text{sample}$  should be the better choice. Since it is now our aim to get the best possible performance from SPS, we investigate this issue in more detail by experiment and carry out the same kind of comparison that we did for SPS and TPS. The results are shown in Fig. 6.2, where the left part is the same plot as Fig. 5.5.

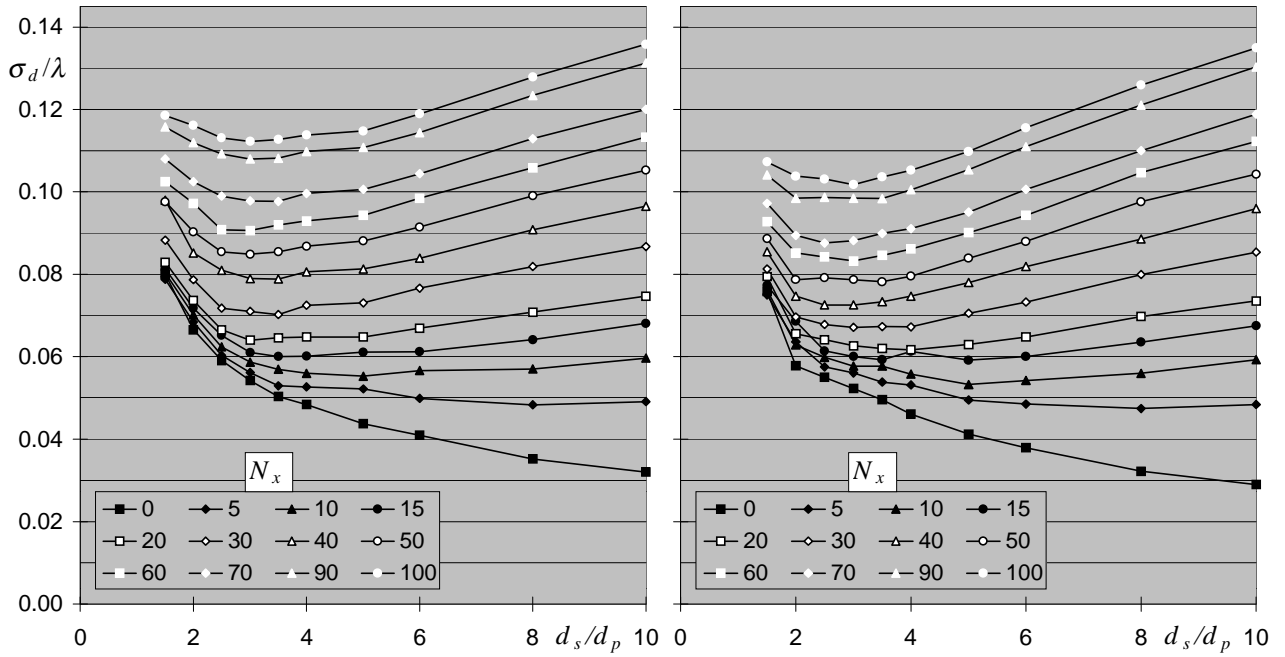


Fig. 6.2:  $\sigma_d$  for ESPI displacement measurements by SPS with  $\alpha_x = 120^\circ/\text{column}$  (left) and  $\alpha_x = 90^\circ/\text{column}$  (right) as a function of speckle size for out-of-plane displacements. The parameter for each curve is  $N_x$ , the number of vertical fringes per 1024 pixels, as indicated in the legend boxes.

The figure shows clearly that  $\alpha_x = 90^\circ/\text{column}$  yields indeed better performance over the whole range of fringe densities. The difference is small at low fringe densities, whereas it gets significant over  $N_x \cong 30$ ; it is most pronounced at the optimum speckle size of  $3 d_p$ .

In the face of these findings, it seems more appropriate to set  $\alpha_x = 90^\circ/\text{sample}$ . As already hinted in 3.2.2.3, it was found out that the phase calculation with the  $90^\circ$  formula (e.g. (3.19)) tolerates large miscalibrations of  $\alpha_x$ ; there is practically no loss in performance for deviations of  $\alpha_x$  of up to  $\pm 15^\circ/\text{sample}$ . Moreover, the error-compensating  $90^\circ$  formulae are more suitable than those with  $\alpha = 120^\circ$  for the averaging procedures described in 3.2.2.4.

The phase determination with  $\alpha_x = 120^\circ/\text{sample}$  quickly loses accuracy when  $\alpha_x > 120^\circ/\text{sample}$  and functions even slightly better when  $\alpha_x \cong 100^\circ/\text{sample}$ . This can be attributed to the facts that (i) the sidebands of the interferogram's power spectrum already contain aliased super-Nyquist frequencies  $|v_x| > |v_N|$  at  $v_{x0} = 1/(3 d_p)$  and  $d_s = 3 d_p$  (cf. 3.4.4), and (ii) also the horizontal MTF of the camera that I used drops considerably for higher spatial frequencies. Hence, the signal power is utilised more efficiently by the  $90^\circ$  method, where the sidebands are neatly centred in the  $(f_{x\pm}, f_y)$  half-planes, as depicted in Fig. 6.3.

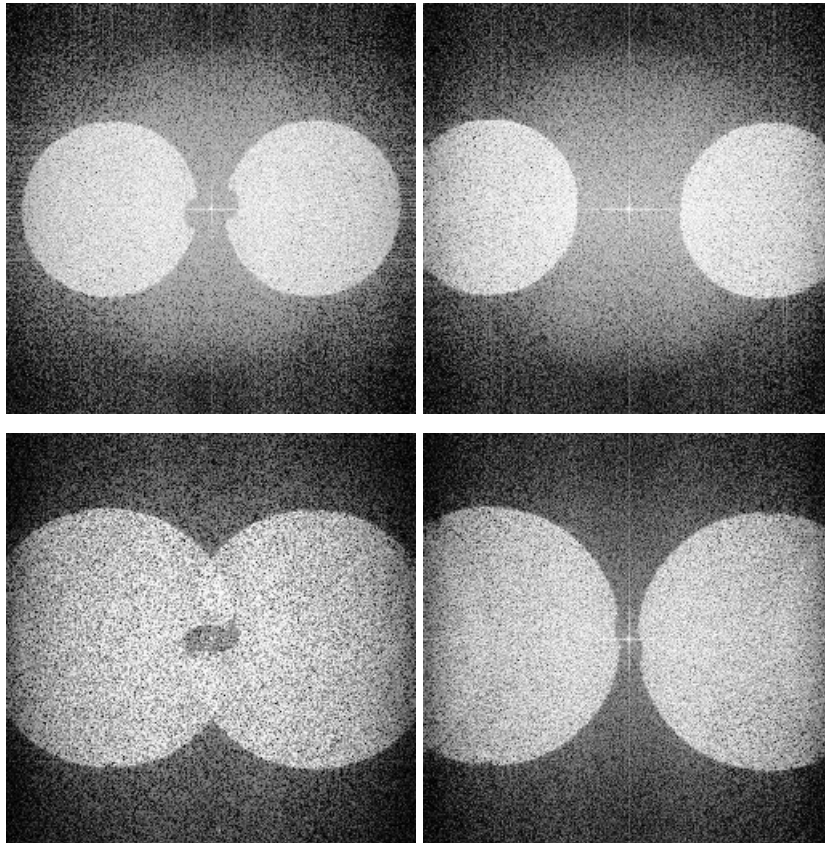


Fig. 6.3: Interferogram power spectra (log scale). Upper row,  $d_s = 3 d_p$ ; lower row,  $d_s = 2 d_p$ ; left,  $\alpha_x = 90^\circ$ /column; right,  $\alpha_x = 120^\circ$ /column. Irregularities in the spectra are due to the fibre guide obscuring part of the aperture. The contrast of the images has been enhanced to make the speckle halo visible.

It is also clear that a decrease of the speckle size, as shown in the lower row, will shift the advantage even more towards  $\alpha_x = 90^\circ$ /sample because this minimises "crosstalk" of the sidebands around both  $\nu = 0$  and  $\nu = \nu_N$ , as discussed in Chapter 3.4.4. On the other hand, the sidebands have less overlap with the speckle halo for larger phase shifts; but evidently, the issue of speckle size is more important.

### 6.1.3 Speckle aspect ratio

In Chapter 5.6, we saw what improvement a change to an elliptical aperture can bring about when the available illumination power is critical. However it is by no means necessary to choose a 1:3-elliptical aperture. For instance, an aspect ratio of, say, 1:2 means less anisotropy, at the cost of light, while an aspect ratio of, say, 1:4 improves the light gain but generates elongated speckles, and accordingly, a distinct anisotropy of measurement. The change in performance need not be restricted to the spatial direction in which the speckle size is reduced: the finer overall phase structure of the speckle pattern could increase the noise in the whole measurement, which would diminish the advantage gained by the larger aperture.

This subsection attempts to answer the question what speckle aspect ratios can be used and at what gain or expense. Since the course of  $\sigma_d$  as a function of object illumination is similar for TPS and SPS (cf. Fig. 5.18), we just retain here that the gain in accuracy may be related to the gain in light as before, only now

we are concerned particularly with the geometrical side-effects due to the anisotropy of the measurement. To find out their nature and extent, we carry out the experiments with sufficient object light in an out-of-plane configuration.

The "overall" effect of decreasing the speckle height  $d_{sy}$ , while keeping the width  $d_{sx}$  constant, can be studied by a series of tilts about the  $y$  axis, giving rise to vertical sawtooth fringes. The speckle decorrelation with increasing  $N_x$  is then governed by  $d_{sx}$  and is therefore the same for all  $d_{sy}$ . Fig. 6.4 presents some results from these series.

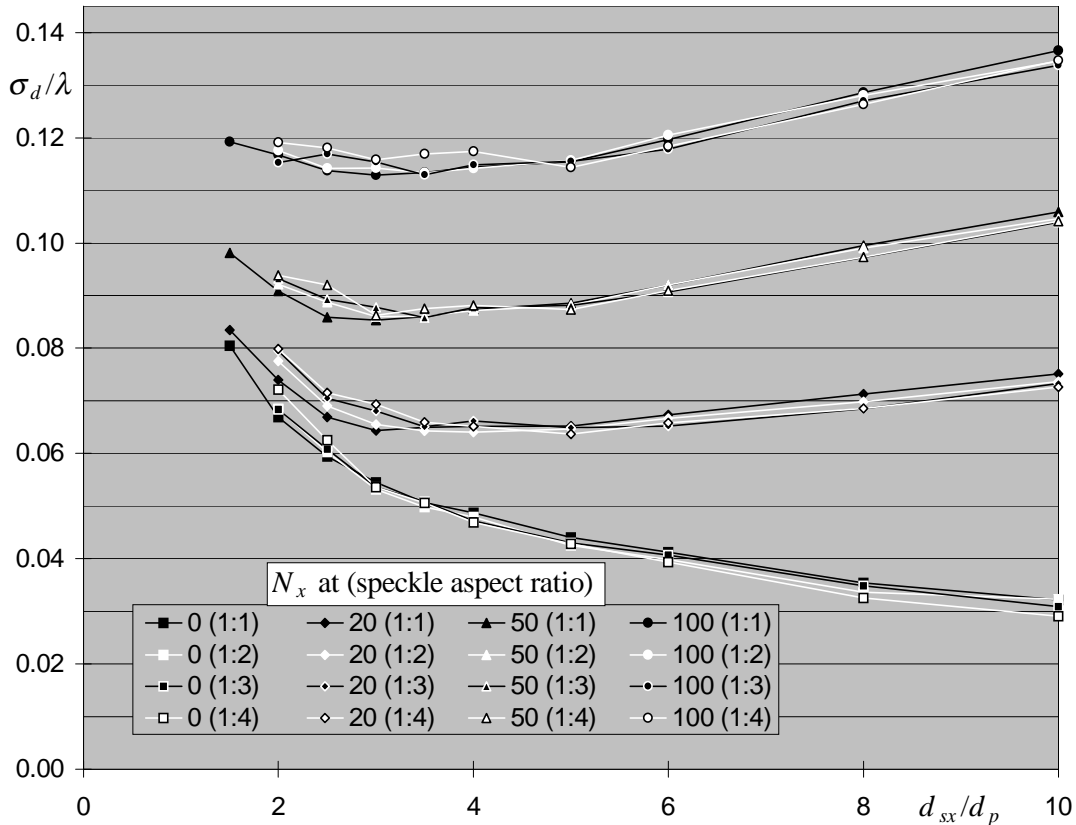


Fig. 6.4:  $\sigma_d$  for ESPI displacement measurements by SPS with various speckle aspect ratios as a function of speckle width  $d_{sx}$  for out-of-plane displacements. The parameters for the curves are  $N_x$  and the respective aspect ratio, as indicated in the legend box.

This figure should be interpreted as follows: given a certain speckle width  $d_{sx}$ , the aspect ratio  $d_{sy}/d_{sx}$  indicates the respective speckle height  $d_{sy}$  indirectly; e.g. at a speckle width  $d_{sx}$  of  $3 d_p$  and an aspect ratio of 1:2, the corresponding speckle height  $d_{sy}$  is  $1.5 d_p$ . Consequently,  $d_{sx} \geq d_{sy}$  in this study.

For zero displacement,  $\sigma_d$  is virtually independent of the speckle aspect ratio. For the other curves, corresponding to  $N_x = 20, 50,$  and  $100$ , there is indeed a very slight systematic dependence of  $\sigma_d$  on the aspect ratio from  $d_{sx} = 4 d_p$  downwards. This corresponds to  $d_{sy} \leq 2 d_p$  and shows that the finer phase structure does reduce the accuracy; but compared to the performance gain that a wider aperture offers under critical light conditions, the effect is negligible.

Things are different when we consider a series of tilts about the  $x$  axis; in this case we test the effect of the varying speckle heights and investigate the measurement anisotropy. Fig. 6.5 shows the results for the same fringe densities as above.

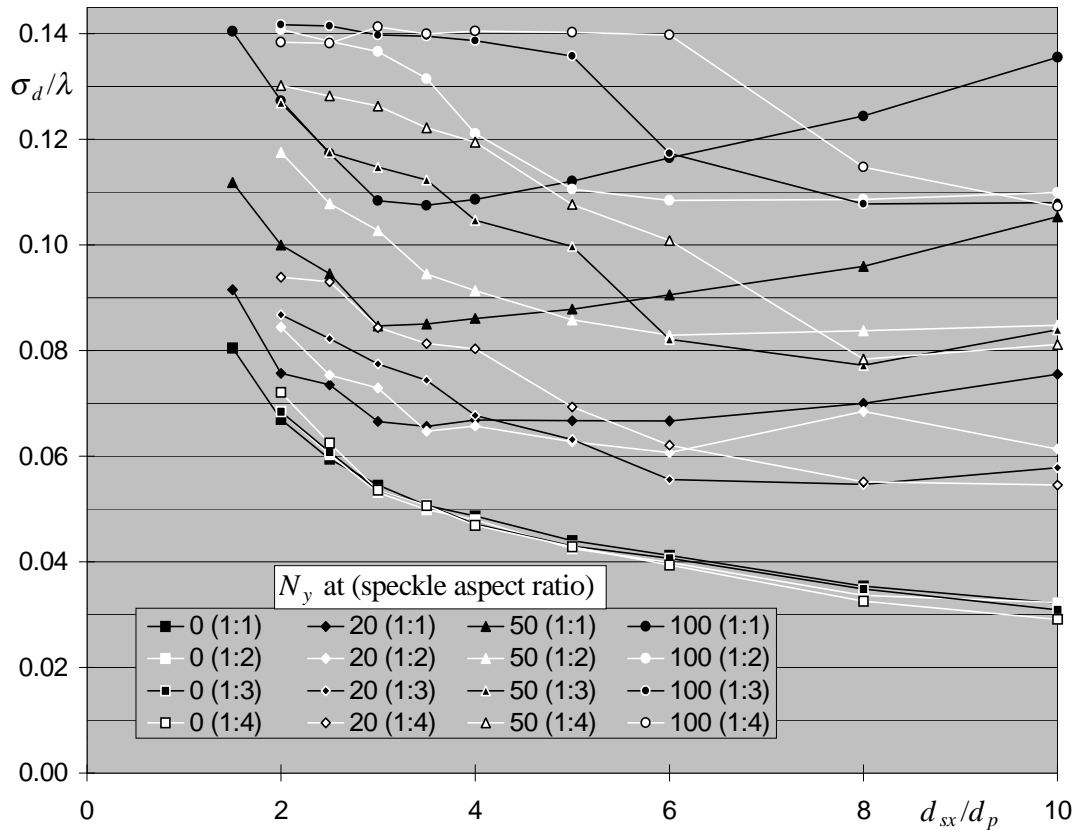


Fig. 6.5:  $\sigma_d$  for ESPI displacement measurements by SPS with various speckle aspect ratios as a function of speckle width  $d_{sx}$  for out-of-plane displacements. The parameters for the curves are  $N_y$  and the respective aspect ratio, as indicated in the legend box.

The order in this graph is best understood if the data are first read vertically: for small speckle widths, a reduction of  $d_{sy}$ , and therefore the aspect ratio, is accompanied by a larger  $\sigma_d$ . This effect increases with the fringe density, for reasons already discussed in Chapter 5.4. However for larger  $d_{sx}$ , smaller  $d_{sy}$  tend to yield lower  $\sigma_d$  than for an aspect ratio of 1:1 because the fringes are better resolved and decorrelate more slowly, as also described in Chapter 5.4.

No general recommendations can be derived from this behaviour because the anisotropy effects are specific of the used interferometer. The decision for or against elliptical speckle depends on the expected result of the experiment, as well as on the amount of light actually available, and there may also be cases where an elliptical aperture is very helpful in suppressing aperture-plane decorrelation.

For moderate fringe densities, it is always possible to gain twice the object light by using a 1:2 aperture without sacrificing too much of the isotropy. In this work however, there is no shortage of object light; and later on, we will also use a phase shift in  $x$ - and  $y$ -direction to make use of the 2-D extent of circular speckles. Hence we will keep using circular apertures.

## 6.2 Modified phase reconstruction formulae

Besides the optimisation of optical parameters, it is of course desirable to utilise some of today's knowledge about phase-sampling methods to tailor phase calculation methods specially for SPS. As mentioned before, the most stringent restriction for error suppression is the small number of sampling points available in the speckles that we even wish to make as small as possible. In the following paragraphs, we explore possibilities to construct few-sample formulae with reasonable rejection of errors due to speckle intensity and phase gradients, and eventually we test the combination of these approaches in out-of-plane ESPI deformation measurements.

### 6.2.1 Consideration of speckle intensity gradients

One possible way to reduce the phase errors induced by the fluctuations of the object wave's intensity has already been shown in 6.1.1. As we have seen in Chapter 2.2.3.1, it would be very difficult to account for the  $I_x$  statistics of a speckle field in SPS: the assumptions that we could model by a modified three-sample formula would be too crude in the case of speckle intensity.

There is however an exact method of compensating the errors due to intensity fluctuations; it relies on an additional measurement of the speckle intensity alone before or during the displacement observation. In the linear equation system constituted by (3.68), we usually assume  $O$ , and hence  $I_b$  and  $M_I$ , to be constant in all the equations. If however each equation gets its own  $O_n$  from a speckle intensity image stored beforehand, it is still possible to solve for  $\varphi_O$ , as long as we use three phase steps of  $(-\alpha, 0, \alpha)$ . Details of this procedure are outlined in Appendix C; with  $D_n := I_n - O_n$ , we arrive at [Bot97]

$$\varphi_O \bmod 2\pi = \arctan \frac{\sqrt{O_0}(D_1 - D_{-1}) + \cos\alpha(\sqrt{O_{-1}}(D_0 - D_1) + \sqrt{O_1}(D_{-1} - D_0))}{\sin\alpha(\sqrt{O_1}(D_{-1} - D_0) - \sqrt{O_{-1}}(D_0 - D_1))}, \quad (6.4)$$

which is for  $\alpha = 90^\circ$ :

$$\varphi_O \bmod 2\pi = \arctan \frac{\sqrt{O_0}(D_1 - D_{-1})}{\sqrt{O_1}(D_{-1} - D_0) - \sqrt{O_{-1}}(D_0 - D_1)} \quad (6.5)$$

and for  $\alpha = 120^\circ$ :

$$\varphi_O \bmod 2\pi = \arctan \frac{2\sqrt{O_0}(D_1 - D_{-1}) - \sqrt{O_{-1}}(D_0 - D_1) - \sqrt{O_1}(D_{-1} - D_0)}{\sqrt{3}(\sqrt{O_1}(D_{-1} - D_0) - \sqrt{O_{-1}}(D_0 - D_1))}. \quad (6.6)$$

Of course, these formulae collapse to their standard versions (3.18) and (3.17) when  $O_{-1}=O_0=O_1$ .

A disadvantage of this method is the necessity to record speckle images before and, if decorrelation occurs, also during the measurement. This will rule out highly dynamic phenomena and reduce the

temporal resolution in other measurements. Moreover, (6.4) assumes  $R$  and  $O$  to be fully interferent, which is not the case when depolarising objects are being tested. In this case, one must accept that the treatment overestimates  $M_I$  (which is related to the square roots), or re-polarise the waves appropriately.

A comparison of (3.19) and (6.6) with stable speckle patterns is given in Fig. 6.1, which shows  $\sigma_d$  from phase calculations without (black squares) and with intensity correction (black squares filled white) as a function of  $B$ . The data leading to the curves were the very same set of interferograms in both cases. For the intensity correction, I used both the initial and final speckle patterns for the respective object states. The figure shows that (6.6) is indeed able to keep  $\sigma_d$  almost constant for  $1 \leq B \leq 10$ . When we compare the best  $\sigma_d$  of either evaluation series, the improvement by the intensity correction amounts to  $\cong 3\%$ . This is quite small a difference and it may seldom be worthwhile to record extra speckle images to make use of it. Moreover, it will not help against the most likely problem in SPS, namely too low speckle intensity.

With increasing  $B$ , i.e. fading  $\langle O \rangle$ , the performance of (6.6) quickly worsens. This is because speckle intensity readings of zero are obviously not permissible in (6.4): the phase calculation will not function for points of the speckle image that are digitised to zero. But as  $B$  is increased, as desirable from a practical point of view, exactly this will occur more and more frequently. Then (6.4) breaks down on a fraction of image pixels that grows larger as the speckle pattern gets darker.

In practice, one can circumvent this by simply replacing the zeros under the square roots by a non-zero value (for simplicity, a factor of one); this introduces some arbitrariness in the calculation and is justified only by the observation that this *ad hoc* remedy is better than none in this case, and that (6.5) and (6.6) then become their standard versions (3.18) and (3.17) also for  $O_{-1}=O_0=O_1=0$ . Therefore the advantage gained by the modified calculation must vanish as the  $O_n$  approach each other. This is also shown in Fig. 6.1: the modified intensity-correcting formula overriding zero readouts for the  $O_n$  (black curve, white squares) links smoothly to the curve without error correction; from  $B \cong 50$  on, both curves are very nearly the same. Therefore the  $\sigma_d$  from the intensity-correcting formula are not plotted anymore for  $B \gtrsim 160$ , all the more as using (6.4) would only lead to superfluous computational effort for higher  $B$ .

The data shown pertain to the depolarised speckle patterns which the test object generates directly; no substantial improvement was found when the intensity correction was applied to speckle patterns exclusively co-polarised with the reference light. This shows that the subtraction of the speckle background, taking place in the  $D_n$ , is more important than the exact  $M_I$ ; also, the background subtraction is justified for any polarisation state.

To check the preliminary results of Fig. 6.1, I carried out several tilt series with  $\alpha_x = 90^\circ/\text{sample}$  and  $B \in \{3, 10, 30, 100, 300\}$ . As seen before, this quasi-geometric series of  $B$  values is sufficient to find the best performance of either method. Fig. 6.6 presents an overview of the best results for  $d_s=3 d_p$ .

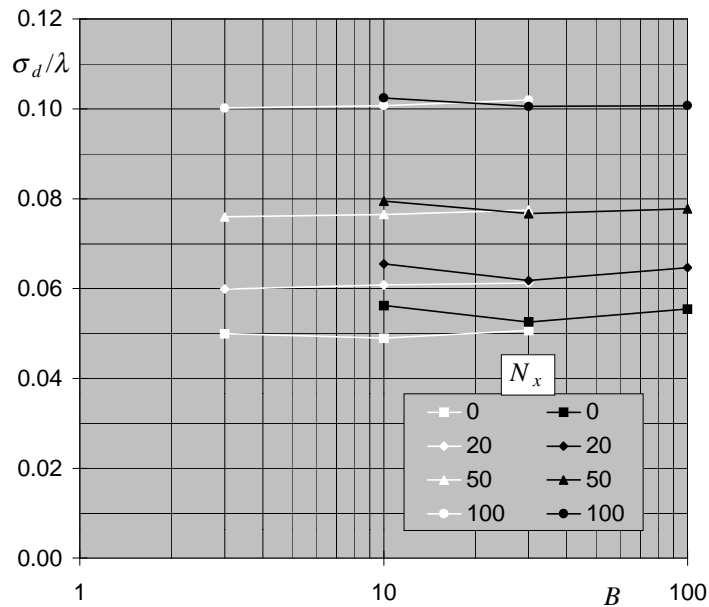


Fig. 6.6:  $\sigma_d$  for ESPI displacement measurements by SPS with and without intensity correction as a function of  $B$ . White, phase calculation according to (6.5); black, phase calculation by (3.19). Selected  $N_x$  as indicated in the legend box.

We have seen before in Fig. 6.1 that the advantage of using the intensity correction will vanish at  $B \cong 30$ ; therefore we look at (6.5) for  $B \in \{3, 10, 30\}$  only. On the other hand, without intensity correction the lowest  $\sigma_d$  occur around  $B \cong 30$ , which is why we select  $B \in \{10, 30, 100\}$  to investigate the phase calculation with (3.19). Fig. 6.6 confirms that the phase calculation by (3.19) (corresponding  $\sigma_d$ : black symbols) produces the lowest  $\sigma_d$  at  $B \cong 30$ , while (6.5) (corresponding  $\sigma_d$ : white symbols) operates most advantageously at  $B=3$  and  $B=10$  and slightly worse at  $B=30$ . As familiar by now, the differences of the two calculation methods are most pronounced at low fringe densities: initially, a reduction of  $\sigma_d$  by some 5% can be attained by using the intensity correction; but as  $N_x$  rises and decorrelation sets in, the difference vanishes almost completely. Hence, in most situations it will suffice to set  $B \cong 30$  and to record interferograms only.

### 6.2.2 Consideration of speckle phase gradients

When the speckles are as small as  $3 d_p$ , the phase structure of speckle patterns cannot be measured with sufficient sampling resolution by the pixels - and less so with SPS -, so that there is no possibility to go the same way as above with the intensities and use the speckle phases for error compensation. Yet remembering the findings of Chapter 2.2.5, the speckle phases seem to be less harmful for interferometry than the intensities anyway. Therefore we will use the simple assumption that not the speckle phase  $\varphi_O$ , but its gradient  $\varphi_{O,x}$  be constant over the short sequence of pixels that we use for phase retrieval. This is quite rough an approximation but it may be seen from Fig. 2.14 that it holds reasonably for the brighter parts of the image that we are mainly interested in. Treating the phase gradients in this way is equivalent to assuming local linear miscalibrations of the phase shift, as detailed in Chapter 3.2.2. We may then



construct our two consecutive sets of samples needed to apply the error compensation of (3.56) from a sequence of pixels as shown in Fig. 6.7.

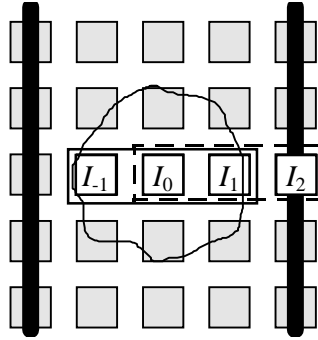


Fig. 6.7: Arrangement of sampling points for a simple phase-shift error compensating formula (3.56) with  $\alpha_x=90^\circ/\text{column}$ , indicated by the black bars. The intensity readings  $I_{-1}$  to  $I_2$  are taken from consecutive columns.

If  $\varphi'_{o_0}$  (cf. (3.56)) is constructed from  $I_{-1}$  through  $I_1$  (indicated by the solid-line box) and  $\varphi'_{o_1}$  from  $I_0$  through  $I_2$  (broken-line box) and these two phase measurements are averaged, the error in  $\varphi'_{o_0}$  will be almost cancelled by that in  $\varphi'_{o_1}$  thanks to their relative offset of  $\cong 90^\circ$ . (If the phase offset of  $\varphi'_{o_0}$  and  $\varphi'_{o_1}$  were exactly  $90^\circ$ , there would be no need for error correction.) It is true that this method of averaging requires four instead of three pixels and seemingly requires still larger speckles; we will discuss this issue shortly, in the context of the experimental findings. The improvement of phase calculation by (3.56) is shown in Fig. 6.8 for  $B = 30$  and  $d_s=3 d_p$ ; both curves have been calculated from the same set of interferograms.

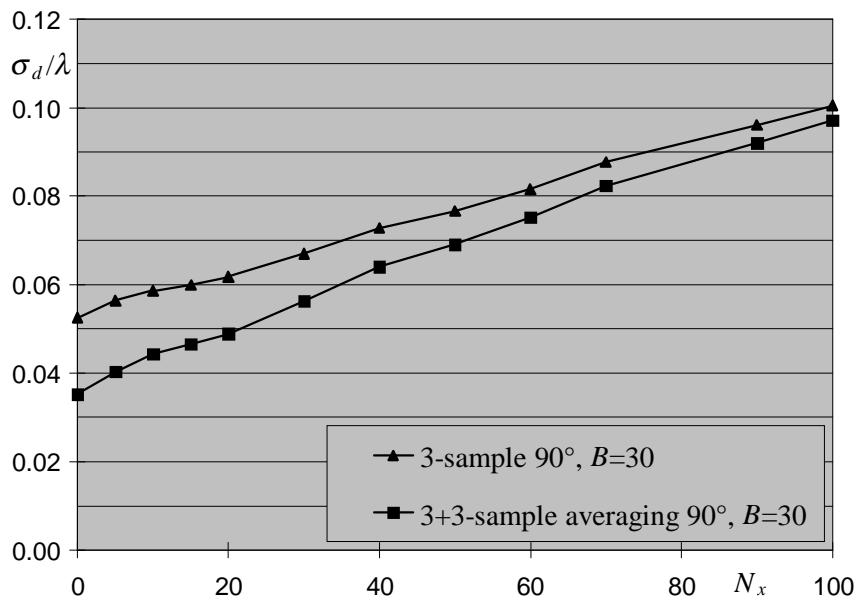


Fig. 6.8:  $\sigma_d$  for ESPI displacement measurements for  $B=30$  and  $d_s=3 d_p$  by SPS, with and without phase-shift error compensation, as a function of  $N_x$ . Triangles, phase calculation by (3.19); squares, phase calculation according to (3.56).

The modified phase calculation reduces  $\sigma_d$  very efficiently; and again the improvement is most relevant at low fringe densities. The substantial decrease of  $\sigma_d$  comes somewhat unexpected in this situation, since

Fig. 6.7 tells us that the complete sampling window is now definitely larger than the mean speckle size of  $d_s=3 d_p$ . But in addition to the phase-error compensation, (3.56) also constitutes stronger spatial averaging. Here, the sine and cosine functions are averaged before phase retrieval, which has been shown to be a better choice than averaging phase maps after the arctangent operation [Hun97].

Although the 3+3 averaging formula still calculates the phase separately for each pixel, there is a loss of spatial resolution associated with the larger sampling window. But since our "resolution cell" has already been 3 pixels wide before, the relative change is not significant; and up to (at least)  $N_x=100$ , the phase gradient of the object displacement is well resolved and shows less noise than with the standard phase calculation.

### 6.2.3 Combined intensity and phase gradient compensation

Each of the error-suppression strategies proposed suffers from the drawback that its effectiveness to cope with  $I_x$  or  $\varphi_{O,x}$  could be reduced by the fluctuations not accounted for, i.e.  $\varphi_{O,x}$  or  $I_x$ . Hence it is natural to combine both of the approaches to obtain a formula that reduces the  $\sigma_d$  caused by the speckle structure of both object intensity and phase. The simplest way to construct such a phase calculation is to establish an averaging formula for terms as in (6.4). With  $\alpha=90^\circ/\text{sample}$ , we rewrite (6.5) for the two "boxes" of Fig. 6.7 [Bur98a]:

$$\begin{aligned} \tan \varphi_{O_0} &= \frac{\sqrt{O_0}(D_1 - D_{-1})}{\sqrt{O_1}(D_{-1} - D_0) - \sqrt{O_{-1}}(D_0 - D_1)} := \frac{K_2}{K_3 - K_1}, \\ \tan \varphi_{O_1} &= \frac{\sqrt{O_1}(D_2 - D_0)}{\sqrt{O_2}(D_0 - D_1) - \sqrt{O_0}(D_1 - D_2)} := \frac{K_5}{K_6 - K_4}, \end{aligned} \quad (6.7)$$

with pixel indices according to Fig. 6.7, and numbering of the  $K_n$  according to the order of indices of the square roots at the beginning of each term. Now applying what we have learnt in Chapter 3.2.2.4, we can easily compose these two intensity-corrected phase calculations according to (3.55) and arrive at

$$\bar{\varphi}_O \bmod \pi = \arctan \frac{K_2 + K_4 - K_6}{-K_1 + K_3 + K_5}, \quad (6.8)$$

which is an averaging formula correcting for both intensity and phase fluctuations. As already indicated in Fig. 6.6, the intensity correction works best for  $B=3$ ; the contribution to  $\sigma_d$  coming from speckle phase gradients was assumed to be independent of  $B$ . Fig. 6.9 gives an overview of the best results from all combinations of phase-calculation methods and  $B$  values tested in this subsection. The black curves are repeated from Fig. 6.8 for comparison; for the intensity-correcting formulae, the underlying set of interferograms is necessarily a different one, with  $B=3$ , but also  $d_s=3 d_p$ .

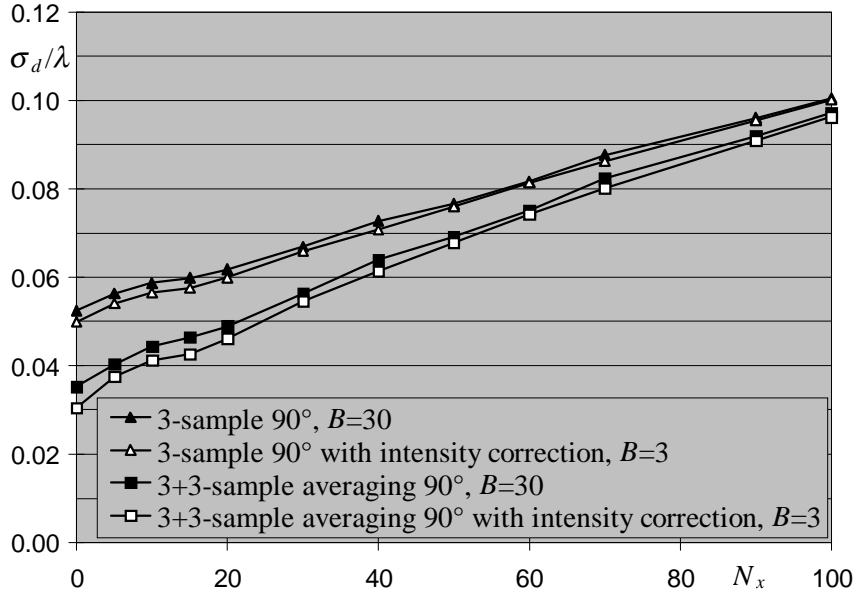


Fig. 6.9: Overview of  $\sigma_d$  from ESPI displacement measurements as a function of  $N_x$ , obtained with various phase calculation formulae from two series of interferograms: without intensity correction,  $B=30$  (black symbols); with intensity correction,  $B=3$  (black symbols filled white); 3-sample formulae, triangles; 3+3-averaging formulae, squares.

The summary presented in Fig. 6.9 allows some conclusions: (i) the use of a 3+3 averaging scheme alone is definitely a better choice than an intensity-error compensating formula alone. (ii) The combination of both error-reduction methods leads to the lowest overall error; at  $d_s=3 d_p$ ,  $\sigma_d$  remains below  $\lambda/20$  up to  $N_x=20$ . (iii) Introducing the intensity-error correction effects indeed a slightly greater improvement in  $\sigma_d$  when a phase-shift error elimination is already present, and vice versa. (In other words, the lower two curves are farther apart than the upper two.) This confirms the initial presumption that motivated this subsection: the two methods profit from each other if used together. However, as mentioned before, in most practical cases it will suffice to set  $B \cong 30$  and to do without the small benefit of the intensity correction, all the more since this speeds up the calculations considerably and even makes them accessible to the use of look-up tables.

Finally, it may be worth noting that a 3+3 averaging formula according to [Bur98a]

$$\bar{\varphi}'_O \bmod \pi = \arctan \frac{K_2 + K_5}{-K_1 + K_3 - K_4 + K_6} \quad (6.9)$$

is error-compensating only by averaging, but does not eliminate the cyclical errors shown in Fig. 3.39, since it constitutes the average over  $\varphi_O$  and  $\varphi_O+90^\circ$ . Hence, (6.9) will do little more for error reduction than the intensity correction without averaging, which means that even the pure phase-shift error compensation of (3.56) would perform better. This was in fact found in [Bur98a], where (6.9) was used instead of (6.8), and emphasises the relevance of an optimal composition of the averaging formula.

Finally, both (6.5) and (6.8) were checked for their spectral transfer properties by means of  $bsc(v_x)$ . With the same input interferograms and averaging of the same portions of the  $bsc(v_x, v_y)$  maps as in 3.4.5, this gives the plots shown in Fig. 6.10.

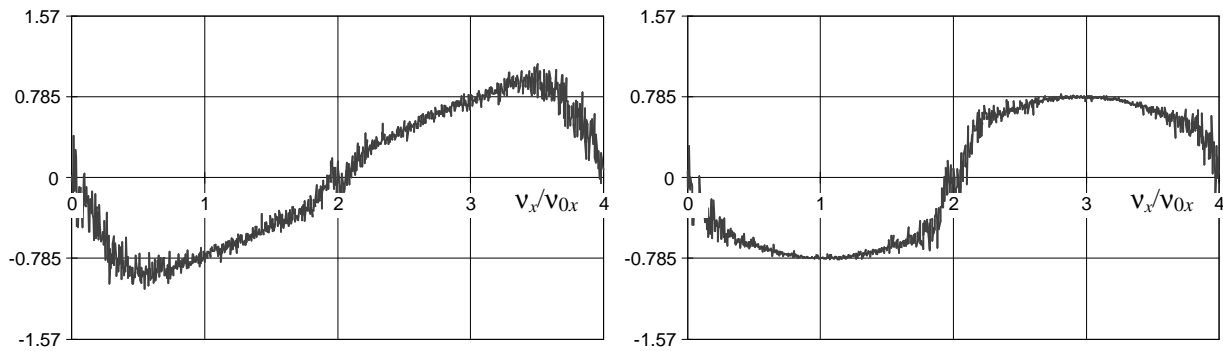


Fig. 6.10: Left:  $bsc(v_x)$  for (6.5); right:  $bsc(v_x)$  for (6.8).

By comparison with the graphs in Fig. 3.33 and Fig. 3.36, it can be seen that the noise has got higher; but for (6.8), the region of low detuning errors is distinctly increased as compared to (6.5). However it was found that the phase error  $\delta\varphi_O(\Delta\varphi)$  (cf. Fig. 5.4) produced by (6.8) has small maxima at  $\Delta\varphi=\pi/2$  and  $3\pi/2$  (cf. Fig. 3.39), which indicates that  $\delta\varphi_O$  due to phase-shift errors is suppressed less efficiently when the intensity correction is used.

### 6.3 Modified phase shifting geometry

If we use a circular aperture with a phase shift  $\alpha_x$  only, and if the measuring points are arranged as in Fig. 3.26, we discard the phase information that would be accessible via the vertical coherence length of the speckles. But due to the general shortage of spatial coherence in our small-speckle patterns, we should use it as exhaustively as possible. During the comparison of different phase retrieval approaches that will be described in this subsection, the  $\sigma_d$  refer to just two sets of interferograms, namely a tilt series with  $B=3$  when intensity correction is involved, and another with  $B=30$  when it is not. In both cases,  $N_x \in [0, 100]$  and  $d_{sx} = 3 d_p$ .

Provided a frame-transfer or line-transfer camera with progressive scan readout is available, all image lines can be acquired simultaneously. Then it is possible to introduce an additional vertical phase shift  $\alpha_y$  by simply shifting the origin of the reference wave to  $(\Delta x, \Delta y)$ . This results in a slant of the carrier fringes and allows to choose any desired direction for the set of pixels to use. Examples of composite phase shifting have been given in [Küch91, Küch97] for classical and in [Wil91] for speckle interferometry.

When the speckle shape can be fully exploited for measurement, the measurement's accuracy should improve, since the ideal situation of Fig. 3.26, where all the used pixels are inside the same bright speckle, is unlikely to occur. More often, speckle "boundaries" are crossed, which results in an unreliable phase measurement. To diminish the noise, it should help to include the possibly better data of the orthogonal direction and to establish an averaged phase value.

A phase shift of  $(\alpha_x, \alpha_y)=(90^\circ, 90^\circ)$  yields carrier fringes slanted by  $45^\circ$  and permits arranging the evaluated pixels in various ways. This is shown in Fig. 6.11: the target pixel of the phase calculation is  $I_3$ , with some arbitrary phase of  $\varphi_0$ , and the surrounding pixels have nominal phase shifts of  $\varphi_0 \pm 90^\circ$  as indicated. Note that the pixel numbering can no longer indicate relative phase shifts (e.g.,  $\alpha_1 = \alpha_2$ ); besides, we will identify the intensities  $I_n$  simply by pixel numbers  $n$  where appropriate for simplicity of notation. The geometry in Fig. 6.11 on the left suffices to use (3.19) for phase retrieval in both  $x$ - and  $y$ -direction;  $I_3$  will be assigned the average of the calculations. To the right, some additional pixels with  $\varphi_0 + 180^\circ$  give the possibility to use 3+3 averaging formulae; both of the methods will be explained below.

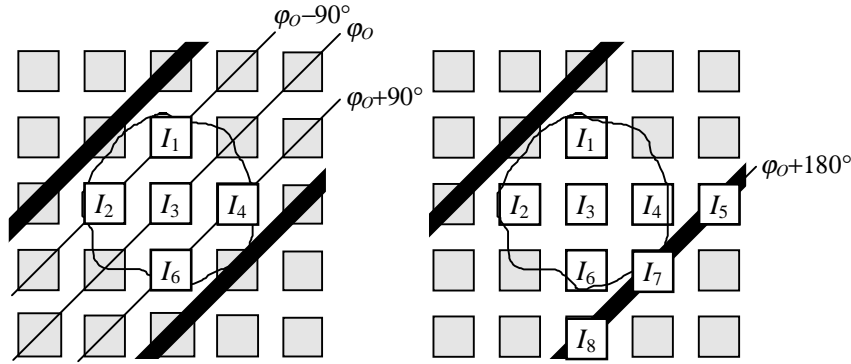


Fig. 6.11: Pixel clusters for phase calculation from oblique carrier fringes; orientation and spacing indicated by black bars. For simplicity, pixels are numbered consecutively. Left-hand side: pixels usable for 3-point formulae; right-hand side: pixels usable for 3+3-point formulae.

At this point it should be noted that the reduction in  $M_I$  now needs to be determined by (3.67), since the carrier frequency has an  $x$ - and a  $y$ -component. Therefore, for  $\alpha_x = \alpha_y = 90^\circ$ , we get  $(\sin(\pi/4)/(\pi/4))^2 = 0.81$ . Consequently, another 10% of modulation is lost, which will lower the optimum value of  $B$  somewhat.

Now, using (3.19), a double phase determination is possible for pixel 3, according to

$$\tan \varphi_0 = \frac{I_4 - I_3}{I_2 - I_3} = \frac{I_6 - I_3}{I_1 - I_3}, \quad (6.10)$$

which corresponds to the  $x$ - and  $y$ -direction, respectively. The phase is then determined from

$$\tan \bar{\varphi}_0 = \frac{(I_4 - I_3) + (I_6 - I_3)}{(I_2 - I_3) + (I_1 - I_3)} = \frac{I_4 - 2I_3 + I_6}{I_1 - 2I_3 + I_2}; \quad (6.11)$$

this is neither a new phase-shifting formula, nor an extended averaging scheme in the sense of [Schmi95]. Instead we get an average that, despite being spatial, does not reduce the resolution of the measurement. It serves to decrease  $\sigma_d$ , although the phase measurements involved are not completely statistically independent, since the central pixel 3 is used twice. Note also that the other two possibilities of calculating the phase, with pixels  $\{1, 3, 4\}$  and  $\{2, 3, 6\}$ , would just double the numerator and denominator in (6.11), which has no effect.

To use the intensity correction, we re-define our auxiliary quantities, the  $K_n$ :

$$\begin{aligned} (\tan \varphi_o)_1 &= \frac{\sqrt{O_3}(D_4 - D_2)}{\sqrt{O_4}(D_2 - D_3) - \sqrt{O_2}(D_3 - D_4)} := \frac{K_2}{K_3 - K_1} \\ (\tan \varphi_o)_2 &= \frac{\sqrt{O_3}(D_6 - D_1)}{\sqrt{O_6}(D_1 - D_3) - \sqrt{O_1}(D_3 - D_6)} := \frac{K_5}{K_6 - K_4} \end{aligned} \quad (6.12)$$

and obtain

$$\bar{\varphi}_o \bmod \pi = \arctan \frac{K_2 + K_5}{-K_1 + K_3 - K_4 + K_6}, \quad (6.13)$$

which method of averaging is correct for this purpose, since both expressions should yield the same phase. (In this case, the inclusion of two more quotients from pixels {1, 3, 4} and {2, 3, 6} is not equivalent to a doubling of the terms; but on doing so, the reduction of  $\sigma_d$  is minimal.) The spectral transfer properties of (6.11) and (6.13) are now genuinely two-dimensional, so that we can rewrite (3.73) as

$$\begin{aligned} bsc(v_x, v_y) &= \arg\left(\tilde{I}(v_x, v_y) \cdot \tilde{C}(v_x, v_y) + \tilde{I}(v_x, v_y) \cdot \tilde{S}(v_x, v_y)\right) - \arg\left(\tilde{I}(v_x, v_y) \cdot \tilde{C}(v_x, v_y)\right) \\ &= \arg\left(1 + \frac{\tilde{S}(v_x, v_y)}{\tilde{C}(v_x, v_y)}\right) \end{aligned} \quad (6.14)$$

and examine the course of  $bsc(v_x, v_y)$  experimentally by the now familiar 2-D representation. This is done in Fig. 6.12. Both maps of  $bsc(v_x, v_y)$  are calculated from the same input interferogram, only (6.13) processes also the previously stored speckle pattern  $O(x, y)$ . Since  $\alpha_x = \alpha_y = 90^\circ/\text{sample}$ , one can use  $d_s = 2.5 d_p$  (cf. 3.4.4), whereby each signal band fills approximately one quadrant of the spatial frequency plane. The left-hand image in Fig. 6.12 visualises this arrangement.

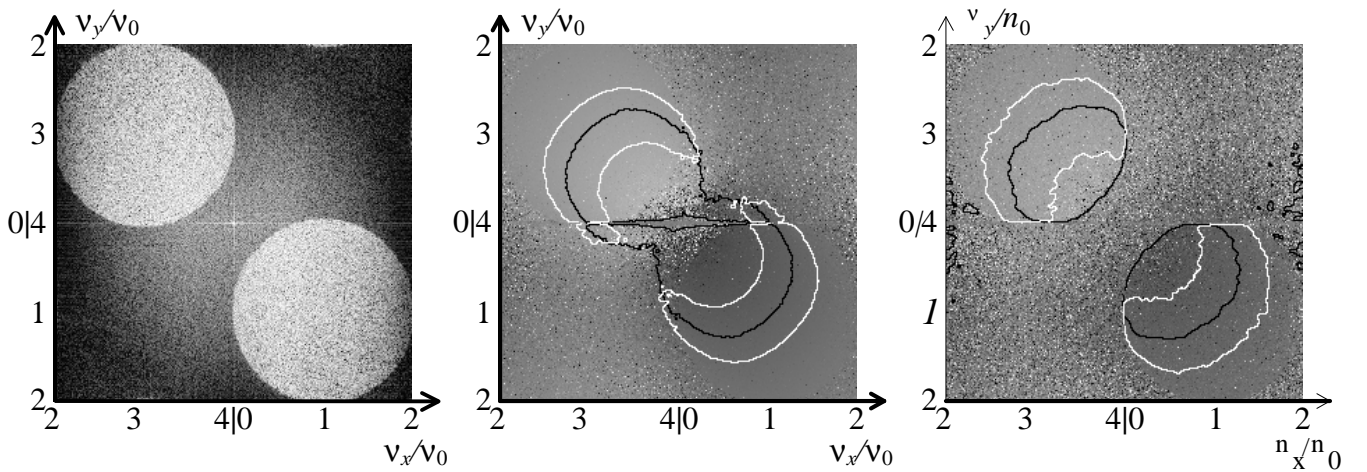


Fig. 6.12: Left: power spectrum of input interferogram (displayed in contrast-enhanced log scale); centre:  $bsc(v_x, v_y)$  for (6.11); right:  $bsc(v_x, v_y)$  for (6.13). Black lines: frequency co-ordinates leading to correct phase calculation,  $bsc(v_x, v_y) = \pm 45^\circ$ ; white outlines: areas of  $-10^\circ \leq \delta\varphi \leq 10^\circ$ .

In these images, the behaviour of  $bsc(v_x, v_y)$  on the line given by  $v_x = v_y$  corresponds to the one-dimensional cases we have considered before. The black lines indicate correct phase calculation

( $b_{sc}(v_x, v_y) = \pm 45^\circ$ ), and of course, one point on these lines is  $v_x = v_y = v_0$ . But also for  $v_x = v_0$  and  $v_y = 0$ , and vice versa, it is easy to see that the phase-extraction formulae will operate correctly, although only one-dimensionally in either case. By the addition of phasors from both directions however, the interesting fact results that  $b_{sc}(v_x, v_y)$  has the correct value all along the black lines in Fig. 6.12; this means that compositions of two "wrong" frequencies can still yield the correct phase. These lines are almost circles for (6.11); and also (6.13) delivers a similar shape, but only within the range of the signal frequency bands. We will not go into details as to the theoretical interpretation of these "circles of quadrature"; but one could argue that the signal bands should be re-positioned to obtain signal frequencies wherever there are black lines, which would maximise the fraction of signal frequencies yielding correct phases. Unfortunately, this is not true: one must bear in mind that phase-extraction formulae have weak response for low spatial frequencies, and none for zero frequency (cf. Chapter 3.2.2), so that signal energy would be wasted if the sidebands were shifted to touch at  $v_x = v_y = 0$ . An experimental test confirmed that this strategy leads to slightly worse measurements than with the nominally correct value of  $(v_x, v_y)$ .

The white outlines show those areas for which  $b_{sc}(v_x, v_y)$  stays within  $\pm 10^\circ$  deviation of its nominal value; as discussed above in Chapter 3.2.2.3, this means that the p-v phase errors  $\delta\phi_0$  are confined to  $10^\circ$  within these regions. They are broadest in the vicinity of  $v_x = v_y = v_0$ , which, in analogy to Fig. 2.13, shows that the phase calculation is more stable when the phasors  $\tilde{S}(v_x, v_y)$  and  $\tilde{C}(v_x, v_y)$  are long, i.e. when both  $v_x$  and  $v_y$  contribute to the phase determination.

The measured performance of (6.11) and (6.13) is summarised in Fig. 6.13, where the averaging of horizontal and vertical phase calculations is abbreviated by "90°/90°". The graphs for the usual 3-sample 90° formula are repeated from Fig. 6.9 to simplify the comparison. The interferograms for the "90°/90°" error evaluations have  $d_s = 3 d_p$  as well.

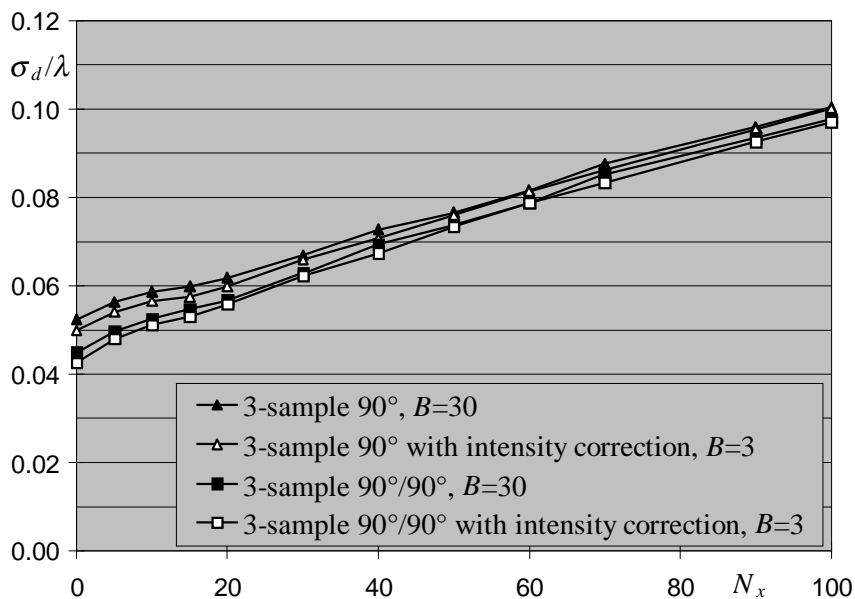


Fig. 6.13: Overview of  $\sigma_d$  from ESPI displacement measurements as a function of  $N_x$ , obtained with merely horizontal (triangles) and averaged horizontal/vertical phase determination (squares) from four series of interferograms (two of them already used for Fig. 6.9), all with  $d_s = 3 d_p$  but various phase shifts and  $B$  values.

The improvement in  $\sigma_d$  by averaging phase measurements can be clearly seen; but a comparison with the 3+3 averaging formulae of Fig. 6.9 reveals that their performance is not being reached. Therefore our next step will be to apply these as well in the averaging process, which can be done by extending the sampling pixel cluster as already shown on the right side of Fig. 6.11.

To use 3+3 averaging formulae horizontally and vertically, we have the four different possibilities to use pixels  $\{2, 3, 4, 5\}$ ,  $\{1, 3, 6, 8\}$ , being the familiar horizontal and vertical calculations, and  $\{1, 3, 4, 7\}$ ,  $\{2, 3, 6, 7\}$ . The latter combinations will still work in the presence of a constant speckle phase gradient  $\varphi_{O,x}$ , or  $\varphi_{O,y}$ ; but since the pixels involved are not on a straight line, they would additionally impose  $\varphi_{O,x} = \varphi_{O,y}$ , which cannot reasonably be inferred from Fig. 2.14. On the other hand, pixel 7 is spatially closer to pixel 3, which is again our target point for all the calculations, and hence has greater spatial coherence with respect to pixel 3 than pixels 5 or 8. Therefore we use

$$\tan \varphi_O \bmod 2\pi = \frac{2(I_4 - I_3)}{I_2 - I_3 - I_4 + I_5} = \frac{2(I_6 - I_3)}{I_1 - I_3 - I_6 + I_8} = \frac{2(I_4 - I_3)}{I_1 - I_3 - I_4 + I_7} = \frac{2(I_6 - I_3)}{I_2 - I_3 - I_6 + I_7} \quad (6.15)$$

to establish

$$\bar{\varphi}_O \bmod 2\pi = \arctan \frac{8I_3 - 4I_4 - 4I_6}{2I_1 + 2I_2 - 4I_3 - 2I_4 + I_5 - 2I_6 + 2I_7 + I_8}. \quad (6.16)$$

There is also the possibility to inscribe four more pixel sequences in the shape of an L (plus appropriate reflections and rotations) into the pixel cluster of Fig. 6.11; but again, this would merely double the terms in (6.16) and we do not take them into account.

Since the definitions for the corresponding intensity-correction formulae are rather lengthy, I do not go into detail here; the principle is already indicated in (6.12) and (6.13) where only the pixel indices have to be inserted appropriately. It may suffice to note that again only the pixel sets  $\{2, 3, 4, 5\}$ ,  $\{1, 3, 6, 8\}$ ,  $\{1, 3, 4, 7\}$ , and  $\{2, 3, 6, 7\}$  need be used. Also in this case, it will be interesting to examine the two-dimensional frequency characteristics of these approaches experimentally with the help of  $b_{sc}(v_x, v_y)$ . These are shown in Fig. 6.14, with the same input interferogram (and speckle pattern,  $d_s=2.5 d_p$ ) as for Fig. 6.12 above.

In the plot for (6.16), the same circle structure of  $b_{sc}(v_x, v_y)=\pm 45^\circ$  shows up as above; but thanks to the correction of improper  $v_x$  and/or  $v_y$ , another line of correct phase determination appears at higher spatial frequencies. This enlarges the region where  $|\delta\varphi| \leq 10^\circ$  to cover almost the complete sidebands, which is of course incidental for this particular speckle size. While the shape of  $b_{sc}(v_x, v_y)=\pm 45^\circ$  looks qualitatively different for the intensity-correcting formula, the stabilisation effect on the phase extraction is almost the same.



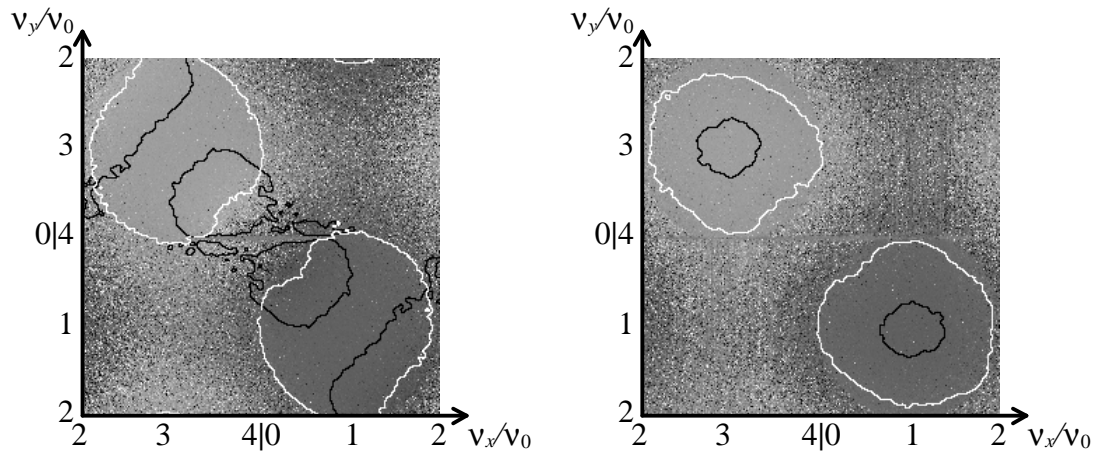


Fig. 6.14:  $b_{sc}(v_x, v_y)$  for (6.16) (left) and its intensity-correcting version (right). Black lines: frequency co-ordinates leading to correct phase calculation,  $b_{sc}(v_x, v_y) = \pm 45^\circ$ ; white outlines: areas of  $-10^\circ \leq \delta\phi \leq 10^\circ$ .

A summary of the results from (6.16) and from its intensity-correcting version is given in Fig. 6.15; note that the ordinate is scaled to a maximum of  $\sigma_d = 0.1\lambda$  to make differences visible. The graphs for the horizontal 3+3-sample averaging  $90^\circ$  formula are repeated from Fig. 6.9.

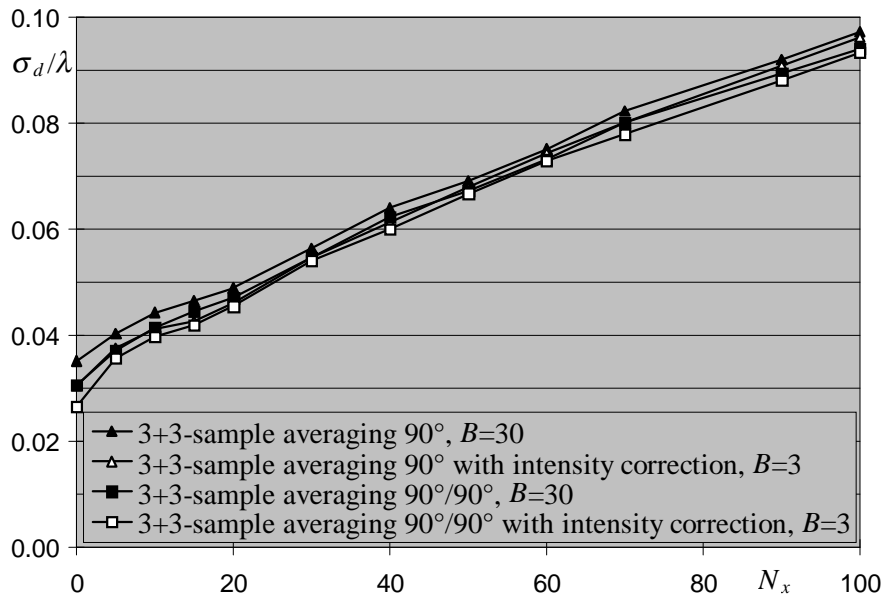


Fig. 6.15: Overview of  $\sigma_d$  from ESPI displacement measurements as a function of  $N_x$ , obtained with horizontal (triangles) and averaged horizontal/vertical phase determination (squares) by a 3+3-sample averaging formula; without intensity correction,  $B=30$  (black symbols); with intensity correction,  $B=3$  (black symbols filled white). Input interferograms were the same four series as for Fig. 6.13.

In this case, the improvement obtained by switching from  $(\alpha_x, 0)$  to  $(\alpha_x, \alpha_y)$ , with pertinent phase-evaluation formulae, is rather small; but its remarkable property is that it lasts up to (at least)  $N_x=100$ . This is in contrast to the other improvement strategies we have discussed so far (where the  $\sigma_d$  tended to become more or less the same for higher  $N_x$ ); it indicates that the speckle correlation remaining after displacements that give high fringe densities is indeed more efficiently utilised by the 2-D phase retrieval.

On the whole, it proves rewarding to use the full speckle extent for phase calculation, provided there is sufficient object light to afford a circular aperture. For practical reasons, one would wish to decrease  $d_s$  as far as possible; but in SPS, this has effects that we have encountered in Chapter 5 before: for  $d_s \leq 3 d_p$ ,  $\sigma_d$  increases, regardless of the respective fringe density.

#### 6.4 Reduction of speckle size

It seems worthwhile to see whether the methods to reduce  $\sigma_d$  developed so far can assist in obtaining "good" measurements from smaller speckles as well. Therefore we test two more speckle sizes, namely 2.5 and 2 pixels. The best phase calculation found in 6.3 was the average over four 3+3-sample phase determinations for each pixel, where the intensity correction contributed only a small improvement. Therefore we apply both (6.16) and its intensity-correcting extension to carry out these additional measurements. The results are shown in Fig. 6.16, where the last two curves for  $d_s=3 d_p$  are repeated from Fig. 6.15 for comparison.

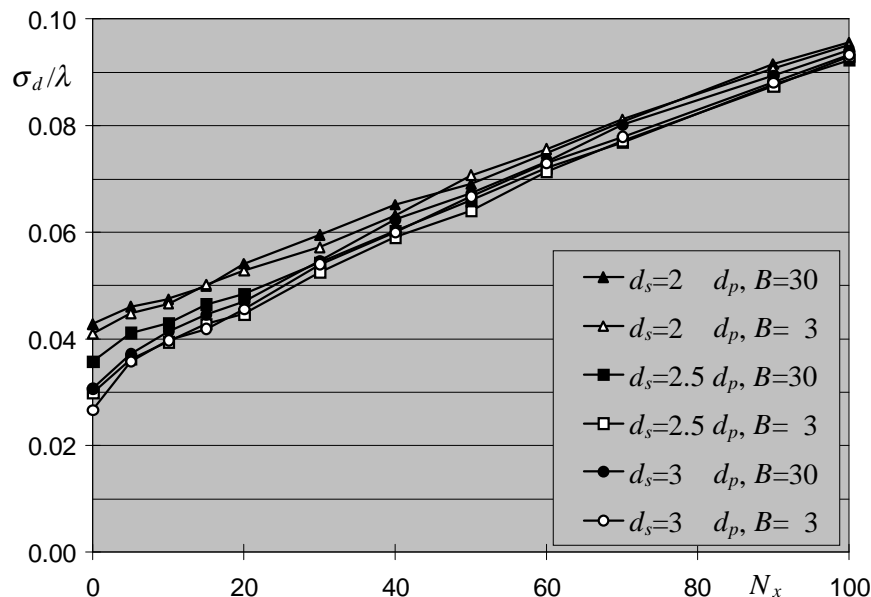


Fig. 6.16:  $\sigma_d$  from ESPI displacement measurements as a function of  $N_x$ , as calculated by (6.16) (black symbols) and its intensity-correcting extension (white filled symbols), with various  $d_s$  as listed in the legend box.

The results from  $d_s=3$  and  $2.5 d_p$  are very close together (except for  $d_s=2.5 d_p, B=30$  and low  $N_x$ ), they even cross each other sometimes, which means that the corresponding  $\sigma_d$  match within the determination uncertainty as explained in 5.2.2. This allows the conclusion that we may reduce the speckle size to  $2.5 d_p$  at virtually no harm for the measurement's accuracy. Considering the curves for  $d_s=2 d_p$ , the beginning increase of  $\sigma_d$  vs.  $d_s$  is clearly noticeable, especially at lower  $N_x$ . Hence we can conclude that an optimal adjustment of  $d_s$  should be between 2.5 and  $2 d_p$  for SPS, which is anyhow sufficient to collect between 1.5 and 2 times more light than with the "standard" choice of  $3 d_p$ .

One could think up even smaller evaluation clusters to deal with small speckles and possibly enhance the spatial resolution. Re-considering the arrangements of Fig. 6.11, it would be possible to use pixels  $\{1, 2, 3, 4, 6, 7\}$  only, which still allows for two 3+3-sample calculations, or even  $\{3, 4, 6, 7\}$ , where it is possible to average over two sets of 3 samples,  $\{3, 4, 7\}$  and  $\{3, 6, 7\}$ . But in both cases we have no

straight lines of pixels anymore, which leads to drawbacks already mentioned; and in the latter case, the averaging hardly makes sense due to very poor statistical independence of the pixel sets. Accordingly, these approaches do not deliver any improvement in the whole range of  $N_x$  values over the results already shown. Therefore it is also doubtful whether the formally expected increase in spatial resolution would actually turn up: very fine fringes might just disappear in higher noise.

To continue our quest for maximal accuracy in sawtooth images from spatially phase shifted interferograms, we will now put aside the phase-shifting methods in favour of the more general concept of the spatial frequency plane.

## 6.5 Fourier transform method of phase determination

In the discussion of 3.2.2, we saw that the spectral transfer functions of phase-sampling formulae are designed to function correctly at their nominal frequency only. While considerable improvements are possible by simple means, all phase-shifting formulae tend the more to falsify the signal the broader the sidebands are. So, instead of looking for a phase-evaluation window that delivers low noise while being as small as possible, one could switch to the other end of the scale and use instead a very large window: the whole image. Since the signal is encoded in a spectral sideband, it is quite natural – and convenient – to retrieve its phase from frequency space by a Fourier transform method (henceforth abbreviated by FT or FTM). It has been applied also to interferograms without a signal carrier [Kre86]; but that approach requires a-priori knowledge or one temporal phase shift to eliminate the sign ambiguity.

Although it would require sophisticated hard- and software even today to maintain the real-time capability of an ESPI system with carrier frequency and FT phase calculation, we do investigate the effect of it as a possible means of *a posteriori* data processing that still can run entirely automatically. It is intuitively clear that this approach should offer a distinct advantage over phase sampling: while phase sampling always works with local information from a very short sequence of samples, the FTM, as a global method, has access to all the image information simultaneously.

The way to retrieve phase information modulated on a carrier frequency by means of Fourier transforms has been described in [Tak82, Rod87]. The FTM lends itself to, *inter alia*, profilometry [Tak83], moiré [Mor94a], holographic [Qua96] and speckle interferometry [Sal96]. Here, we will of course consider the method with emphasis on speckle interferometry and also generalise the original 1-D treatment to two frequency dimensions, as first suggested in [Bon86].

There are numerous analyses as to the attainable accuracy [Mac83, Gre88, Kuj91c, Jož92], with the main results that the interferogram should be multiplied by an appropriate window function, or extrapolated, to minimise edge truncation effects; but as shown in [Koz99], they can also be eliminated exactly. We will not deal with such refined methods because (i) our digital resolution is rather large ( $1024 \times 1024$  pixels), so that the edge effects play a relatively small role, and (ii) the benefit for speckle images would hardly be significant.

In classical interferometry, it is necessary to determine and remove the carrier frequency for wavefront reconstruction [Nug85, dNic98, Li 98, Fer98]; in ESPI, this is fortunately done automatically by the image subtraction of the initial from the final speckle phase map.

Let  $|o(x,y)|\exp(i\varphi_o(x,y))=\mathbf{o}(x,y)$  be the complex amplitude of the speckle field; then the speckle intensity is  $O(x,y)=\mathbf{o}(x,y)\cdot\mathbf{o}^*(x,y)=|o(x,y)|^2$ , which we assume to be unity. Adding a reference wave  $\mathbf{r}(x,y)$ , the amplitude of the interferogram is  $\mathbf{i}(x,y)=\mathbf{o}(x,y)+\mathbf{r}(x,y)$ . By  $\mathbf{r}(x,y)=\sqrt{B}\cdot\hat{\mathbf{r}}\cdot\exp(i(2\pi\nu_{0x}x+2\pi\nu_{0y}y))$ ,  $\hat{\mathbf{r}}$  being the complex amplitude's unit, we adjust the beam intensity ratio to  $B$ , which is a real, positive and spatially constant factor, and the spatial carrier frequencies to  $\nu_{0x}$  and  $\nu_{0y}$ . The intensities in the interferogram are then

$$\begin{aligned} I(x,y) &= (\mathbf{o}(x,y)+\mathbf{r}(x,y))(\mathbf{o}(x,y)+\mathbf{r}(x,y))^* \\ &= O(x,y)+B\hat{\mathbf{r}}^2 \\ &\quad +\mathbf{o}^*(x,y)\sqrt{B}\hat{\mathbf{r}}\exp(i(2\pi\nu_{0x}x+2\pi\nu_{0y}y))+\mathbf{o}(x,y)\sqrt{B}\hat{\mathbf{r}}\exp(-i(2\pi\nu_{0x}x+2\pi\nu_{0y}y)), \end{aligned} \quad (6.17)$$

which terms represent the speckle intensity, the reference intensity, and the complex representation of the cosinusoidal interference term, respectively. The spectrum of this intensity distribution will be

$$\begin{aligned} \text{FT}(I(x,y)) &= \tilde{I}(\nu_x,\nu_y) \\ &= \tilde{O}(\nu_x,\nu_y)+B\tilde{\mathbf{r}}^2\delta(\nu_x,\nu_y) \\ &\quad +\tilde{\mathbf{o}}^*(\nu_x,\nu_y)*\sqrt{B}\tilde{\mathbf{r}}\delta(\nu_x-\nu_{0x},\nu_y-\nu_{0y})+\tilde{\mathbf{o}}(\nu_x,\nu_y)*\sqrt{B}\tilde{\mathbf{r}}\delta(\nu_x+\nu_{0x},\nu_y+\nu_{0y}), \end{aligned} \quad (6.18)$$

where  $*$  denotes convolution. This spectrum is a superposition of the speckle halo  $\tilde{O}$ , the central peak mostly due to the uniform reference illumination, proportional to  $B$ , and two sidebands in which  $\mathbf{o}(x,y)$ , and therefore  $\varphi_o$ , is encoded. Remembering the so-called sifting property of the  $\delta$ -function [Bra87, p. 74], we can account for the convolution by rewriting (6.18) as

$$\begin{aligned} \tilde{I}(\nu_x,\nu_y) &= \tilde{O}(\nu_x,\nu_y)+B\tilde{\mathbf{r}}^2\delta(\nu_x,\nu_y)+\sqrt{B}\tilde{\mathbf{r}}\tilde{\mathbf{o}}^*(\nu_x-\nu_{0x},\nu_y-\nu_{0y})+\sqrt{B}\tilde{\mathbf{r}}\tilde{\mathbf{o}}(\nu_x+\nu_{0x},\nu_y+\nu_{0y}). \end{aligned} \quad (6.19)$$

As already explained in Chapter 3.3.1, the shape of the sidebands in the frequency plane is that of the aperture, only now they are shifted by  $(\nu_x,\nu_y)$ ; see also [Vla94, p. 272]. The situation is depicted in Fig. 6.17 where the measured spectral power density  $|\tilde{I}(\nu_x,\nu_y)|^2$  of a speckle interferogram with  $d_s=3d_p$ ,  $\alpha_x=90^\circ/\text{column}$  and  $\alpha_y=90^\circ/\text{row}$  is shown in a logarithmic scale; nevertheless, the reference-wave peak has been clipped to bring the details out more clearly.

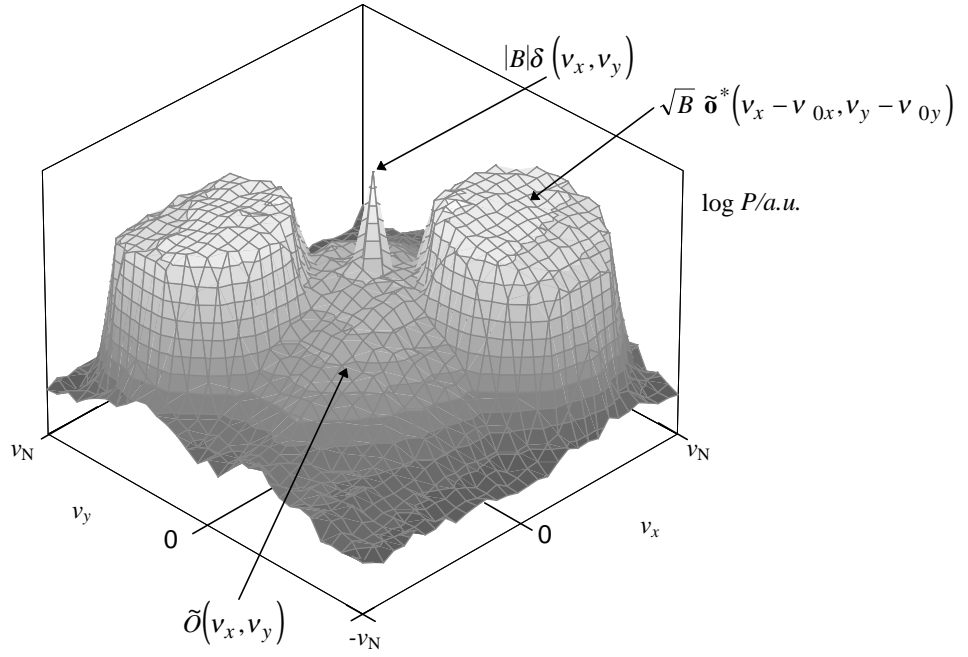


Fig. 6.17: Pseudo-3D plot of the spectral power density  $P(v_x, v_y) = |\tilde{I}(v_x, v_y)|^2$  in a speckle interferogram with a spatial carrier frequency. Since the spectrum comes from the DFT of a quadratic image with  $N \times N$  pixels, the Nyquist frequencies  $\pm v_N$  correspond to  $N/2$  carrier fringes on the sensor.

All contributions from (6.18) are clearly discernible in the plot. Now we enclose one of the sidebands by a suitable frequency filter whose size follows directly from the speckle size; its diameter in the frequency plane should be half of that of the speckle halo (cf. 3.3.1). The rest of the spectrum is discarded; the selected sideband is shifted to the centre of the frequency plane by subtraction of the carrier frequencies, and then transformed back to the spatial domain:\*

$$\text{FT}^{-1}\left(\sqrt{B}\tilde{\mathbf{r}}\tilde{\mathbf{o}}(v_x, v_y)\right) = \sqrt{B}\hat{\mathbf{r}}\mathbf{o}(x, y) = \sqrt{B}\hat{\mathbf{r}}|\mathbf{o}(x, y)| \exp(i\varphi_O(x, y)); \quad (6.20)$$

finally, we obtain the speckle phases  $\varphi_O$  by

$$\varphi_O(x, y) \bmod 2\pi = \arg\left(\sqrt{B}\hat{\mathbf{r}}\mathbf{o}(x, y)\right) = \arctan\left(\frac{\text{Im}\left(\sqrt{B}\hat{\mathbf{r}}\mathbf{o}(x, y)\right)}{\text{Re}\left(\sqrt{B}\hat{\mathbf{r}}\mathbf{o}(x, y)\right)}\right), \quad (6.21)$$

whereby the fluctuations of  $M_I$ , here appearing as  $\sqrt{B}\hat{\mathbf{r}}|\mathbf{o}(x, y)|$ , are cancelled.

By shifting back the sidebands, one obtains the true speckle phases  $\varphi_O$ . However, when two speckle phase maps  $\varphi_{O,i}$  and  $\varphi_{O,f}$ , belonging to two object states, are subtracted from each other, the carrier frequency will automatically be removed. Therefore, the signal shift in the frequency plane is not

\* The filtering operations destroy the point symmetry about  $v_x=v_y=0$  that  $\tilde{I}(v_x, v_y)$  possesses as the FT of a real signal [Bra87, p.14]; therefore the inverse transform will be genuinely complex.

generally necessary in speckle interferometry (nevertheless, it may sometimes be useful to inspect the speckle phases *per se*).

In classical interferometry, the variations of the background intensity may reasonably be assumed to be so low-frequent that the spectrum of the variations of  $I_b$  is easily separated from the signal in frequency space. In speckle interferometry however, the high frequencies in  $O(x,y)$  cause a significant deficiency of the FTM: as is clearly seen from Fig. 6.17,  $\tilde{O}(v_x, v_y)$  is not separated from the sidebands. The speckle halo overlaps the sidebands at any practicable speckle size, so that a considerable noise background adds to most of the signal's frequency content. This disturbs the phase reconstruction in a similar way as in the phase-shifting investigations.

But as familiar as the problems are the ways to cope with them. From (6.19), it is clear that increasing  $B$  will again help to suppress the speckle noise, provided  $\mathbf{r}(x,y)$  has a narrow spectrum and can be eliminated in the frequency plane. This can be fulfilled in an excellent way if a fibre is used to illuminate the sensor: then  $\mathbf{r}(x,y)$  will be a very broad Gaussian profile, and its spectrum a very narrow Gaussian that will not overlap with the signal sidebands. It turns out that the performance of the FTM depends on  $B$  much in the same way as for the phase-sampling methods. To quantify this, Fig. 6.1 also contains a plot of  $\sigma_d$  as calculated by (6.19) -(6.21) (black, circle symbols) from the same interferograms as used for the SPS tests.

Furthermore, we note that the quantity  $\tilde{O}(v_x, v_y)$  in (6.19) is directly accessible because of

$$\tilde{O}(v_x, v_y) = \text{FT}(O(x, y)) = \text{FT}(\mathbf{o}(x, y)\mathbf{o}^*(x, y)), \quad (6.22)$$

so that we should be able to eliminate the speckle background from the phase calculation if we first record the speckle pattern alone, calculate its spectrum and subtract it from (6.18). This correction for speckle intensity is similar to that in 6.2.1, and the remaining phase errors are then mainly from electronic noise and pixels with insufficient  $M_I$ . The same would be possible for the reference wave if its spectrum would overlap the signal spectra. This approach resembles the background subtraction suggested in [Liu97] for classical interferometry.

Using the linearity of the Fourier transform, we could even subtract the speckle pattern in the space domain (6.17) before switching to the frequency domain; but the benefit is easier to see in the frequency representation. Fig. 6.18 provides an example of how the speckle noise is removed in the Fourier plane when  $d_s=2 d_p$ . The aliased frequencies over  $v_N$  remain usable for the FTM by pasting them back to where they got cut off [Bon86]. The reference wave need not be accounted for, since its spectrum is indeed easily separated from the sidebands.

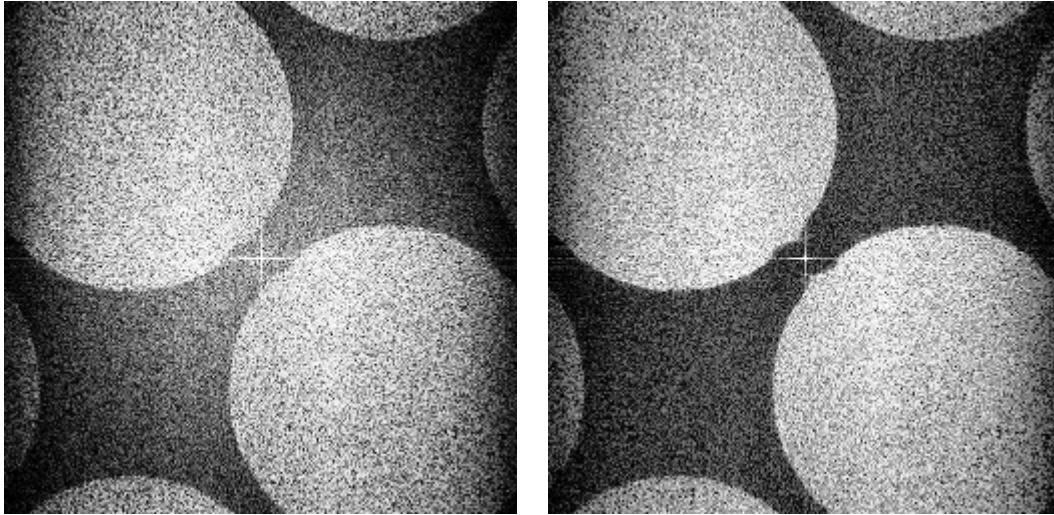


Fig. 6.18: Interferogram power spectra for  $d_s=2 d_p$  and  $B=3$  without (left) and with (right) speckle subtraction. The speckle halo is larger than the frequency plane; the attenuation of high horizontal frequencies is mostly due to the pixel clock (cf. 3.4.5). Spatial frequency scales are as in, e.g., Fig. 6.12 on the left.

This approach eliminates the problem of growing overlap of speckle halo and signal band with decreasing speckle size, so that a very large part of the frequency plane can now conveniently be utilised. Also, the "crosstalk" of the sidebands addressed in 6.1.2 (cf. Fig. 6.3) is avoided. The setting of  $v_x=v_y= \frac{1}{2} v_N$ , chosen for convenience of phase sampling (cf. 6.3), also appears to be the optimum choice in frequency space: it has been used in [Küch91] for a high-performance interferometer, and a computer simulation in [Che91] showed it to yield the error minimum.

The vacant regions of the frequency spectrum can even be used to record further information [McLa86, Hor90, Sim93, Pir95, Ped97a, Ped97b, Tak97a, Tak97b, Sched99], e.g. about a second deformation direction; this approach has become popular under the name of spatial frequency multiplexing. Including time as a parameter enables spatio-temporal frequency multiplexing with one [Tak90a] or two [Tak92, Mor94b] spatial dimensions.

The improvement of speckle subtraction over the non-correcting FTM for varying  $B$  is also shown in Fig. 6.1 for  $d_s=3 d_p$  (black, white circle symbols). The behaviour of the correction is the same as for the phase-shifting method: the effect vanishes for  $B \gtrsim 30$ .

When the same interferograms as in Chapter 6.4 are processed by the FTM, again at  $B=30$  without and  $B=3$  with the intensity correction, one comes to the results plotted in Fig. 6.19. To use a  $1024 \times 1024$  pixel FFT, the standard input images consisting of  $1024 \times 768$  pixels were padded with zeros in the last 256 rows. In a comparison of genuine  $1024^2$  pixel images processed entirely and partly, the difference in the  $\sigma_d$  values remained within  $\pm 1\%$ .

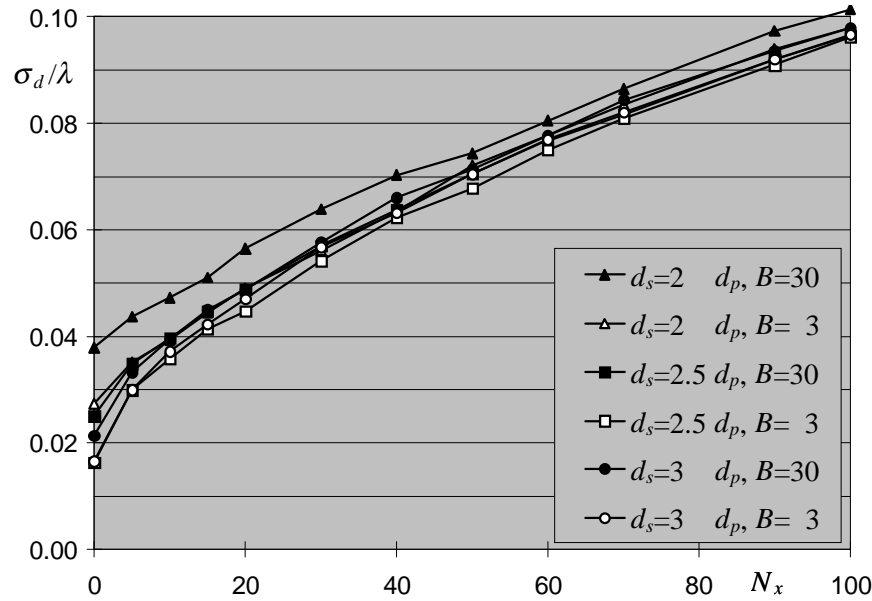


Fig. 6.19:  $\sigma_d$  from ESPI displacement measurements as a function of  $N_x$ , as calculated by (6.19)-(6.21) (black) and its intensity-correcting extension according to (6.22) (white filled symbols), with various  $d_s$  and  $B$  as listed in the legend box.

By the intensity correction, a pronounced improvement is attained for  $d_s=2 d_p$ . This could be expected since the overlap of speckle halo and sidebands is largest at the smallest  $d_s$ , and hence a subtraction of the speckle noise should have the largest effect. Again, there is not much difference between the curves for  $d_s=2.5$  or  $3 d_p$ , and the improvement by the intensity correction is similar to that in Fig. 6.16. Generally, the curves shown here are rather similar to those of Fig. 6.16, but a careful comparison reveals a qualitative difference. The FTM yields lower  $\sigma_d$  for  $N_x < 20$ , while from  $N_x=20$  on, the multiple-averaging formulae lead to better results. The curves for the FTM begin with a steeper slope and then flatten out towards higher fringe densities; those from the phase-sampling formulae are essentially straight. This shows that the FTM can be very accurate but is more sensitive to speckle decorrelation than the SPS calculation: the spatial extent of the sampling pixel cluster slightly tends to smooth the calculated phase maps. At very small decorrelation however, the information in the interferograms is more efficiently used by the FTM. Both sets of curves would of course approach the noise limit of  $\sigma_{d,max} \cong 0.146\lambda$  (see Chapter 5) asymptotically if we further increased the fringe density.

On the whole, the development of phase evaluation methods specially for interferograms with spatial phase shift – or carrier frequency, whichever interpretation one prefers – proves rewarding and contributes an important part to the applicability of the spatial fringe analysis technique in ESPI. The expected noise due to intensity and phase gradients in the speckle pattern can be efficiently suppressed, and also the matter of spatial resolution does not seem to constitute a serious drawback for SPS at practicable fringe densities.



## 6.6 Use of depolarisation to eliminate invalid pixels

A main error source in ESPI and, to a lesser extent, in holographic interferometry, are pixels where  $M_I(x,y)$  falls below the electronic noise or even vanishes due to low or zero speckle intensity. This occurs quite frequently (cf. Chapter 2.2.5) and leads to a relevant fraction of uncertain or invalid outputs of  $\Delta\varphi(x,y)$  in displacement measurements. This phenomenon, with the associated discontinuities of the speckle phase, is the origin of the "salt and pepper" noise in ESPI phase maps, and its effect on phase unwrapping has been investigated recently [Hun95].

On the other hand, it is known that the speckle intensity pdf described by (2.6) changes significantly when an incoherent sum of two uncorrelated speckle patterns is considered [Goo75, p.21, Enn75, p.211]. In that case, the maximum of the intensity pdf is shifted away from  $O(x,y)=0$ , so that the probability of finding "dark" pixels will decrease. Such a case is encountered in the interferometric investigation of rough objects that give rise to multiple scattering and thus introduce depolarisation, i.e. generate two mutually incoherent speckle fields. In this subsection it will be shown how these can be exploited to improve ESPI measurements [Bro98].

In this context, we call an object depolarising if the state of polarisation (SOP) of the light scattered back from it differs from the SOP of the incident light. In many samples, for instance natural stone, this is a consequence of volume scattering due to the transparency of the material under investigation. Hence, we obtain a scattered wave field with fluctuations of intensity, phase, and polarisation.

If the scattered light is split into two orthogonal linearly polarised states (vertical,  $v$ , and horizontal,  $h$ ), two speckle patterns  $S_v(x,y)$  and  $S_h(x,y)$  are generated with a normalised correlation coefficient  $c$ . As described in [Fre90d], the value of  $c$  is chiefly governed by a surface-specific constant, called the depolarisation coefficient  $\rho$ . This quantity is defined by the ratio of cross- to co-polarised scattered speckle intensity:  $0 \leq \rho = \langle S_v \rangle / \langle S_h \rangle \leq 1$ , where  $h$  is the SOP of the incident light and  $v$  the orthogonal one. Then, we can use

$$c = \frac{(1-\rho)^2}{1+\rho^2} \quad (6.23)$$

as a very good approximation to determine the correlation of the orthogonally polarised speckle patterns. This theoretical prediction was confirmed by measurements of depolarising natural stones [Ada97]. Such surfaces are for example involved in ESPI-based measurements of deformations and surface changes of historical monuments, which application was developed in the last few years [Gül96].

Even moderate amounts of depolarisation cause a significant decay of  $c$ : for  $\rho > 0.5$ , we find  $c < 0.2$ , so that in practice there is a good chance to obtain a pair of almost uncorrelated speckle patterns. When a depolarising object is investigated by speckle interferometry, the low correlation between  $S_v(x,y)$  and  $S_h(x,y)$  may be utilised to decrease  $\sigma_d$  in displacement measurements: the points of phase singularities or low object wave intensity in the speckle fields, where the phase  $\varphi_{O,v}(x,y)$  or  $\varphi_{O,h}(x,y)$  is undefined or

uncertain, frequently occur at locations that are different in the  $v$  and  $h$  fields. This gets clear when we express the probability of finding a "bad" pixel (denoted by subscript  $b$ ) at  $(x,y)$  in either speckle pattern by  $P_{vb}(x,y)$  and  $P_{hb}(x,y)$  and that of finding a bad pixel in both speckle patterns by  $P_{bb}(x,y)$ . Then we have

$$P_{bb}(x,y) \cong P_{vb}(x,y)P_{hb}(x,y), \quad (6.24)$$

which is exact when  $c=0$ . Provided both  $P_{vb}(x,y)$  and  $P_{hb}(x,y)$  are distinctly smaller than unity, this means that it is possible to replace most of the bad pixels from one speckle pattern by valid pixels from the other one. There are of course always several points (even for  $c=0$ ) where bad pixels in both speckle fields coincide. But in any case, the number of bad points in the phase map can be minimised by suitable merging of  $\varphi_{O,v}(x,y)$  and  $\varphi_{O,h}(x,y)$ .

The merging process is carried out by analysing  $M_I(x,y)$  in the interferograms between the reference wave (ideally linearly polarised at  $45^\circ$ ) and the vertically or horizontally polarised object wave [Cre88],

$$\begin{aligned} M_{I,vi}(x,y) &= \sqrt{3(I_{1vi} - I_{3vi})^2 + (2I_{2vi} - I_{1vi} - I_{3vi})^2} \\ M_{I,hi}(x,y) &= \sqrt{3(I_{1hi} - I_{3hi})^2 + (2I_{2hi} - I_{1hi} - I_{3hi})^2}, \end{aligned} \quad (6.25)$$

where  $\alpha=120^\circ/\text{sample}$  and the index  $i$  refers to the initial object state, for reasons to become clear shortly. It should be emphasised that these  $M_I$  are derived from the "sine" and "cosine" terms of (3.17), which must then be used for the subsequent phase determination; if other  $\alpha$ , or phase-calculation formulae, are used, the respective "sine" and "cosine" terms have to be inserted under the square root. Due to the low correlation between the  $v$  and  $h$  speckle patterns, the two maps of  $M_{I,vi}(x,y)$  and  $M_{I,hi}(x,y)$  will also be different, and the higher of the two values ought to indicate the prospect of a more accurate phase measurement. Admittedly, (6.25) is not as reliable in SPS as in TPS [Su 94] due to the underlying speckle structure that may yield bogus modulation when the pixel triplet crosses speckle "boundaries"; but as far as a comparison of  $M_{I,vi}(x,y)$  and  $M_{I,hi}(x,y)$  is concerned, this approach still works rather well, as we shall see.

The interferograms are recorded by a CCD camera behind a polariser in the vertical or horizontal position; setting the plane of polarisation of the reference wave to ideally  $45^\circ$  assures  $P_{vb}(x,y) \cong P_{hb}(x,y)$ . For each point  $(x,y)$  in both interferograms we determine  $M_{I,vi}(x,y)$  and  $M_{I,hi}(x,y)$  and the phase distributions  $\varphi_{O,vi}(x,y)$  and  $\varphi_{O,hi}(x,y)$ . Then, starting with  $\varphi_{O,vi}(x,y)$ , we replace all phase values in this map by those from  $\varphi_{O,hi}(x,y)$  at all the locations where  $M_{I,vi}(x,y) < M_{I,hi}(x,y)$ . Thus, a pixel is considered "bad" in the sense of (6.24) when a better measurement is available. The locations of replaced pixels are stored in a binary mask  $B_i(x,y)$ .

Repeating this modulation analysis for the final object state would lead to a slightly different map  $B_f(x,y)$  due to speckle decorrelation by the object deformation and statistical temporal fluctuations like camera noise. Therefore,  $B_i(x,y)$  is used for the final object state too. That is, the phase values in the map  $\varphi_{O,vf}(x,y)$  are replaced by those of the map  $\varphi_{O,hf}(x,y)$  at the same locations where the replacement is done

for the initial object state. By this approach, two merged (index  $m$ ) phase maps  $\varphi_{O,mi}(x,y)$  and  $\varphi_{O,mf}(x,y)$  are generated, whose correlation is maintained with respect to the pixel replacement.

Since the phase offsets  $N_{0v}$  and  $N_{0h}$  (cf. Chapter 4.2) should be the same for both sawtooth images to merge, they should be kept constant during the recording of the two interferogram pairs  $I_{vi}$ ,  $I_{hi}$  and  $I_{vf}$ ,  $I_{hf}$ . In principle, it is possible to correct a phase offset *a posteriori* and make both fringe systems fit together by subtracting a constant phase from one of the sawtooth images; but the error fringe profiles (cf. Fig. 3.39) are related to the actual physical phase offset, so that such a "makeshift" will produce artefacts and lead to unsatisfactory results. Therefore, a phase stabilisation system to compensate phase fluctuations by, e.g., vibrations or temperature drifts is incorporated in the interferometer as shown in Fig. 6.20.

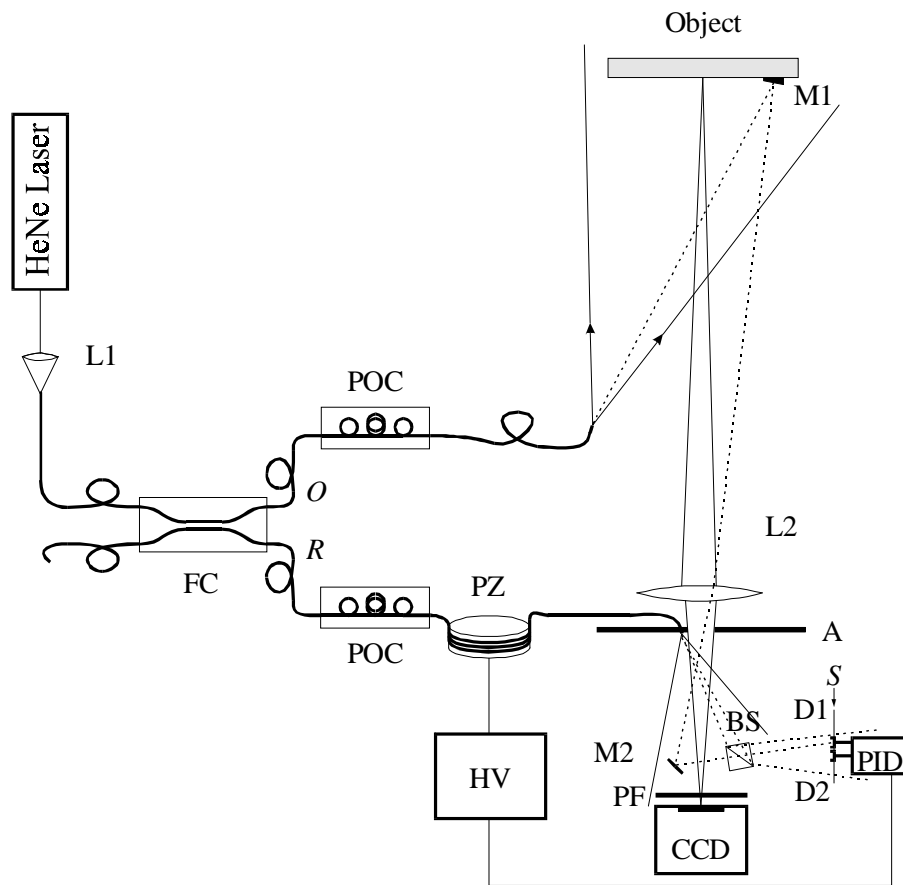


Fig. 6.20: ESPI out-of-plane set-up with SPS and active phase stabilisation. Dashed lines: beams for the stabilisation system. Abbreviations: see text.

The light of a HeNe laser (25 mW @ 632.8 nm) is coupled with a microscope objective L1 into a standard single mode fibre (Corning Flexcor 633). A fibre coupler FC (Gould) splits the light into an object wave  $O$  and a reference wave  $R$  with a coupling ratio of 9:1. Both output fibres contain a polarisation controller POC [Lef80] to adjust the SOP at the fibre ends; we use linear  $45^\circ$  polarisation for  $O$  and not  $45^\circ$  but  $48^\circ$  for  $R$ , which difference will be justified below. Although a standard single mode fibre is used, both SOPs remain almost constant under the given laboratory conditions for a long time. This was verified by long-term measurements with a real-time Stokes polarimeter [Dir97]: for a time period of about four hours, the azimuthal SOP angle changes by less than  $2^\circ$ , and the angle of ellipticity by less than  $4^\circ$ .

To obtain performance data for our approach, we use the  $\sigma_d$  values from a simple out-of-plane tilt. The test object is a white painted metal plate that scatters with strong depolarisation ( $\rho = 0.78 \pm 0.01$ ). The light scattered off the object is imaged with a lens L2 onto the target of the CCD camera, with  $1024 \times 768$  pixels. A polariser PF in front of the camera target selects either the vertical or horizontal SOP of the scattered light. The measured correlation coefficient for the corresponding speckle fields  $S_{vi}(x,y)$  and  $S_{hi}(x,y)$  is  $c = 0.02 \pm 0.005$  which is in acceptable agreement with the value of  $c = 0.03 \pm 0.003$  expected for the measured depolarisation coefficient. Since  $\langle S_v \rangle / \langle S_h \rangle \cong 0.78$ , the plane of polarisation of the reference wave is set to  $48^\circ$  instead of  $45^\circ$  by the POC to obtain  $P_{vb}(x,y) \cong P_{hb}(x,y)$ , this is, we intend to replace some 50% of  $\varphi_{O,vi}(x,y)$  ( $\varphi_{O,vf}(x,y)$ ) by entries from  $\varphi_{O,hi}(x,y)$  ( $\varphi_{O,hf}(x,y)$ ), whereby the best utilisation of both speckle patterns is assured.

The reference wave's fibre end is placed in the aperture plane A of the imaging system and positioned to yield  $\alpha_x = 120^\circ/\text{column}$  on the CCD sensor.

The phase stabilisation works as follows: part of the object light is reflected by the small mirror M1 mounted on the object. It passes through the lens L2 and is then reflected by another small mirror M2, close beside the CCD chip, towards the plane S. On the opposite side of the CCD sensor, a small beamsplitter BS reflects a part of the reference wave towards S. By proper adjustment of M1, M2 and BS, both waves can interfere in S, forming an interference pattern of concentric fringes as shown in Fig. 6.21. This is far easier to achieve than broad fringes of stable shape.

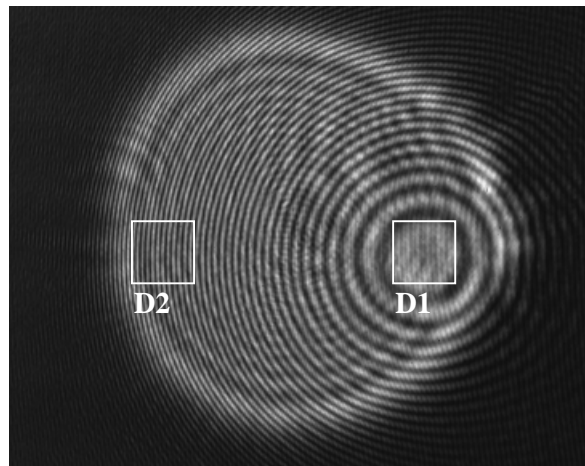


Fig. 6.21: Interference pattern in the plane S of the PID unit; the white squares indicate the locations and areas of the photodiodes. The circular boundary of the pattern is due to the imaging aperture.

A photodiode D1 is placed in the centre of this pattern where a broad fringe occurs. Another one, D2, is placed outside the centre, integrating the intensity distribution over some 12 fringes. Thus, the output of D2 is insensitive to phase variations and tracks the intensity fluctuations of the laser instead. Whenever phase changes occur between the object and the reference wave, the intensity in the centre of the fringe system changes. This variation is detected by D1, while intensity fluctuations of the laser are detected by

D2 and D1. The difference signal of the detectors D1 and D2 is processed by a PID controller and then fed into a high voltage amplifier HV. The amplifier drives a piezo electric cylinder PZ (Ferroperm PZ 27), onto which some turns of the reference fibre are wound and which works as a phase shifter [Dav74]. By this closed-loop control system, the phase difference between  $O$  and  $R$  is stabilised with respect to that point of the object surface where M1 is mounted. The achieved cut-off frequency of the phase compensating unit of about 1.4 kHz is found to be adequate for the desired purpose. Also, the long-term stability of this arrangement was found to be satisfactory [Sag98].

At the beginning of the measurement,  $\langle B \rangle \cong 10$  and  $d_s \cong 3 d_p$  were adjusted. Unfortunately, we have to use an average for  $R$ , and hence for the beam ratio, here: as can be seen in Fig. 6.20, the reference wave was directed so as to illuminate BS sufficiently. The maximum of its intensity profile lay beside the CCD array, which caused the local intensity of  $R$  to vary between  $2\langle R \rangle$  and  $\langle R \rangle/3$  from edge to edge of the sensor. Hence,  $3\langle B \rangle < 20$  over the image, which leads to slight spatial variations of  $M_I$ , and thereby, the fringe quality. Note, however, that rotating the polariser does not affect the profile of  $B$ , so that the modulation criterion remains applicable.

For the initial object state, speckle interferograms were captured for the vertical and horizontal position of the polariser, respectively. The phase map  $\varphi_{O,mi}(x,y)$  was calculated from these interferograms as described above. According to  $B_i(x,y)$ ,  $\varphi_{O,mi}(x,y)$  contained 49.2% of the pixels from  $\varphi_{O,vi}(x,y)$  and 50.8% from  $\varphi_{O,hi}(x,y)$ .

The object tilt was applied to generate  $N_x \cong 10$ , which moved M1 forward (towards the camera) by some  $\lambda$ ; the associated phase change was tracked and compensated by the stabilisation unit, whose bias output voltage was therefore shifted by some 10% of its complete range. This means that the "I" part of the PID stabilisation would have to be reset regularly if larger tilts were present. The consequences of the tilt for the shape of the fringe pattern in Fig. 6.21 are however negligible. Nevertheless, some work has been done subsequently to get rid of the necessity to attach a mirror on the object, and a highly sensitive heterodyne system was built that uses the light of one or few object speckles for stabilisation [Bro00].

After the object deformation,  $I_{vf}(x,y)$  and  $I_{hf}(x,y)$  were recorded and a phase map  $\varphi_{O,mf}(x,y)$  for the final object state was calculated. Finally, the merged deformation phase map  $\Delta\varphi_m(x,y) = \varphi_{O,mf}(x,y) - \varphi_{O,mi}(x,y)$  was determined, with  $\sigma_d = 0.051 \lambda$ . For comparison, we generated  $\Delta\varphi_v(x,y) = \varphi_{O,vf}(x,y) - \varphi_{O,vi}(x,y)$  with only one SOP (here  $v$ ), and found  $\sigma_d = 0.067 \lambda$ . Hence, the noise reduction by using both SOPs is about 24%. A visual impression of the resulting phase maps is provided by Fig. 6.22.

The experiment demonstrates that even a simple phase-calculation formula is sufficient to obtain an accuracy of  $\lambda/20$  in SPS if it is allowed to process "good" interferogram data. And as described above, there is still space left for improvements.

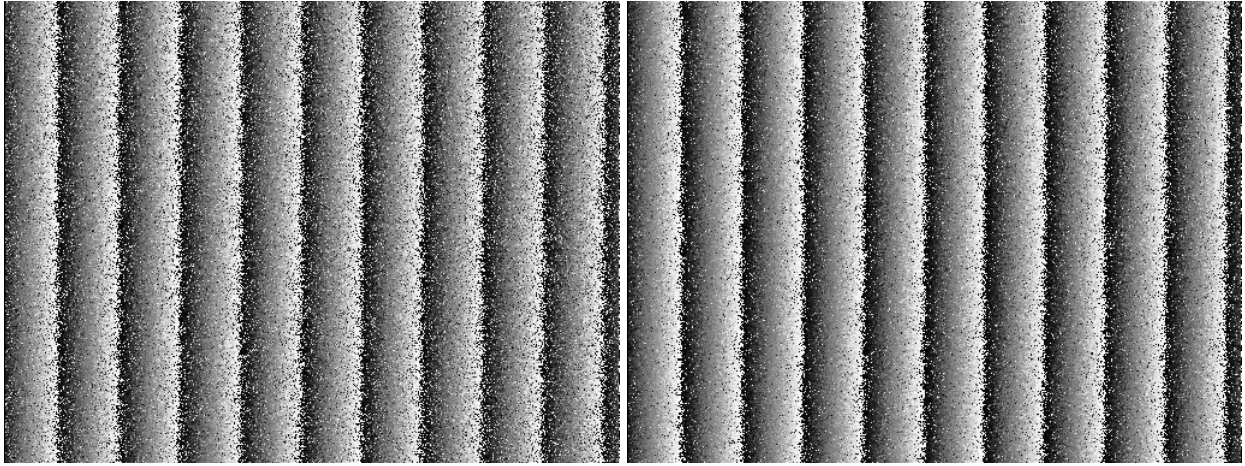


Fig. 6.22: Comparison of sawtooth images from an out-of-plane tilt; left,  $\Delta\phi_v(x,y)$  measured with one SOP,  $\sigma_d=0.067 \lambda$ ; right,  $\Delta\phi_m(x,y)$  by merging of measurements from two SOPs,  $\sigma_d=0.051 \lambda$ .

An attempt to use the intensity-correcting formula (6.6) to derive a modulation criterion that includes speckle intensities remained unsuccessful. While both  $\Delta\phi_v(x,y)$  and  $\Delta\phi_h(x,y)$  were better than their non-corrected counterparts,  $\Delta\phi_m(x,y)$  was slightly worse in terms of  $\sigma_d$ . Apparently, the simple modulation analysis of (6.25) rejects unreliable pixels well enough, and the inclusion of speckle intensities tends to complicate the procedure.

In the version of the system described here, the polariser is rotated manually. Of course, it could be replaced by an electro-optical device, so that the interferograms for both SOPs can be captured in subsequent video frames. Furthermore, with a polarising beamsplitter and two cameras, it would even be possible to record the two interferograms simultaneously. In that case, the phase compensating unit can be given up, provided SPS is used.

## 6.7 Extensions of SPS by temporal unwrapping

While the reduced spatial resolution in ESPI does not seem to constitute practical limitations for SPS, the temporal resolution is increased in comparison with TPS by a factor of at least 3. This has been used for high-precision classical interferometry to obtain and average phase maps at a higher rate [Fre90b], and the single-frame measuring capability has enabled successful measurements of high-speed events [Kuj88, Sho90, Ped93]. But not only can the phase front be monitored at video real-time: it can additionally be tracked and unwrapped pixelwise in time, which immediately yields displacement and deformation data and possibly eliminates the need for *a posteriori* data processing. This approach is known as temporal phase unwrapping [Hun93a] and abbreviated by TPU. It has been used for profilometry [Tak94, Sal97, Joe98b] and shearography [vBru98] and was applied to ESPI deformation measurements in combination with TPS [vBru98, Hun99] and also with temporal FT evaluation [Joe98a]. A method utilising carrier fringes with TPU for a shearography ESPI system has recently been described in [Mar00]. The principle of TPU is shown in Fig. 6.23.

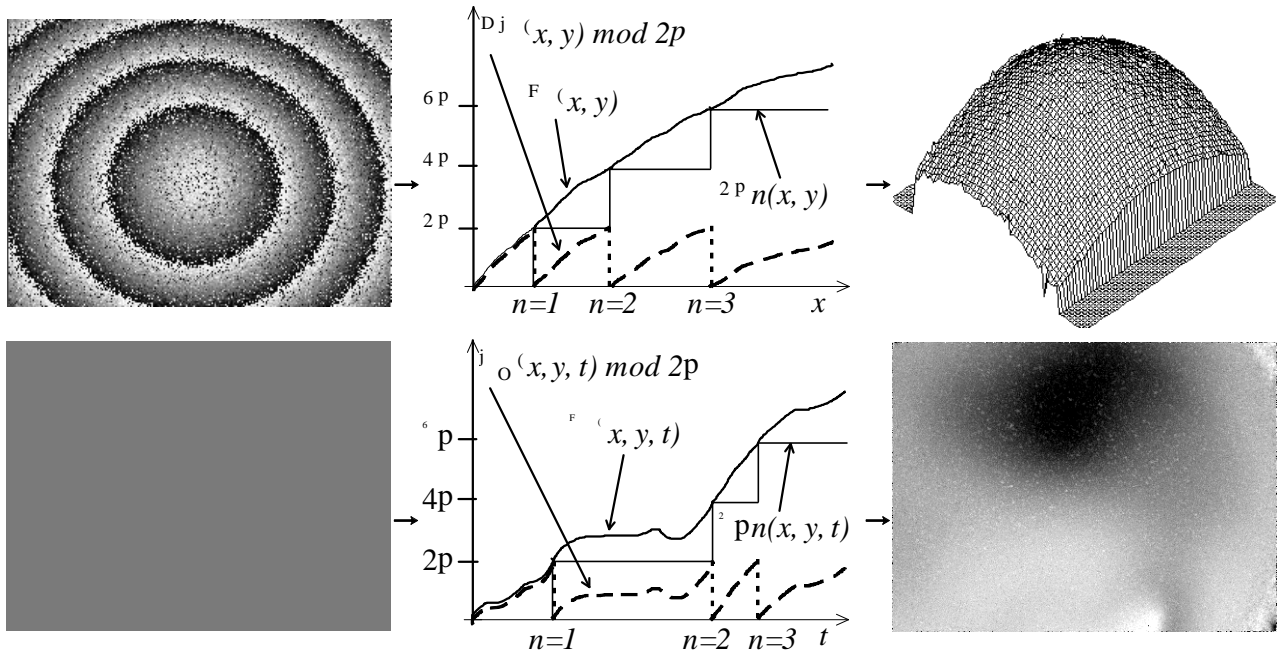


Fig. 6.23: Principle sketch of spatial (top row) and temporal (bottom row) phase unwrapping; for details, see text.

In spatial unwrapping, a sawtooth image (top, left), representing a temporal phase history  $\Delta\varphi(x, y) \bmod 2\pi = (\varphi_O(x, y, t_f) \bmod 2\pi - \varphi_O(x, y, t_i) \bmod 2\pi) \bmod 2\pi$ , with  $i$  and  $f$  referring to undeformed and deformed object state, is converted to a continuous displacement phase  $\Phi(x, y)$  (top, right) by appropriate additions of  $\pm 2\pi$ , i.e. by finding the correct step function  $2\pi n(x, y)$ ,  $n \in \mathbb{Z}$ . This is done by a simple criterion: when the data satisfy the sampling theorem spatially, there will be no phase changes  $> \pi$  from pixel to pixel. If such a transition is detected nevertheless, it must then be a  $0 \leftrightarrow 2\pi$  jump that is wrapped back onto  $[0, \pi)$  by in- or decrementing  $n$ . This procedure along the  $x$  direction at an image row  $y$  is sketched in Fig. 6.23 in the centre of the upper row.

Temporal unwrapping starts from an empty displacement map (bottom, left) and tracks the phase history of every pixel  $(x, y)$  in time by comparing it with an initial phase map  $\varphi_O(x, y, t_i)$ . The unwrapping criterion is applied temporally, as shown in the centre of the bottom row for some pixel  $(x, y)$ ; the temporal sampling rate must be high enough to keep differences of  $\varphi_O(x, y, t)$  from frame to frame smaller than  $\pi$  on each pixel, this is, the sampling theorem must be fulfilled temporally. The phase differences are unwrapped by addition of  $2\pi n(x, y, t)$  as required and used to continuously update  $\Phi(x, y, t)$ , which may conveniently be represented by grey levels as well, as on the right in the bottom row. The advantage of this method is that errors due to faulty – mostly badly modulated – pixels will not spread across the image as this may be the case for spatial unwrapping.

In longer monitoring sequences however, the advantage of TPU can become a disadvantage: it accumulates data, including errors, and severely corrupted unwrapped phase maps  $\Phi(x, y)$  cannot be restored *a posteriori*. It is therefore favourable to store both the temporally unwrapped data and several phase maps  $\varphi_O(x, y, t)$ . If the former are doubtful, the latter may yield conventional sawtooth images  $\Delta\varphi(x, y)$  that can easily be unwrapped spatially when they contain few fringes.

This procedure requires a storage interval  $\Delta t$  for the phase maps  $\varphi_o(x, y, t)$  which is matched to the possibly varying velocity of object deformation and displacement. The implicit fringe counting capability of TPU lends itself for driving such a matched course of  $\Delta t$  automatically. As far as I know, this issue has only once been dealt with before on the basis of speckle decorrelation analysis [Gül93]; here however, the quantity of interest that we want to limit is the number of fringes in  $\Delta\varphi(x, y)$  instead of the speckle decorrelation [Bur00b].

In practice, ESPI often deals with objects consisting of several independent parts that may undergo different displacements and deformations. However, sawtooth fringes do not allow to determine rigid body movements or the sign of the deformation itself, unless the fringe orders are tracked by additional devices like, for instance, a phase stabilisation unit [Bro00]. We will see that temporal unwrapping delivers these data for each object part automatically.

### 6.7.1 Temporal unwrapping of speckle phases

The use of temporal unwrapping is not entirely straightforward in speckle interferometry; we will therefore briefly consider the cumulative impact of speckle noise on displacement data.

Not surprisingly, badly modulated pixels cause problems also in this application. The statistical fluctuations of the calculated phase should yield a displacement of zero when monitored over a sufficient number of frames. It was however observed that even for longer observation sequences with hundreds of frames, some of these pixels seemed to change their phase constantly in one direction; both signs of displacement were present. In a fringe counting procedure, these pixels would trigger data storage even when no actual displacement has occurred. Therefore such outliers have to be suppressed; and as usual in speckle interferometry, a low-pass filter can serve to do so. This may be objectionable in TPS, because it impairs the spatial resolution; but for larger speckle sizes, as used in SPS, the resolution will not suffer greatly.

There are sophisticated and well-founded filtering schemes [Hun97] that give excellent rejection of noise in the displacement map over long, albeit not infinite, times of observation [Cog99]. For reasons of processing speed, a simpler filtering scheme is used here. The accumulated phase  $\Phi(x, y, t)$  of a pixel at time  $t$  is considered faulty when it differs by more than  $\pi$  from the accumulated phase of at least one out of its nearest neighbours. In that case,

$$\Phi(x, y, t) := (\Phi(x, y - 1, t) + \Phi(x - 1, y, t) + \Phi(x + 1, y, t) + \Phi(x, y + 1, t)) / 4 \quad (6.26)$$

and the outlier is eliminated.

By the selection criterion, filtering takes place only when necessary, and processing time is saved. This helps to obtain a high frame rate, which is very important since also temporal unwrapping relies on the sampling theorem, as detailed above; and due to the cumulative nature of the process, errors due to missed fringes (violation of the sampling condition) will last in the map of  $\Phi(x, y, t)$  until it is cleared. The phase



maps were generated by a look-up table for  $\alpha_x=120^\circ/\text{sample}$  (cf. 3.2 and Appendix B). The frame rate of the image processing system (a Data Translation DT3852 frame grabber connected to an Alacron FT200 processor board with two 50-MHz i860 processors) was  $\cong 0.5$  Hz for an image size of  $800 \times 600$  pixels.

The method of filtering was tested by running the temporal unwrapping for some 30000 frames without disturbing the system. At the end, the fringe counting procedure reported some 1.5 fringes; this error suppression is sufficient for our purpose. However, the fluctuations in  $\Phi(x, y)$  do not appear to be perfectly random, since they do not vanish even in such a long averaging process. Their structure may be seen in Fig. 6.24, where the displacement information corresponding to a range of 1.5 fringes has been converted to grey values and expanded to the whole grey scale for better visibility of the effect.

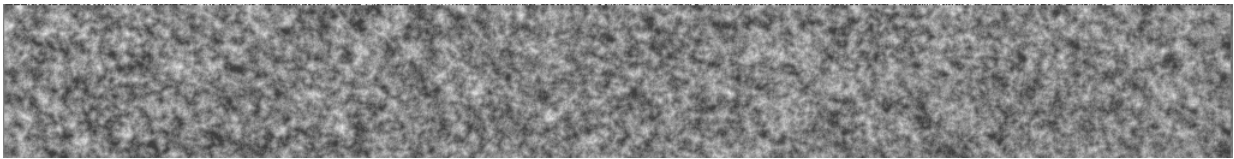


Fig. 6.24: Errors in  $\Phi(x, y)$  related to "random" noise, accumulated during  $\cong 30000$  temporal unwrapping runs without actual object displacement.

Another problem occurs in the observation of real displacements. While noisy pixels are not necessarily detected as such in every frame, their calculated  $\Phi(x, y, t)$  will not follow the true course; instead, for most of the noisy pixels it will hover around zero. If such a  $\Phi(x, y, t)$  happens to be included in the averaging operation (6.26) before it is re-aligned with its neighbours, its error will propagate into the surrounding pixels. In the long run, this will lead to pixel clusters whose  $\Phi(x, y, t)$  is dragged behind, i.e. will be somewhere between zero – from where all observations start – and the true value. An example is given in Fig. 6.25, where an out-of-plane tilt about the  $y$  axis has been tracked. The tilt was controlled by applying a linear voltage ramp to a PZT which rotated the object holder slowly enough to satisfy the temporal sampling requirement for all pixels in the image.

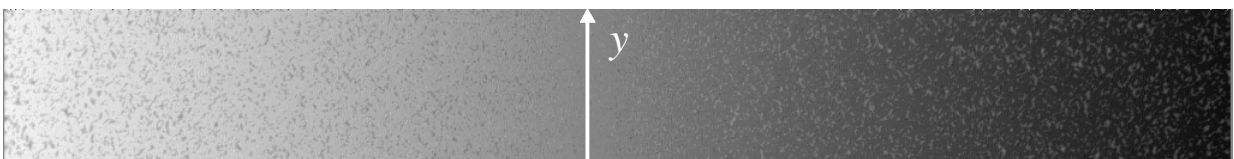


Fig. 6.25: Errors in  $\Phi(x, y)$  related to object motion; "slow" pixels due to imperfect error rejection.

The line of zero displacement is marked by the white line and the accumulated displacement range  $\Phi(x, y)$  is  $+5\pi$  at the left and  $-5\pi$  at the right edge. The bright/dark backgrounds tend to deceive the eye; indeed, the "slow" pixels on the left are brighter than those on the right, which means that the sign of motion is correctly determined for all of them, but the measured displacement is underestimated. When spatial averaging takes place in every frame, this behaviour can be suppressed by pixel weighting [Cog99]. In this subsection, the faulty pixel clusters are selectively removed *a posteriori*; they must not be included in the displacement computation [Hun93a], for they will generate a systematic error that is proportional to the absolute displacement.

### 6.7.2 Long-term observation of biological object

Many industrial ESPI experiments allow to predict the number and shape of fringes with which a test object will respond to a certain load. On the other hand, being a non-destructive examination technique, ESPI is particularly useful for unique objects about whose properties little is known. Therefore it is in general difficult to foresee changes in the fringe pattern, all the more when the objects are not subjected to test sequences or cycles but left to fluctuations – or attempts of stabilisation – of ambient parameters. In such cases, eventful periods may alternate with hours of little or no changes. A "good" experiment requires that the object motion be adequately tracked in time, this is, neither fringe density nor speckle decorrelation must grow too large between the capturing of consecutive interferograms; and on the other hand, no redundant data should be produced. While there may be tasks where a human operator can make such decisions, this is undesirable from an economical point of view. Also, some observations exclude the presence of a person.

Temporal phase unwrapping is well suited to utilise the fringe order count  $n(x, y, t)$  to generate matched data storage intervals  $\Delta t$ : from the continuously updated values  $\Phi(x, y, t)$ , the extreme values  $\Phi_{max}$  and  $\Phi_{min}$  can be extracted in every run of the temporal phase unwrapping loop. When the difference exceeds a certain threshold  $\Phi_T$ , it is assumed that the corresponding sawtooth phase map  $\Delta\varphi(x, y) = \varphi_O(x, y, t_f) - \varphi_O(x, y, t_i)$  between the present phase distribution  $\varphi_O(x, y, t_f)$  and the stored initial one,  $\varphi_O(x, y, t_i)$ , has acquired  $m$  fringes with  $m = \Phi_T/2\pi$ . In that case  $\varphi_O(x, y, t_f)$  is stored and re-labelled  $\varphi_O(x, y, t_i)$ ,  $\Phi(x, y, t)$  is cleared and the procedure begins anew. This technique yields a sequence of few-fringe sawtooth images that constitute no problem for spatial unwrapping. Note, however, that this method of fringe counting does not limit the fringe density: when small defects generate high local phase gradients, it may possibly come to unresolvable sawtooth fringe patterns. The phase gradient is easily accessible with the help of the co-ordinates of  $\Phi_{max}$  and  $\Phi_{min}$ ; but this procedure was omitted for the sake of simplicity.

Of course, the most convenient data evaluation would be to accumulate  $\Phi(x, y, t)$  throughout the whole observation, whereby it may even become obsolete to save phase maps  $\varphi(x, y)$  regularly. But with the type of filter used here (6.26), it is safer to eliminate accumulated noise or accidental errors (e.g. by abrupt stress relaxation in the interferometer) by clearing  $\Phi(x, y, t)$  when a phase map is stored. Thereby the continuous tracking of phases  $\Phi(x, y, t)$  is given up, but the propagation of errors is being limited to one measurement of  $\Phi(x, y, t)$ , corresponding to only one storage interval  $\Delta t$ . Nevertheless, the whole series of  $k$  phase maps  $\Phi_k(x, y, t)$  may be stored and, if usable, added up later on to yield  $\Phi(x, y, t_{total}) = \Sigma\Phi_k(x, y, t)$ .

To test this approach of dynamic data storage, I examined a biological test object whose likely deformation is not known in advance. The white spot on a fresh chestnut, as shown in Fig. 6.26, was found to be quite co-operative for interferometry: its surface is reasonably reflective and maintains speckle correlation over sufficient time intervals. We can expect the displacements to proceed most rapidly at the beginning of the experiment because the object will relax in its holder. Also, the loss of water from the surface should result in a constant shrinking, relatively fast initially and then levelling off.

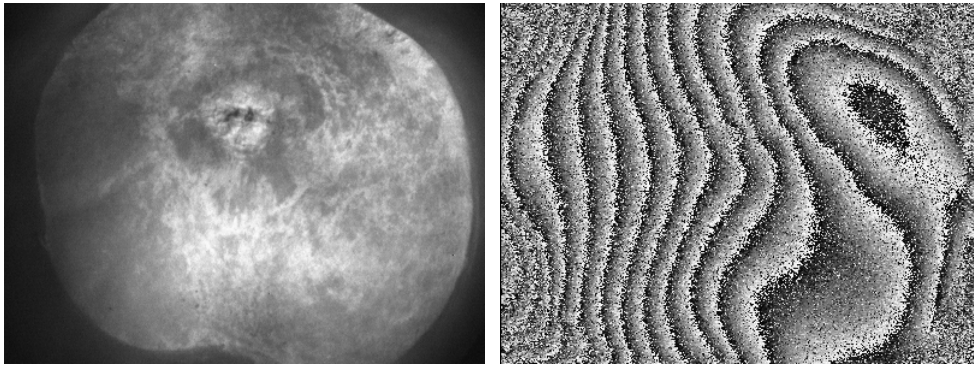


Fig. 6.26: White-light image (left) and deformation map (right) of fresh chestnut.

The changes of the chestnut's surface were monitored over some days from shortly after its fastening in the interferometer (which was the set-up of Fig. 5.1) until the deformation had settled somewhat. Besides the matched storage of phase maps  $\varphi(x, y)$  whenever the threshold of  $m=5$  fringes was reached, additional ones were stored at the steady rate of 1 frame per 10 min to study possible performance differences between the methods. Fig. 6.27 provides an overview of the deformation dynamics. The black curves (left ordinate) show the courses of the matched and static storage intervals  $\Delta t$  versus time after the beginning of the observation. The white curves (right ordinate) show the corresponding courses of the hard disk space required for storing the phase maps.

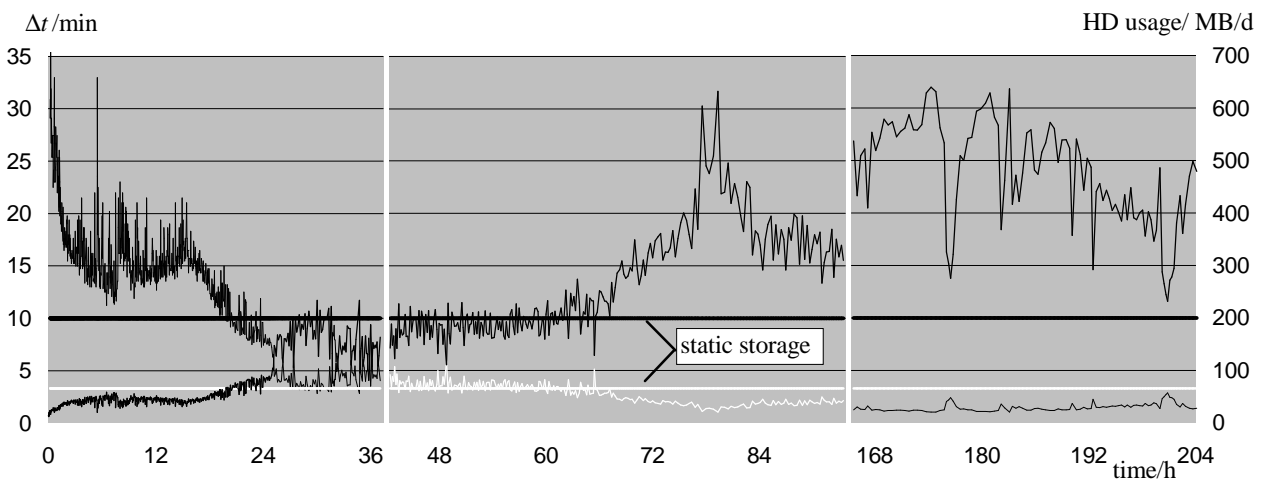


Fig. 6.27: Course of the matched and static storage interval  $\Delta t$  (black curves, left ordinate) during several days; for static storage  $\Delta t$  is fixed to 10 min. White curves: hard disk space required in MBytes/day (right ordinate).

The matched data storage went through several phases: in the first 3 hours, the chestnut appeared to settle in its spring-loaded holder and short storage intervals  $\Delta t$  were necessary. After  $\cong 15$  h, the deformation slowed down; the matched  $\Delta t$  were incidentally similar to the static ones in the time period between  $\cong 25$  h and  $\cong 60$  h. After  $\cong 60$  h, a distinct slowing down of the shrinkage took place, and the matched  $\Delta t$  remained around 20 – 25 min for the rest of the observation. Hence, temporal unwrapping was able to avoid undersampling (in the sense of appropriate data storage) initially and to save disk space later on.

To illustrate the value of this approach, we shall consider images from the two situations. In Fig. 6.28, a comparison of a 10-minutes' deformation measurement at  $t \cong 7\frac{3}{4}$  h is shown. Since the automatic routine determined the instant of saving by itself, the initial and final object states are only by chance very nearly, but not exactly, the same for the two storage series.

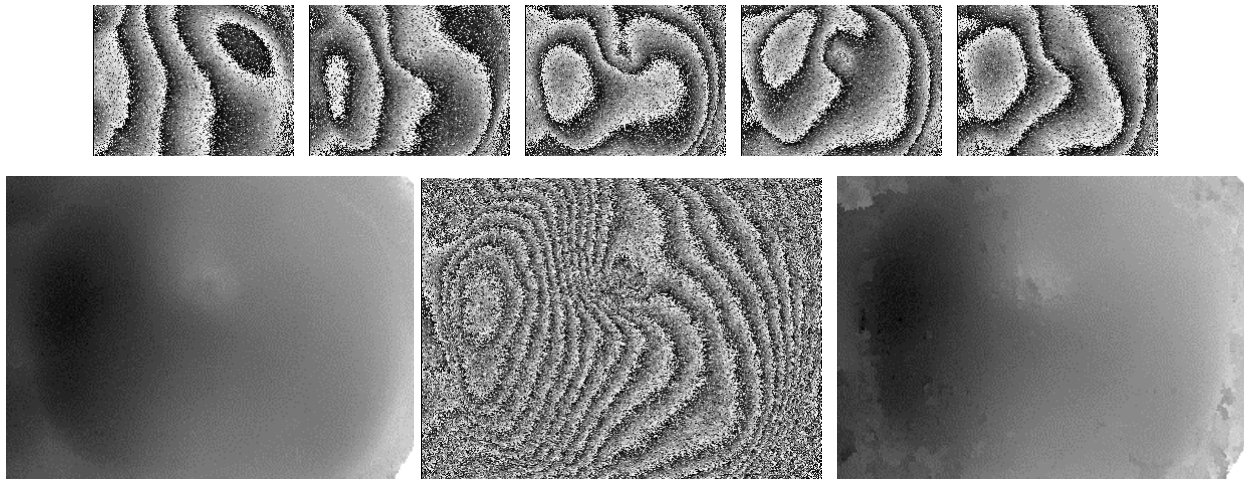


Fig. 6.28: Comparison of matched vs. static data acquisition. Upper row: sequence of sawtooth images calculated from 5 automatically saved phase maps  $\varphi_f(x, y)$  (matched  $\Delta t$ ), leading to the resulting grey-scale height map on the left in the lower row when spatially unwrapped, converted to heights and added. Lower row, centre: sawtooth image for almost the same displacement calculated from only one phase map  $\varphi_f(x, y)$  (static  $\Delta t$ ); right: resulting height map.

The deformation is decomposed into five parts (upper row) by the matched phase map acquisition, and the corresponding sawtooth images indeed show  $m \cong 5$  fringes each. The incremental sawtooth images can all be spatially unwrapped with no problems, and the corresponding height data can be added to yield a flawless deformation map (lower row, left). Depending on the individual phase gradients, the sum of these incremental phase maps may contain well below 25 fringes, but not more. The single sawtooth image (lower row, centre) from the static data storage indeed contains only  $\cong 19$  fringes. Their strongly fluctuating density causes problems in spatial unwrapping, so that some height assignments are faulty in the result (lower row, right). While one would not lose track of the course of displacement in this example, there may be cases where only a higher image rate can ensure getting safely through the process. After  $t \cong 65$  h, the situation is reversed: the deformation is oversampled by the static acquisition, which generates a large amount of superfluous data. Fig. 6.29 gives an example from  $t \cong 79$  h.

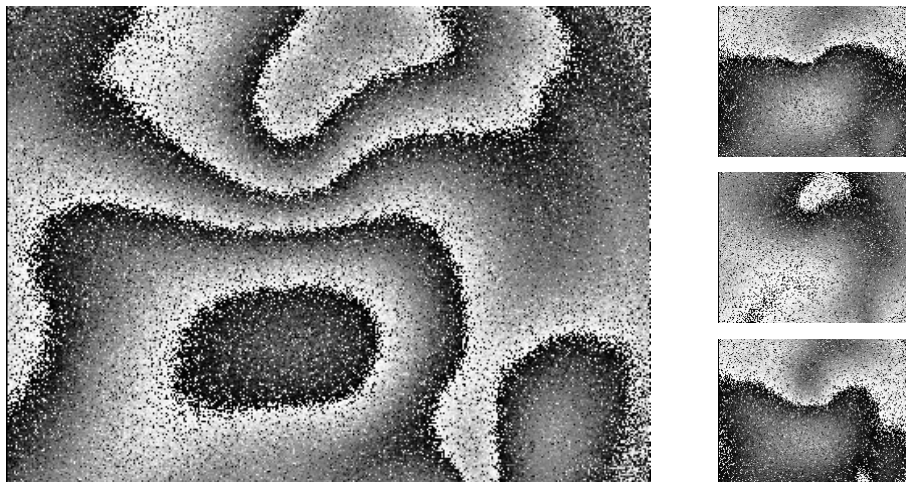


Fig. 6.29: Sawtooth image for matched data storage (left) and corresponding sequence of sawtooth images from static storage interval (right).

At that stage of the experiment, the automatic storage interval had expanded to  $\Delta t \cong 32$  min. Consequently, the fringe density in the images from the fixed-rate series is unnecessarily low, disk space is wasted and the data evaluation gets more laborious.

In Fig. 6.29, we also find a hint that our cautious decision to regularly reset  $\Phi(x, y, t_i)$  after each storage is justified. As the object deformation grows slower,  $\Delta t$  becomes larger, more noise is accumulated in the temporally unwrapped data, reduces the accuracy and also triggers storage too early: in the automatically saved image, we find less than 4 fringes instead of  $m \cong 5$ .

The shown experiment demonstrates that fringe counting by means of temporal unwrapping is suitable to adapt the data storage rate to the actual displacements. This is helpful not only for long-term observations: in any experiment where no assumptions about the object's dynamics can be made, its motion can reliably be tracked by the approach proposed here.

### 6.7.3 Relative displacements of discontinuous object

Especially in the investigation of historical material, one frequently encounters cracks in the surface under inspection [Gül96] and it is important to know the relative motion of neighbouring sub-areas of the object. As a realistic specimen of an aged material, a slice of a historical brick ( $\cong 2$  cm thick) was observed under temperature changes. The interferometer was again the out-of-plane assembly of Fig. 5.1, only the test object had been replaced by the brick slice in upright position. The heat source was an infrared radiator positioned some 30 cm behind the object. Fig. 6.30 shows a white-light image of the measuring field.

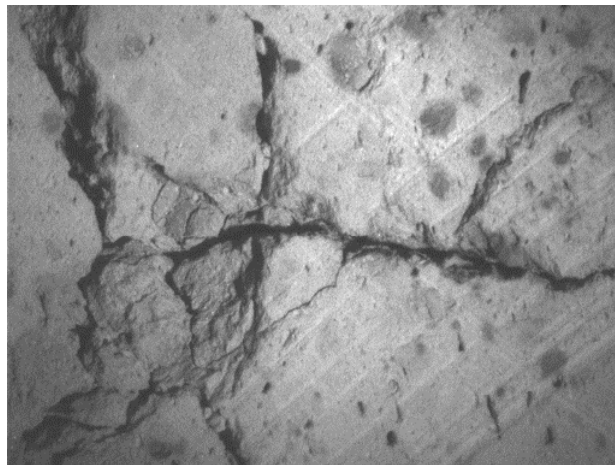


Fig. 6.30: White-light image of historical brick.

When this sample is subjected to cycles of alternately 15 min of heating from the backside and 15 min of cooling, the resulting deformations reveal 9 separately moving portions with rather different fringe densities and complicated boundaries, as Fig. 6.31 demonstrates. The dashed line does not mark a cleavage; but the fringes slightly change their orientation, as may be verified by viewing them along the black-white edges at a small angle to the paper. The shown displacements each have evolved in time intervals of  $\cong 10$  min. For the heating period,  $\varphi_O(x, y, t_i)$  was stored at an ambient temperature  $T_1$  when

the heater was switched on, while for the cooling period  $\varphi_o(x, y, t_i)$  was stored at an ambient temperature  $T_2$  when the heater was switched off.

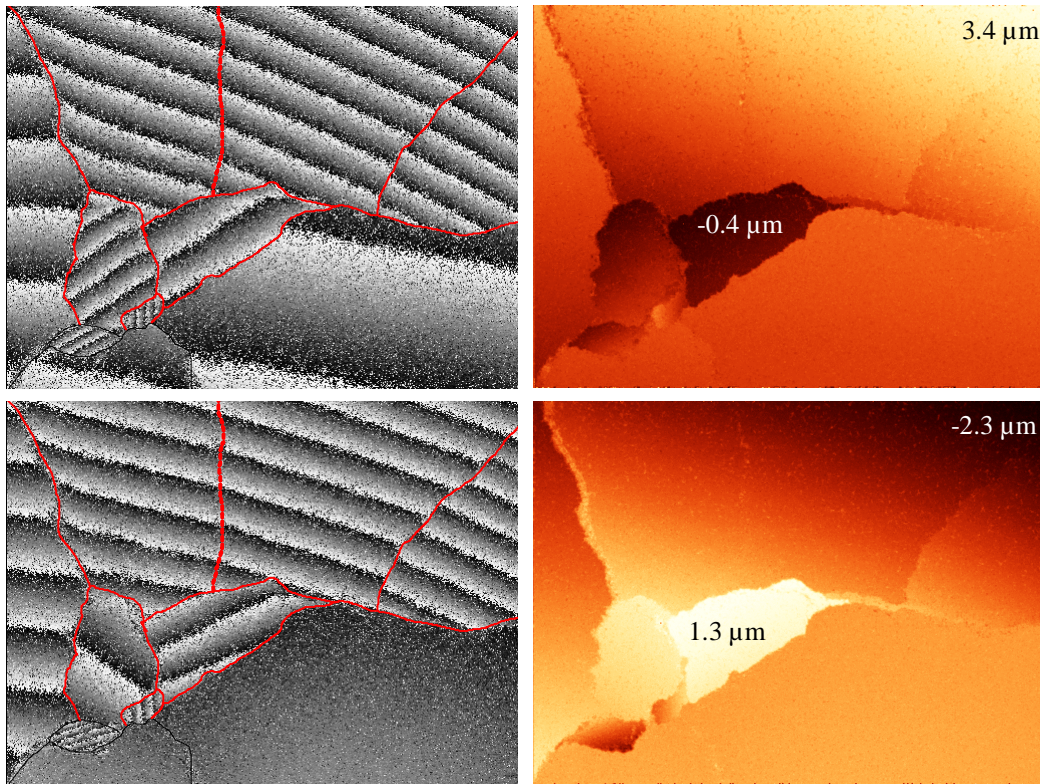


Fig. 6.31: Displacement phases mod  $2\pi$  (left) and corresponding "temperature" height maps as delivered by temporal unwrapping (right), for heating (top) and cooling period (bottom). Numerical values denote maximum and minimum displacements.

While it would be very laborious to define and spatially unwrap all the regions separately, it is even impossible to determine their relative heights from the sawtooth images on the left. When such displacements are monitored with temporal unwrapping, the problems are overcome. Without the need to fit data from different sub-areas together, a complete profile of the surface changes is obtained. One can, and should, test its reliability by checking the obtained surface tilts for consistency with those following from the number of sawtooth fringes. On removing the abovementioned "slow" pixels,  $\Phi(x, y)$  from temporal phase unwrapping did not deviate by more than  $0.1 \lambda$  from  $\Phi(x, y)$  as produced by spatial unwrapping of the corresponding sawtooth images, which also justifies some confidence in the absolute heights that are given in Fig. 6.31.

According to the height maps from temporal unwrapping on the right, the deformations that developed in the heating period are almost reversed during cooling, apart from some remaining displacements and deformations that are clearly emphasised by an addition of the height data from the two states, as demonstrated in Fig. 6.32 on the right. Most of the remaining displacement is presumably caused by an ambient temperature at the end of the cooling period that differed from  $T_1$ .

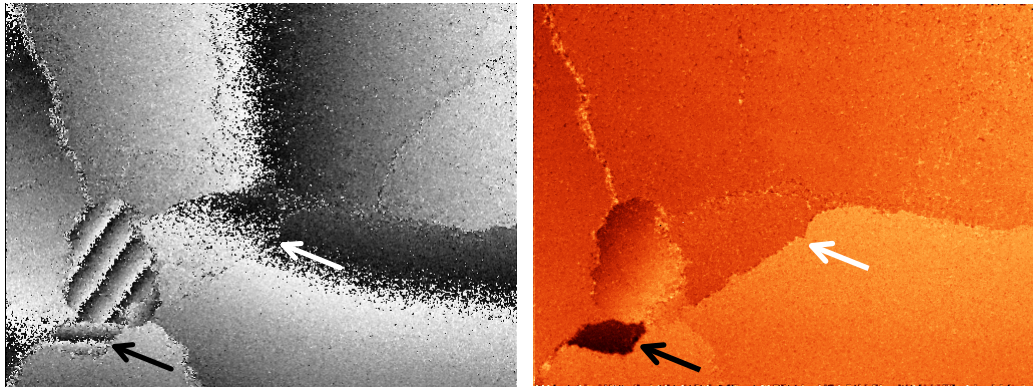


Fig. 6.32: Overall displacement after heating and cooling. Residual tilts are visible in the sawtooth image (left); rigid-body displacements are revealed in the "temperature" height map (right). Arrows mark locations of possible misinterpretations of the sawtooth image.

On the other hand, the sum of the sawtooth images lacks important information. At the black arrow, a substantial piston-type displacement is not discernible from the sawtooth image, while at the white arrow, the nearly matching fringe positions almost conceal the step of  $\cong 0.3 \mu\text{m}$  (1 fringe) that has actually remained. On the contrary, the results based on the height maps from the temporally unwrapped data are unambiguous. They need no interpretation and thus allow an easier assessment of object changes.





## 7 Summary

This thesis work has presented a detailed investigation of various aspects that concern the application of spatial phase shifting (SPS) in ESPI. The objective was to broaden the previously somewhat sparse knowledge of what happens in spatial phase sampling on speckle fields, and to utilise the findings to introduce some improvements of SPS.

The ground on which to base such an investigation is, first of all, an extensive study of the nature of speckle fields. Fortunately, speckle statistics have been an important topic in optical research for some 40 years, so that many useful results could be collected and grouped. The theoretical studies were accompanied by experimental validations of some results.

With respect to SPS, the one-dimensional intensity and phase gradients deserve particular interest, and it was found that the speckle intensity is correlated with the intensity gradient and anticorrelated with the phase gradient. This simple rule of thumb provided valuable guidance as to the assistance of speckle statistics in improving SPS. The speckle intensity field, showing more spatial structure than the phase field, hardly allows reasonable assumptions to be modelled in the phase calculation, but is directly accessible in the experiment. This extra information can be used to counteract the disadvantageous influence of speckle intensity fluctuations on the interferogram. The speckle phase field was seen to be co-operative for interferometry: the phase gradients are low where the speckle field is bright, and those regions of the field where the phase "leaps" or is even undefined, were seen to be rather dark anyway. Since constant speckle phase gradients can be envisaged as linear phase-shift miscalibrations, the use of phase-calculation formulae that are tolerant of this type of error seemed to be the most sensible decision for effectively reducing measurement errors.

After getting familiar with the properties of the speckled object wavefront, it was necessary to turn towards optimisation of the way to process speckle interferograms. For this purpose, digital speckle interferometry and the phase-sampling process have been reviewed. It was found that it is always better, in SPS and TPS, to subtract speckle phase maps than to work with correlation fringes; this has been confirmed by experimental results.

The aspects of speckle interferometry that pertain especially to SPS have been discussed in detail. The spatial phase shift was seen to be geometrically quasi-constant to a very high degree of accuracy; however the spatial frequency content of speckle interferograms supersedes this theoretical result, and the subjects of speckle size and phase-shift setting have been addressed from the viewpoint of spatial frequencies.

Since speckle phase gradients cause significant distortions in the carrier fringe pattern, its spatial frequency spectrum will be considerably broadened. It is therefore worthwhile to examine the effect in the spatial frequency domain. Consequently, the well-established and powerful Fourier description of phase-shifting formulae has been used. It interprets phase extraction as a digital signal filtering process in the spectral domain, with characteristic spectral amplitude and phase transfer functions. When using this

method to search for a phase-shifting formula with high phase-shift error resistance, the question arose whether it would be better to optimise the amplitude or the phase spectrum of the phase extraction formula for low phase-measurement errors. To settle the question, a simple auxiliary function was introduced which is invariant under the various optimisations and thus showed that nothing is to be gained by simply representing a formula in different ways. This behaviour was confirmed in SPS experiments.

Another valuable means of characterising the spatial phase evaluation is the dependence of the phase-measurement error on the phase to be measured. It was elucidated how the phase reconstruction generates periodic errors in the sawtooth fringes and systematic biases for the phase calculation, and what role the choice of the phase-calculation formula plays for this effect.

The quest for a reliable performance figure of ESPI phase measurements, which is indispensable to carry out comparisons and quantify improvements, has led to the creation of a standardised noise quantification method that fits an ideal data set to a real one and delivers the standard deviation of the remaining phase differences. The displacements to use this method were standardised as well. The advantages of the fitting method have been demonstrated by confrontation with various other methods of generating reference data.

The noise quantification tool was then extensively used to compare the performance of SPS with that of TPS in various measuring geometries, where a simple phase-shifting scheme was used under stable laboratory conditions. A multi-purpose interferometer allowed to carry out this comparison under the best possible constancy of experimental parameters. By varying quantities like fringe densities, speckle size and shape, and object illumination intensity, characteristic behaviours of SPS and TPS were explored. It was found that TPS offers advantages for in-plane measurements and under severe shortage of laser power; for out-of-plane configurations, the difference was found to vanish with increasing fringe density.

As an extension of the performance study with standard experimental parameter settings and data processing, several ways to improve the SPS technique have been implemented and tested. A very important result is the finding that the role of the beam ratio is decisive in SPS but has far less impact on TPS. Then, in agreement with the hints from theoretical considerations on spatial phase sampling, a phase shift of  $90^\circ$  per sample was found to yield better measurements than  $120^\circ$  per sample.

Based on the conclusion from the investigation of speckle statistics, a formula was established that can make use of a separate recording of the speckle pattern alone to correct phase-calculation errors introduced by speckle intensity gradients. The performance thus gained is however almost reached by uncorrected measurements when the beam ratio is set to its optimum, which was around 30 for the experimental set-up used.

To compensate measurement errors by speckle phase gradients, a simple averaging formula was used and seen to bring about a relevant improvement. This improvement can only partly be ascribed to the cancellation of phase-shift errors; also the enlargement of the spatial sampling window from 3 to 4 pixels plays a role.

The feasibility of combining intensity- and phase-gradient correction was demonstrated and shown to yield the least measurement error; however the intensity-gradient correction does not recommend itself strongly, since almost the same fringe quality can be achieved without it and at an optimised beam ratio instead.

An important step is the extension of the phase shift to two dimensions, which allows to use the spatial frequency plane more efficiently; thus, multiple phase measurements can be carried out and averaged for each image pixel to make up more reliable values. The combination of this experimental modification with the computational solutions decreases the rms of the phase-measurement error in unfiltered phase maps to below  $\lambda/20$  for moderate fringe densities, which remains valid when the speckle size is reduced to 2.5 pixels.

This accuracy is about the best that one can obtain by phase-shifting; therefore the Fourier-transform approach to phase extraction has been tested, for which a speckle-intensity correction can also be carried out by simple subtraction of the speckle pattern from the interferogram or, equivalently, the speckle halo in the spatial frequency plane. It turned out that the Fourier method yields an improvement only at very low fringe densities. For higher fringe densities, the intrinsic data smoothing property of SPS formulae due to the spatial extent of the phase-calculation window gets apparent, and the noise introduced by speckle decorrelation is somewhat smaller than in the Fourier transform method.

Another method of error reduction is to use a "standard" phase-shifting method and to enable it to process only reliable data, i.e. to eliminate invalid pixels from the measurement. This has been realised by merging valid phase data obtained from orthogonally polarised speckle patterns.

Finally, SPS has been used to implement temporal phase unwrapping, and the combination of the two techniques has successfully been applied to deal with the practical problems of automating data storage in long-term experiments and of measuring deformations of discontinuous objects.

On the whole, the collection of aspects of and possibilities for SPS presented in this work should prove useful for its successful application in various ESPI measurements. It could be shown that the suspected disadvantages of SPS constitute no serious restrictions in practice, all the less as some simple and effective performance enhancements are possible. With its ease of use not being the least, there are good arguments to consider SPS as an alternative also for situations where TPS is applicable, and to use it just as confidently.



## 8 References

- [Ada97] M. Adams, K. Hinsch, F. Lange, K. Wolff: Polarization effects in speckle correlation metrology, *Opt. Eng.* 36.8 (1997), 2225-2228
- [Aebi97] H. Aebischer, E. Mazza: Measurement of the nanometre deformation field in metallic microbars with microscopical ESPI, in: *Optical Inspection and Micromasurement II*, Proc. SPIE 3098 (1997), 400-410
- [Aebi99] H. Aebischer, S. Waldner: A simple and effective method for filtering speckle-interferometric phase fringe patterns, *Opt. Comm.* 162 (1999), 205-210
- [Alb99] D. Albrecht: Estimation of the 2D measurement error introduced by in-plane and out-of-plane ESPI measurements, *Opt. Las. Eng.* 31 (1999), 63-81
- [All63] L. Allen, D. Jones: An analysis of the granularity of scattered optical maser light, *Phys. Lett.* 7.5 (1963), 321-323
- [Ara96] Y. Arai, S. Yokozeiki, T. Yamada: High-speed fringe analysis method using frequency-demodulation technology, *Opt. Eng.* 35.8 (1996), 2341-2344
- [Ara97] Y. Arai, S. Yokozeiki, K. Shiraki, T. Yamada: High-precision two-dimensional spatial fringe analysis method, *J. Mod. Opt.* 44.4 (1997), 739-751
- [Bah80] R. Bahuguna, K. Gupta, K. Singh: Expected number of intensity level crossings in a normal speckle pattern (Letter), *JOSA* 70.7 (1980), 874-876
- [Bar80] R. Barakat: The level-crossing rate and above-level duration time of the intensity of a Gaussian random process, *Inf. Sci.* 20 (1980), 83-87
- [Bar81] N. Baranova, B. Zel'dovich: Dislocations of the wave-front surface and zeros of the amplitude, *Sov. Phys. JETP* 53.5 (1981), 925-929
- [Bar83] N. Baranova, A. Mamaev, N. Pilipetskii, V. Shkunov, B. Zel'dovich: Wave-front dislocations: topological limitations for adaptive systems with phase conjugation, *JOSA* 73.5 (1983), 525-528
- [Bar85] R. Barakat: The statistical properties of partially polarized light, *Opt. Act.* 32.3 (1985), 295-312
- [Bar87] R. Barakat: Second-order statistics of integrated intensities and of detected photoelectrons, *J. Mod. Opt.* 34.1 (1987), 91-102
- [Bar88] R. Barakat: Level-crossing statistics of aperture-integrated isotropic speckle, *JOSA A* 5.8 (1988), 1244-1247
- [Bar91] R. Barakat: Probability density of the radial gradient of aperture-averaged isotropic-speckle intensity (Letter), *JOSA A* 8.2 (1991), 450-451
- [Bar99] B. Barrientos García, A. Moore, C. Pérez López, L. Wang, T. Tschudi: Spatial phase-stepped interferometry using a holographic optical element, *Opt. Eng.* 38.12 (1999), 2069-2074
- [Bas95] I. Basistiy, M. Soskin, M. Vasnetsov: Optical wavefront dislocations and their properties, *Opt. Comm.* 119 (1995), 604-612
- [Ber78] M. Berry: Disruption of wavefronts: statistics of dislocations in incoherent Gaussian random waves, *J. Phys. A* 11.1 (1978), 27-37
- [Ber97] E. Berger, W. von der Linden, V. Dose, M. Ruprecht, A. Koch: Approach for the evaluation of speckle deformation measurements by application of the wavelet transformation, *Appl. Opt.* 36.29 (1997), 7455-7460
- [Bie89] E. Bieber, W. Osten: Improvement of speckled fringe patterns by Wiener filtration, in: *Interferometry '89*, Proc. SPIE 1121 (1989), 393-399
- [Bon86] D. Bone, H. Bachor, R. Sandeman: Fringe-pattern analysis using a 2-D Fourier transform, *Appl. Opt.* 25.10 (1986); D. Bone, H. Bachor, R. Sandeman: Spectral line interferometry with temporal and spatial resolution, *Opt. Comm.* 57 (1986), 39-44

- [Bot97] T. Bothe, J. Burke, H. Helmers, Spatial phase shifting in ESPI: minimization of phase reconstruction errors, *Appl. Opt.* 36.22 (1997), 5310-5316
- [Bra87] R. Bracewell: *The Fourier transform and its applications*, McGraw-Hill, New York (1987), 2<sup>nd</sup> edition
- [Bro87] I. Bronshtein, K. Semendyaev: *Taschenbuch der Mathematik*, G. Grosche, V. Ziegler, D. Ziegler, eds., Harri Deutsch Verlag, Thun, 23<sup>rd</sup> edition (1987)
- [Bro98] A. Brozeit, J. Burke, H. Helmers, H. Sagehorn, R. Schuh: Noise reduction in ESPI fringes by merging orthogonally polarised speckle fields, *Opt. Las. Technol.* 30 (1998), 325-329
- [Bro00] A. Brozeit, J. Burke, H. Helmers: Active phase stabilisation in ESPI without additional optical components, *Opt. Comm.* 173 (2000), 95-100
- [Bru74] H. Bruning, D. Herriott, J. Gallagher, D. Rosenfeld, A. White, D. Brangaccio: Digital wavefront measuring interferometer for testing optical surfaces and lenses, *Appl. Opt.* 13.11 (1974), 2693-2703
- [vBru98] H. van Brug: Temporal phase unwrapping and its application in shearography systems, *Appl. Opt.* 37.28 (1998), 6701-6706
- [vBru99] H. van Brug: Temporal phase unwrapping with two or four images per time frame: a comparison, in: *Interferometry 99: Techniques and Technologies*, Proc. SPIE 3744 (1999), 358-365
- [Bur78] C. Burckhardt: Speckle in ultrasound B-mode scans, *Trans. IEEE SU-25.1* (1978), 1-6
- [Bur98a] J. Burke, H. Helmers, C. Kunze, V. Wilkens, Speckle intensity and phase gradients: influence on fringe quality in spatial phase shifting ESPI systems, *Opt. Comm.* 152 (1998), 144-152
- [Bur98b] J. Burke, H. Helmers: Complex division as a common basis for calculating phase differences in ESPI in one step - Technical Note, *Appl. Opt.* 37.13 (1998), 2589-2590
- [Bur99a] J. Burke, H. Helmers: Performance of spatial vs. temporal phase shifting in ESPI, in: *Interferometry 99: Techniques and Technologies*, Proc. SPIE 3744 (1999), 188-199
- [Bur00a] J. Burke, H. Helmers: Spatial vs. temporal phase shifting in ESPI: noise comparison in phase maps, *Appl. Opt.* 39.25 (2000), 4598-4606
- [Bur00b] J. Burke, H. Helmers: Matched data storage in ESPI by combination of spatial phase shifting with temporal phase unwrapping, *Opt. Las. Technol.* (2000), in press
- [Cap97] A. Capanni, L. Pezzati, D. Bertani, M. Cetica, F. Francini: Phase-shifting speckle interferometry: a noise reduction filter for phase unwrapping, *Opt. Eng.* 36.9 (1997), 2466-2472
- [Car66] P. Carré: Installation et utilisation du comparateur photoélectrique et interférentiel, *Metrologia* 2.1 (1966), 13-23
- [Cha79] P. Chandley, H. Escamilla: Speckle from a rough surface when the illuminated region contains few correlation areas: the effect of changing the surface height variance, *Opt. Comm.* 29 (1979), 151-154
- [Cha85] M. Chang, C. Hu, P. Lam, J. Wyant: High precision deformation measurement by digital phase shifting holographic interferometry, *Appl. Opt.* 24.22 (1985), 3780-3783
- [Che85] Y. Cheng, J. Wyant: Phase shifter calibration in phase-shifting interferometry, *Appl. Opt.* 24.18 (1985), 3049-3052
- [Che91] J. Chen, R. Zhu, L. Liu, D. Chen: Two dimensional Fourier transform algorithm analyzing the interferogram and the fringe shift, in: *Laser Interferometry IV: Computer-Aided Interferometry*, Proc. SPIE 1553 (1991), 616-625
- [Cog99] R. Coggrave, J. Huntley: Real-time speckle interferometry fringe analysis system, in: *Interferometry 99: Techniques and Technologies*, Proc. SPIE 3744 (1999), 464-473
- [Col92] D. Colucci, P. Wizinowich: Millisecond phase acquisition at video rates, *Appl. Opt.* 31.28 (1992), 5919-5925
- [Cre85a] K. Creath: Phase-shifting speckle interferometry, in: *International Conference on Speckle*, Proc. SPIE 556 (1985), 337-346

- [Cre85b] K. Creath: Phase-shifting speckle interferometry, *Appl. Opt.* 24.18 (1985), 3053-3058
- [Cre85c] K. Creath: Averaging double-exposure speckle interferograms, *Opt. Lett.* 10.12 (1985), 582-584
- [Cre87] K. Creath, I. Bowler: The smoothing of ESPI images, *Opt. Las. Eng.* 7 (1987), 163-173
- [Cre88] K. Creath: Phase-measurement interferometry techniques, in: *Progress in Optics XXVI*, E. Wolf, ed., Elsevier, Amsterdam (1988), 349-393
- [Cre94] K. Creath: Phase-shifting holographic interferometry, in: *Holographic interferometry – Principles and methods*, P. Rastogi, ed., Springer, Berlin (1994), p. 143
- [Cre96] K. Creath, J. Schmit: *N*-point spatial phase-measurement techniques for non-destructive testing, *Opt. Las. Eng.* 24 (1996), 365-379
- [Cri85] T. Crimmins: Geometric filter for speckle reduction, *Appl. Opt.* 24.10 (1985), 1438-1443
- [Dav74] D. Davies, S. Kingsley: Method of phase-modulating signals in optical fibres: application to optical-telemetry systems, *Electron. Lett.* 10 (1974), 21-22
- [Dáv94] A. Dávila, D. Kerr, G. Kaufmann: Digital processing of ESPI addition fringes, *Appl. Opt.* 33.25 (1994), 5964-5969
- [Dáv96] A. Dávila, G. Kaufmann, D. Kerr: Scale-space filter for smoothing ESPI fringes, *Opt. Eng.* 35.12 (1996), 3549-3554
- [Dec96] L. Deck: Vibration-resistant phase-shifting interferometry, *Appl. Opt.* 35.34 (1996), 6655-6662
- [Dec98] L. Deck, P. de Groot: Punctuated quadrature phase-shifting interferometry, *Opt. Lett.* 23.1 (1998), 19-21
- [Dir97] H. Dirks, K. Lindner: Zum Einsatz von Glasfasern in der ESPI, Diploma thesis, Carl von Ossietzky University Oldenburg, 1997
- [Dob97] A. Dobroiu, P. Cătălin Logofătu, D. Apostol, V. Damian: Statistical self-calibrating algorithm for three-sample phase-shift interferometry, *Meas. Sci. Technol.* 8 (1997), 738-745
- [Don79] S. Donati, G. Martini: Speckle-pattern intensity and phase: second-order conditional statistics, *JOSA* 69.12 (1979), 1690-1694
- [Dör82] B. Dörband: Die 3-Interferogramm-Methode zur automatischen Streifenbewertung in rechnergesteuerten digitalen Zweistrahlinterferometern, *Optik* 60.2 (1982), 161-174
- [Dor99] B. Dorrió, J. Fernández: Phase-evaluation methods in whole-field optical measurement techniques, *Meas. Sci. Technol.* 10 (1999), R33-R55
- [Dov00] Á. Doval: A systematic approach to TV holography, *Meas. Sci. Technol.* 11 (2000), R1-R36
- [Ebe79a] K. Ebeling: Experimental investigation of some statistical properties of monochromatic speckle patterns, *Opt. Act.* 26 (1979), 1345-1349
- [Ebe79b] K. Ebeling: Statistical properties of spatial derivatives of the amplitude and intensity of monochromatic speckle patterns, *Opt. Act.* 26 (1979), 1505-1521
- [Ebe80] K. Ebeling: *K*-distributed spatial intensity derivatives in monochromatic speckle patterns, *Opt. Comm.* 35 (1980), 323-326
- [Eich88] N. Eichhorn, W. Osten: An algorithm for the fast derivation of line structures from interferograms, *J. Mod. Opt.* 35.10 (1988), 1717-1725
- [ElJa99] A. El Jarad: Anwendung der Videoholographie für mikroskopische Bereiche zur Untersuchung von Alterungsprozessen historischer Farbschichten, Diploma thesis, Carl von Ossietzky University Oldenburg (1999)
- [Enn75] A. Ennos: Speckle interferometry, in: *Laser Speckle and Related Phenomena*, J. Dainty, ed., Springer, Berlin (1975)
- [Enn97] A. Ennos: A look back at the early developments of speckle metrology, *Opt. Las. Eng.* 26 (1997), 87-92

- [Ett97] Unwrapping and visualisation software ISTR A 2.01 (1997), Qualitätssicherung Dr. Ettemeyer GmbH & Co., Neu-Ulm
- [Fac93] M. Facchini, D. Albrecht, P. Zanetta: Phase detection algorithm in ESPI fringes with speckle noise reduction by using preliminary time averaging, in: *Proc. 2<sup>nd</sup> International workshop on automatic processing of fringe patterns, FRINGE '93*, Bremen, Akademie Verlag, Berlin (1993), 45-50
- [Far94] C. Farrell, M. Player: Phase-step insensitive algorithms for phase-shifting interferometry, *Meas. Sci. Technol.* 5 (1994), 648-652
- [Fer98] A. Fernández, G. Kaufmann, Á. Doval, J. Blanco García, J. Fernández: Comparison of carrier removal methods in the analysis of TV holography fringes by the Fourier transform method, *Opt. Eng.* 37.11 (1998), 2899-2905
- [Fie82] J. Fienup: Phase retrieval algorithms: a comparison, *Appl. Opt.* 21.15 (1982), 2758-2769
- [Flo93] T. Floureaux: Improvement of electronic speckle fringes by addition of incremental images, *Opt. Las. Technol.* 25.4 (1993), 255-258
- [Fre90a] K. Freischlad, C. Koliopoulos: Fourier description of digital phase-measuring interferometry, *J. Opt. Soc. Am. A* 7.4 (1990), 542-551
- [Fre90b] K. Freischlad, M. Küchel, W. Wiedmann, W. Kaiser, M. Mayer: High precision interferometric testing of spherical mirrors with long radius of curvature, in: *Optical Testing and Metrology III: Recent Advances in Industrial Optical Inspection*, Proc. SPIE 1332 (1990), 8-17
- [Fre90c] K. Freischlad, M. Küchel, K. Schuster, U. Wegmann, W. Kaiser: Real-time wavefront measurement with  $\lambda/10$  fringe spacing for the optical shop, in: *Optical Testing and Metrology III: Recent Advances in Industrial Optical Inspection*, Proc. SPIE 1332 (1990), 18-24
- [Fre90d] I. Freund, M. Kaveh, R. Berkovits, M. Rosenbluh: Universal polarization correlations and microstatistics of optical waves in random media, *Phys. Rev. B* 42.4 (1990), 2613-2616
- [Fre92] K. Freischlad, M. Küchel: Speckle reduction by virtual spatial coherence, in: *Interferometry: Techniques and Analysis*, Proc. SPIE 1755 (1992), 38-43
- [Fre93] I. Freund, N. Shvartsman, V. Freilikher: Optical dislocation networks in highly random media, *Opt. Comm.* 101 (1993), 247-264
- [Fre94a] I. Freund: Optical vortices in random wave fields: statistical probability densities, *JOSA A* 11.5 (1994), 1644-1652
- [Fre94b] I. Freund, N. Shvartsman: Wave-field phase singularities: the sign principle, *Phys Rev. A* 50.6 (1994), 5164-5172
- [Fre95a] I. Freund: Optical phase maps, in: *Optical Tomography, Photon Migration, and Spectroscopy of Tissue and Model Media: Theory, Human Studies, and Instrumentation*, Proc. SPIE 2389.1 (1995), 411-419
- [Fre95b] I. Freund: Amplitude topological singularities in random electromagnetic wavefields, *Phys. Lett. A* 198 (1995), 139-144
- [Fre95c] I. Freund: Saddles, singularities, and extrema in random phase fields, *Phys. Rev. E* 52.3 (1995), 2348-2360
- [Fre95d] I. Freund, N. Shvartsman: Structural correlations in Gaussian random wave fields, *Phys. Rev. E* 51.4 (1995), 3770-3773
- [Fre96a] I. Freund, D. Kessler: Phase autocorrelation of random wave fields, *Opt. Comm.* 124 (1996), 321-332
- [Fre96b] I. Freund: Intensity critical point correlation functions in random wave fields, *Opt. Comm.* 128 (1996), 315-324
- [Fre97a] I. Freund, V. Freilikher: Parameterization of anisotropic vortices, *JOSA A* 14.8 (1997), 1902-1910
- [Fre97b] I. Freund: Critical-point level-crossing geometry in random wave fields, *JOSA A* 14.8 (1997), 1911-1927



- [Fre98a] I. Freund: '1001' correlations in random wave fields, *Wav. Rand. Med.* 8 (1998), 119-158
- [Fre98b] I. Freund: Phase correlations at neighboring intensity critical points in Gaussian random wave fields, *Appl. Opt.* 37.32 (1998), 7560-7567
- [Fre99] I. Freund: Critical point explosions in two-dimensional wave fields, *Opt. Comm.* 159 (1999), 99-117; Corrigendum, *Opt. Comm.* 173 (2000), 435
- [Fre00] I. Freund, A. Belenkiy: Higher-order extrema in two-dimensional wave fields, *JOSA A* 17.3 (2000), 434-446
- [Fri92] D. Fried, J. Vaughn: Branch cuts in the phase function, *Appl. Opt.* 31.15 (1992), 2865-2882
- [Fri98] D. Fried: Branch point problem in adaptive optics, *JOSA A* 15.10 (1998), 2759-2768
- [Ger72] R. Gerchberg, W. Saxton: A practical algorithm for the determination of phase from image and diffraction plane pictures, *Optik* 35.2 (1972), 237-246
- [Gol65] L. Goldfischer: Autocorrelation function and power spectral density of laser-produced speckle patterns, *JOSA* 55.3 (1965), 247-253
- [Goo75] J. Goodman: Statistical Properties of Laser Speckle Patterns, in: *Laser Speckle and Related Phenomena*, J. C. Dainty, ed., Springer, Berlin, 1<sup>st</sup> edition (1975)
- [Gra94] I. Gradshteyn, I. Ryzhik: Table of integrals, series, and products, A. Jeffrey, ed., Academic Press, London, 5<sup>th</sup> edition (1994)
- [Gre84] J. Greivenkamp: Generalized data reduction for heterodyne interferometry, *Opt. Eng.* 23.4 (1984), 350-352
- [Gre88] R. Green, J. Walker, D. Robinson: Investigation of the Fourier-transform method of fringe pattern analysis, *Opt. Las. Eng.* 8 (1988), 29-44
- [Gre92] J. Greivenkamp, J. Bruning: Phase shifting interferometers, in: *Optical Shop Testing*, D. Malacara, ed., Wiley, New York (1992), pp. 518-532
- [dGro95] P. de Groot: Derivation of algorithms for phase-shifting interferometry using the concept of a data-sampling window, *Appl. Opt.* 34.22 (1995), 4723-4730
- [dGro96] P. de Groot, L. Deck: Numerical simulations of vibration in phase-shifting interferometry, *Appl. Opt.* 35.13 (1996), 2172-2178
- [dGro97] P. de Groot: 101-frame algorithm for phase-shifting interferometry, in: *Optical Inspection and Micromasurement II*, Proc. SPIE 3098 (1997), 283-292
- [Gül93] G. Gülker, H. Helmers, K. Hinsch, C. Hölscher: Automatic timing of ESPI fringe storage in long-term measurements based on speckle correlation formalism, in: *Proc. 2<sup>nd</sup> International workshop on automatic processing of fringe patterns, FRINGE'93*, Bremen, Akademie Verlag, Berlin (1993), 411-416
- [Gül96] G. Gülker, H. Helmers, K. Hinsch, P. Meinschmidt, K. Wolff: Deformation mapping and surface inspection of historical monuments, *Opt. Las. Eng.* 24 (1996), 183-213
- [Gut93] J. Gutjahr: New developments in phase-shifting interferometry, in: *Proc. 2<sup>nd</sup> International workshop on automatic processing of fringe patterns, FRINGE'93*, Bremen, Akademie Verlag, Berlin (1993), 60-65
- [vHaa94] A. van Haasteren, H. Frankena: Real-time displacement measurement using a multicamera phase-stepping speckle interferometer, *Appl. Opt.* 33.19 (1994), 4137-4142
- [Hac00] E. Hack: ESPI – principles and prospects, in: *Trends in optical nondestructive testing and inspection*, P. Rastogi, D. Inaudi, eds., Elsevier, Amsterdam (2000), p. 213
- [Har82] P. Hariharan, B. Oreb, N. Brown: A digital phase-measurement system for real-time holographic interferometry, *Opt. Comm.* 41 (1982), 393-396
- [Har87] P. Hariharan, B. Oreb, T. Eiju: Digital phase-shifting interferometry: a simple error-compensating phase calculation algorithm, *Appl. Opt.* 26.13 (1987), 2504-2505

- [Har94] P. Hariharan: Basic principles, in: *Holographic interferometry – Principles and methods*, P. Rastogi, ed., Springer, Berlin (1994), 7-31
- [Her96] M. Hertwig, T. Flemming, T. Floureux, H. Aebischer: Speckle interferometric damage investigation of fibre-reinforced composites, *Opt. Las. Eng.* 24 (1996), 485-504
- [Het00] A. Hettwer, J. Kranz, J. Schwider: Three channel phase-shifting interferometer using polarization optics and a diffraction grating, *Opt. Eng.* 39.4 (2000), 960-966
- [Hib95] K. Hibino, B. Oreb, D. Farrant, K. Larkin: Phase shifting for nonsinusoidal waveforms with phase-shift errors, *JOSA A* 12.4 (1995), 761-768
- [Hib97] K. Hibino, B. Oreb, D. Farrant, K. Larkin: Phase-shifting algorithms for nonlinear and spatially nonuniform phase shifts, *JOSA A* 14.4 (1997), 918-930
- [Hib98] K. Hibino, K. Larkin, B. Oreb, D. Farrant, Phase-shifting algorithms for nonlinear and spatially nonuniform phase shifts: reply to comment, *JOSA A* 15.5 (1998), 1234-1235
- [Hon97] S. Hong, J. Han: Considerations on speckle pattern interferometry of ultrasonic speckles, *Ultrasonics* 35 (1997), 329-332
- [Hor90] B. Horwitz: Multiplex techniques for real-time shearing interferometry, *Opt. Eng.* 29.10 (1990), 1223-1232
- [Hun92] J. Huntley, L. Benckert: Speckle interferometry: noise reduction by correlation fringe averaging, *Appl. Opt.* 31.14 (1992), 2412-2414 (Letter)
- [Hun93a] J. Huntley, H. Saldner: Temporal phase-unwrapping algorithm for automated interferogram analysis, *Appl. Opt.* 32.17 (1993), 3047-3052
- [Hun93b] J. Huntley, L. Benckert: Measurement of dynamic crack tip displacement field by speckle photography and interferometry, *Opt. Las. Eng.* 19 (1993), 299-312
- [Hun95] J. Huntley, J. Buckland: Characterization of sources of  $2\pi$  phase discontinuity in speckle interferograms, *JOSA A* 12.9 (1995), 1990-1996
- [Hun97] J. Huntley: Random phase measurement errors in digital speckle interferometry, *Opt. Las. Eng.* 26 (1997), 131-150
- [Hun98] J. Huntley: Suppression of phase errors from vibration in phase-shifting interferometry, *JOSA A* 15.8 (1998), 2233-2241
- [Hun99] J. Huntley, G. Kaufmann, D. Kerr: Phase-shifted dynamic speckle pattern interferometry at 1 kHz, *Appl. Opt.* 38.31 (1999), 6556-6563
- [Ich72] Y. Ichioka, M. Inuiya: Direct phase detecting system, *Appl. Opt.* 11.7 (1972), 1507-1514
- [Joż92] R. Joźwicki, M. Kujawińska, L. Sałbut: New contra old wavefront measurement concepts for interferometric optical testing, *Opt. Eng.* 31.3 (1992), 422-433
- [Joe94] C. Joenathan: Phase-measuring interferometry: new methods and error analysis, *Appl. Opt.* 33.19 (1994), 4147-4155
- [Joe95] C. Joenathan, A. Sohmer, L. Bürkle: Increased sensitivity to in-plane displacements in ESPI, *Appl. Opt.* 34.16 (1995), 2880-2885
- [Joe98a] C. Joenathan, B. Franze, P. Haible, H. Tiziani: Speckle interferometry with temporal phase evaluation for measuring large object deformation, *Appl. Opt.* 37.13 (1998) 2608-2614
- [Joe98b] C. Joenathan, B. Franze, P. Haible, H. Tiziani: Shape measurement by use of temporal Fourier transformation in dual-beam illumination speckle interferometry, *Appl. Opt.* 37.16 (1998), 3385-3390
- [Joh89] S. Johansson, K. Predko: performance of a phase-shifting speckle interferometer for measuring deformation and vibration, *J. Phys. E: Sci. Instrum.* 22 (1989), 289-292
- [Kad85] H. Kadono, N. Takai, T. Asakura: Experimental study of the laser speckle phase in the image field, *Opt. Act.* 32 (1985), 1223-1234

- [Kad91] H. Kadono, S. Toyooka: Statistical interferometry based on the statistics of speckle phase, *Opt. Lett.* 16.12 (1991), 883-885
- [Kad97] H. Kadono, H. Takei, S. Toyooka: A noise-immune method of phase unwrapping in speckle interferometry, *Opt. Las. Eng.* 26 (1997), 151-164
- [Kat97] J. Kato, I. Yamaguchi, T. Nakamura, S. Kuwashima: Video-rate fringe analyzer based on phase-shifting electronic moiré patterns, *Appl. Opt.* 36.32 (1997), 8403-8412
- [Kau94] G. Kaufmann, D. Kerr, N. Halliwell: Contrast enhancement of pulsed ESPI addition fringes, *Opt. Las. Eng.* 20 (1994), 25-34
- [Kau96] G. Kaufmann, G. Galizzi: Speckle noise reduction in TV holography fringes using wavelet thresholding, *Opt. Eng.* 35.1 (1996), 9-14
- [Kem99] Q. Kemaο, M. Hong, W. Xiaoping, Real-time polarisation phase shifting technique for dynamic deformation measurement, *Opt. Las. Eng.* 31 (1999), 289-295
- [Ker88] D. Kerr, J. Tyrer: Use of high-resolution real-time image processing techniques in generation and analysis of ESPI fringe patterns, *Opt. Las. Eng.* 8 (1988), 109-121
- [Ker89] D. Kerr, F. Mendoza Santoyo, J. Tyrer: Manipulation of the Fourier components of speckle fringe patterns as part of an interferometric analysis process, *J. Mod. Opt.* 36.2 (1989), 195-203
- [Ker90] D. Kerr, F. Mendoza Santoyo, J. Tyrer: Extraction of phase data from ESPI fringes using a single-phase-step method: a novel approach, *JOSA A* 7.5 (1990), 820-826
- [Kes98] D. Kessler, I. Freund: Level-crossing densities in random wave fields, *JOSA A* 15.6 (1998), 1608-1618
- [Kim97] S. Kim, M. Kang, G. Han: Accelerated phase-measuring algorithm of least squares for phase-shifting interferometry, *Opt. Eng.* 36.11 (1997), 3101-3106
- [Kin77] J. Kingman, S. Taylor: Introduction to measure and probability, Cambridge University Press, Cambridge, 3<sup>rd</sup> edition (1977)
- [Kol99] E. Kolenović, W. Osten, W. Jüptner: Non-linear speckle phase changes in the image plane caused by out of plane displacement, *Opt. Comm.* 171 (1999), 333-344
- [Kow83] M. Kowalczyk: Density of 2-D gradient of intensity in fully developed speckle pattern, *Opt. Comm.* 48 (1983), 233-236
- [Koz99] J. Kozłowski, G. Serra: Analysis of the complex phase error introduced by the application of the Fourier transform method, *J. Mod. Opt.* 46.6 (1999), 957-971
- [Kra98] J. Kranz, J. Lamprecht, A. Hettwer, J. Schwider: Fiber optical single frame speckle interferometer for measuring industrial surfaces, in: *International Conference on Applied Optical Metrology*, Proc. SPIE 3407 (1998), 328-331
- [Kre86] T. Kreis: Digital holographic interference-phase measurement using the Fourier-transform method, *JOSA A* 3.6 (1986), 847-855
- [Küch90] M. Küchel, W. Wiedmann: In-process metrology for large astronomical mirrors, in: *Advanced Optical Manufacturing and Testing*, Proc. SPIE 1333 (1990), 280-294
- [Küch91] M. Küchel: Verfahren zur Messung eines phasenmodulierten Signals, German patent DE-OS 4014019 A1, Nov 7, 1991
- [Küch94] M. Küchel, A. Hof: Method for analyzing periodic brightness patterns, US patent 5343294, Aug 30, 1994
- [Küch97] M. Küchel: Some progress in phase measurement techniques, in: *Automatic Processing of Fringe Patterns, Fringe 97*, Akademie Verlag, Berlin (1997), 27-44
- [Kuj88] M. Kujawińska, D. Robinson: Multichannel phase-stepped holographic interferometry, *Appl. Opt.* 27.2 (1988), 312-320

- [Kuj89] M. Kujawińska, A. Spik, D. Robinson: Quantitative analysis of transient events by ESPI, in: *Interferometry '89*, Proc. SPIE 1121 (1989), 416-423
- [Kuj91a] M. Kujawińska, L. Sałbut, K. Patorski: Three-channel phase stepped system for moiré interferometry, *Appl. Opt.* 30.13 (1991), 1633-1635
- [Kuj91b] M. Kujawińska, J. Wójciak: Spatial-carrier phase shifting technique of fringe pattern analysis, in: *Industrial Applications of Holographic and Speckle Measuring Techniques*, Proc. SPIE 1508 (1991), 61-67
- [Kuj91c] M. Kujawińska, J. Wójciak: High accuracy Fourier transform fringe pattern analysis, *Opt. Las. Eng.* 14 (1991), 325-339
- [Kuj93] M. Kujawińska: Spatial Phase Measurement Methods, in: *Interferogram Analysis*, D. Robinson, G. Reid, eds., IoP, Bristol (1993), 141-193
- [Kun97] C. Kunze, V. Wilkens: Optimierung der räumlichen Phasenschiebetechnik in der elektronischen Specklemuster-Interferometrie zur Messung von 3-D-Verformungen, Diploma thesis, Carl von Ossietzky University Oldenburg (1997)
- [Kwo84] O. Kwon: Multichannel phase-shifted interferometer, *Opt. Lett.* 9.2 (1984), 59-61
- [Lai91] G. Lai, T. Yatagai: Generalized phase-shifting interferometry, *JOSA A* 8.5 (1991), 822-827
- [Lar92a] K. Larkin, B. Oreb: Design and assessment of symmetrical phase-shifting algorithms, *JOSA A* 9.10 (1992), 1740-1748
- [Lar92b] K. Larkin, B. Oreb: A new seven-sample symmetrical phase-shifting algorithm, in: *Interferometry: Techniques and Analysis*, Proc. SPIE 1755 (1992), 2-11
- [Lar92c] K. Larkin, B. Oreb: Propagation of errors in different phase-shifting algorithms: a special property of the arctangent function, in: *Interferometry: Techniques and Analysis*, Proc. SPIE 1755 (1992), 219-227
- [Lar96] K. Larkin: Efficient nonlinear algorithm for envelope detection in white light interferometry, *JOSA A* 13.4 (1996), 832-843
- [Lar99] K. Larkin, personal communication, October 1999
- [Lee70] J. Leendertz: Interferometric displacement measurement on scattering surfaces utilising speckle effect, *J. Phys. E: Sci. Inst.* 3 (1970), 214-218
- [Lef80] H. Lefèvre: Single-mode fibre fractional wave devices and polarisation controllers, *Electron. Lett.* 16 (1980), 778-780
- [Leh95] M. Lehmann: Optimisation of wave intensities in phase-shifting speckle interferometry, *Opt. Comm.* 118 (1995), 199-206
- [Leh97a] M. Lehmann: Measurement optimization in speckle interferometry: the influence of the imaging lens aperture, *Opt. Eng.* 36.4 (1997), 1162-1168
- [Leh97b] M. Lehmann: Decorrelation-induced phase errors in phase-shifting speckle interferometry, *Appl. Opt.* 36.16 (1997), 3657-3667
- [Leh98] M. Lehmann: Statistical theory of two-wave speckle interferometry and its application to the optimization of deformation measurements, Ph.D. thesis N° 1797, École Polytechnique Fédérale de Lausanne (1998)
- [Lei62] E. Leith, J. Upatnieks: Reconstructed wavefronts and communication theory, *JOSA* 52.10 (1962), 1123-1130
- [Leu90] L. Leushacke, M. Kirchner: Three-dimensional correlation coefficient of speckle intensity for rectangular and circular apertures, *JOSA A* 7.5 (1990), 827-832
- [Li 92] Q. Li, F. Chiang: Three-dimensional dimension of laser speckle, *Appl. Opt.* 31.29 (1992), 6287-6291

- [Li 98] J. Li, X. Su, H. Su, S. Cha: Removal of carrier frequency in phase-shifting techniques, *Opt. Las. Eng.* 30 (1998), 107-115
- [Lir99] I. Lira, G. Kyriazis: Bayesian inference from measurement information, *Metrologia* 36 (1999), 163-169
- [Liu97] J. Liu, P. Ronney: Modified Fourier transform method for interferogram fringe pattern analysis, *Appl. Opt.* 36.25 (1997), 6231-6241
- [Løk87] O. Løkberg, G. Slettemoen: Basic ESPI, in: *Applied Optics and Optical Engineering*, Vol. X, R. Shannon, J. Wyant, eds., Academic Press, San Diego (1987)
- [Løk97] O. Løkberg, B. Seeberg, K. Vestli: Microscopic video speckle interferometry, *Opt. Las. Eng.* 26 (1997), 313-330
- [Lon60] M. Longuet-Higgins: Reflection and refraction at a random moving surface, *JOSA* 50.9 (1960), 838-856
- [Lóp00] J. Hernández López, D. Malacara Hernández: Exact linear detuning error in phase-shifting algorithms, *Opt. Comm.* 180 (2000), 9-14
- [Low70] S. Lowenthal, H. Arsenault: Image formation for coherent diffuse objects: statistical properties, *JOSA* 60.11 (1970), 1478-1483
- [Lüh93] B. Lührig: Special filter methods for reducing speckle noise in saw-tooth phase images, in: *Proc. 2<sup>nd</sup> International workshop on automatic processing of fringe patterns, FRINGE '93*, Bremen, Akademie Verlag, Berlin (1993), 361-366
- [Mło95] J. Młokosiewicz, W. Para, W. Śmietański: Application of the Fourier description of discrete phase change method to synthesis of the five-point algorithms, *Opt. Appl.* XXV.1 (1995), 5-14
- [Maa97] T. Maack, R. Kowarschik, G. Notni: Optimum lens aperture in phase-shifting speckle interferometric setups for maximum accuracy of phase measurement, *Appl. Opt.* 36.25 (1997), 6217-6224
- [Maa98] T. Maack, R. Kowarschik, G. Notni: Effect of the reference beam in speckle interferometry, *Opt. Comm.* 154 (1998), 137-144
- [Mac83] W. Macy, Jr.: Two-dimensional fringe-pattern analysis, *Appl. Opt.* 22.23 (1983), 3898-3901
- [Mai60] T. Maiman: Stimulated optical radiation in ruby, *Nature* 187 (1960), 493-494
- [Mal97] D. Malacara Doblado, M. Servín, D. Malacara Hernández: Graphical vector description of sampling weights in phase-detecting algorithms, *Opt. Eng.* 36.7 (1997), 2086-2091
- [Mal98] D. Malacara, M. Servín, Z. Malacara: *Interferogram analysis for optical testing*, Marcel Dekker, New York (1998)
- [Mal00] D. Malacara Doblado, B. Dorrío, D. Malacara Hernández: Graphic tool to produce tailored symmetrical phase-shifting algorithms, *Opt. Lett.* 25.1 (2000), 64-66
- [Mar00] R. Martínez Celorio, A. Dávila, G. Kaufmann, G. Mendiola: Extension of the displacement measurement range for shearing ESPI using carrier fringes and a temporal phase-unwrapping method, *Opt. Eng.* 39.3 (2000), 751-757
- [Mar91] I. Markhvida, L. Tanin, I. Drobot: Experimental investigation of speckle size distribution, in: *Industrial applications of holographic and speckle measuring techniques*, Proc. SPIE 1508 (1991), 128-134
- [Mar97] J. Marroquin, M. Servín, R. Rodríguez Vera: Adaptive quadrature filters and the recovery of phase from fringe pattern images, *JOSA* 14.8 (1997), 1742-1753
- [Mat88] D. Matthys, J. Gilbert, T. Dudderar, K. Koenig: A windowing technique for the automated analysis of holo-interferograms, *Opt. Las. Eng.* 8 (1988), 123-136
- [McKe74] T. McKechnie: Measurement of some second order statistical properties of speckle, *Optik* 39.3 (1974), 258-267

- [McLa86] J. McLaughlin, B. Horwitz: Real-time snapshot interferometer, in: *Surface Characterization and Testing*, Proc. SPIE 680 (1986), 35-43
- [Mer83] L. Mertz: Complex interferometry, *Appl. Opt.* 22.10 (1983), 1530-1534; Real-time fringe-pattern analysis, *Appl. Opt.* 22.10 (1983), 1535-1539
- [Mid60] D. Middleton: *Introduction to Statistical Communication Theory*, McGraw-Hill, New York (1960)
- [Mol90a] G. Molesini, M. Pires de Souza, F. Quercioli, M. Trivi: Experimental statistics of partially developed speckle fields, *Opt. Lett.* 15.11 (1990), 646-648
- [Mol90b] G. Molesini, M. Pires de Souza, F. Quercioli, M. Trivi: Experimental statistics of fully developed speckle fields by phase-shifting interferometry, *Opt. Comm.* 77 (1990), 129-134
- [Moo80] R. Moore, F. Slaymaker: Direct measurement of phase in a spherical-wave Fizeau interferometer, *Appl. Opt.* 19.13 (1980), 2196-2200
- [Moo94] A. Moore, J. Tyrer, F. Mendoza Santoyo: Phase extraction from ESPI addition fringes, *Appl. Opt.* 33.31 (1994), 7312-7320
- [Mor94a] Y. Morimoto, H. Gascoigne, D. Post: Carrier pattern analysis of moiré interferometry using the Fourier transform moiré method, *Opt. Eng.* 33.8 (1994), 2646-2653
- [Mor94b] Y. Morimoto, M. Fujisawa: Fringe pattern analysis by a phase-shifting method using Fourier transform, *Opt. Eng.* 33.11 (1994), 3709-3714
- [Nak83] S. Nakadate, T. Yatagai, H. Saito: Computer-aided speckle pattern interferometry, *Appl. Opt.* 22.2 (1983), 237-243
- [Nak85] S. Nakadate, H. Saito: Fringe scanning speckle-pattern interferometry, *Appl. Opt.* 24.14 (1985), 2172-2180
- [Nak95] S. Nakadate: Real-time fringe pattern processing and its applications, in: *Interferometry VII: Techniques and Analysis*, Proc. SPIE 2544 (1995), 74-86
- [Ng 96] T. Ng: The one-step phase-shifting technique for wave-front interferometry, *J. Mod. Opt.* 43.10 (1996), 2129-2138
- [dNic98] S. De Nicola, P. Ferraro: Fourier-transform calibration method for phase retrieval of carrier-coded fringe pattern, *Opt. Comm.* 151 (1998), 217-221
- [Nug85] K. Nugent: Interferogram analysis using an accurate fully automatic algorithm, *Appl. Opt.* 24.18 (1985), 3101-3105
- [Nye74] J. Nye, M. Berry: Dislocations in wave trains, *Proc. R. Soc. Lond. A* 336 (1974), 165-190
- [Nye88] J. Nye, J. Hajnal, J. Hannay: Phase saddles and dislocations in two-dimensional waves such as the tides, *Proc. R. Soc. Lond. A* 417 (1988), 7-20
- [Och83] E. Ochoa, J. W. Goodman, Statistical properties of ray directions in a monochromatic speckle pattern, *JOSA* 73.7 (1983), 943-949
- [Och98] N. Ochoa, J. Huntley: Convenient method for calibrating nonlinear phase modulators for use in phase-shifting interferometry, *Opt. Eng.* 37.9 (1998), 2501-2505
- [Oht82] J. Ohtsubo: Exact solution of the zero crossing rate of a differentiated speckle pattern, *Opt. Comm.* 42 (1982), 13-18
- [Ohy86] N. Ohyama, T. Shimano, J. Tsujiuchi, T. Honda: An analysis of systematic phase errors due to nonlinearity in fringe scanning systems, *Opt. Comm.* 58.4 (1986), 223-225
- [Ohy88] N. Ohyama, S. Kinoshita, A. Cornejo Rodriguez, T. Honda, J. Tsujiuchi: Accuracy of phase determination with unequal reference phase shift, *JOSA A* 5.12 (1988), 2019-2025
- [Oka91] K. Okada, A. Sato, J. Tsujiuchi: Simultaneous calculation of phase distribution and scanning phase shift in phase shifting interferometry, *Opt. Comm.* 84 (1991), 118-124

- [Ono96] R. Onodera, Y. Ishii: Phase-extraction analysis of laser-diode phase-shifting interferometry that is insensitive to changes in laser power, *JOSA A* 13.1 (1996), 139-146
- [Ost87] W. Osten, R. Höfling, J. Saedler: Two computer-aided methods for data reduction from interferograms, in: *Industrial optoelectronic measurement systems using coherent light*, Proc. SPIE 863 (1987), 105-113
- [Own88] M. Owner Petersen, P. Damgård Jensen: Computer-aided ESPI. Deformation analysis by fringe manipulation, *NDT International* 21.6 (1988), 422-426
- [Own91a] M. Owner Petersen: Decorrelation and fringe visibility: on the limiting behavior of various electronic speckle-pattern correlation interferometers, *JOSA A* 8.7 (1991), 1082-1089
- [Own91b] M. Owner Petersen: Digital speckle pattern shearing interferometry: limitations and prospects, *Appl. Opt.* 30.19 (1991), 2730-2738
- [Own91c] M. Owner Petersen: Phase-map unwrapping: a comparison of some traditional methods and a presentation of a new approach, in: *Industrial applications of holographic and speckle measuring techniques*, Proc. SPIE 1508 (1991), 73-82
- [Pap65] A. Papoulis: Probability, random variables, and stochastic processes, McGraw-Hill, New York (1965), 1<sup>st</sup> edition
- [Ped93] G. Pedrini, B. Pfister, H. Tiziani: Double-pulse ESPI, *J. Mod. Opt.* 40.1 (1993), 89-96
- [Ped94] G. Pedrini, H. Tiziani: Double-pulse ESPI for vibration analysis, *Appl. Opt.* 33.34 (1994), 7857-7863
- [Ped97a] G. Pedrini, Y. Zou, H. Tiziani: Simultaneous quantitative evaluation of in-plane and out-of-plane deformations by use of a multidirectional spatial carrier, *Appl. Opt.* 36.4 (1997), 786-792
- [Ped97b] G. Pedrini, H. Tiziani: Quantitative evaluation of two-dimensional dynamic deformations using digital holography, *Opt. Las. Technol.* 29.5 (1997), 249-256
- [Ped97c] G. Pedrini, P. Fröning, H. Fessler, H. Tiziani: Transient vibration analysis using multi-pulse digital holography, *Opt. Las. Technol.* 29.8 (1997), 505-511
- [Pet98] J. Petzing, A. Dávila, D. Kerr, J. Tyrer: Pulsed carrier out-of-plane speckle interferometry for transient vibration analysis, *J. Mod. Opt.* 45.4 (1998), 825-836
- [Pet99] J. Petzing, J. Tyrer: In-plane pulsed carrier speckle interferometry for structural surface intensity measurement, *J. Mod. Opt.* 46.14 (1999), 1947-1959
- [Pfi93] B. Pfister: Speckleinterferometrie mit neuen Phasenschiebemethoden, *Berichte aus dem ITO der Universität Stuttgart* Vol. 18, Ph. D. thesis, Stuttgart (1993)
- [Phi97] D. Phillion: General methods for generating phase-shifting interferometry algorithms, *Appl. Opt.* 36.31 (1997), 8098-8115
- [Pir95] M. Pirga, M. Kujawińska: Two directional spatial-carrier phase-shifting method for analysis of crossed and closed fringe patterns, *Opt. Eng.* 34.8 (1995), 2459-2466
- [Pou95] B. Pouet, S. Krishnaswamy: Technique for the removal of speckle phase in ESPI, *Opt. Lett.* 20.3 (1995), 318-320
- [Pre88] W. Press, B. Flannery, S. Teukolsky, W. Vetterling: *Numerical Recipes in C*, Cambridge University Press, Cambridge (1988), p. 305
- [Qua96] C. Quan, H. Shang, P. Bryanston-Cross: Application of the holographic carrier fringe and FFT technique for deformation measurement, *Opt. Las. Technol.* 28.1 (1996), 7-13
- [Ran86] P. Ransom, J. Kokal: Interferogram analysis by a modified sinusoid fitting technique, *Appl. Opt.* 25.22 (1986), 4199-4204
- [Rao91] V. Rao Gudimetla: Three-point joint density functions for the intensities of partially and fully developed monochromatic laser speckle patterns, *JOSA A* 8.12 (1991), 1943-1946
- [Rat95] C. Rathjen: Statistical properties of phase-shift algorithms, *JOSA A* 12.9 (1995), 1997-2008

- [Rav99] I. Raveh, E. Marom, D. Mendlovic: Phase retrieval algorithms in the Fresnel domain, in: *18<sup>th</sup> Congress of ICO: Optics for the next millennium*, Proc. SPIE 3749 (1999), 172-173
- [Rob86] D. Robinson, D. Williams: Digital Phase Stepping Interferometry, *Opt. Comm.* 57 (1986), 26-30
- [Rod87] C. Roddier, F. Roddier: Interferogram analysis using Fourier transform techniques, *Appl. Opt.* 26.9 (1987), 1668-1673
- [Ryu97] H. Ryu, C. Hong: Maximum-likelihood phase estimation in phase-shifting ESPI and its comparison with least-squares estimation, *JOSA A* 14.5 (1997), 1051-1057
- [Sag98] H. Sagehorn, R. Schuh: Aktive Phasenregelung in einem elektronischen Specklemuster-Interferometer mit Glasfaserstrahlführung, Diploma thesis, Carl von Ossietzky University Oldenburg, 1998
- [Sal96] H. Saldner, N. Molin, K. Stetson: Fourier-transform evaluation of phase data in spatially phase-biased TV holograms, *Appl. Opt.* 35.2 (1996), 332-336
- [Sal97] H. Saldner, J. Huntley: Temporal phase unwrapping: application to surface profiling of discontinuous objects, *Appl. Opt.* 36.13 (1997), 2770-2775
- [Sał92] L. Sałbut, K. Patorski, M. Kujawińska: Polarization approach to high-sensitivity moiré interferometry, *Opt. Eng.* 31.3 (1992), 434-439
- [Sched97] S. Schedin, P. Gren: Phase evaluation and speckle averaging in pulsed TV holography, *Appl. Opt.* 36.17 (1997), 3941-
- [Sched99] S. Schedin, G. Pedrini, H. Tiziani, F. Mendoza Santoyo: Simultaneous three-dimensional dynamic deformation measurement with pulsed digital holography, *Appl. Opt.* 38.34 (1999), 7056-7062
- [Schmi95a] J. Schmit, K. Creath: Extended averaging technique for derivation of error-compensating algorithms in phase-shifting interferometry, *Appl. Opt.* 34.19 (1995), 3610-3619
- [Schmi95b] J. Schmit, K. Creath: Fast calculation of phase in spatial  $N$ -point phase-shifting techniques, in: *Interferometry VII: Techniques and Analysis*, Proc. SPIE 2544 (1995), 102-111
- [Schmi96] J. Schmit, K. Creath: Window function influence on phase error in phase-shifting algorithms, *Appl. Opt.* 35.28 (1996), 5642-5649
- [Schmi97] D. Schmitt, R. Hunt: Optimization of fringe pattern calculation with direct correlations in speckle interferometry, *Appl. Opt.* 36.34 (1997), 8848-8857
- [Schmi98] D. Schmitt, R. Hunt: Model-based inversion of speckle interferometer fringe patterns, *Appl. Opt.* 37.13 (1998), 2573-2578
- [Schwi83] J. Schwider, R. Burow, K. Elßner, J. Grzanna, R. Spolaczyk, K. Merkel: Digital wave-front measuring interferometry: some systematic error sources, *Appl. Opt.* 22.21 (1983), 3421-3432
- [Schwi90] J. Schwider: Advanced evaluation techniques in interferometry, in *Progress in Optics XXVIII*, E. Wolf, ed., Elsevier, Amsterdam (1990), pp. 271-359
- [Schwi93] J. Schwider, O. Falkenstörfer, H. Schreiber, A. Zöllner, N. Streibl: New compensating four-phase algorithm for phase-shift interferometry, *Opt. Eng.* 32.8 (1993), 1883-1885
- [Sea98] R. Seara, A. Gonçalves jr., P. Uliana: Filtering algorithm for noise reduction in phase-map images with  $2\pi$  phase jumps, *Appl. Opt.* 37.11 (1998), 2046-2050
- [Ser93] M. Servín, R. Rodríguez Vera: Two-dimensional phase locked loop demodulation of interferograms, *J. Mod. Opt.* 40.11 (1993), 2087-2094
- [Ser95] M. Servín, F. Cuevas: A novel technique for spatial phase-shifting interferometry, *J. Mod. Opt.* 42.9 (1995), 1853-1862
- [Ser97a] M. Servín, J. Marroquin, F. Cuevas: Demodulation of a single interferogram by use of a two-dimensional regularized phase-tracking technique, *Appl. Opt.* 36.19 (1997), 4540-4548
- [Ser97b] M. Servín, D. Malacara, J. Marroquin, F. Cuevas: Complex linear filters for phase shifting with very low detuning sensitivity, *J. Mod. Opt.* 44.7 (1997), 1269-1278



- [Sho90] D. Shough, O. Kwon, D. Leary: High-speed interferometric measurements of aerodynamic phenomena, in: *Propagation of High-Energy Laser Beams through the Earth's Atmosphere*, Proc. SPIE 1221 (1990), 394-403
- [Shva94] N. Shvartsman, I. Freund: Vortices in random wave fields: nearest neighbor anticorrelations, *Phys. Rev. Lett.* 72.7 (1994), 1008-1011; Erratum, *Phys. Rev. Lett.* 72.26 (1994), 4156
- [Shva95] N. Shvartsman, I. Freund: Speckle spots ride phase saddles sidesaddle, *Opt. Comm.* 117 (1995), 228-234; Erratum, *Opt. Comm.* 120 (1995), 369
- [Sim93] E. Simova, K. Stoev: Automated Fourier transform fringe-pattern analysis in holographic moiré, *Opt. Eng.* 32.9 (1993), 2286-2294
- [Sin94] H. Singh, J. Sirkis: Direct extraction of phase gradients from Fourier-transform and phase-step fringe patterns, *Appl. Opt.* 33.22 (1994), 5016-5020
- [Sir93] R. Sirohi, N. Krishna Mohan: In-plane displacement measurement configuration with twofold sensitivity, *Appl. Opt.* 32.31 (1993), 6387-6390
- [Sir97a] R. Sirohi, J. Burke, H. Helmers, K. Hinsch: Spatial phase shifting for pure in-plane displacement and displacement-derivative measurements in ESPI, *Appl. Opt.* 36.23 (1997), 5787-5791
- [Sir97b] R. Sirohi, J. Burke, T. Bothe, H. Helmers, K. Hinsch, "New applications of Michelson stellar interferometer in speckle metrology using spatial phase shifting", in: *Automatic Processing of Fringe Patterns, Fringe 97*, Akademie Verlag, Berlin (1997), 489-496
- [Sla95] P. Slangen, C. de Veuster, Y. Renotte, L. Berwart, Y. Lion: Computer-aided interferometric measurements of drift and phase shifter calibration for DSPI, *Opt. Eng.* 34.12 (1995), 3526-3530
- [Sle79] G. Slettemoen: General analysis of fringe contrast in ESPI, *Opt. Act.* 26.3 (1979), 313-327
- [Sle86] G. Slettemoen, J. Wyant: Maximal fraction of acceptable measurements in phase-shifting speckle interferometry: a theoretical study, *JOSA A* 3.2 (1986), 210-214
- [Smy84] R. Smythe, R. Moore: Instantaneous phase measuring interferometry, *Opt. Eng.* 23.4 (1984), 361-364
- [Ste85] K. Stetson, W. Brohinsky: Electrooptic holography and its application to hologram interferometry, *Appl. Opt.* 24.21 (1985), 3631-3637
- [Ste90] K. Stetson: Theory and applications of electronic holography, in: *Hologram Interferometry and Speckle Metrology*, Proc. SEM (1990), 294-300
- [Ste91] H. Steinbichler, J. Gutjahr: Verfahren zur direkten Phasenmessung von Strahlung, insbesondere Lichtstrahlung, und Vorrichtung zur Durchführung dieses Verfahrens, German patent DE-OS 3930632 A1, Mar 14, 1991
- [Sto97] G. Stoilov, T. Dragostinov: Phase-stepping interferometry: five-frame algorithm with an arbitrary step, *Opt. Las. Eng.* 28 (1997), 61-69
- [Stroe96] B. Stroebel, Processing of interferometric phase maps as complex-valued phasor images, *Appl. Opt.* 35.13, 2192-2198 (1996)
- [Su 94] X. Su, A. Zarubin, G. von Bally: modulation analysis of phase-shifted holographic interferograms, *Opt. Comm.* 105 (1994), 379-387
- [Sur93] Y. Surrel: Phase stepping: a new self-calibrating algorithm, *Appl. Opt.* 32.19 (1993), 3598-3600
- [Sur96] Y. Surrel: Design of algorithms for phase measurements by the use of phase stepping, *Appl. Opt.* 35.1 (1996), 51-60
- [Sur97a] Y. Surrel: Additive noise effect in digital phase detection, *Appl. Opt.* 36.1 (1997), 271-276
- [Sur97b] Y. Surrel: Design of phase-detection algorithms insensitive to bias modulation, *Appl. Opt.* 36.4 (1997), 805-807
- [Sur98a] Y. Surrel: Phase-shifting algorithms for nonlinear and spatially nonuniform phase shifts: comment, *JOSA A* 15.5 (1998), 1227-1233

- [Sur98b] Y. Surrel: Design of algorithms for phase measurement, in: *International Conference on Applied Optical Metrology*, Proc. SPIE 3407 (1998), 67-72
- [Sur98c] Y. Surrel: Extended averaging and data windowing techniques in phase-stepping measurements: an approach using the characteristic polynomial theory, *Opt. Eng.* 37.8 (1998), 2314-2319
- [Sur00] Y. Surrel: Customized phase shift algorithms, in: *Trends in Optical Nondestructive Testing and Inspection*, P. Rastogi, D. Inaudi, eds., Elsevier, Amsterdam (2000), p.77
- [Tak75] N. Takai: Relation between statistical properties of surface roughness and the averaged speckle intensity in the diffraction field, *Opt. Comm.* 14 (1975), 24-29
- [Tak82] M. Takeda, H. Ina, S. Kobayashi: Fourier-transform method of fringe-pattern analysis for computer-based topography and interferometry, *JOSA* 72.1 (1982), 156-160
- [Tak83] M. Takeda, K. Mutoh: Fourier transform profilometry for the automatic measurement of 3-D object shapes, *Appl. Opt.* 22.24 (1983), 3977-3982
- [Tak86] N. Takai, H. Kadono, T. Asakura: Statistical properties of the speckle phase in image and diffraction fields, *Opt. Eng.* 25.5 (1986), 627-635
- [Tak90a] M. Takeda, H. Iijima: Spatio-temporal heterodyne interferometry, in: *Optics in Complex Systems*, Proc. SPIE 1319 (1990), 210-211
- [Tak90b] M. Takeda: Spatial-carrier fringe-pattern analysis and its applications to precision interferometry and profilometry: an overview, *Indust. Metrol.* 1 (1990), 79-99
- [Tak92] M. Takeda, M. Kitoh: Spatio-temporal frequency multiplex heterodyne interferometry, *JOSA A* 9.9 (1992), 1607-1614
- [Tak94] M. Takeda, H. Yamamoto: Fourier transform speckle profilometry: three-dimensional shape measurements of diffuse objects with large height steps and/or spatially isolated surfaces, *Appl. Opt.* 33.34 (1994), 7829-7837
- [Tak97a] M. Takeda, Q. Gu, M. Kinoshita, H. Takai, Y. Takahashi: Frequency-multiplex Fourier-transform profilometry: a single-shot three-dimensional shape measurement of objects with large height discontinuities and/or surface isolations, *Appl. Opt.* 36.22, 5347-5354
- [Tak97b] T. Takatsuji, B. Oreb, D. Farrant, J. Tyrer: Simultaneous measurement of three orthogonal components of displacement by ESPI and the Fourier transform method, *Appl. Opt.* 36.7 (1997), 1438-1445
- [Tan68] L. Tanner: A study of fringe clarity in laser interferometry and holography, *J. Sci. Instr. (J. Phys. E)* 2.1 (1968), 517-522
- [Toy84] S. Toyooka, M. Tominaga: Spatial fringe scanning for optical phase measurement, *Opt. Comm.* 51 (1984), 68-70
- [Toy86] S. Toyooka, Y. Iwaasa: Automatic profilometry of 3-D diffuse objects by spatial phase detection, *Appl. Opt.* 25.10 (1986), 1630-1633
- [Tur82] M. Tur, K. Chin, J. Goodman: When is speckle noise multiplicative?, *Appl. Opt.* 21.7 (1982), 1157-1159 (Letter)
- [Var82] P. Varman, C. Wykes: Smoothing of speckle and Moiré fringes by computer processing, *Opt. Las. Eng.* 3 (1982), 87-100
- [dVe97] C. De Veuster, P. Slangen, Y. Renotte, L. Berwart, Y. Lion: Influence of the geometry of illumination and viewing beams on displacement measurement errors in interferometric metrology, *Opt. Comm.* 143 (1997), 95-101
- [Vik90] E. Vikhagen: Nondestructive testing by use of TV holography and deformation phase gradient calculation, *Appl. Opt.* 29.1 (1990), 137-144
- [Vik91] E. Vikhagen: TV holography: spatial resolution and signal resolution in deformation analysis, *Appl. Opt.* 30.4 (1991), 420-425

- [Vik93] C. Vikram, W. Witherow, J. Trolinger: Algorithm for phase-difference measurement in phase-shifting interferometry, *Appl. Opt.* 32.31 (1993), 6250-6252
- [Vla94] V. Vlad, D. Malacara: Direct spatial reconstruction of optical phase from phase-modulated images, in: *Progress in Optics XXXIII*, E. Wolf, ed., 261-317
- [Voe91] D. Voelz, D. Dayton: Experimental measurements of the statistical properties of a monochromatic speckle pattern, *Opt. Lett.* 16.21 (1991), 1635-1637
- [Vro91] H. Vrooman, A. de Maas: Image-processing algorithms for the analysis of phase-shifted speckle interference patterns, *Appl. Opt.* 30.13 (1991), 1636-1641
- [Vry86] U. Vry, A. Fercher: Higher-order statistical properties of speckle fields and their application to rough-surface interferometry, *JOSA A* 3.7 (1986), 988-1000
- [Wag83] R. Wagner, S. Smith, J. Sandrik, H. Lopez: Statistics of speckle in ultrasound B-scans, *IEEE Trans. SU-30.3* (1983), 156-163
- [Wei77] G. Weigelt, B. Stoffregen: The longitudinal correlation of a three-dimensional speckle intensity distribution, *Optik* 48.4 (1977), 399-407
- [Wei82a] A. Weinrib: Percolation threshold of a two-dimensional continuum system, *Phys. Rev. B* 26.3 (1982), 1352-1361
- [Wei82b] A. Weinrib, B. Halperin: Distribution of maxima, minima, and saddle points of the intensity of laser speckle patterns, *Phys. Rev. B* 26.3 (1982), 1362-1368
- [Wei99] C. Wei, M. Chen, Z. Wang: General phase-stepping algorithm with automatic calibration of phase steps, *Opt. Eng.* 38.8 (1999), 1357-1360
- [Wil91] D. Williams, N. Nassar, J. Banyard, M. Virdee: Digital phase-step interferometry: a simplified approach, *Opt. Las. Technol.* 23.3 (1991), 147-150
- [Win95] R. Windecker, H. Tiziani: Semispacial, robust, and accurate phase evaluation algorithm, *Appl. Opt.* 34.31 (1995), 7321-7326
- [Wom84] K. Womack: Interferometric phase measurement using spatial synchronous detection, *Opt. Eng.* 23.4 (1984), 391-395
- [Wya75] J. Wyant: Use of an ac heterodyne lateral shear interferometer with real-time wavefront correction systems, *Appl. Opt.* 14.11 (1975), 2622-2626
- [Wya82] J. Wyant: Interferometric optical metrology: Basic principles and new systems, *Laser Focus* 5 (1982), 65-714
- [Wyk87] C. Wykes: A theoretical approach to the optimisation of ESPI fringes with limited laser power, *J. Mod. Opt.* 34.4 (1987), 539-554
- [Yat82] T. Yatagai, S. Nakadate, M. Idesawa, H. Saito: Automatic fringe analysis using digital image processing techniques, *Opt. Eng.* 21.3 (1982), 432-435
- [Yos93] T. Yoshimura, S. Iwamoto: Dynamic properties of three-dimensional speckles, *JOSA A* 10.2 (1993), 324-328
- [Yos95] T. Yoshimura, M. Zhou, K. Yamahai, Z. Liyan: Optimum determination of speckle size to be used in ESPI, *Appl. Opt.* 34.1 (1995), 87-91
- [You96] N. Youssef, T. Munakata, M. Takeda: Rice probability functions for level-crossing intervals of speckle intensity fields, *Opt. Comm.* 123 (1996), 55-62
- [Yu 98] E. Yu, S. Cha: Two-dimensional phase regression for interferometric phase extraction, *Appl. Opt.* 37.8 (1998), 1370-1376
- [Zha95] B. Zhao, Y. Surrel: Phase-shifting: six-sample self-calibrating algorithm insensitive to the second harmonic in the fringe signal (Letter), *Opt. Eng.* 34.9 (1995), 2821-2822
- [Zha99] H. Zhang, M. Lalor, D. Burton: Error-compensating algorithms in phase-shifting interferometry: a comparison by error analysis, *Opt. Las. Eng.* 31 (1999), 381-400



## Appendix A: Counting events

### Intensity level crossings per unit length

In Chapter 2 we have encountered two occasions where probabilistic events had to be counted. The derivation is similar for both of them. The level-crossing problem of (2.14) starts from the integral [Bar80]

$$\langle N_d(I_t) \rangle = \int_d \delta(I - I_t) |\partial I / \partial x| dx; \quad (\text{A.1})$$

here  $N_d(I_t)$  is the number of times that the intensity crosses the value  $I_t$  on a path  $d$  (the probability for the point  $I=I_t$  being an extremum has measure zero on a straight line). The  $\delta$  function assures that the integral responds only when  $I=I_t$ ; to make each such contribution equal to one, i.e. to establish a counting function, the integration over  $x$  must be undone by the derivative  $\partial I / \partial x$ ; the modulus signs ensure that +1 is being counted for each event. However, since now  $I_x$  appears, which is not independent of  $I$ , we need to know its expectation value at a given  $I$ , which requires the joint pdf  $p(I, I_x)$  and changes the integral to

$$\begin{aligned} \langle N_d(I_t) \rangle &= \int_d \int_{I_x} \delta(I - I_t) p(I, I_x) |I_x| dI_x dx \\ &= \int_d \int_{I_x} p(I_t, I_x) |I_x| dI_x dx \quad ; \end{aligned} \quad (\text{A.2})$$

on integrating over unit length, one obtains the density of the level-crossings,

$$\langle \rho(I_t) \rangle = \int_{I_x} p(I_t, I_x) |I_x| dI_x, \quad (\text{A.3})$$

which is (2.14).

### Intensity zero points per unit area

By the same line of argument as above, we can start from [Ber78, Bar81]

$$\langle N_{dist} \rangle = \iint_S \delta(A_r) \delta(A_i) |\partial(A_r, A_i) / \partial(x, y)| dx dy, \quad (\text{A.4})$$

where the dislocation is expressed by the vanishing of  $A_r$  and  $A_i$ , the integral is over an area  $S$  and the quantity between the modulus signs is the Jacobian  $\|\mathbf{J}\| = |A_{r,x} A_{i,y} - A_{r,y} A_{i,x}|$ . Obviously, we need  $p(A_r, A_i, A_{r,x}, A_{i,x}, A_{r,y}, A_{i,y})$  to evaluate this integral, or, more specifically,  $p(0, 0, A_{r,x}, A_{i,x}, A_{r,y}, A_{i,y})$  after the  $\delta$  functions are accounted for. In analogy to above, we write

$$\begin{aligned} \langle N_{dist} \rangle &= \iint_S \int_{A_{r,x}} \int_{A_{i,x}} \int_{A_{r,y}} \int_{A_{i,y}} p(0, 0, A_{r,x}, A_{i,x}, A_{r,y}, A_{i,y}) |\partial(A_r, A_i) / \partial(x, y)| dA_{r,x} dA_{i,x} dA_{r,y} dA_{i,y} dx dy, \end{aligned} \quad (\text{A.5})$$

and with  $S$  equal to the area unit we then have

$$\langle \rho_{dist} \rangle = \int_{A_{r,x}} \int_{A_{i,x}} \int_{A_{r,y}} \int_{A_{i,y}} p(0, 0, A_{r,x}, A_{i,x}, A_{r,y}, A_{i,y}) \left| \partial(A_r, A_i) / \partial(x, y) \right| dA_{r,x} dA_{i,x} dA_{r,y} dA_{i,y} ; \quad (\text{A.6})$$

with  $p(A_r, A_i, A_{r,x}, A_{i,x}, A_{r,y}, A_{i,y})$  given by (2.1), the integration is not trivial; it has been shown in [Ber78, Eq. 43] that the integral is best evaluated in polar co-ordinates, i.e. after conversion to  $I$  and  $\varphi$ , similar to (2.4). Fortunately, this needed be done only once and for all, since the "threshold" intensity is fixed to zero in this case.

## Appendix B: Real-time phase calculation

To utilise the real-time phase measuring capability that SPS offers, the generation of phase maps must be accelerated by saving as many processor operations as possible. Particularly the arctangent calls, usually one for each pixel, lead to a great computational burden that is unnecessary when the input "sine" and "cosine" terms have a reasonably narrow range of discrete values.

Given the expression

$$\varphi_O \bmod 2\pi = \arctan \sqrt{3} \frac{I_{-1} - I_1}{2I_0 - I_{-1} - I_1}, \quad (\text{B.1})$$

the `atan2` call, and the division, can be circumvented by generating a 2-D array from all possible values of numerator and denominator and assigning the corresponding  $\varphi_O$  (converted to a discrete grey value) to each grid point, as shown in Fig. B.1. Also, the construction of  $M_I$  is indicated; it can be seen that it is simply the length of the phasor composed by the sine and cosine terms.

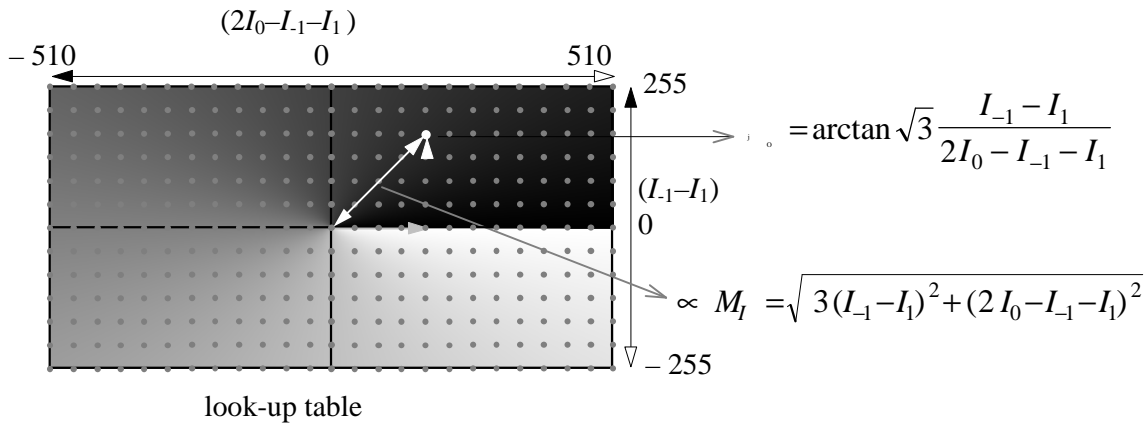


Fig. B.1: Calculation of  $\varphi_O$  and  $M_I$  for 3-sample phase shifting formula with  $\alpha=120^\circ$ .

For 8-bit digitisation of the  $I_n$ , the size of the array thus defined ( $1021 \times 511$  points) is still manageable with a formula involving terms from 2 or 3 intensity samples. It is well known that for  $\alpha=90^\circ$  and (3.16) or (3.19), only  $511 \times 511$  points are necessary. However, Fig. B.1 shows that also (3.17) can be implemented by a LUT without exaggerated expense. It is unnecessary to use the factor of  $\sqrt{3}$  for the arrangement of grid points; instead it can be integrated in the LUT. Fig. B.2 presents the central portion of the LUT, where the anisotropy is visualised by reduction of the grey scale to 4 bits.

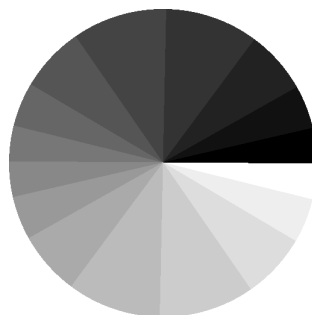


Fig. B.2: Anisotropy of LUT for (3.17) due to horizontal stretching and inclusion of  $\sqrt{3}$  from the sine term.

The stretching in the horizontal direction is clearly discernible; it accounts for the maximal "stroke" of the cosine term being twice that of the sine term.

Depending on the number of involved intensity samples and their coefficients, the byte arrays needed for the LUT may nevertheless get larger; for instance, a LUT for (3.56) would need  $511 \times 1021$  entries. In that case, the coefficient of 2 for both intensity samples in the numerator thins out the grid of possible values and space can be saved. However, the very same formula in the representation of (3.57) requires a  $1531 \times 1531$ -point LUT, and for (3.58),  $2041 \times 1021$  possible values must be accounted for. This shows that a careful choice of the formula can be useful in practice.

Non-integer coefficients in the numerator and/or denominator can only be implemented if a suitable factor can be found that converts all the coefficients for the respective expression into integers, i.e. if the coefficients are rational numbers. As seen above, a common factor of  $\sqrt{3}$  constitutes no problem in (3.17) or (3.58); however, if we had, say,  $\sqrt{3}$  and 3 as coefficients in the sine or cosine term, we would have to use a rational integer approximation of their values, for instance 7 and 12; this would allow to put up a LUT, but remains a complicated procedure. Hence, while it is possible to accelerate phase calculation by LUTs on more occasions than one might think, the appeal of simplicity gets lost in some cases.



## Appendix C: Derivation of intensity-correcting formulae

To include the influence of the speckle intensity, we can rewrite (3.68) as

$$I_n(x_{k+n}, y_l, t) = O_i(x_{k+n}, y_l) + R + 2\sqrt{O_i(x_{k+n}, y_l)R} \cdot \cos(\varphi_O(x_{k+n}, y_l, t) + \alpha_n(x_{k+n}, y_l)), \quad (\text{C.1})$$

where  $R$  is assumed constant,  $O_i(x_{k+n}, y_l) + R = I_b$  and  $2\sqrt{O_i(x_{k+n}, y_l)R} = M_I$ ; we drop the spatial dependencies for convenience of notation. With  $D_n := I_n - O_n$ , we can write

$$D_n = R + 2 \cdot \sqrt{O_n} \cdot R \cdot \cos(\varphi_O + \alpha_n) \\ \stackrel{\underline{R}}{:=a_0} + \underbrace{2\sqrt{R} \cos \varphi_O}_{:=a_1} \cos \alpha_n \sqrt{O_n} - \underbrace{2\sqrt{R} \sin \varphi_O}_{:=a_2} \sin \alpha_n \sqrt{O_n}, \quad (\text{C.2})$$

where the quantities of interest are  $a_1$  and  $a_2$ , since they contain  $\varphi_O$ . Setting  $n \in \{-1, 0, 1\}$ , thus assuming phase steps of  $(-\alpha, 0, \alpha)$ , the linear equation system is given by

$$\begin{pmatrix} 1 & \cos \alpha \sqrt{O_{-1}} & \sin \alpha \sqrt{O_{-1}} \\ 1 & \sqrt{O_0} & 0 \\ 1 & \cos \alpha \sqrt{O_1} & -\sin \alpha \sqrt{O_1} \end{pmatrix} \begin{pmatrix} a_0 \\ a_1 \\ a_2 \end{pmatrix} = \begin{pmatrix} D_{-1} \\ D_0 \\ D_1 \end{pmatrix}, \quad (\text{C.3})$$

which we abbreviate by  $\mathbf{Pa} = \mathbf{D}$ . As long as  $O_{-1}, O_0, O_1 \neq 0$  and  $0 \neq \alpha \neq 180^\circ$ ,  $\mathbf{P}$  is regular and  $\text{rank}(\mathbf{P}) = \text{rank}(\mathbf{P}, \mathbf{D}) = 3$  is valid; hence we can solve the equation system by inverting:  $\mathbf{a} = \mathbf{P}^{-1}\mathbf{D}$ . This can be carried out by Cramer's rule [Bro87, p. 159]. With the abbreviations

$$\underbrace{\begin{pmatrix} 1 & C1 & S1 \\ 1 & C2 & 0 \\ 1 & C3 & S3 \end{pmatrix}}_{:=\mathbf{P}} \begin{pmatrix} a_0 \\ a_1 \\ a_2 \end{pmatrix} = \begin{pmatrix} D_{-1} \\ D_0 \\ D_1 \end{pmatrix}, \quad (\text{C.4})$$

we have

$$\begin{aligned}
\mathbf{P} &= \begin{pmatrix} 1 & C1 & S1 \\ 1 & C2 & 0 \\ 1 & C3 & S3 \end{pmatrix}, \quad \det(\mathbf{P}) = C2S3 - C1S3 + S1C3 - S1C2 \\
\mathbf{P}_0 &= \begin{pmatrix} D_{-1} & C1 & S1 \\ D_0 & C2 & 0 \\ D_1 & C3 & S3 \end{pmatrix}, \quad \det(\mathbf{P}_0) = D_{-1}C2S3 - C1D_0S3 + S1D_0C3 - S1C2D_1 \\
\mathbf{P}_1 &= \begin{pmatrix} 1 & D_{-1} & S1 \\ 1 & D_0 & 0 \\ 1 & D_1 & S3 \end{pmatrix}, \quad \det(\mathbf{P}_1) = D_0S3 - D_{-1}S3 + S1D_1 - S1D_0 \\
\mathbf{P}_2 &= \begin{pmatrix} 1 & C1 & D_{-1} \\ 1 & C2 & D_0 \\ 1 & C3 & D_1 \end{pmatrix}, \quad \det(\mathbf{P}_2) = C2D_1 - D_0C3 + C1D_0 - C1D_1 + D_{-1}C3 - D_{-1}C2,
\end{aligned} \tag{C.5}$$

from which we get  $a_0, a_1, a_2$  by

$$a_0 = \frac{\det(\mathbf{P}_0)}{\det(\mathbf{P})}, \quad a_1 = \frac{\det(\mathbf{P}_1)}{\det(\mathbf{P})}, \quad a_2 = \frac{\det(\mathbf{P}_2)}{\det(\mathbf{P})}. \tag{C.6}$$

For the quotient  $a_2/a_1 = \tan \varphi_O$ , we obtain

$$\begin{aligned}
\frac{a_2}{a_1} &= \frac{\det(\mathbf{A}_2)}{\det(\mathbf{A}_1)} = \frac{C1(D_0 - D_1) + C2(D_1 - D_{-1}) + C3(D_{-1} - D_0)}{S1(D_1 - D_0) + S3(D_0 - D_{-1})} \\
&= \frac{\sqrt{O_0}(D_1 - D_{-1}) + \cos \alpha (\sqrt{O_{-1}}(D_0 - D_1) + \sqrt{O_1}(D_{-1} - D_0))}{\sin \alpha (\sqrt{O_{-1}}(D_1 - D_0) + \sqrt{O_1}(D_{-1} - D_0))},
\end{aligned} \tag{C.7}$$

which is (6.4).

## Appendix D: Alternative error-compensating formulae

In Chapter 3.2.2, we have restricted ourselves to a maximum of four intensity samples in the phase reconstruction formulae. If we do allow the inclusion of a fifth sample, we obtain one more degree of freedom to customise the compensation of errors. In the context of spatial phase shifting, an interesting solution has been presented in [Küch91, Küch97]. The derivation is based on the realisation that it is possible to find three phase-shifting angles, or signal frequencies, for which the phase is determined without error when five intensity samples are available. With one of them fixed at  $\alpha=90^\circ/\text{sample}$ , the other two can be arranged symmetrically with respect to the nominal phase shift. In [Küch91], a formula is described which works correctly at  $\alpha=30, 90,$  and  $150^\circ/\text{sample}$ , and with little error in between. When the intensity samples are weighted according to

$$\bar{\varphi}_O \bmod 2\pi = \arctan \frac{-I_0 + 3(I_1 - I_3) + I_4}{-I_0 - I_1 + 4I_2 - I_3 - I_4}, \quad (\text{D.1})$$

this formula is produced. The corresponding amplitude and phase spectra are as shown in Fig. D.1; note that the frequency is now labelled  $\nu_{xy}$ , since the formula works diagonally, as detailed below.

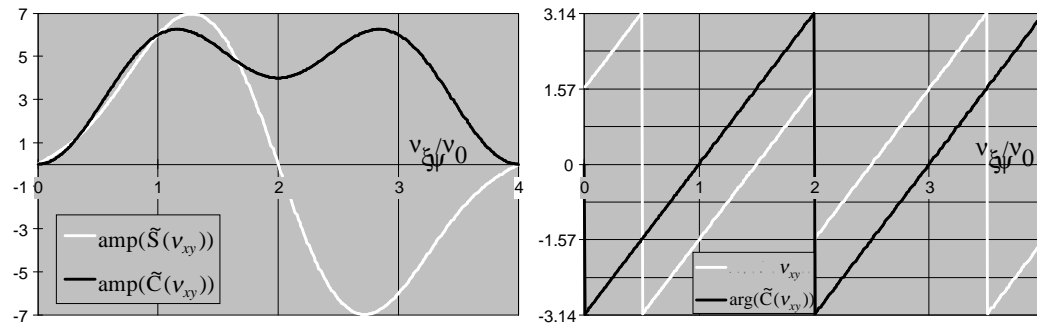


Fig. D.1: Filter spectrum for 5-step-30/90/150° phase-sampling formula (D.1); left: amplitudes, right: phases.

It can be seen that the phases are always in quadrature, which follows from the fact that the formula has a Hermitian arrangement of sample weights. The amplitudes are equal not at one, but at three points in the frequency spectrum between  $0 < \nu_{xy} < \nu_N = 2\nu_0$ . The convolution, or more precisely, correlation kernels  $S_{xy}(n)$  and  $C_{xy}(n)$  – subscript  $xy$  denoting the 2D arrangement – for the spatial implementation of the sampling functions are shown in Fig. D.2; to make  $C_{xy}(n)$  symmetrical while maintaining integer coefficients, it is necessary to expand (D.1) by a factor of two.

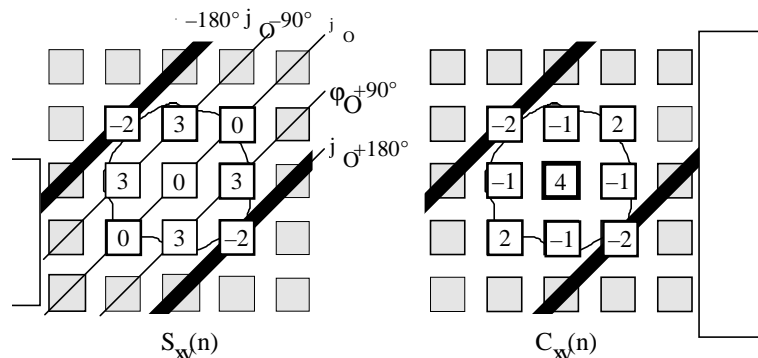


Fig. D.2: Spatial weighting of the intensity samples for the application of formula (D.1) in spatial phase shifting; the numbers on the pixels now indicate relative weights, and the phase calculation refers to the central pixel. Although the method was developed for high-precision classical interferometry, the outline of a speckle is still included in the drawing, to compare with Fig. 6.11.

The sampling window thus defined offers excellent phase-shift error suppression while sacrificing only little spatial resolution; it has been pointed out in [Küch91] that the slant of the carrier fringes saves a factor of  $\sqrt{2}$  in this respect.

It is also possible to make all three points of zero error coincide at  $\alpha=90^\circ$ /sample, which was already remarked in [Küch91] and later derived independently by [Mł095, Schmi95a]; in this case the phase calculation is very stable around  $\alpha=90^\circ$  but does not reach zero error again when  $\alpha \neq 90^\circ$ . The corresponding sampling formula reads

$$\bar{\varphi}_O \bmod 2\pi = \arctan \frac{-I_0 + 4(I_1 - I_3) + I_4}{-I_0 - 2I_1 + 6I_2 - 2I_3 - I_4}, \tag{D.2}$$

and the corresponding filter spectrum is shown in Fig. D.3.

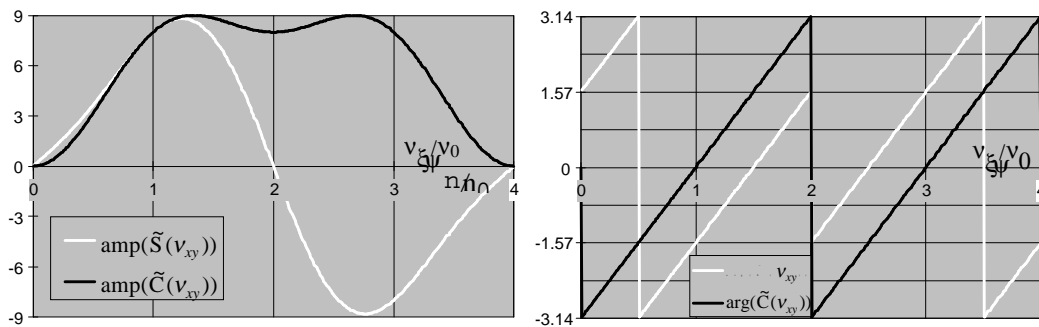


Fig. D.3: Filter spectrum for 5-step-90° phase-sampling formula (D.2); left: amplitudes, right: phases.

As familiar from the discussion of symmetrical formulae in 3.2.2.4, the phase spectrum is the same as above; the amplitudes are very similar over a broad range of  $v_{xy}$ , which assures low errors even for large phase-shift miscalibration. A possible implementation of (D.2) is presented in Fig. D.4.

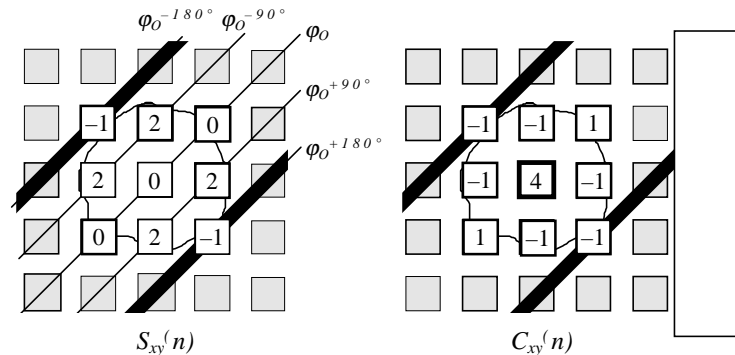


Fig. D.4: Spatial weighting of the intensity samples for the application of formula (D.2) in spatial phase shifting; the numbers on the pixels indicate relative weights, and the phase calculation refers to the central pixel.

To address the interesting question how these formulae will perform in speckle interferometry, we consider again the experimentally obtained distributions of  $b_{sc}(v_x, v_y)$  in the frequency plane. With the same input interferogram as was already used in 6.3, we obtain the results shown in Fig. D.5.

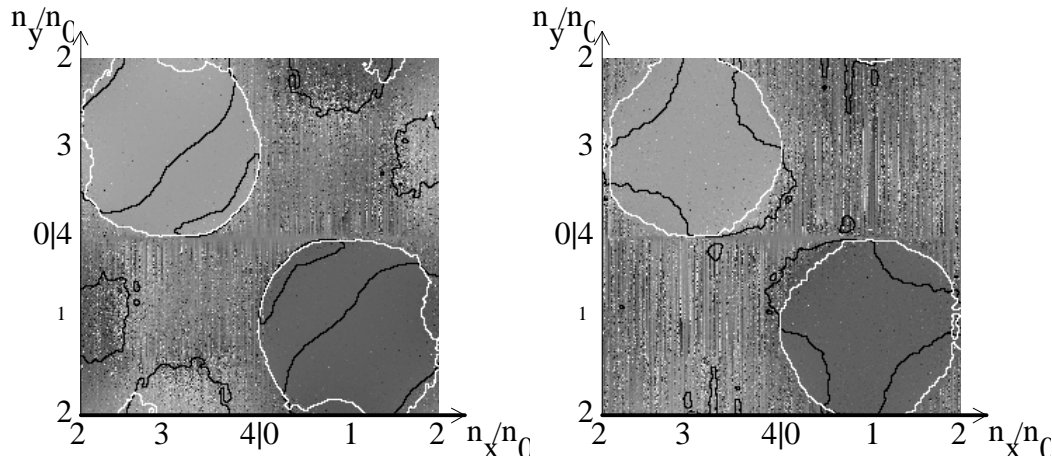


Fig. D.5:  $bsc(v_x, v_y)$  for (D.1) (left) and (D.2) (right). Black lines: frequency co-ordinates leading to correct phase calculation,  $bsc(v_x, v_y) = \pm 45^\circ$ ; white outlines: areas of  $-10^\circ \leq \delta\varphi \leq 10^\circ$ .

As to be seen, both formulae are capable of calculating  $\varphi_O$  with  $|\delta\varphi| \leq 10^\circ$  in a very wide range of  $(v_x, v_y)$ ; (D.1) exhibits a slightly worse phase calculation at very high spatial frequencies, so that we can expect to find small performance differences in phase measurements. When the interferograms already used for 6.3-6.5 were re-evaluated with the formulae presented here, the resulting  $\sigma_d(N_x)$  were as graphed in Fig. D.6.

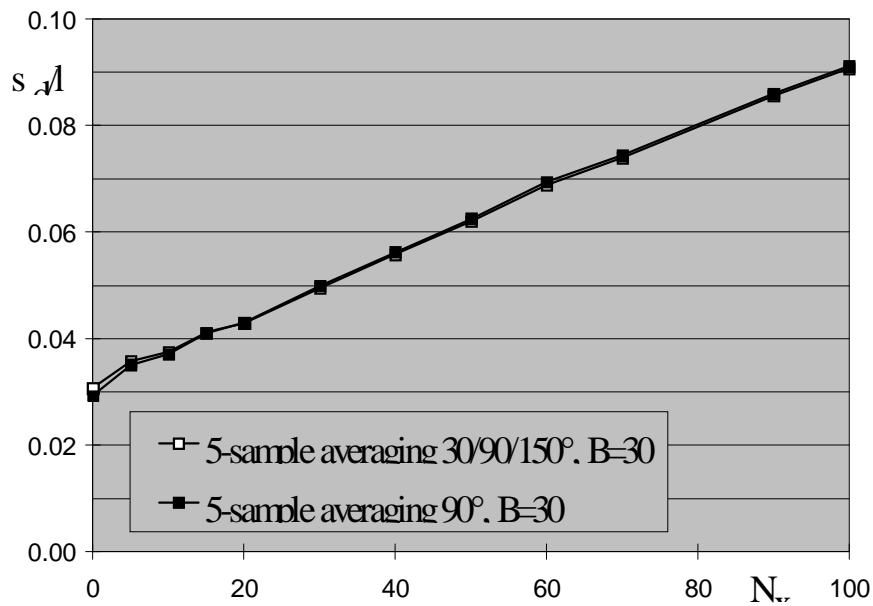


Fig. D.6:  $\sigma_d$  from ESPI displacement measurements as a function of  $N_x$ , obtained with (D.1) (white filled symbols) and (D.1) (black symbols). Input interferograms were from the same tilt series as in 6.3.

The plots show that the performance of (D.1) and (D.2) is indeed very similar<sup>\*</sup>; by comparison with the results in terms of  $\sigma_d$  in 6.3-6.5, it can be seen that they are also well suited for phase evaluation in SPS and yield a performance similar to that obtained by (6.16) and its intensity-correcting version, and by the FTM. However a correction for speckle intensity cannot readily be incorporated in these formulae.

Moreover, a careful comparison of  $\sigma_d$  at higher  $N_x$  with that in previous results shows that now the spatial extent of the phase-sampling window contributes significantly to the smoothing of phase maps. In this

<sup>\*</sup> The same applies to formulae with zero error for  $\alpha=45/90/135^\circ$  and  $\alpha=60/90/120^\circ$ , which were tested as well.

respect, the schemes developed in 6.3 may be somewhat more suitable to preserve spatial resolution. The relative pixel weights for (6.11) are visualised in Fig. D.7; it can be seen that the target pixel, in the centre of the cross shape, contributes the largest part to phase calculation.

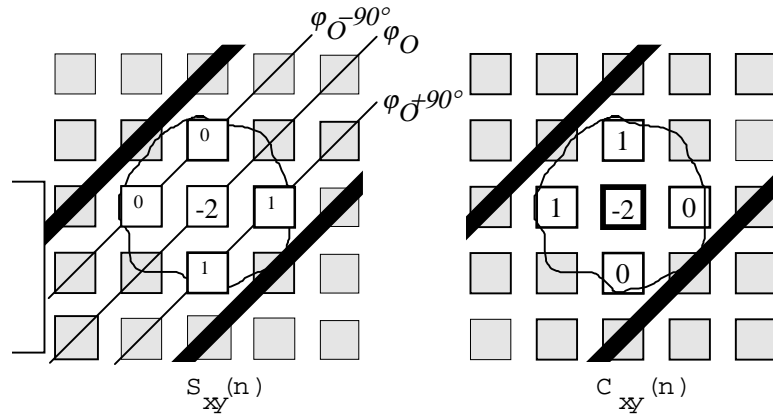


Fig. D.7: Relative pixel weights for spatial intensity sampling by (6.11).

When the sampling pixel cluster is enlarged to enable the application of (6.16), we get the weighting windows depicted in Fig. D.8.

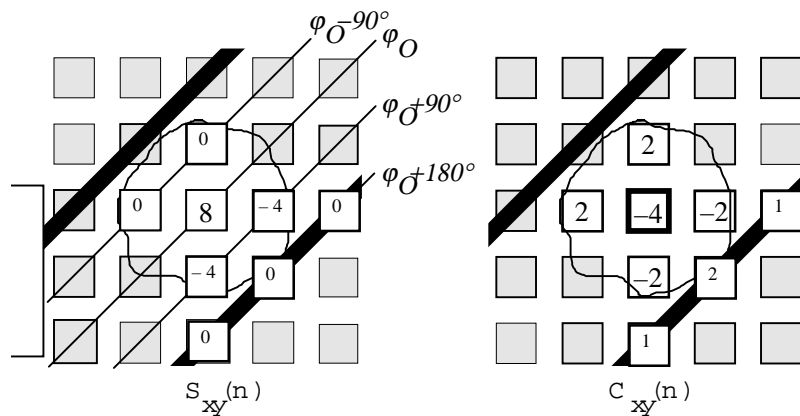


Fig. D.8: Relative pixel weights for spatial intensity sampling by (6.16).

Also in this case, the intensity sample from the target pixel enters the phase calculation with the greatest weight; however, for  $C_{xy}(n)$  some more remote pixels must be included, fortunately with small contributions.

Comparing the sampling windows shown in Fig. D.7 and Fig. D.8 with those from Fig. D.2 and Fig. D.4, it gets apparent that the 5-sample formulae are associated with significant low-pass filtering of the resulting phase maps. In particular, the central pixel has zero weight in the implementations of the  $S_{xy}(n)$ , this being a necessity in symmetrical 5-sample formulae.

On the other hand, since spatial resolution is generally a small problem in practical ESPI, the formulae that have been briefly investigated here should prove useful as well.

## Acknowledgements

It is with pleasure that I list some of the persons by name who have been involved in this work by being helpful and inspiring.

First of all, I sincerely thank Heinz Helmers for five years of enjoyable and fruitful collaboration, and also for his thorough review of the first version of this thesis that has definitely contributed to making it more readable and consistent.

Also, I am indebted to Klaus Hinsch for valuable comments, and for a considerable freedom to organise and develop my research activities in a way that enabled keeping up a productive atmosphere and good humour all the time.

I am grateful to Volker Mellert for his benevolent readiness to take over the part of the second referee.

Then I would like to mention Christian Kunze and Volker Wilkens for the joint research of our large-speckle measurements, which was an enriching and memorable experience.

The same is true of the research project about pure in-plane SPS that R. S. Sirohi and I performed together when he was with our workgroup; in fact he taught while we were working, and I am grateful for what I learnt from him.

Alexander Brozeit, Henning Sagehorn and Roman Schuh contributed the phase stabilisation unit and a good deal of teamwork, which enabled bringing our expertises together successfully.

I thank my office colleague, Thomas Fricke-Begemann, for many interesting discussions, in particular the exciting excursions through the frequency plane, occasional co-operation, and his large contribution to the pleasant working atmosphere.

Also the other members of the Applied Optics workgroup at Oldenburg are a great staff to work with, and I appreciate the collegial and easy ambience in which this work was done, as well as their interest, comments, their help and asking for help.

The exchange of ideas with colleagues from other laboratories, and their pleasant and inspiring company at conferences, have contributed to the progress of the work and always added an extra push of community feeling and motivation.

I am deeply grateful to my parents who have provided every kind of support and encouragement one can wish, which I feel was an essential basis to cope with the strains associated with such a project.

Another big thankyou goes to Tatjana, for her patience with my always being busy, for all her successes in keeping me from working on week-ends, and for the constant sunshine of her love.

Finally, thank you, dear reader, for your interest.





---

## **Erklärung nach Promotionsordnung**

Hiermit erkläre ich, daß ich die vorliegende Arbeit selbständig verfaßt und nur die angegebenen Hilfsmittel benutzt habe.

*Jan Burk*



## The author

### Person

Name	Jan Burke
Address	Hunoldstr. 16, D-26203 Hundsmühlen
Place of birth	Kiel
Date of birth	July 13, 1967
Nationality	German
Marital status	single

### School

1973-1977	Primary school: Jahn-Schule, Kiel
1977-1986	High school: Gymnasium Kiel-Altenholz (sets: music/physics)
May 28, 1986	Abitur

### Studies

Mar 1988-Dec 1990	Physics: Basic studies at the Christian-Albrechts-Universität zu Kiel
Jan 1991-Jul 1991	Chemistry: Practical training in the Bundesanstalt für Milchforschung, Kiel
Sep 1991-Oct 1995	Physics: Principal studies at the Carl von Ossietzky University Oldenburg
Oct 6, 1995	Physics: Diploma degree

### Working life

Nov 1995-Nov 1997	Scientific collaborator in the project "Contributions to the automatisisation of displacement measurements on complex-structured surfaces with coherent optical methods", CvO University Oldenburg, Physics Department, Applied Optics Group
Apr 1998-Jul 1999	Scientific collaborator for the prolongation of the above project, <i>ibid.</i>
Aug 1999-Oct 1999	Scientific assistant, <i>ibid.</i>
Jan 2000-Feb 2000	Scientific assistant, <i>ibid.</i>

### List of publications

1. T. Bothe, J. Burke, H. Helmers: Spatial phase shifting in ESPI: minimization of phase reconstruction errors, *Appl. Opt.* 36.22 (1997), 5310-5316
2. R. Sirohi, J. Burke, H. Helmers, K. Hinsch: Spatial phase shifting for pure in-plane displacement and displacement-derivative measurements in ESPI, *Appl. Opt.* 36.23 (1997), 5787-5791
3. J. Burke, H. Helmers, C. Kunze, V. Wilkens: Speckle intensity and phase gradients: influence on fringe quality in spatial phase shifting ESPI systems, *Opt. Comm.* 152 (1998), 144-152
4. J. Burke, H. Helmers, K. Hinsch, C. Kunze, V. Wilkens: Messung schnell veränderlicher Verformungen mit räumlich phasenschiebender elektronischer Specklemuster-Interferometrie (ESPI), *Z. Angew. Math. Mech.* 78, Suppl. 1 (1998), 321-322
5. J. Burke, H. Helmers: Complex division as a common basis for calculating phase differences in ESPI in one step - Technical Note, *Appl. Opt.* 37.13 (1998), 2589-2590
6. A. Brozeit, J. Burke, H. Helmers, H. Sagehorn, R. Schuh: Noise reduction in ESPI fringes by merging orthogonally polarised speckle fields, *Opt. Las. Technol.* 30 (1998), 325-329
7. A. Brozeit, J. Burke, H. Helmers: Active phase stabilisation in ESPI without additional optical components, *Opt. Comm.* 173 (2000), 95-100
8. J. Burke, H. Helmers: Spatial vs. temporal phase shifting in ESPI: noise comparison in phase maps, *Appl. Opt.* 38.25 (2000), 4598-4606
9. J. Burke, H. Helmers: Matched data storage in ESPI by combination of spatial phase shifting with temporal phase unwrapping, *Opt. Las. Technol.* 32.4 (2000), 235-240

### Conference contributions

#### Oral presentations

Messung schnell veränderlicher Verformungen mit räumlich phasenschiebender ESPI, Annual conference of the Ges. Angew. Math. Mech. (GAMM), March 24-27 (1997), Regensburg

Quantitativer Vergleich räumlich und zeitlich phasenschiebender ESPI-Systeme, 99<sup>th</sup> annual conference of the Deutsche Gesellschaft für angewandte Optik (DGaO), June 2-6 (1998), Bad Nenndorf

Quantitative comparison of SPS vs. TPS in ESPI, International Conference on Applied Optical Metrology (ICAOM), June 8-11 (1998), Balatonfüred

Aktive Phasenstabilisierung in ESPI: ein Echtzeit-Regelkonzept ohne Zusatzoptik, 100<sup>th</sup> annual conference of the DGaO, May 25-29 (1999), Berlin

Performance of spatial vs. temporal phase shifting in ESPI, Interferometry '99, September 20-23 (1999), Pułtusk

---

**Articles**

1. J. Burke, T. Bothe, H. Helmers, C. Kunze, R. Sirohi, V. Wilkens: Spatial phase shifting in ESPI: influence of second-order speckle statistics on fringe quality, in: *Automatic Processing of Fringe Patterns, Fringe 97*, Akademie Verlag, Berlin (1997), 111-116
2. R. Sirohi, J. Burke, T. Bothe, H. Helmers, K. Hinsch: New applications of Michelson stellar interferometer in speckle metrology using spatial phase shifting, in: *Automatic Processing of Fringe Patterns, Fringe 97*, Akademie Verlag, Berlin (1997), 489-496
3. J. Burke, H. Helmers: Performance of spatial vs. temporal phase shifting in ESPI, in: *Interferometry 99: Techniques and Technologies*, Proc. SPIE 3744 (1999), 188-199
4. H. Helmers, J. Burke: How knowledge about speckle intensity and phase gradients can improve electronic speckle pattern interferometry, in: *18<sup>th</sup> Congress of ICO: Optics for the next millennium*, Proc. SPIE 3749 (1999), 216-217

